High Temperature Superconducting Partial Core Transformers

Andrew Lapthorn

A thesis presented for the degree of
Doctor of Philosophy
in
Electrical and Computer Engineering
at the
University of Canterbury,
Christchurch, New Zealand.

2012

I dedicate this thesis to my wife Naomi. Without your patience, understanding, support, and most of all love, the completion of this work would not have been possible.

ABSTRACT

The thesis begins by providing an introduction to transformer theory. An ideal transformer is examined first, followed by full core transformer theory. The partial core transformer is then introduced and compared to the full core design. An introduction to superconductors is then presented where a simplified theory of superconductivity is given. High temperature superconductors are then examined including their physical structure, superconducting properties and the design of the superconducting wire.

The early development of high temperature superconducting partial core transformers at the University of Canterbury is then examined. Early partial core development is discussed followed by some material testing at cryogenic temperatures. This work lead into the development of the first high temperature superconducting partial core transformer. This transformer failed during testing and an examination of the failure mechanisms is presented. The results of the failure investigation prompted an alternative winding insulation design which was implemented in a full core superconducting transformer.

The modelling used to design a high temperature superconducting partial core transformer is then presented. Based upon the reverse design method, the modelling is used to determine the components of the Steinmetz equivalent transformer circuit. The modelling includes a combination of circuit theory and finite element analysis. An ac loss model for high temperature superconductors is also presented.

A new 15 kVA, 230-230 V high temperature superconducting partial core transformer was designed, built and tested. The windings are layer wound with first generation Bi2223 high temperature superconductor. The modelling was used to predict the performance of the transformer as well as the ac losses of the high temperature superconductor. A series of electrical tests were performed on the transformer including open circuit, short circuit, resistive load, overload, ac withstand voltage and fault ride through tests. The test results are compared with the model. The transformer was found to be 98.2 % efficient at rated power with 2.86 % voltage regulation.

LIST OF PUBLICATIONS

The following is a list of papers that have been accepted for publication during the research presented in this thesis.

JOURNAL PAPERS

LAPTHORN, A.C., CHEW, I., ENRIGHT, W.G. AND BODGER, P.S. (2011), 'HTS Transformer: Construction Details, Test Results, and Noted Failure Mechanisms', *Power Delivery, IEEE Transactions on* , Vol. 26, No. 1, pp.394-399.

LAPTHORN, A.C., BODGER, P.S. AND ENRIGHT, W.G. (2012), 'A 15 kVA High Temperature Superconducting Partial Core Transformer: Part 1 - Transformer Modelling', submitted to *IEEE Transactions on Power Delivery* on 26/01/12.

LAPTHORN, A.C., BODGER, P.S. AND ENRIGHT, W.G. (2012), 'A 15 kVA High Temperature Superconducting Partial Core Transformer: Part 2 - Construction Details and Experimental Testing', submitted to *IEEE Transactions on Power Delivery* on 26/01/12.

CONFERENCE PAPERS

LAPTHORN, A.C., CHEW, I., ENRIGHT, W.G. AND BODGER, P.S. (2011), 'Experiences Determining the AC Current Rating of HTS Tapes in Power Transformers', In *Asia-Pacific Power and Energy Engineering Conference (APPEEC)*, Wuhan, Hubei, China, March, pp.1-4.

LAPTHORN, A. AND BODGER, P. (2010), 'An AC loss model for Bi2223 superconductors in partial core transformers', In *Australasian Universities Power Engineering Conference. (AUPEC)*, Christchurch, New Zealand, December, pp.1-4.

LAPTHORN, A.C., CHEW, I. AND BODGER, P.S. (2010), 'An Experimental High Temperature Superconducting Transformer: Design, Construction and Testing', In *Electricity Engineers' Association (EEA) Conference*, Christchurch, New Zealand, June, pp.1-9.

LAPTHORN, A. AND BODGER, P. (2009), 'A Comparison Between the Circuit Theory Model and Finite Element Model Reactive Components', In *Australasian Universities Power Engineering Conference. (AUPEC)*, Adelaide, South Australia, September, pp.1-6.

CHEW, I., LAPTHORN, A., BODGER, P. AND ENRIGHT, W. (2009), 'Superconducting transformer failure: Testing and investigation', In *Australasian Universities Power Engineering Conference. (AUPEC)*, Adelaide, South Australia, 27-30 September, pp.1-5.

OTHER PRESENTATIONS

LAPTHORN, A.C., CHEW, I., ENRIGHT, W.G. AND BODGER, P.S. (2010), 'HTS Transformers', In *18th International Superconductivity Industry Summit (ISIS-18)*, Wellington, New Zealand, February, poster presentation.

Additionally, a 20 minute oral presentation titled 'Superconducting Transformer Failure: Testing and Investigation' was presented at the *Electricity Engineers' Association (EEA) Annual Power Engineering Exchange (APEX 09) Southern Summit*, Christchurch, New Zealand, 20 August 2009.

ACKNOWLEDGEMENTS

CONTENTS

LIST OF FIGURES

LIST OF TABLES

GLOSSARY

The following glossary contains a list of the commonly used nomenclature and abbreviations found in this thesis.

NOMENCLATURE

$\lvert k \rvert$	Magnitude of k
$\mathfrak{R}$	Magnetic reluctance
μ	Magnetic permeability in henries per meter
μ_0	Magnetic permeability of free space equal to $4\pi \times 10^{-7}$
ω	Angular frequency in radians per second
ϕ_k	Magnetic flux of k in webers
ρ_k	Resistivity of k in ohm meters
a	Nominal turns ratio
A_k	Area of k in square meters
B	Magnetic field density in tesla
e_k, E_k	Induced emf of k in volts
f	Frequency in hertz
H	Magnetic field intensity in ampere-turns
i_k, I_k	Current of k in amperes
j_k, J_k	Current density of k in amperes per square meter
L_k	Inductance of k in henries
l_k	Length of k in meters
N_k	Number of turns of winding k
P_k	Power dissipated from k in watts
R_k	Resistance of k in ohms
v_k, V_k	Voltage of k in volts
WT_k	Weight of k in kilograms
X_k	Reactance of k in ohms
E_C	Electric field criterion equal to $100\mu V/m$
H_C	Critical magnetic field

J_C Critical current density
T_C Critical temperature

ABBREVIATIONS

CuO Copper oxide
LN_2 Liquid nitrogen
ac   Alternating current
BSCCO   Bismuth strontium calcium copper oxide
CAM   computer-aided manufacturing
CTM   Circuit theory method
dc   Direct current
DMM   digital multi-meter
emf   Electromotive force
FEA   Finite element analysis
FEM   Finite element method
HTS   High temperature superconductor
HTSPCT   High temperature superconducting partial core transformer
IR   infra red
LED   light emitting diode
mmf   Magnetomotive force
PCT   Partial core transformer
PIT   Powder in tube
RABiTS   Rolling assisted biaxially textured substrates
RDM   Reverse design method
RMS   Root mean squared
TDP   Transformer Design Program
UoC   University of Canterbury
VBA   Visual Basic for Applications
YBCO   Yttrium barium copper oxide

Chapter 1

INTRODUCTION

1.1 GENERAL OVERVIEW

Transformers have been around for over a century and their design and construction have advanced over the years to the point where there is little room for improvement and they can be considered a mature technology. After the discovery of superconductivity in the early part of the 20th century it was thought that these new materials could be used in transformer construction. Unfortunately, due to the extremely low temperatures required for superconductivity, $< 5\,\mathrm{K}$, expensive cryogenic technology using liquid helium was needed and the refrigeration energy required at room temperature to remove the low temperature heat generated was over 1000 to 1. These factors limited the use of superconductors to dc applications such as MRI scanners and large magnets where the losses were at acceptability low levels.

In the late 1980's, a new class of superconductors was discovered which was previously thought impossible. This new type of material had critical temperatures greater than the boiling temperature of liquid nitrogen and became known as high temperature superconductors. These new superconductors could be cooled far more economically using liquid nitrogen and the ratio of room temperature energy input required to remove low temperature energy was reduced to around 25 to 1. With the development of high temperature superconducting wire into long lengths and high current densities it became far more feasible to use this material in power frequency applications including transformers.

Many research groups around the globe have developed various high temperature superconducting transformers [Therond *et al.* 1998, Schwenterly *et al.* 1999, Pleva and Schwenterly 2004, Kim *et al.* 2005]. These designs have tended to be rather conventional in terms of transformer design where a standard copper winding set was replaced with a superconducting coil. One of the major advantages to using superconductors is the extremely high current density possible in the winding compared to that of conventional materials such as copper. This allows for the winding window to be much smaller than a similar rated copper transformer reducing the size and weight of the transformer.

Another way to further reduce the size and weight of a transformer is use a partial core. This differs from the conventional design because the outer limbs and connecting yokes are absent. Instead the flux return path is air. By combining the partial core concept with high temperature superconductors, a new novel and compact transformer will be possible. With careful design, the performance of this type of transformer should be comparable to similar rated conventional transformers at a reduced size and weight.

1.2   THESIS OBJECTIVES

The objective of this thesis is to develop a design methodology for a high temperature superconducting partial core transformer. To be able to demonstrate this design methodology, a prototype high temperature superconducting partial core transformer was designed, built, and tested.

To be able to achieve this objective, various modelling and analysis techniques were developed and a program was written that was able to design partial core transformers with either copper, aluminium or high temperature superconducting windings.

1.3   THESIS CONTRIBUTION

The work in this thesis has lead to the production of the world's first, fully functional, high temperature superconducting partial core transformer. This has been achieved through three significant steps;

- The testing to failure of the original prototype high temperature superconducting partial core transformer and subsequent failure investigation. This work lead to the development of an alternative winding design enabling greater cooling of the superconductor wire whilst maintaining excellent structural properties.

- The development of an ac loss model for the superconductor used in the transformer. This model uses a combination of empirical and theoretical calculations combined with detailed finite element analysis of the magnetic field in the winding space to obtain the losses for every turn in the winding space. The losses are then added together to obtain the overall winding loss.

- The proof of the design via the construction and thorough testing of a new high temperature superconducting partial core transformer. The validity of the modelling was tested through comparisons to measured data with good results. The structural integrity and

thermal properties of the winding design were validated through extensive testing of the transformer prototype.

1.4   THESIS OUTLINE

Chapter 2 provides an overview of the basic theory behind high temperature superconducting transformers. This overview begins with examining an ideal transformer followed by introducing typical loss mechanisms. A look at some of the properties of full core transformers is next, then the concept of partial core transformers is developed. The chapter finishes with a section on superconductors where the origins and basic theories of the material are discussed with a special emphasis on high temperature superconductors.

Chapter 3 details the steps taken to develop working superconducting transformer prototypes at the University of Canterbury. It contains a look at early partial core development with copper windings at room temperature and the design methods used during this development, including experiments testing materials at cryogenic temperatures. A prototype 15 kVA high temperature superconducting partial core transformer is presented including design, construction details and test results. A failure of this prototype occurred and an investigation into the failure was conducted. This lead to an alternative winding design that is also presented in this chapter. A discission of the lessons learned throughout the development process finishes off the chapter.

Chapter 4 is where the modelling of the transformer is developed. A general model of partial core transformers is given based on the Steinmetz equivalent circuit for transformers. This includes a new modelling method for calculating the eddy current losses in partial core transformers. The second part of the chapter relates to developing a model for calculating ac losses for superconducting tapes, specifically 1G BSCCO, which is then verified by experimental data.

Chapter 5 discusses the design and construction of a new high temperature superconducting partial core transformer. A program for designing high temperature superconducting partial core transformers was written in Visual Basic and is presented here. The program is used to design and construct a new prototype transformer based on some design constraints from the previous failed transformer in Chapter 3. Details of the construction of the new transformer are given including the insulation design, a cooling system, and a quench detection system.

Chapter 6 tests the performance of the high temperature superconducting partial core transformer. The test results are compared to the modelling from Chapter 4. A discussion of the results follows.

Chapter 7 discusses possible directions for future research and development

Chapter 8 presents the main conclusions of this thesis

Chapter 2

BACKGROUND

2.1 INTRODUCTION

There are many different types of transformers available in the world today such as pulse transformers, isolating transformers and motor starting transformers. One of the most common types of transformer is the power transformer. This type of transformer is designed to change the voltage of an alternating current (ac) electric system from one level to another. Doing this usually allows for a higher efficiency of power transfer and a near constant output voltage regardless of the load.

Power transformers, and indeed the electric power system as we know it today, became possible in part by the discovery of electromagnetic induction by Michael Faraday in 1831 [Faraday 1834]. He was the first to perform experiments on induction between coils of wire by winding the coils around an iron ring creating the first transformer. Faraday's experiments showed that the induced electromotive force (emf) in any closed circuit is equal to the time rate of change of the magnetic flux through the circuit,

$$|e| = \left| \frac{d\phi}{dt} \right| \tag{2.1}$$

where $|e|$ is the magnitude of the induced emf in volts and ϕ is the magnetic flux in webers. Researchers soon discovered that by adding more turns to the secondary coil, the induced emf in the secondary could be increased.

The first transformers, known as induction coils, were used by scientists and inventors to obtain larger voltages from batteries [Dolbear 1896]. This was achieved by using a vibrating interrupter to create the time varying flux. It was not long however, before transformers started to be used in electrical lighting systems. These first systems consisted of a number of series connected coils with near unity turns ratio, and were used to connect low voltage lights to a higher voltage transmission system. The drawback of this system was that if one light switched off, the voltage

across all the other lights was affected. These first induction coils were primarily open core devices and were not very efficient.

In 1884, a team of engineers lead by K. Zipernowsky, O. Bláthy and M. Déri from the Ganz factory in Budapest invented the first closed core, shunt connected device. The Ganz team were the first to use the term transformer in their patent application [Zipernowsky *et al.* 1886]. The Z.B.D. transformer, as it became known, had an efficiency of 98%, much higher than the existing induction coils of the time. Around the same time, George Westinghouse Jr. of the Westinghouse company assigned William Stanley to develop a device for commercial use in the United States. Stanley's device used an adjustable air gap for voltage regulation [Stanley and Westinghouse 1886]. Westinghouse quickly followed up this design in 1887 with the first E shaped laminated core [Westinghouse 1887].

These early practical transformer designs enabled the efficient transformation of voltage from low voltage ac generators to high voltage transmission lines. The higher voltages greatly reduced the current in the transmission lines and therefore the power losses, because the power loss is proportional to the square of the current. This was one of the main reasons why the ac electrical system prevailed over the direct current (dc) system in the *War of the Currents* between George Westinghouse and Thomas Edison in the 1880s and is still dominant today [Surhone *et al.* 2010].

2.2   TRANSFORMER FUNDAMENTALS

In order to understand the operation of a transformer, it is useful to look at an ideal transformer and then the departure from the ideal.

2.2.1   Ideal Transformers

Ideal transformers consist of two or more coils of wire wound around a common core of perfect ferromagnetic material. The core provides a path for the magnetic flux linking the two windings. Furthermore, by using coils of wire with N_1 primary turns and N_2 secondary turns, an emf proportional to the number of turns of that winding is produced.

$$|e_1| = N_1 \left| \frac{d\phi}{dt} \right| \tag{2.2}$$

and

$$|e_2| = N_2 \left| \frac{d\phi}{dt} \right| \tag{2.3}$$
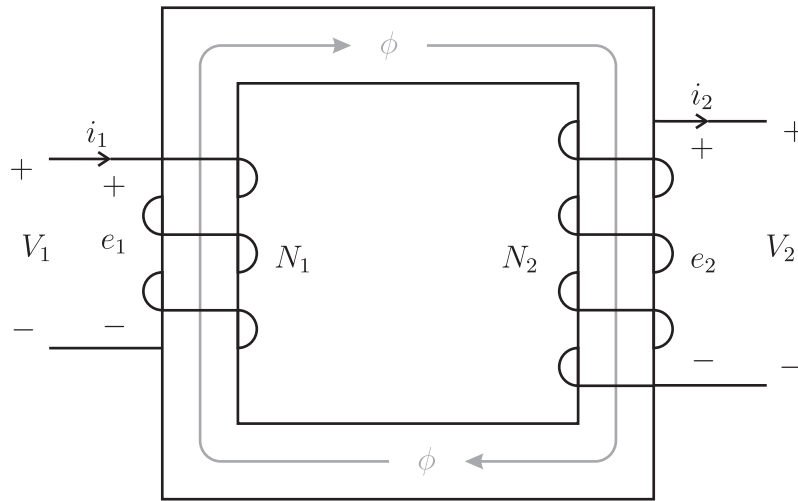
(a) The schematic.
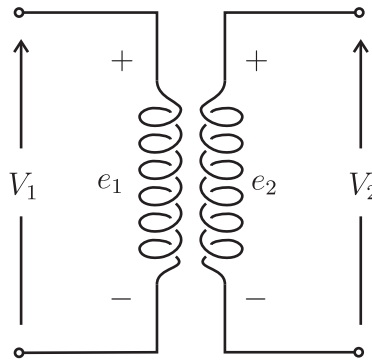
(b) Equivalent circuit.

Figure 2.1   An ideal full-core transformer.

By changing the ratio of N_1 to N_2, the induced emf in the secondary winding can be changed with respect to the primary. In an ideal transformer, such as that depicted in Figure 2.1, $e_1 = V_1$ and $e_2 = V_2$ which leads to,

$$\frac{e_1}{e_2} = \frac{V_1}{V_2} = \frac{N_1}{N_2} = a \tag{2.4}$$

where a is the nominal turns ratio.

Generally in transformers, the flux varies sinusoidally so that the induced emf linking an N turn winding is given by Faraday's law as

$$e = \omega N \phi_m cos(\omega t) \tag{2.5}$$

where ω is the frequency in radians per second and ϕ_m is the peak amplitude of the magnetic

flux. From Equation 2.5, the root mean squared (RMS) value of the induced voltage is therefore,

$$E = \frac{\omega N \phi_m}{\sqrt{2}} = 4.44 f N \phi_m \tag{2.6}$$

where f is the frequency in hertz (Hz). Equation 2.6 is often referred to as the emf or Transformer equation.

In an ideal transformer, the magnetomotive force (mmf) required to produce the flux in Figure 2.1(a) is negligibly small. The mmf is due to a combination of the primary current, i_1, and the secondary current, i_2 so that,

$$N_1 i_1 = N_2 i_2 \tag{2.7}$$

and

$$\frac{i_1}{i_2} = \frac{N_2}{N_1} = \frac{1}{a} \tag{2.8}$$

From Equations 2.4 and 2.8 it can be shown that,

$$e_1 i_1 = e_2 i_2 \tag{2.9}$$

Thus the apparent power of the primary winding is equal to the apparent power of the secondary winding. The primary winding absorbs power from the source while the secondary winding delivers it to the load. In an ideal transformer there is no internal power loss so that these two quantities are equal.

2.2.2   Departure From The Ideal

As with all things in the physical world, power transformers are not ideal. While they are quite efficient at power transfer, typically in the high 90% region, they do experience losses due to their design and the physical properties of the materials used. Figure 2.2 is an equivalent circuit for a power transformer operated at power system frequencies. The diagram shows an ideal transformer coupled with other components to model the various non ideal characteristics.

When a conductor, such as the copper or aluminium used in transformer windings, has a current flowing in it, heat is dissipated. This process is known as Joule heating or resistive heating and is caused by the interaction of particles (normally electrons) that form the current and the atomic
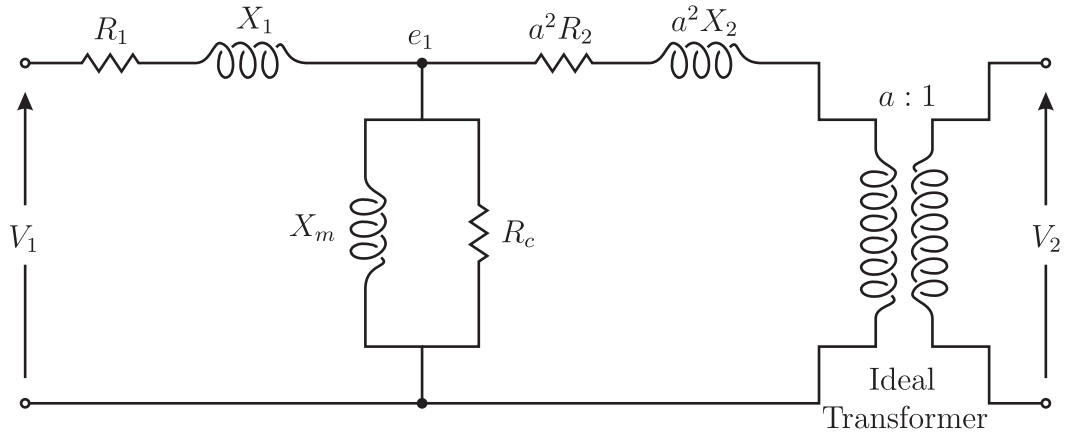
Figure 2.2   Equivalent circuit for a mains frequency transformer.

ions of the conductor. The electrons are accelerated by an electric field and can collide with ions, converting some of their kinetic energy into heat. J. P. Joule discovered that the heat produced was proportional to the square of the current multiplied by the resistance of the conductor, (R_1 and R_2 represent the resistances of the primary and secondary windings respectively).

The time varying magnetic flux in the core of the transformer also causes heating of the core. The heating is due to a combination of hysteresis and eddy current losses. Hysteresis losses are caused by movement of the magnetic dipoles of the core material as they align themselves with the external time varying magnetic field. The eddy current losses are Joule heating due to induced currents circulating in the core material. The time varying magnetic field in the core induces a current in the core in a direction that opposes the field according to Lenz's law. The hysteresis and eddy current losses are proportional to the square of the induced emf and so the core resistance, R_c, is sized so that the power dissipated in it is equal to the combined hysteresis and eddy current losses.

In order to set up a time varying magnetic field in the core a mmf is needed.

$$mmf = \phi\mathfrak{R} \tag{2.10}$$

where $\mathfrak{R}$ is the magnetic reluctance of the core material. Because a real world core material has a finite reluctance, a finite current is needed to produce the ampere-turns required to drive the flux through the core. This current is referred to as the magnetising current and is present regardless of the load. X_m is the magnetising reactance and is valued such that the current through it is equal to the magnetising current.

In an ideal transformer, all the flux generated by the primary winding links with the secondary winding. In a real world transformer, some of the flux generated traverses through the air and does not couple with the other winding, (flux ϕ_{l1} and ϕ_{l2} of Figure 2.3). This is referred to as
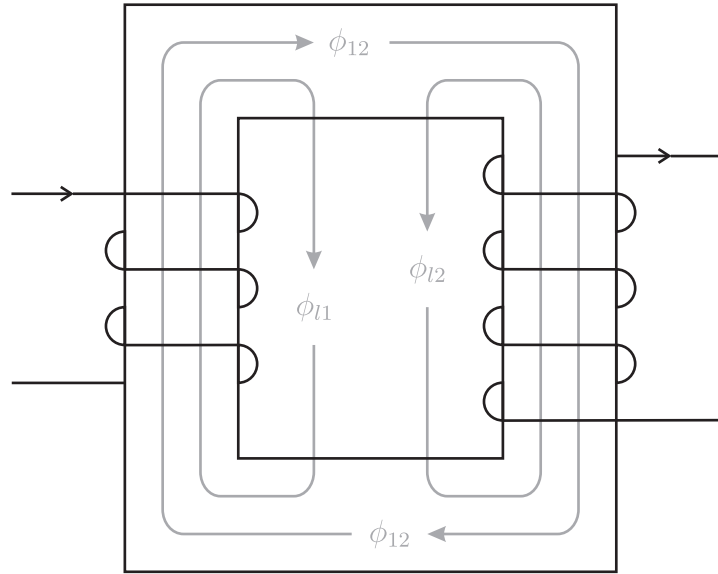
Figure 2.3   Diagram of leakage and mutual flux in a two winding transformer.

leakage flux and is modelled by an inductance in series with the ideal transformer. The leakage flux contributes to the voltage regulation of the transformer causing the voltage ratio to no longer be equal to the turns ratio under heavy loads. X_1 and X_2 are referred to as the leakage reactances of the primary and secondary windings respectively, where in general $X = \omega L$.

2.3   FULL CORE TRANSFORMERS

The most common type of power transformers are full core transformers. There are many different types of full core transformer such as single phase, three phase three limb, and three phase five limb. These devices all use a closed core of low reluctance magnetic material to contain the time varying flux. This means that the mmf required to drive the flux is minimised and the magnetising current is negligibly small when compared to the load current. The drawbacks are that the cross sectional area of the core needs to be maintained over the whole length of the magnetic path to prevent magnetic saturation, which adds to the overall weight and losses of the transformer.

A phasor diagram for a typical two winding full core transformer with an inductive load of lagging power factor $cos\theta_2$ is depicted in Figure 2.4. The open circuit current, I_{oc}, is comprised of two components, the core loss component, I_c, and the magnetising current, I_m. This current is present regardless of the load conditions and is often referred to as the no load current. The primary load current, I_1, is a phasor summation of the open circuit current and the primary load current, I_2'. The primary load current is a transpose of the secondary load current I_2 scaled by the transformer turns ratio.
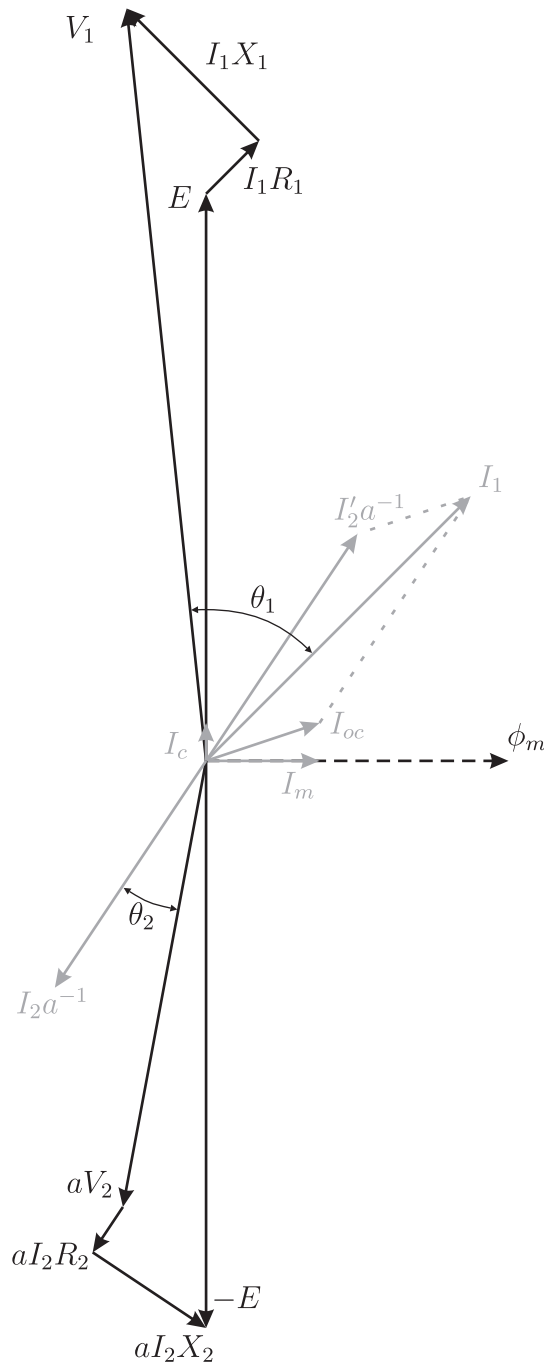
Figure 2.4   Phasor diagram of a full core single phase transformer supplying a partially inductive load.

The magnetising current produces the magnetic flux, ϕ_m, which creates an induced emf, E, according to Faraday's law. The terminal voltages, V_1 and V_2, are a phasor sum of the induced emf and the voltage drops across the resistances and reactances of the primary and secondary windings.

In order to produce a sinusoidal voltage, there must be a sinusoidal flux present in the magnetic circuit as shown in Equation 2.5. The flux in the transformer core is related to the magnetising
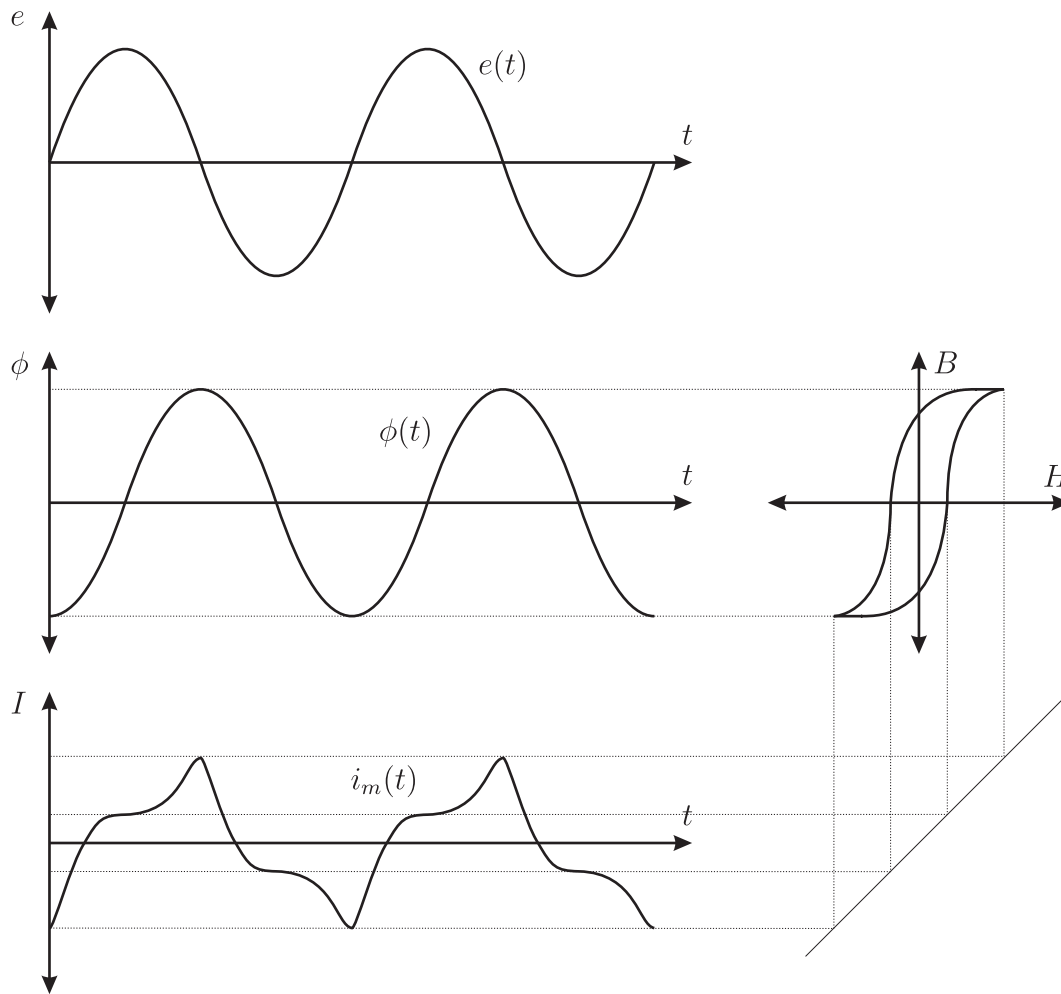
Figure 2.5   Diagram of non linear magnetising current in a full core transformer.

current by the B-H curve of the core material. The steel used in most transformer cores has a non linear B-H relationship as seen in Figure 2.5 which results in a non sinusoidal magnetising current. While this current has a high harmonic content, the magnitude of the current tends to be very small when compared to normal load currents and has minimal effect. In this thesis, sinusoidal voltages, fluxes and currents are assumed.

2.4   PARTIAL CORE TRANSFORMERS

Partial core transformers (PCT) have been designed as an alternative to full core transformers [Liew and Bodger 2001, Bodger *et al.* 2005, Bell 2008], the difference being that the outer limbs and connecting yokes are absent from the PCT, Figure 2.6. This means that the magnetic circuit for a PCT consists of the core and the surrounding air, which results in a high magnetic reluctance when compared with similar full core transformers. Despite this, it is possible to design a PCT that performs comparably to a full core transformer under full load conditions
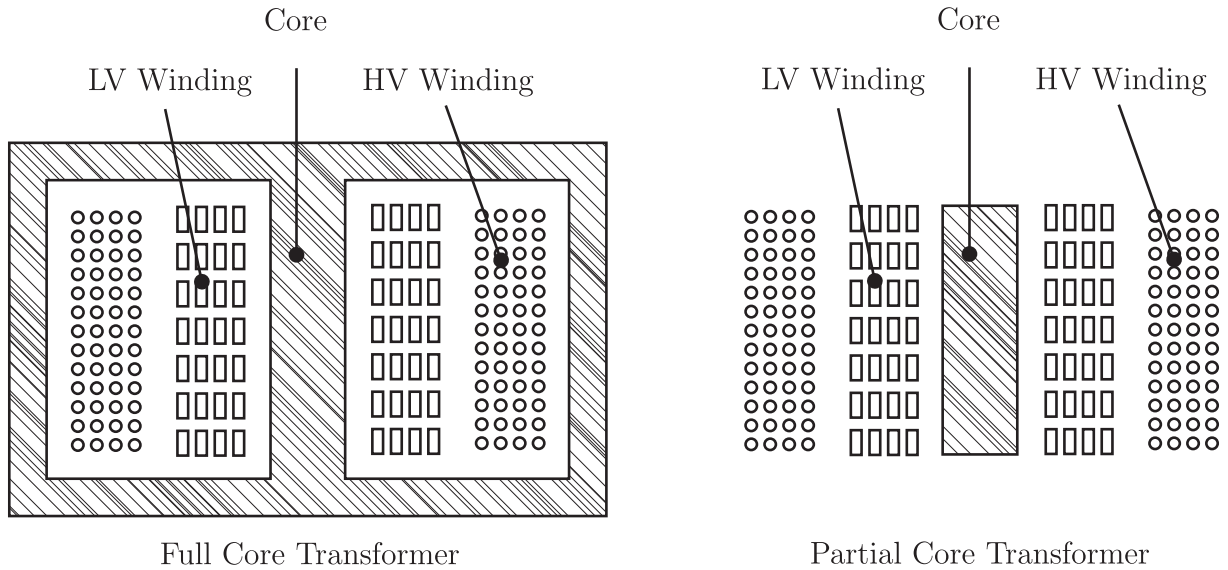
Figure 2.6   A cross-sectional view of the differences between full core and partial-core transformers.

while making significant savings on core material and weight.

Figure 2.7 is a phasor diagram of a partial core single phase transformer supplying an resistive/inductive load. Comparing this diagram with the one from Figure 2.4, it is noticed that the magnetising current is much larger for the partial core transformer. This results in the primary current increasing, but it has a minimal effect on the voltages and secondary current.

Figure 2.8 illustrates the effect of an air gap in the magnetic circuit on the B-H curve of a typical partial core transformer and the resulting magnetising current. When an air gap is introduced, the B-H curve will "flatten out". This results in a larger but more sinusoidal magnetising current compared to that of a full core transformer. In addition, the distortion due to magnetic saturation is greatly reduced.

A significant reason why there are not PCTs in the power system is because the copper losses and efficiency can be poor due to the high magnetising current. The transformer can be large because of the larger cross-section of conductor size required due to the extra magnetising current. However, the application of high temperature superconductors (HTS) eliminates these issues, i.e. they have very low conductor losses and small cross-sectional areas, allowing for very compact and light PCTs. Furthermore, the problematic magnetising current reduces with the square of the number of turns,

$$X_m = \omega L = \omega \frac{N^2}{\mathfrak{R}} \tag{2.11}$$

where L is the inductance of the winding and $\mathfrak{R}$ is the reluctance of the magnetic flux path. Small increases in HTS wire length and therefore number of turns, gives significant reductions
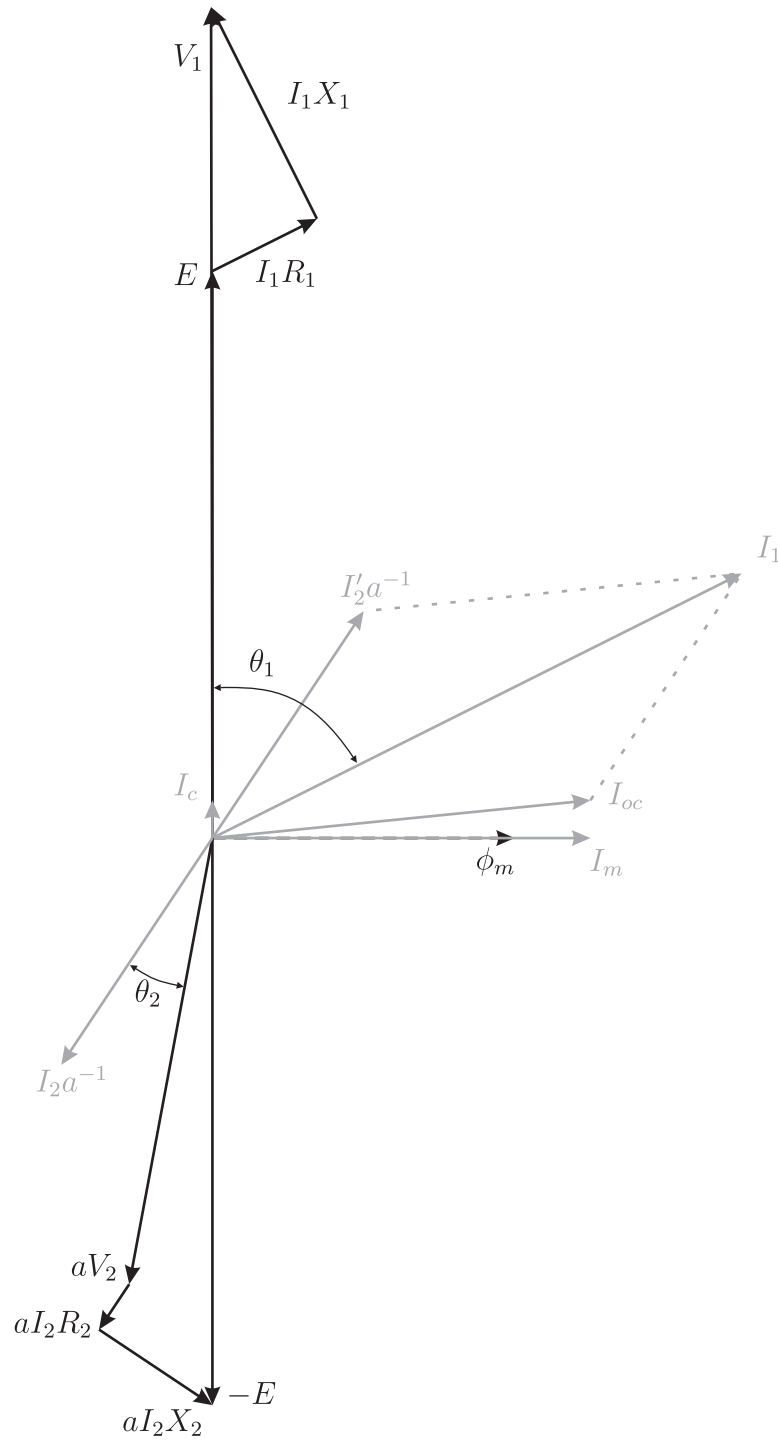
Figure 2.7   Phasor diagram of a partial core single phase transformer supplying a partially inductive load.
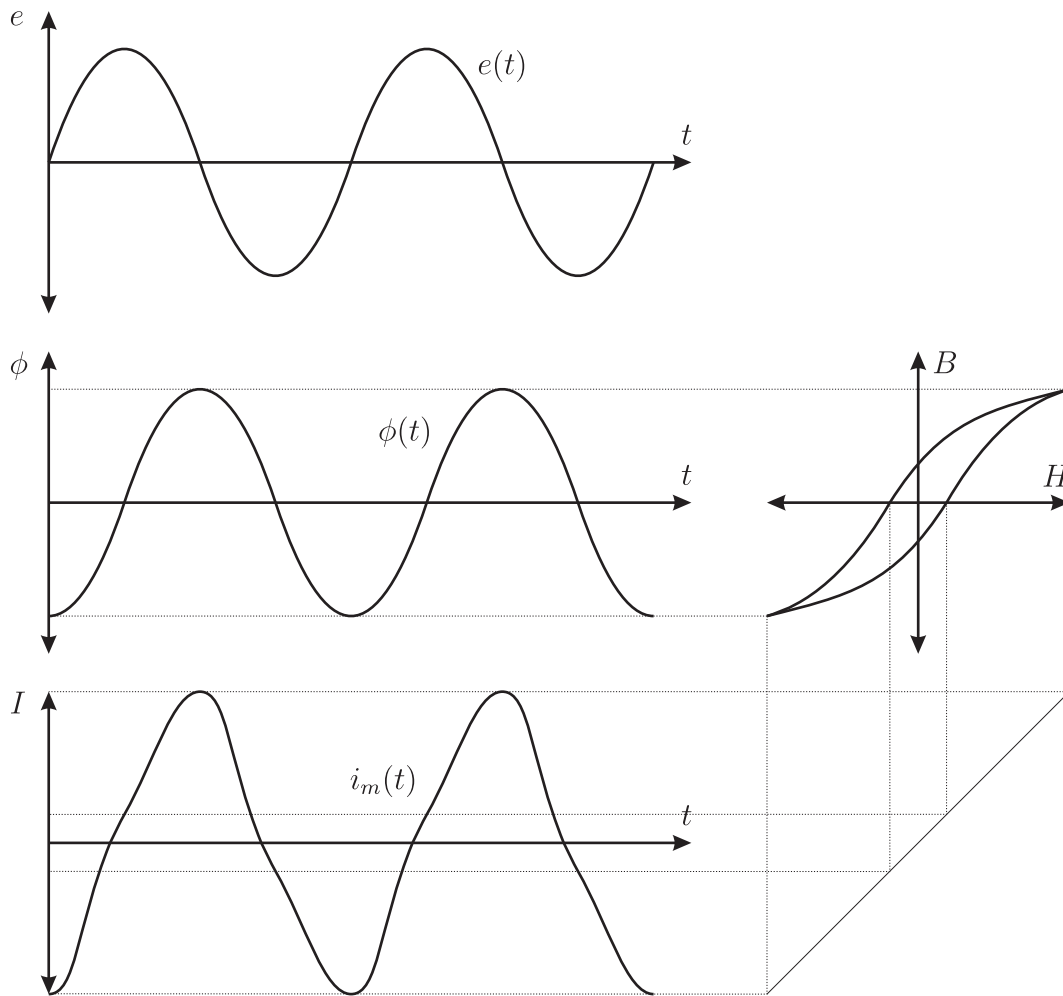
Figure 2.8   Diagram of the magnetising current in a partial core transformer.

in magnetising current without necessarily increasing losses. A disadvantage of using superconductors in the PCT is the cost of the HTS wire. However, as with other technologies, the price of HTS is likely to reduce significantly as the technology matures.

2.5   SUPERCONDUCTORS

As a conductor is cooled, its electrical resistance decreases. However, even at temperatures approaching absolute zero, a measurable resistance still exists in most conductors such as copper. This is due to impurities and imperfections in the material. In some materials, the electrical resistance suddenly drops to zero when the material is cooled below a critical temperature. These materials are known as superconductors. The discovery was made by Dutch physicist Heike Kamerlingh Onnes in 1911 for which he was awarded the Nobel Prize [Onnes 1911]. While investigating the electrical properties of metals at temperatures approaching absolute zero, Onnes noticed the resistance of mercury abruptly disappear below 4.2 K. Onnes called
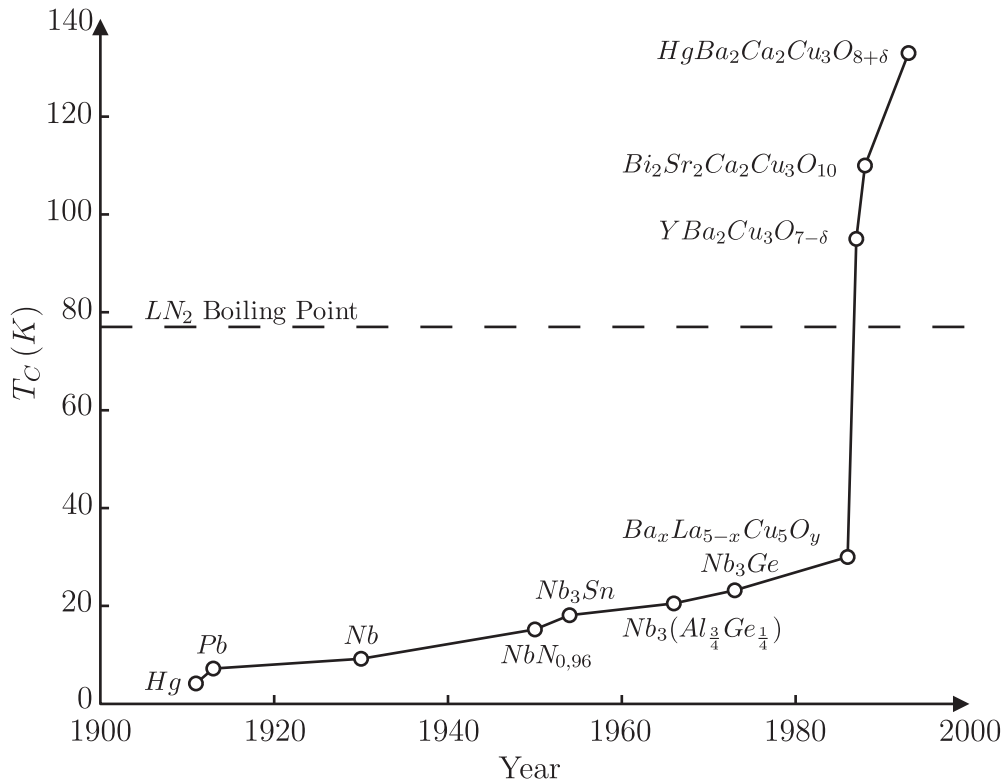
Figure 2.9 Advancement in the critical temperature of superconductors against time. Information gathered from [Poole *et al.* 1995].

this phenomenon *supraconductivity* but later adopted the term superconductivity. Research continued for many years to find other materials that exhibited superconductivity such as lead and niobium (Figure 2.9).

At the same time, theories to explain the behaviour of this new found state were being investigated by many individuals. In 1933, experiments by Walter Meissner and Robert Ochsenfeld found that superconductors expelled external magnetic fields [Meissner and Ochsenfeld 1933]. This phenomenon was later known as the Meissner effect. A phenomenological theory of superconductivity was devised by Vitalij Ginzburg and Lev Landau in 1950 [Ginzburg and Landau 1950], giving a good explanation of the macroscopic properties of superconductors. A complete microscopic theory was developed by John Bardeen, Leon Cooper and John Schrieffer in 1957 [Bardeen *et al.* 1957]. This theory became known as the BCS theory and lead to Bardeen, Cooper and Schrieffer being awarded the Nobel Prize in 1972 making John Bardeen the only person to be awarded the Nobel Prize in Physics twice! His first Nobel Prize in Physics was for inventing the transistor in 1956.

It was widely believed, due to BCS theory, that the maximum critical temperature for superconductivity was 30 K. This all changed in 1986 when Johannes Bednorz and Karl Müller discovered superconductivity in $BaLaCuO$ system in the 30 K range [Bednorz and Müller 1986]. The work earned Bednorz and Müller the Nobel Prize in Physics in 1987. The following year, researchers

from the universities of Alabama and Houston using yttrium instead of lanthanum were able to observe superconductivity transitions between 80 and 93 K [Wu *et al.* 1987]. These materials came to be known as high temperature superconductors due to their greatly increased critical temperature (T_C). This discovery was important because liquid nitrogen (LN_2) could then be used as a coolant instead of liquid helium. LN_2 has a boiling point of 77 K at atmospheric pressure and is cheap and easy to produce from the atmosphere thus avoiding some of the expenses associated with liquid helium.

2.5.1   Theory of Superconductivity

In this section an attempt is made to give an overview into some of the theories of superconductivity. These theories explain the properties of non HTS quite well and the field was considered mature. This changed with the discovery of HTS. While HTS has some similar properties to these theories, there are also some differences. At the time of writing, a complete theory of HTS has yet to be developed.

The London Equations and the Meissner Effect

In a perfect conductor, electrons encounter no resistance to motion. Therefore, if a constant electric field $\mathbf{E}$ is applied, a continuously increasing current occurs given by,

$$\dot{\mathbf{J}}_S = \frac{n_s q^2}{m}\mathbf{E} \tag{2.12}$$

where $\mathbf{J}_S$ is the current density in the conductor, n_s is the number of superconducting electrons per unit volume and m and q are their mass and charge respectively.

Using Maxwell's equations applied to Equation 2.12 [Rose Innes and Rhoderick 1978], an expression for the magnetic field properties of a perfect conductor is given by,

$$\nabla^2 \dot{\mathbf{B}} = \frac{1}{\alpha}\dot{\mathbf{B}} \tag{2.13}$$

where α is the constant $m/\mu_0 n_s q^2$ and μ_0 is the permeability of free space . For the simple case where $\mathbf{B}$ is uniform and parallel to the plane boundary surface of a perfect conductor and x is the direction normal to the boundary, Equation 2.13 simplifies to,

$$\frac{\partial^2 \dot{B}}{\partial x^2} = \frac{1}{\alpha}\dot{B} \tag{2.14}$$
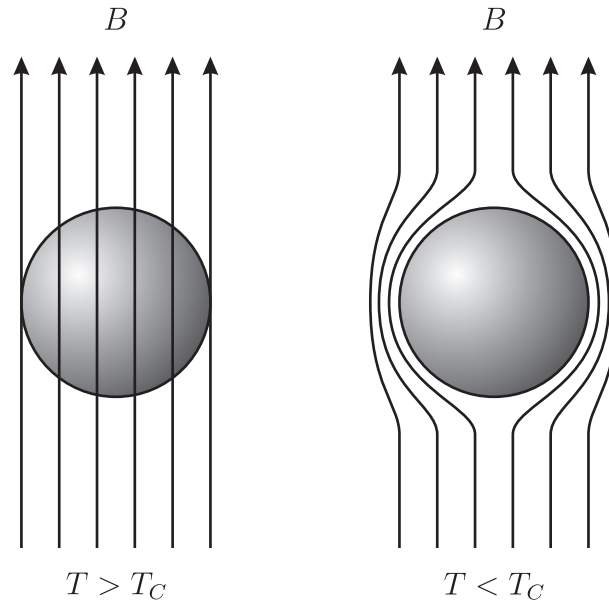
Figure 2.10   When a superconductor drops below its T_C, magnetic fields are expelled from within the conductor due to the Meissner effect. This is explained by the London equations.

Which has the solution,

$$\dot{B}(x) = \dot{B}_a e^{-\left(\frac{x}{\sqrt{\alpha}}\right)} \tag{2.15}$$

where $B(x)$ is the flux density at a distance x inside the conductor and $\dot{B}_a$ is the value of $\dot{B}$ outside the material and e is the exponential constant. What this means is that changes in flux density fall away exponentially and do not penetrate much below the surface of the conductor. Thus, inside the conductor, the flux density is constant regardless of what is happening to the applied field.

While Equations 2.12 and 2.13 describe the electromagnetic behaviour of a perfect conductor, it does not describe those of a superconductor. Ochsenfeld and Meissner discovered that the applied magnetic field induces screening currents in the superconductor which generate an internal flux density equal and opposite to the applied field. The Meissner effect demonstrated that not only is the magnetic field inside a superconductor constant, it is always zero as shown in Figure 2.10. This means that both $\dot{B}$ and B must decay below the surface.

German physicists Fritz and Heinz London developed a set of equations relating current to electromagnetic fields in and around a superconductor [London and London 1935]. London and London suggested that a superconductor would be correctly described if Equation 2.13 applied not only to changing magnetic fields but also to **B**. The London equations are,

$$\nabla \times \mathbf{J}_S = -\frac{n_s q^2}{m}\mathbf{B} \tag{2.16}$$

and

$$\frac{\partial \mathbf{J}_S}{\partial t} = \frac{n_s q^2}{m}\mathbf{E} \tag{2.17}$$

The same logic that was used to arrive at Equation 2.15 can be used on the more restrictive case of Equation 2.16. This shows the flux density falling exponentially inside the superconductor to $1/e$ of B_a at a distance $x = \sqrt{\alpha}$, commonly referred to as the London penetration depth λ_L.

The Two Fluid Model

The zero resistance of superconductors is only true for a constant direct current. If the current changes over time, Equation 2.12 states there will be an electric field developed and some power will be dissipated. This can be explained by dividing the conduction electrons into two classes below T_C. Some of the electrons will behave as superconducting electrons and have no resistance and some will behave as normal conducting electrons which encounter collisions and scatter.

At $0\,K$, all of the conducting electrons are superconducting. As the temperature is increased, some of the electrons become normal. Further heating increases the proportion of normal electrons until the critical temperature T_C is reached, whereby there are no more superconducting electrons. Thus the current in a superconductor can be carried by both normal and superconducting electrons.

In the constant direct current case, all of the current is carried by the superconducting electrons. From Equation 2.12, a constant current will result in zero electric field so there will be no field to drive current through the normal electrons. If the current was to increase, there must be an electric field present to accelerate the electrons and some of the current will be in the normal electrons resulting in power dissipated.

The current flowing in the two *fluids* is analogist to superfluidity in liquid helium and was defined in a paper by Cornelis Gorter and Hendrik Casimir [Gorter and Casimir 1934].

BCS Theory

A complete understanding of BCS theory involves complicated, many-body, quantum-mechanical equations and is beyond the scope of what was intended for this section. Therefore, a simplified overview of the important aspects of the theory are presented instead.

(a) Diagram of electron-electron interaction via phonon.

Crystal Lattice

(b) Diagram of electron lattice interaction.
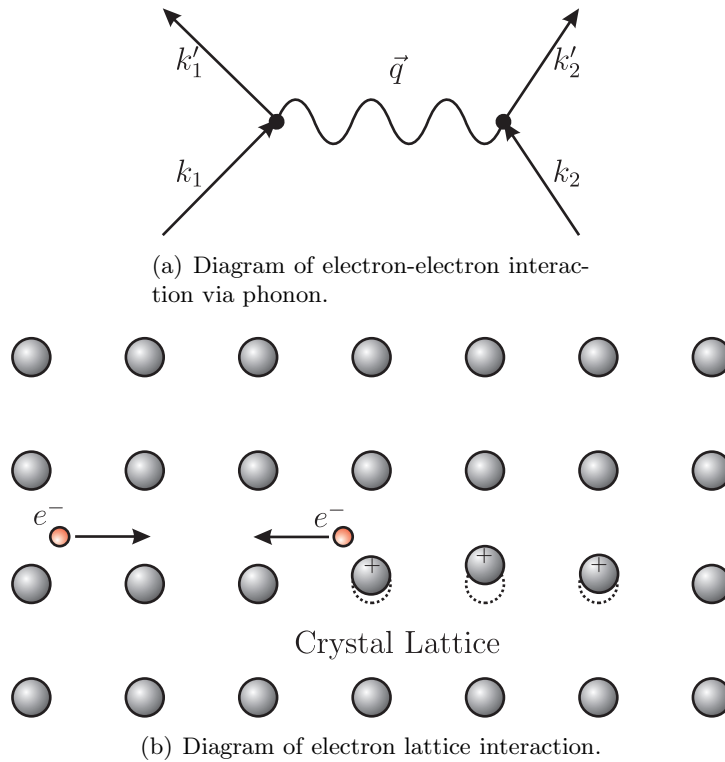
Figure 2.11   Formation of Cooper pairs.

The crystalline structure of a superconductor can be thought of as a lattice of positively charged ions with electrons moving between. Depending on the masses and configuration of the ions, the electrons can be in a number of different quantum mechanical states. At low temperatures, few electrons are excited by thermal oscillations and all the states are filled up to an energy level called the Fermi energy, E_f.

Interactions exist between the electrons, and between the electrons and the lattice. One interaction is repulsion between electrons, due to Colomb's law, because they are negatively charged. On the other hand, the electron lattice interaction causes an attractive force between electrons which can in some cases overcome the Colomb repulsion. Quantum-mechanically, if an electron with wave vector k_1 scatters to wave vector k_1' a phonon with wave vector $q = k_1 - k_1'$ is produced. The phonon q can be absorbed by another electron with wave vector k_2 resulting in a new wave vector $k_2' = k_2 + q$. If q is small, the electron-phonon interaction is attractive, Figure 2.11(a). More physically, this attraction occurs because the electron pulls the surrounding lattice creating an area of positive charge distortion which attracts another electron, Figure 2.11(b).

The attractive force between the electrons is a weak attraction and normally not strong enough to bind a particle. In 1956, Leon Cooper showed that if the electrons have equal and opposite spins they can experience the attractive force in such a way as to have a lower energy than E_f [Cooper 1956]. This causes them to condense into a pair of bound electrons which later became known as a Cooper pair.

Cooper's work explored what would happen to two electrons added to a metal at absolute zero. BCS theory took this idea and expanded it to a superconducting ground state. That is if one pair of electrons can lower their potential energy by forming a Cooper pair then many electrons can form pairs and lower the energy even further, until a point of lowest energy is reached called the ground state. The pairing of the electrons and subsequent reduction in energy results in an absence of single electron states and an energy gap is formed. When the temperature rises above T_C, the energy gap disappears.

By conservation of momentum, the electron-phonon interaction in Figure 2.11(a) can only occur when $k_1 + k_1' = k_2 + k_2'$. This means that every Cooper pair in the superconductor has the same average momentum. To scatter a single electron or Cooper pair into a new momentum would require breaking every Cooper pair. At low temperatures, no energy fluctuations are large enough to overcome this attraction. Thus once the Cooper pairs have a momentum, i.e. current, they will keep it indefinitely and experience no resistance.

2.5.2 High Temperature Superconductors

The previous section described theories for what are now known as conventional superconductors that were well established. With the discovery of high temperature superconductors by Bednorz and Müller, a new wave of research began into finding new materials and theories in this field. However, at the time of writing, no single agreed upon theory exists to explain the observed behaviour of these materials.

As mentioned in Section 2.5, BCS theory predicted an upper limit on T_C of between $30\,K$ and $40\,K$. However, Figure 2.9 indicates T_C in excess of $120\,K$ for the new class of materials. This implies that BCS does not fully explain the behaviour of these materials. Be that as it may, there are similarities between HTS and the BCS theory. For example, in the superconducting state, the electrons are paired together in HTS as demonstrated by experiments in 1987 [Emery 1987] and an energy gap has been found to exist, although it is larger and anisotropic compared to isotropic BCS values [Kirtley 1990].

There are also aspects that do not agree with conventional superconductor theory. These include very high T_C values, linear dc resistivity in the normal state and extremely small coherence lengths.

Physical Structure

Although other high T_C superconductors exist, the research in this thesis is restricted to cuprate superconductors for they are the most common and have the highest T_C values. Cuprates are chemical compounds containing copper anions. More specifically, all cuprate superconductors
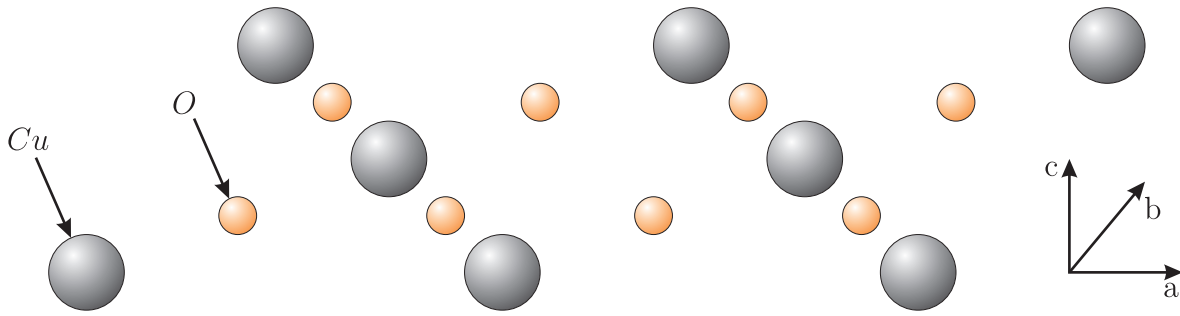
Figure 2.12   Diagram of the CuO plane present in all cuprate high temperature superconductors.

contain planes of copper oxide, CuO, where it is believed that the superconductivity is mostly confined. Figure 2.12 is a sketch of a CuO plane. Each Cu^{2+} ion is surrounded by four O^{2-} ions in a square planar arrangement. The CuO layers group into blocks and the blocks are separated by other elements in the material. It is common for cuprate superconductors to be categorized by their elements and the number of adjacent CuO layers. For example, $YBa_2Cu_3O_{7-\delta}$ is referred to as Y123 and $Bi_2Sr_2Ca_2Cu_3O_{10+\delta}$ is referred to as Bi2223.

The copper in the CuO plane has the potential to release a loosely bound electron which can conduct electricity. How well this happens depends on the doping of the material (the value of δ in the above chemical formula). With no doping, the material is a poor conductor, referred to as a Mott insulator [Mott and Peierls 1937]. The electron repulsion is strong and there is not enough energy to force another electron onto the copper atom. As the doping is increased, vacancies appear in the CuO layer and the electrons are free to move. For a certain range of δ the material becomes superconducting. This is illustrated in Figure 2.13.

As stated earlier, the superconducting phase contains pairs of electrons in the CuO planes. The pairing up results in an energy gap in the material. The unusual property of cuprate superconductors is that as the temperature is raised, the material ceases to be superconductive but the energy gap remains until relatively high temperatures are reached. This region is known as the *pseudogap* and is one of the aspects of HTS that cannot be explained by the BCS theory. The pseudogap region is depicted in Figure 2.13.

Superconducting Properties

Zero resistance implies that there is zero electric field across a superconductor which has current through it. While this is true for low current levels, all superconductors have a limit to the current density they can handle while still maintaining zero electric field. In addition, the transition between the normal and superconducting states is not instantaneous, it is instead a smooth, non linear increase in electric field for increasing current density. This $E-J$ relationship is described well by the following power law,
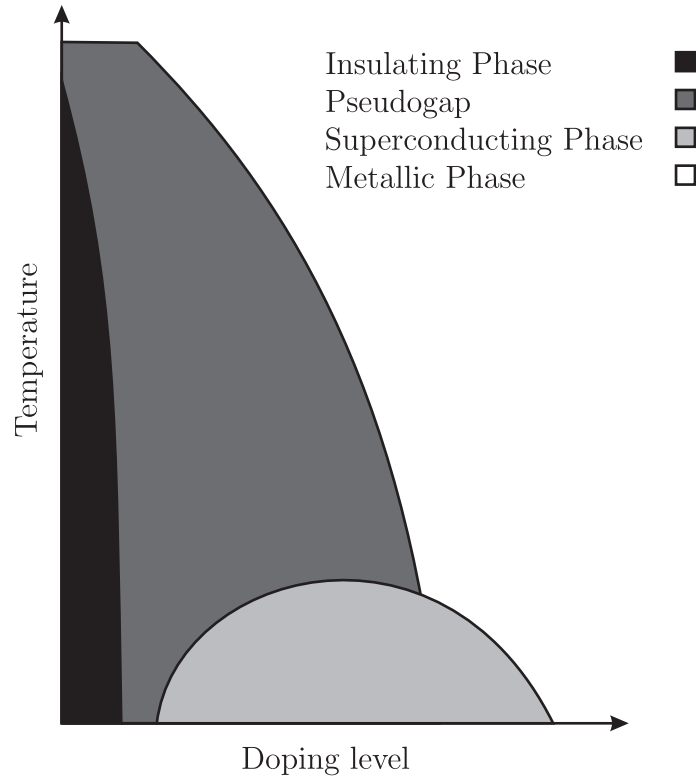
Figure 2.13 Phase diagram for a cuprate superconductor for increasing doping levels versus temperature.

$$E(J) = E_C \left(\frac{J}{J_C} \right)^n \tag{2.18}$$

where E_C is the electric field criterion, usually taken as $100\mu V/m$, and J_C is the critical current density. Different materials have different n values, with conventional superconductors tending to have much higher n values than cuprate superconductors. At liquid helium temperatures, there is a sharp transition in the $E(J)$ relationship at J_C, whereas at LN_2 temperatures the transition is less clear and J_C is defined by the E_C criterion, Figure 2.14.

Current in a superconductor from an external source such as a battery is referred to as *transport* current. In Section 2.5.1 it was shown that an applied magnetic field produces screening currents in the superconductor to oppose the applied field. So the total current in the superconductor is a combination of these two currents. As stated above, there is a limit to the current density that can flow in a superconductor. Therefore, it follows that there must be a limit to the applied magnetic field and there must exist a critical field, H_C, beyond which the superconductor becomes normal. It is also apparent that H_C is temperature dependent, with the critical field decreasing to zero at the critical temperature.

Further to this, all cuprate superconductors are known to be type-II superconductors. In type-II superconductors there are two critical fields, H_{C1} and H_{C2}, called the lower and upper critical
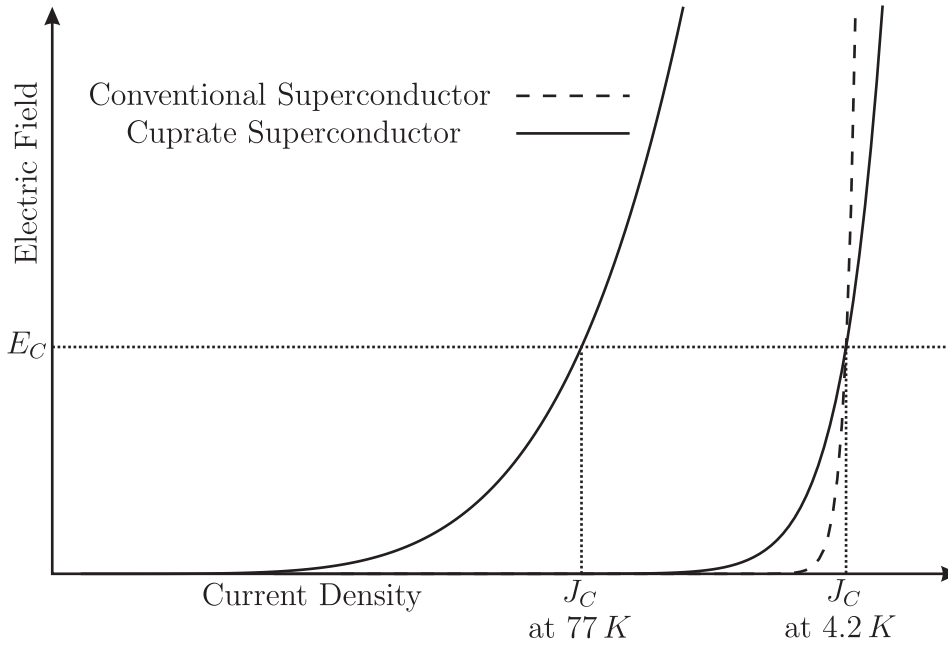
Figure 2.14   Electric field versus current density for different superconductors at different temperatures.

fields respectively, Figure 2.15(a). In fields below H_{C1} the material behaves exactly like a conventional superconductor, i.e. the field is excluded via screening currents. For fields above H_{C2} the magnetic field completely penetrates the material and superconductivity is lost, the same as in conventional superconductors. The difference lies when $H_{C1} \leq H \leq H_{C2}$, and the superconductor is in what is known as the mixed state. Magnetic fields are able to penetrate the superconductor in tubes of normal state material called vortices. The vortex tube is aligned parallel to H. A circulating current around the vortex produces a magnetic field that screens the outside superconducting region.

Figure 2.15(b) illustrates the mixed state of the HTS. It shows the tubes of normal state material where each vortex carries a total flux equal to the fluxoid quantum $\phi_0 = h/2e = 2.07 fTm^2$. The vortices are arranged in a hexagonal array due to the repelling forces of the screening currents around each vortex. As the magnitude of the applied magnetic field is increased, the number and density of the vortices increases until H_{C2} is reached and superconductivity is lost.

If a transport current is applied to the superconductor in the mixed state, the vortices will move in a direction perpendicular to the transport current due to Lorentz forces. This *flux flow* corresponds to a change in the internal magnetic field of the superconductor and an electric field is produced via Faraday's law. The resistivity due to flux flow is usually higher than the resistivity of a good conductor and is not a desired feature of HTS materials. The vortices are able to be pinned at defects in the crystal lattice and prevented from moving. At high current densities the vortices are de-pinned producing flux flow. The strength and density of the pinning centers ultimately determines J_C.
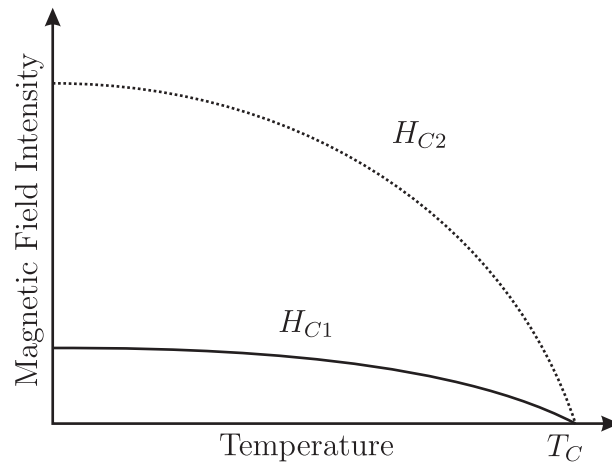
(a) Critical magnetic fields of a type II superconductor versus temperature.
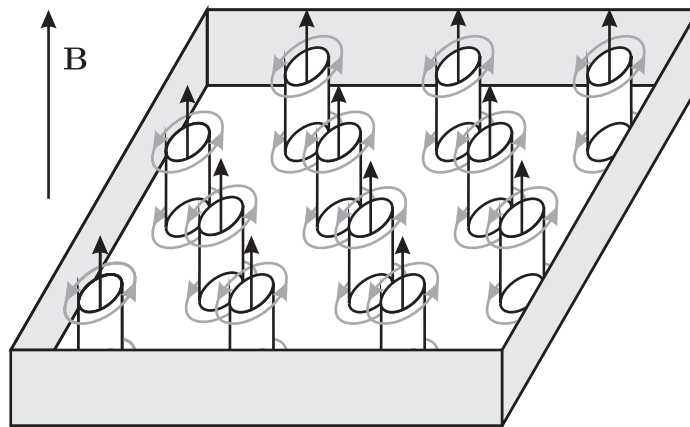
(b) A type II superconductor in the mixed state. The magnetic field (black arrows) results in screening currents (grey arrows).

Figure 2.15 The magnetic properties of type II superconductors.

At higher temperatures, thermal activation can de-pin the vortices and flux flow occurs at lower current densities. This thermally activated flux flow is called flux creep. It is the cause of the slower transition from the superconducting state to the normal state for higher temperatures illustrated in Figure 2.14.

Superconducting Wire

In order to successfully build power transformers with HTS, long lengths of wire will be needed. Most of the scientific data on cuprate superconductors was achieved with small samples grown onto substrates. These are too small to be used in power transformers. The first HTS tapes to be made in lengths usable for power applications were made from Bi2223, commonly called BSCCO wire. The tapes were manufactured using a process called powder in tube (PIT) , first developed in 1979 by C. van Beijnen for Nb_3Sn superconductors [van Beijnen and Elen 1979].
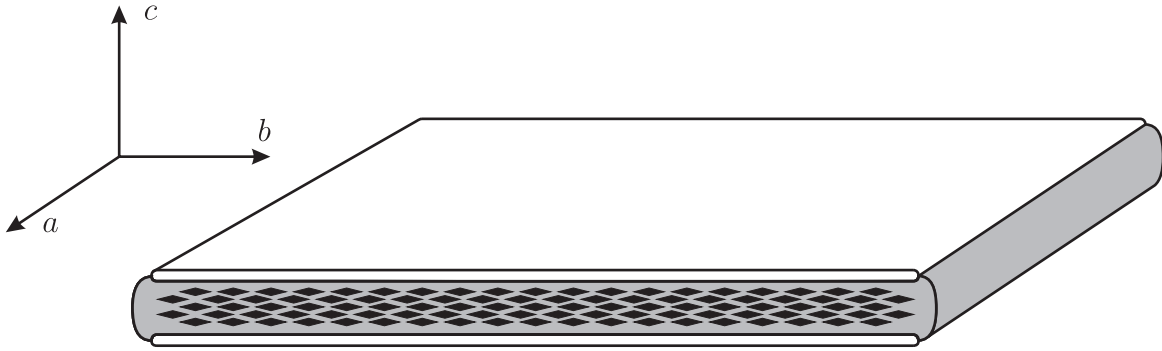
Figure 2.16   Cross-sectional view of a 1G HTS tape.

The process involves filling tubes of silver with Bi based ceramic that has been ground into a powder. The tube is drawn out to a thin wire. In multi-filament tapes, the most common form of BSCCO wire, several tubes are stacked together and then inserted in another Ag tube. The tube is rolled into a flat tape with an aspect ratio of $\approx 10:1$. The superconducting ceramic is then formed by a chemical reaction during a heat treatment process at a temperature between $800 - 900\,^\circ\text{C}$. Ag is used as the tube material because it is permeable to oxygen and does not react with the ceramic.

After the heat treatment, the tape consists of several irregular shaped filaments of BSCCO surrounded by a silver matrix. Figure 2.16 shows a cross-section of a typical HTS conductor made with the PIT process. The black superconducting filaments are largely orientated in the ab plane and surrounded by a silver matrix, (grey). Sometimes the silver matrix has strips of annealed copper or stainless steel, (white) attached for added strength to the tape.

As with all cuprate superconductors, BSCCO is highly anisotropic. The critical current is much higher in the ab plane than in the c direction. This is due to the orientation of the CuO planes in the material. The grains of the BSCCO material are flat, much thinner in the c direction than the ab directions. By rolling the tape, the ab planes more or less align and adjacent grains tend to be parallel. This alignment of the grains is what improves the overall critical current of the tapes.

The multi-filamentary BSCCO wire tape is commonly referred to as first generation (1G) HTS wire. In recent years, a second generation (2G) of HTS wire has come into production based on YBCO . The grains of YBCO are cubical and do not align well in a PIT process. Wire using this technique has very limited critical current. Instead, the superconductor is deposited onto a metal strip epitaxially by a process called, "rolling assisted biaxially textured substrates" or RABiTS . 2G HTS tapes are what is known as coated conductors.

In this system, a metal wire substrate, typically 4 mm wide, has three buffer layers of Y_2O_3, YSZ and CeO_2 deposited on with high-rate reactive sputtering. This is followed by a thin film

of YBCO which is then heat treated and oxygenated to form the HTS. The conductor is then laminated between two metallic stabiliser strips. Using the RABiTS technique, manufacturers have been able to produce long lengths of 2G YBCO wire with similar critical currents and superior mechanical properties to 1G BSCCO tapes [Xiaoping *et al.* 2009].

The primary focus of this thesis is for transformers using 1G BSCCO HTS wire. This is because 1G wire was all that was procurable for the manufacture of the high temperature superconducting partial core transformer.

Chapter 3

PROTOTYPE HIGH TEMPERATURE SUPERCONDUCTING TRANSFORMERS

3.1 OVERVIEW

In this chapter, a background on the development of a high temperature superconducting partial core transformer (HTSPCT) at the University of Canterbury (UoC) is given. Early development of PCTs including design ideas and some motivation behind the partial core idea is presented first. This is followed by a look into the operation of transformers at the cryogenic temperatures required for HTS. Some material characteristics are investigated including the electrical breakdown of LN_2 and the mechanical properties of insulation materials.

A detailed description of the first HTSPCT includes construction details of the windings, core and a vacuum Dewar for containment of LN_2. Experimental results follow with open circuit, short circuit and load testing of the transformer being performed. Unfortunately, a failure of the primary winding occurred during a full load endurance test leading to an investigation as to the cause of the fault. The investigation found that the likely cause of failure was a combination of operating too close to critical conditions and insufficient cooling of the windings.

The results of the failure of the first HTSPCT lead to the development of an alternative winding design to enable greater cooling of the HTS wire. This design was developed for a full core transformer with both a copper winding mock-up and a HTS winding version constructed. The new design demonstrated the ability to remove heat from the conductor while operating around critical limits.

3.2 EARLY PCT DEVELOPMENT

As mentioned in Chapter 2, the first transformers were actually open/partial core devices. Figure 3.1 is a photograph of one of the world's first open core transformers. It was designed and constructed by the same engineers that invented the Z.B.D. transformer at the Ganz factory in

Budapest. The core consists of bundle of soft iron wire with the windings placed on a former around the core. This design of the transformer was largely superseded by full core equivalents except in high frequency applications. However, the use of partial core transformers at power frequencies was not entirely left for museum pieces with research into PCTs at UoC being developed over a number of years.
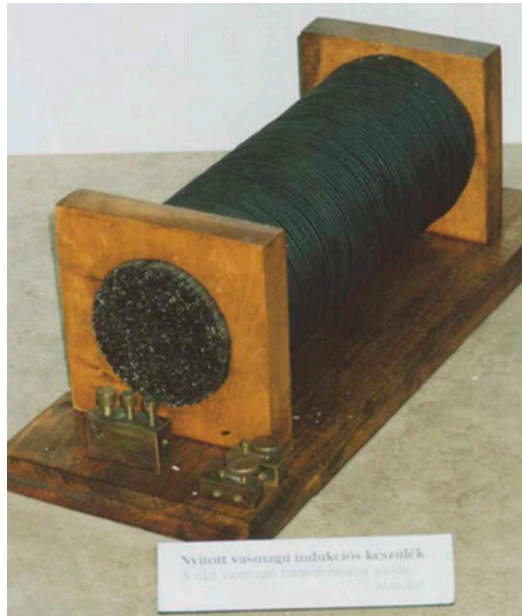
Figure 3.1   An open core transformer from the Budapest Electrotechnical Museum.

The research began with the development of a reverse design method (RDM) for transformer design [Bodger *et al.* 2000, Bodger and Liew 2002]. Traditional transformer design usually involved specifying a set of parameters such as voltage ratings, VA ratings and frequency. From these design parameters, the materials and dimensions for the transformer can be determined. The short coming from this design method is apparent when the materials of the designed dimensions are not economically available. Compromises are then made and there may be differences between the predicted and actual performances of the transformer.

The RDM differs from the conventional design by using the physical dimensions and characteristics of the core and the windings as the specifications. By manipulation of the materials actually used in the design of the transformer, the performance can be calculated and tailored to design needs. This approach to transformer design is the opposite of the conventional method described above. PCT were developed using this reverse method of transformer design [Liew and Bodger 2001, Liew and Bodger 2002, Liew 2001].

A computer program implementing the RDM was written by Bodger and Liew and used to design several PCT. Testing of the built transformers was used to improve the modeling. An example of the test results compared to those calculated from the computer program is given in Table 3.1. The transformer was a 230 V to 20 V step-down device and is shown in Figure 3.2.

The results show good agreement between measured and calculated values with the largest error being in the secondary side voltage. The source of this error would be the over estimation of the series resistance component, R_1, from Table 3.1.

Table 3.1 Calculated and measured test results for the Liew PCT [Liew and Bodger 2002].

Equivalent Circuit	Calculated	Measured	Error (%)
$R_c(\Omega)$	522	551	5
$X_m(\Omega)$	42.0	42.6	1
$R_1(\Omega)$	3.7	3.5	6
$X_{l1}(\Omega)$	4.5	4.6	3
Equivalent Circuit	Calculated	Measured	Error (%)
$V_1(V)$	234	234	0
$I_1(A)$	23	23	0
$V_2(V)$	21	25	16
$I_2(A)$	112	109	3
$P_1(W)$	4.4	4.2	5
$Effy.(\%)$	56	60	7
$Reg.(\%)$	53	51	4
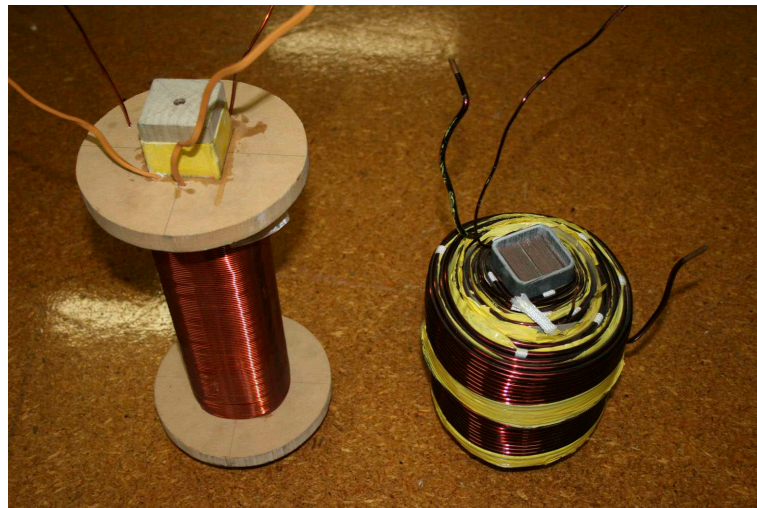
Figure 3.2 Two partial core transformers used for model verification.

In later years, finite element analysis (FEA) was used to refine the modeling of the magnetic components [Bell and Bodger 2007, Bell and Bodger 2008]. This system was used to design a high voltage resonant kit-set comprised of three partial core transformers and a common core set [Bell 2008]. The transformers are used for reactive power compensation in high voltage testing of insulation systems at mains frequency (50 Hz)[Enright and Bodger 2002].

3.3   CRYOGENIC MATERIAL TESTING

Concurrently with the PCT development, research was undertaken into material testing of insulation, winding and core materials at ambient and cryogenic (LN_2 boiling temperature, 77 K) temperatures. One of the first facets of research was to find the dielectric strength of LN_2. O'Neill made several measurements on LN_2 to BS5874:1980 standards [O'Neill *et al.* 2000b]. Traditional transformer oil has average breakdown voltages of greater than 40 kV for good oil and less then 20 kV for bad oil for gaps of 2.5 mm when tested with the BS5874:1980 standard. The results of the testing, presented in Table 3.2, show that LN_2 has comparable dielectric strength to standard transformer oil.

Table 3.2   Breakdown voltage for liquid nitrogen [O'Neill *et al.* 2000b].

Gap separation (mm)	Breakdown voltages ($kVrms$)		
	Average	Minimum	Maximum
1	27.9	25.4	30.5
2	47.4	40.9	54.1
2.5	49.5	45.9	53.5

Also by O'Neill, was research into the mechanical strength of transformer insulating paper. Kraft paper and Nomex® paper were tested. The research found that mechanical strength of Kraft paper was adversely affected by exposure to LN_2 and was not suitable for use at that temperature. Nomex® however, increased in strength in LN_2 when compared to that in room temperature oil. Thus the Nomex® paper was found to be suitable for use in cryogenic transformer applications [O'Neill *et al.* 2000b].

Following this work, a set of full core distribution transformers were tested [Bodger *et al.* 2002a, Bodger *et al.* 2002b]. Four 11 kV / 230 V, pole-top distribution transformers were tested. Two transformers had silicon steel cores (10 kVA) and two amorphous steel cores (15 kVA). The difference in kVA rating between the two core types was an unintentional mistake by the manufacturer of the distribution transformers. One of each type of transformer was tested in oil at room temperature and the others were tested in LN_2 at 77 K. Capacitance and dissipation factor tests were performed on each of the transformers as well as open circuit and short circuit tests. The results of the testing is given in Tables 3.3 and 3.4.

The transformers show a drop in capacitance of the insulation under LN_2 for both the amorphous and silicon steel core types. This increases the first natural resonant frequency resulting in any resonant frequency problems occurring at much higher frequencies. The dissipation factor was also reduced under LN_2, implying that LN_2 has fewer dielectric losses. The open circuit tests showed very little difference in core loss between room temperature and 77 K although the

Table 3.3   Capacitance and Dissipation factor test results for 10kVA transformers [Bodger *et al.* 2002b].

Silicon Steel Core		
Transformer Insulation	Capacitance (nF)	Dissipation Factor
Oil	1.119	0.00670
Liquid Nitrogen	0.363	<0.00001
Amorphous Steel Core		
Transformer Insulation	Capacitance (nF)	Dissipation Factor
Oil	1.003	0.00527
Liquid Nitrogen	0.419	0.00211

Table 3.4   Open and short circuit test results for 10kVA transformers [Bodger *et al.* 2002b].

Silicon Steel Core							
Transformer Insulation	Open Circuit Test			Short Circuit Test			
	V (V)	I (A)	P (W)	V (V)	I (A)	P (W)	I_{sec} (A)
Oil	240	1.15	65	368	0.90	145	41.2
Liquid Nitrogen	240	1.05	62	345	0.86	57	41.4
Amorphous Steel Core							
Transformer Insulation	Open Circuit Test			Short Circuit Test			
	V (V)	I (A)	P (W)	V (V)	I (A)	P (W)	I_{sec} (A)
Oil	240	0.69	19	336	0.95	131	41.5
Liquid Nitrogen	240	0.73	20	304	0.95	22	41.5

amorphous core was more efficient than the silicon steel. This result suggests that the core can be submerged in LN_2. Significant reduction in winding losses was also noted for the LN_2 case and attributed to the reduction in resistivity of the copper at this temperature.

3.4   A 15 KVA HTSPCT PROTOTYPE

The following section gives details of the transformer design, construction, and test results of a 15 kVA HTSPCT prototype. With knowledge gained from the research discussed in the previous two sections, a prototype HTSPCT was designed, built and tested in 2005. However, the HTSPCT was unable to be load tested at that time due to a failure of the LN_2 Dewar. Repairs to the Dewar were made in 2009 by the author and electrical tests were performed. The prototype failed during a full load endurance run and an investigation into the cause of the failure was undertaken [Lapthorn *et al.* 2011].

3.4.1   Transformer Design

The design of the HTSPCT involved computer modelling and empirical experimentation using a program developed from traditional transformer design theory and a reverse as-built design approach [Bodger *et al.* 2000, Bodger and Liew 2002, Liew and Bodger 2002]. The program proved to be approximately 10 % accurate in modelling mains frequency transformer and inductor units, where empirical data helps form the simulation models [O'Neill *et al.* 2000a, O'Neill *et al.* 2000b, Liew and Bodger 2001, Bodger *et al.* 2002a, Bodger *et al.* 2002b]. The computer program was altered to account for the rectangular profile of HTS conductors and used critical current as a parameter for the HTS tape rather than resistivity. The program modifications have been validated through a process of designing and building a number of experimental units. A mock superconducting transformer was built using aluminium tape for its windings [Bodger *et al.* 2002c]. Empirical data recorded was checked against the program predictions for voltages and currents, with very high correlation on most parameters, typically around 2 to 5 %. The program was used to design a single phase, 50Hz, 230/115 V, 15 kVA, HTS power transformer.

Winding Design

The HTSPCT was designed as a three winding transformer with one 230 V winding and two 115 V windings. The windings were wound with 1G-HSP wire from American Superconductors. This tape is a Bismuth based superconductor, $Bi_2Sr_2Ca_2Cu_3O_{10}$ (Bi2223), in which many superconducting filaments are encased in a silver alloy matrix using a powder-in-tube process. The high strength version of the tape includes thin stainless steel laminations sandwiching the silver alloy matrix. The manufacturer's wire specification of the critical dc current at 77 K is 124.2 A in a self field. However, the alternating magnetic fields present in the transformer result in a reduction in critical current [Zhu *et al.* 2004, Leghissa *et al.* 2007, Oomen *et al.* 2003]. For this reason the maximum current for the windings was set to 65 A rms.

The HTS wire was insulated from turn to turn short circuits by using two layers of Nomex®
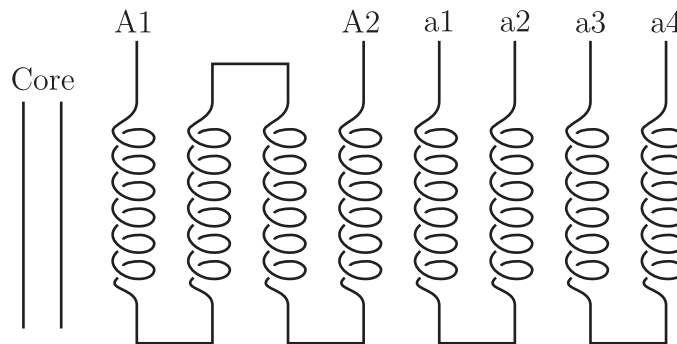
Figure 3.3   A schematic of the winding layout for the HTSPCT.
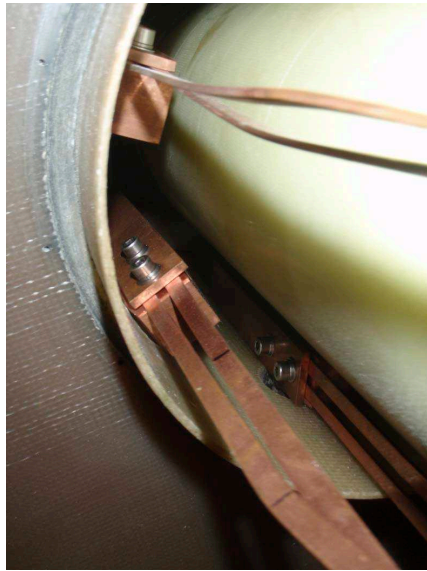
(a) Connection of the copper lead-outs to the bushing busbars.

(b) The upper portion of the copper lead-outs.
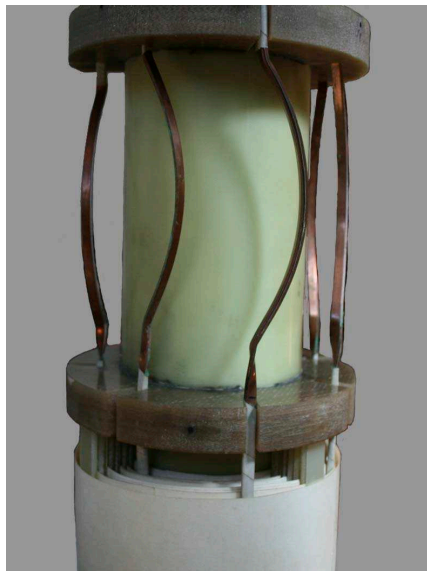
(c) The lower portion of the copper lead-outs.

(d) Photograph of a sample joint between the copper lead-outs and the HTS wire.

Figure 3.4   Photographs of the copper lead-outs connecting the transformer bushings to the HTS windings.
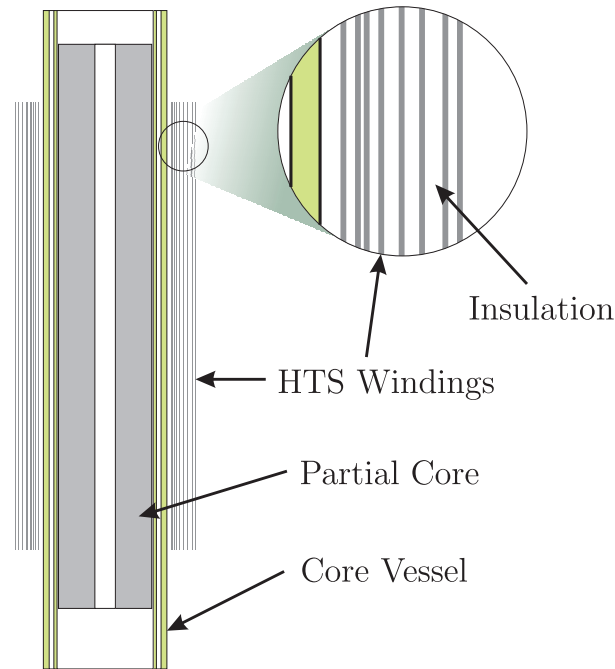
Figure 3.5   A cross-sectional view of the winding layout, insulation and relative position of the core of the HTSPCT.

T-410 (0.13 x 10 mm) tape. The insulation was applied parallel to the wire length on the wide surface of the conductor with the excess insulation folded over the conductor's thin edge to the opposite wide surface. A second layer of insulation was applied and folded on the opposite side to the first so that the conductor was completely covered. The overlap of insulation on the wide surfaces of the conductor was between 3 and 4 mm throughout.

The windings were layer wound with 80 turns per layer as shown in Figure 3.3. The high voltage winding, A1-A2, was located on the inside of the transformer and consisted of four layers for a total of 320 turns. The first low voltage winding, a1-a2, located in the middle of the transformer consisted of two layers and a total of 160 turns. The second low voltage winding, a3-a4, was wound over the a1-a2 winding and also consisted of two layers with 160 turns in total. This arrangement of windings was to allow for the investigation of multiple winding configurations, including autotransformer mode.

Copper lead-outs were used to connect the HTS windings to the transformer bushings as shown in Figure 3.4. The lead-outs consisted of two 1.2 mm x 5 mm copper conductors and were positioned radially around the transformer. The lead-outs were connected to the bushing busbars using a compression joint as shown in Figure 3.4(a), which was located above the LN_2 level (Figure 3.4(b)). The bends in the lower section of the lead-outs photographed in Figure 3.4(c) were present to allow for thermal expansion and contraction of the copper without pulling or pushing on the HTS windings. The copper lead-outs were soldered to the HTS wire using Indium based solder, (97 % In 3 % Ag), and Ersin Red Jelly flux paste. The joint was made by

sandwiching approximately 10 cm of HTS wire between two specially formed copper lead-outs as shown in Figure 3.4(d) and soldering with a temperature limited soldering iron. Too high a temperature during this process would result in the HTS wire delaminating; the soldering temperature was limited to 160 °C.

The winding insulation system used a combination of uncalendered Nomex® 411 and calendered Nomex® 410 insulation paper. Six layers of Nomex® 411 were used directly on the former to provide friction between the windings and the former. Four layers of Nomex® 410 were used either side of the HTS layers to allow room for the copper lead-outs. In addition, four extra layers of Nomex® 410 insulation paper were used for inter-winding insulation. A diagram of the relative spacing of HTS wire to insulation is detailed in Figure 3.5. The uneven insulation spacing is due to allowances for the copper lead-outs as well as extra inter-winding insulation.

Core Design

The core was designed as a parallel stacked circular core, 420 laminations of 0.23 mm, high permeability, grain orientated silicon steel (ABB product code 23JGSD085). The laminations were 484 mm long. They were cut to different widths to provide a circular shape when stacked. The approximate diameter of the circular core was 80 mm. The core was bound with Vidatape S, a woven high shrink polyester tape, and hot dipped twice in an electrical baking varnish. A hole in the center of the core is for a 1240 mm long G-10 fibreglass 5/8" UNC threaded rod. The threaded rod allows for correct positioning of the core inside the core vessel wall relative to the HTS windings.

Main Assembly Design

The transformer main assembly is comprised of three parts, the liquid nitrogen vacuum Dewar, the core vessel, and the head unit as shown in Figure 3.6. The majority of the transformer main assembly was constructed using G-10 fibreglass.

The vacuum Dewar consists of an inner vessel for the containment of LN_2 and an outer vessel exposed to room temperature with a vacuum between them. The vacuum is present to limit thermal convection losses to the LN_2 from the outside. To limit radiation losses, several layers of aluminized non-stretch polyester were wrapped around the inner vessel. Care was taken not to create shorted turns by insulating the aluminized non-stretch polyester with vacuum rated tissue paper. A pressure relief port is present on the outside of the Dewar in case a failure of the inner vessel results in nitrogen gas venting into the vacuum chamber.

In the original 2005 design, the bottom of the inner vessel consisted of a flat disc attached to tube of the inner vessel. However, the disc and the tube contracted at different rates causing a

Figure 3.6   An exploded view of the main transformer assembly.

failure of the joint and nitrogen gas entering the vacuum chamber. This triggered the pressure relief port and meant that testing was unable to proceed. In 2009, the bottom of the inner vessel was changed to be dome shaped so that the joint between the dome and the tube of the inner vessel, when exposed to LN_2, expanded and contracted evenly.

The core vessel is similar to the vacuum Dewar in that a vacuum is formed between the core and the LN_2. A similar arrangement of aluminized polyester and tissue was used in the core vessel. With the core vessel at a vacuum of about 1×10^{-4} torr and the Dewar filled with LN_2, the core temperature fell to approximately -40 °C over a 16 hour period. In addition to providing insulation between the LN_2 and the core, the core vessel was used as the winding former. A float is attached to the core vessel to indicate the minimum and maximum LN_2 levels. A filling tube for the LN_2 is also fitted to the outside of the core vessel. A pressure relief port is present on the top of the core vessel in case a failure vents nitrogen gas into the vacuum chamber.

The head unit provides mountings for the transformer bushings, nitrogen venting valves, a rupture disc for emergency venting, purging lines and a pressure gauge for the LN_2 chamber pressure. The transformer bushings, located on the top of the head unit, are connected to the bushing busbars via a short piece of braided copper wire. Two nitrogen venting valves are present, adjacent to the rupture disc. One valve is a full LN_2 rated manual vent to be used

during initial filling and the other valve is a non return valve for normal operation venting. In case the non return valve is unable to vent sufficient quantities of nitrogen gas, for example during fault conditions, an emergency venting rupture disc is fitted to prevent the pressure in the LN_2 chamber from reaching dangerous levels. The rupture disc consists of a thin aluminium sheet between two flanges of G-10 fibreglass. The diameter of the rupture disc is 80 mm. The purging lines consist of a vacuum line and a dry nitrogen gas line. Prior to filling the chamber with LN_2, a vacuum is held for 24 hours, then the vacuum is broken with dry nitrogen gas.

3.4.2   Experimental Results

A series of electrical tests were conducted on the HTSPCT by the author and Irvin Chew to determine its performance. These tests included an open circuit test, a short circuit test, a load test and a load endurance test. The results from the testing are detailed in Table 3.5. For the open circuit test, the secondary windings (a1-a2 and a3-a4) were left open circuit while for the short circuit test and the load test they were connected in series.

Table 3.5   Electrical test measurements.

Open Circuit Test	
Parameter	Measured
Inside winding voltage (V)	230
Inside winding current (A)	19
Outside winding voltage(s) (V)	113 and 111
Inside winding real power (W)	200
Short Circuit Test	
Parameter	Measured
Inside winding voltage (V)	25
Inside winding current (A)	65
Outside winding current (A)	65
Inside winding real power (W)	80
Load Test	
Parameter	Measured
Inside winding voltage (V)	230.9
Inside winding current (A)	65
Inside winding real power (kW)	13.8
Outside winding voltage (V)	223.6
Outside winding current (A)	61
Outside winding real power (kW)	13.6
Real power loss (kW)	0.2
Efficiency (%)	98.6
Voltage regulation (%)	3.2

The transformer was also used by the author in a demonstration of a large Lightning Arc Drawing [Bell *et al.* 2007] where the load was approximately 25-30 A at 230 V with a power factor of about 0.8 lagging. The transformer performed well during several demonstrations each of which lasted no more than 5 minutes.

Unfortunately, when the HTSPCT was placed on a full load endurance run, a catastrophic failure occurred. Approximately 1 minute 30 seconds into the test, the secondary voltage collapsed and a surge in nitrogen gas venting was observed, at which point power was removed from the transformer. Resistance tests were conducted on the transformer, and the inside winding, A1-A2, was found to be open circuit. The secondary windings, a1-a2 and a3-a4, appeared normal. The sight level indicated that the LN_2 level was within normal operating levels. During the failure, a surge of nitrogen gas was created by the heating of the conductors. The emergency venting rupture disc was successful in preventing excessive build up of nitrogen gas in the LN_2 chamber.

3.4.3   Failure Analysis

After the LN_2 was removed, a visual inspection of the windings was undertaken. The initial inspection revealed contamination of the Nomex® insulation with a black substance as shown in Figure 3.7. Closer inspection revealed that the contaminants were only on the surface of the insulation as evident in Figure 3.7(a) and appeared to be attracted to the windings. On the lower half of the windings, shown in Figure 3.7(b), the vertical white traces in the contamination suggests nitrogen bubbling was occurring.

(a) The contaminants appear only on the outside of the insulation.

(b) The contaminants found on the lower portion of the windings.

Figure 3.7   Photographs of the contaminants found on the insulation after the failure of the A1-A2 winding.

The visual inspection revealed a small area of burnt insulation at the top of the A1-A2 winding with an area of burnt fibreglass immediately above it. It was anticipated that the damage to the

(a) Outside Winding.   (b) Middle Winding.   (c) Inside Winding.

Figure 3.8   Photographs of unwinding the HTSPCT after the failure.

A1-A2 winding was localised to the solder joint with the copper lead-outs so a decision was made to unwind the transformer and attempt to repair the damage. Photographs of the unwinding are displayed in Figure 3.8. The outside winding, a3-a4, appeared normal. It was not until the middle winding, a1-a2, was exposed that Nomex® damage was found. The insulation of the a1-a2 winding was burnt in an area in the upper region of the winding. The HTS wire of this winding was not visibly damaged. The same could not be said of the inside winding, A1-A2, where extensive thermal damage was found over a significant area.

Of interest is the combustion of the Nomex® and the G-10 fibreglass, suggesting the presence of liquid oxygen. Figure 3.9 is a closeup photograph of the burnt insulation. It illustrates how the insulation has become fully carbonised. The source of the oxygen could have been from the LN_2 as the supplier of the LN_2 was having equipment problems at the time of the noted transformer tests and oxygen levels in the LN_2 were approximately 4-5%. Alternatively, there could have been residue oxygen in the Nomex® because the purging lines were not used prior to filling with LN_2 for the endurance run and the filling was not performed under vacuum; a procedural error.

Also, radial buckling was found on the inner winding layers as shown in Figure 3.10. It is believed that this buckling has been caused by thermal expansion of the HTS wire rather than short circuit forces referred to in traditional transformer literature [Bertagnolli 2007]. As stated in [Weiss *et al.* 2007], the thermal expansion of the HTS wire over the temperature range experienced could have been 2-3 mm/m. This would result in thermal expansion of the A1-A2 winding of nearly 400 mm over the length of the winding. As the inner winding was tightly wrapped in Nomex® insulation and the layers of HTS wire of the outer windings, the thermal expansion of the inner layers could result in the radial buckling observed.

Figure 3.9   A closeup photograph of the burnt Nomex® insulation.

Figure 3.10   A photograph of the radial buckling that occurred on the inside windings.

It was presumed that the failure was because the HTS tape quenched due to a combination of the transport current, magnetic field and temperature of the windings. With the HTS in a resistive state, the losses dissipated would have increased the temperature in the inner windings where the cooling was poorest. Eventually the increase in temperature would result in the insulation failing, shorted turns in the windings and final breakdown of the HTS.

Ooman et al. provides a model for calculating the decrease in critical current with respect to magnetic field [Oomen *et al.* 2003]. Applying Ooman's model to the HTS tape gives Figure 3.11. Subsequent finite element modelling of the magnetic field by the author has indicated that the peak parallel and perpendicular fields in the winding area were 60.4 mT and 49.2 mT respectively. The conclusion is that the selected transformer ac rating of 65 A (92 A peak), present during
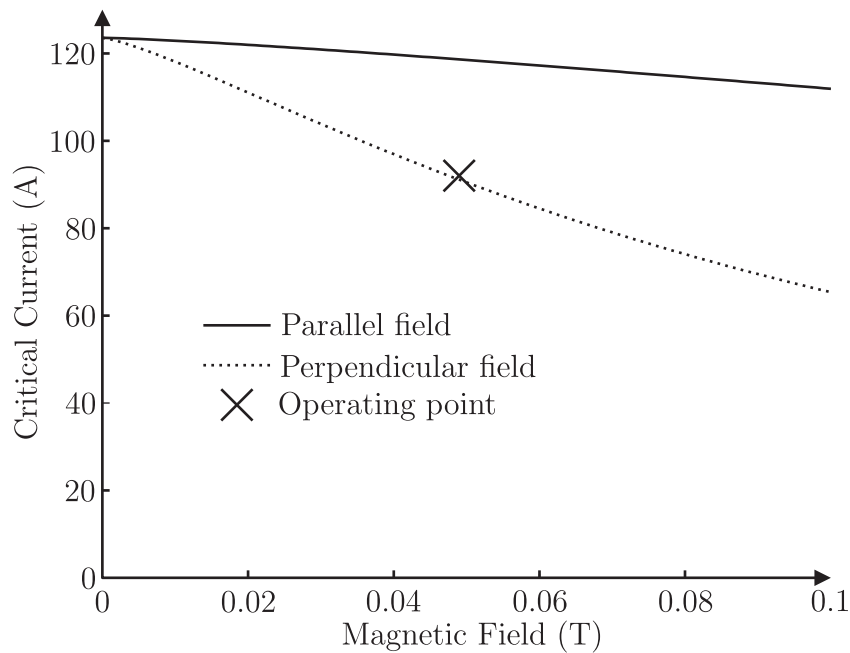
Figure 3.11   Predicted critical current at 77 K of the Bi2223 HTS tape with increasing magnetic field.

the full load test, meant that the transformer was operated close to the critical conditions. A lesson from this work is that a 92 A peak load current in comparison with a design adjusted critical current of approximately 92 A for the tape in a perpendicular field is a poor choice. In the future, a reasonable margin between these two figures should be selected.

Insufficient cooling from the large amount of insulation material used to pack out the windings also required some reflection. In hindsight, it is believed that this packing should have used axial G-10 fibreglass sticks to allow for better contact of the HTS wire with LN_2. Experiments performed by Kim et al. on the over current characteristics of HTS tapes indicate that with sufficient cooling, HTS tapes can be operated at currents higher than the critical current for short periods of time [Kim *et al.* 2008]. The radial sticks may also help keep the coil in form during conductor expansion/contraction associated with temperature change and may eliminate the radial buckling observed.

3.5   THE CHEW TRANSFORMER

Following the failure of the partial core HTS transformer and the subsequent investigation into the cause of that failure, a new design for the windings was developed by the author and Chew [Chew 2010]. This design was to incorporate cooling channels in the winding area to enable greater contact of the liquid nitrogen with the HTS windings and prevent another thermal related failure. Chew designed two full core transformers, a copper mock-up and an HTS design, using a combination of RDM and computer aided design software. The two transformers would

(a) The full core assembly of the Chew transformer.

(b) The Chew transformer core with the top yoke removed for winding assembly.
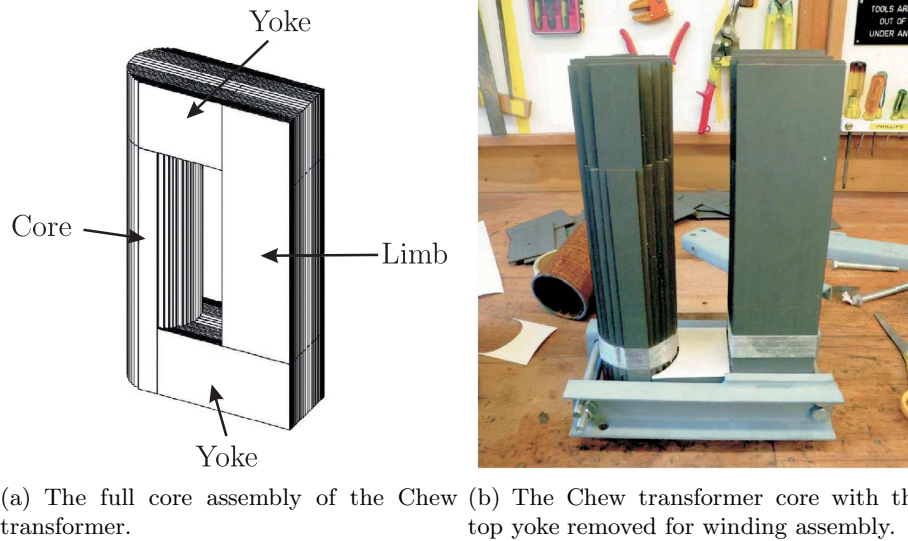
Figure 3.12   The core design of the Chew transformer [Chew 2010].

share the same core and have the same winding dimensions so that their performance could be compared directly. Due to financial constraints, the transformers were designed to be completely submerged in liquid nitrogen rather than designing a winding Dewar.

3.5.1   Core Design

The two winding designs, copper and HTS, shared the one core. Therefore, the core was designed so that it could be easily pulled apart and put together again. The core was also designed to minimise the weight and core losses. The core was constructed from high permeability, grain orientated silicon steel. It was designed as a circular core of parallel stacked laminations with a square limb and yokes present to keep construction simple as shown in Figure 3.12(a).

The design parameters used in the RDM for the core are given in Table 3.6. Of note is the lower than usual stacking factor for a laminated core which was due to the use of polyurethane for gluing the lamination sections together. These sections, comprised of ten laminations, enabled the core to be assembled and disassembled easily. Figure 3.12(b) shows the partially assembled core with the top yoke removed to enable assembly of the transformer windings.

3.5.2   A Full Core Copper Mock-up

With the core construction complete, a set of copper windings were constructed on a fiberglass former. The design data used in the RDM for the copper mock-up is given in Table 3.7. The priority of the design was to ensure enough cooling of both windings. Working with the materials available in the university, 2 mm thick composite fibreglass spacers were used for the inter-layer

Table 3.6 Chew transformer full core design data.

Parameter	Dimension
Core length	200 mm
Core diameter	75 mm
Winding window	42 mm
Lamination thickness	0.23 mm
Stacking factor	0.85
Operating temperature	77 K

insulation. The spacers were placed radially around the winding as depicted in Figure 3.13. As the number of layers increased, the width of the spacers was also increased to ensure a firm circular/round winding and to prevent kinks in the HTS conductor.

Table 3.7 Chew transformer copper mock-up design data.

Parameter	Inside winding	Outside winding
Winding height	190 mm	190 mm
Number of layers	8	8
Turns per layer	37	37
Conductor length	92.6 m	125.6 m
Wire width	4.83 mm	4.83 mm
Wire thickness	0.30 mm	0.30 mm
Wire insulation thickness	0.11 mm	0.11 mm
Insulation layer space	2 mm	2 mm
Operating temperature	77 K	77 K

To prevent inter-turn short circuits, the copper wire was insulated with Nomex® tape. The windings were wound on a composite former made with an epoxy-resin lacquered fabric. Both these materials were tested by submerging them in LN_2 to observe material contraction or other adverse effects. No significant contraction was observed.

Copper Mock-up Test Results

A series of electrical tests were performed on the copper mock-up transformer submerged in liquid nitrogen. The tests included an open circuit test, a short circuit test and a load test. The results of the testing are presented in Table 3.8.

For the open circuit test, the inside winding (referred to as the primary winding) was energised to 230 V with the outside winding (referred to as the secondary winding) left open circuit. Open circuit test results demonstrate how the full core design has a significantly lower magnetising
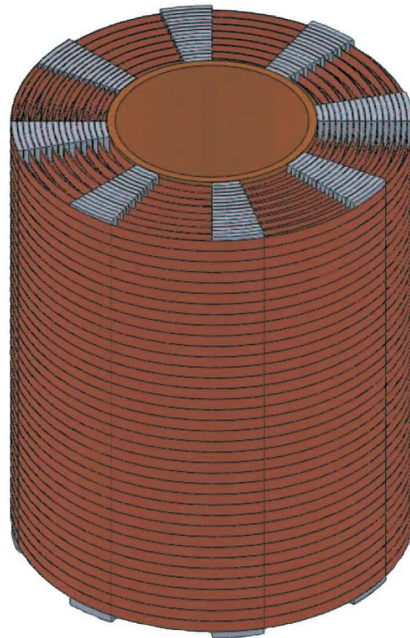
(a) Trimetric view of the copper winding assembly.
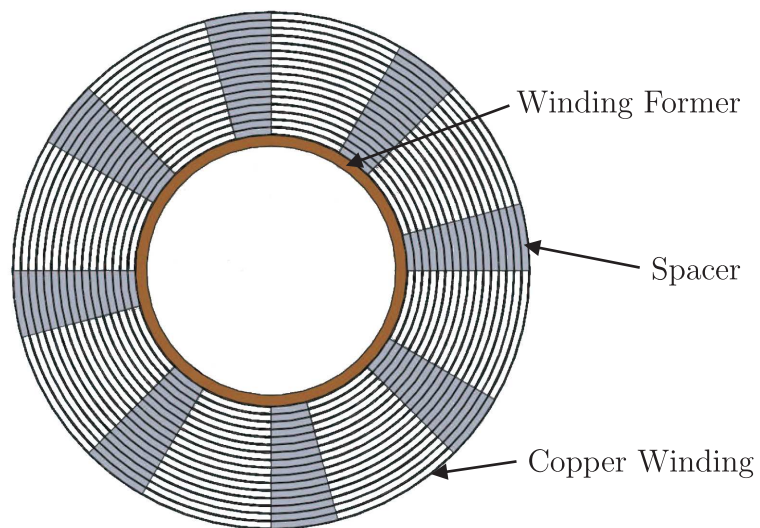
(b) Top-down view of winding assembly detailing the former, windings and spacers.

Figure 3.13   CAD drawings of the winding and spacer arrangement for the copper mock-up for the Chew transformer [Chew 2010].

Table 3.8   Test results for the copper mock-up transformer.

Open Circuit Test	
Parameter	Measured
Primary voltage (V)	230
Primary current (A)	0.12
Primary real power (W)	19
Primary apparent power (VA)	28
Primary power factor	0.7
Secondary voltage (V)	226
Voltage ratio	0.98
Short Circuit Test	
Parameter	Measured
Primary voltage (V)	35.3
Primary current (A)	30.6
Primary real power (W)	410
Primary apparent power (VA)	1080
Primary power factor	0.38
Secondary current (A)	30.9
Current ratio	1.01
Load Test	
Parameter	Measured
Primary voltage (V)	229
Primary current (A)	49.3
Primary real power (kW)	10.2
Primary apparent power (kVA)	11.3
Primary power factor	0.9
Secondary voltage (V)	189
Secondary current (A)	49
Secondary real power (kW)	9
Secondary apparent power (kVA)	9.3
Secondary power factor	0.97
Efficiency (%)	88
Voltage regulation (%)	17

current compared to that of the partial core design of Section 3.4.2. Also there is a small reduction of the secondary voltage attributed to leakage reactance.

The short circuit test was performed with the secondary winding short circuit and the primary winding voltage increased until 31 A was measured in the primary winding. The short circuit test results show that even at the cryogenic temperatures, the resistance of the copper windings is enough to cause 410 W of losses. However, the current density during the short circuit test was approximately $20 \, \text{A/mm}^2$, which is a much larger current density than copper is usually

operated at.

Finally, a load test was performed by connecting the secondary winding to a resistance and applying a voltage to the primary winding. The load current was set to a value beyond that of the short circuit test which would normally be the rated current. The difference between the short circuit current and load current was due to significant nitrogen boil off from 30 A. Chew believed there would not be enough LN_2 to complete the experiments so the short circuit test was completed at a lower current rating. The load test shows quite large voltage regulation indicating a significant series impedance. This is likely to be caused by the 2 mm spacing between each layer increasing the leakage flux.

3.5.3   A Full Core HTS Transformer

Following the testing of the copper mock-up transformer, a design using HTS BSCCO wire was completed by Chew. The spacers and insulation design of the HTS winding was the same as used in the the copper mock-up design. The HTS wire differed in wire width to the copper wire by 0.73 mm less than the copper tape. The windings in the HTS design still had the same number of turns per layer as the copper version. Design data for the HTS transformer is given in Table 3.9.

Table 3.9   Chew transformer HTS design data.

Parameter	Inside winding	Outside winding
Winding height	190 mm	190 mm
Number of layers	8	8
Turns per layer	37	37
Conductor length	92.6 m	125.6 m
Wire width	4.10 mm	4.10 mm
Wire thickness	0.30 mm	0.30 mm
Wire insulation thickness	0.11 mm	0.11 mm
Insulation layer space	2 mm	2 mm
Operating temperature	77 K	77 K

Copper lead-outs were used to connect the HTS windings to the terminals. The lead-outs were soldered to the HTS wire using the same technique as used for the partial core HTS transformer of Section 2. Due to the poor voltage regulation of the copper mock-up transformer, Chew decided to wind some extra turns on the secondary winding of the HTS transformer as a means of compensation. Unfortunately, the exact number of extra turns is unknown. The completed transformer is illustrated in Figure 3.14(a).
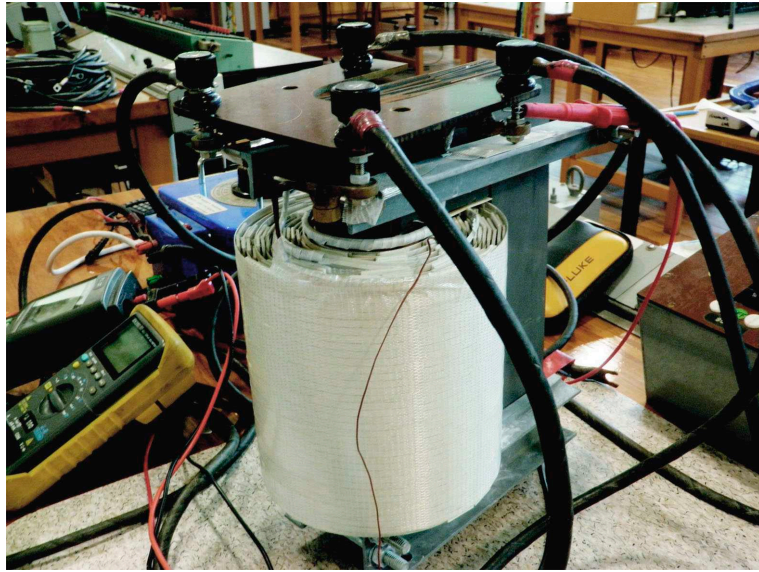
(a) The completed full core HTS transformer ready for testing.
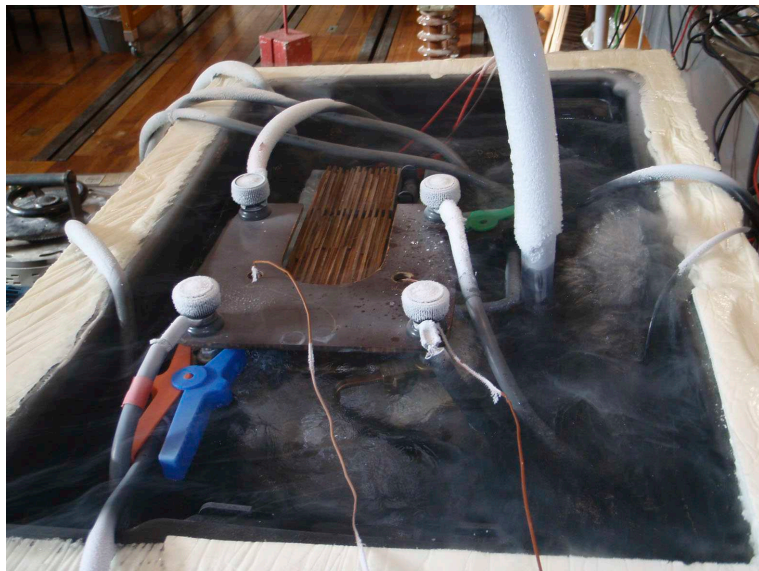
(b) Testing of the full core HTS transformer while submerged in LN_2.

Figure 3.14   The Chew HTS transformer before and during electrical testing.

HTS Test Results

A series of electrical tests were performed on the HTS transformer while submerged in LN_2 Figure 3.14(b). Once again, open circuit, short circuit and load tests were performed. Measurements were taken of the inside (primary) and outside (secondary) winding's voltage and current. The temperature of the core and windings were also monitored throughout the duration of testing. The results of the testing are summarised in Table 3.10.

The open circuit test results show a higher power loss and a larger current than that of the copper

Table 3.10   Test results for the Chew HTS transformer.

Open Circuit Test	
Parameter	Measured
Primary voltage (V)	232
Primary current (A)	0.25
Primary real power (W)	30
Primary apparent power (VA)	57
Primary power factor	0.57
Secondary voltage (V)	238
Voltage ratio	1.03
Short Circuit Test	
Parameter	Measured
Primary voltage (V)	75.1
Primary current (A)	64.9
Primary real power (W)	185
Primary apparent power (VA)	4878
Primary power factor	0.04
Secondary current (A)	62.4
Current ratio	0.96
Load Test	
Parameter	Measured
Primary voltage (V)	226
Primary current (A)	64.5
Primary real power (kW)	12.97
Primary apparent power (kVA)	14.60
Primary power factor	0.89
Secondary voltage (V)	207
Secondary current (A)	62.0
Secondary real power (kW)	12.72
Secondary apparent power (kVA)	12.86
Secondary power factor	0.99
Efficiency (%)	98.1
Voltage regulation (%)	9.1

mock-up. This could be due to the reassembly of the core being slightly different compared to the copper mock-up. It could also indicate that the core material may have been damaged through thermal cycling. The test also shows an increase in secondary voltage due to the extra turns on the final secondary layer that was added to compensate for the loaded volt-drop of the copper mock-up.

The short circuit test results show a dramatic reduction in the real power losses compared to the copper mock-up, from 185 W to 410 W, even though the current density was much higher

($53\,\mathrm{A/mm^2}$ compared to $20\,\mathrm{A/mm^2}$). This demonstrates the HTS winding's ability to transport very high current densities with low losses while superconducting. The losses may well be associated with the copper leads connecting the HTS tapes to the transformer terminals.

The load test results show an improvement across the board compared to the copper mock-up. The efficiency has been greatly improved over the copper transformer from $88\,\%$ to $97\,\%$ even though the load has been increased from $9\,\mathrm{kW}$ to $12\,\mathrm{kW}$. The voltage regulation, at $9\,\%$, is still quite large compared to conventional transformers of similar ratings. Once again this is due to the excess leakage flux caused by the $2\,\mathrm{mm}$ spacers. The load test was performed for around 60 minutes with no measurable increase in winding temperature. This suggests that the cooling channels are beneficial to the ability of the superconducting windings to continue to be superconductive under high transport currents and magnetic fields.

3.6 DISCUSSION

Development of the RDM for transformer design has been successful. The RDM was adapted to PCT with good agreement between measured and calculated results for the Liew designed transformer. The enhancement of the modelling by using FEA was also successful. Further discussion of the modelling is given in Chapter 4.

The cryogenic material testing provided some useful information, not the least of which was discovery of what is a common material in traditional power transformers being unsuitable for use in LN_2 cooled transformers. The fact that Kraft paper's strength is adversely affected when exposed to LN_2 temperatures is an important finding. Fortunately, the performance of Nomex® proved to be sufficient. The dielectric strength of LN_2 was comparable to that of regular transformer oil and as such it is a suitable dielectric material.

In the work by Bodger et al. there was very little difference between the oil tested core losses and the LN_2 core losses, Table 3.4, leading to the belief that the core can be fully submerged in LN_2. However, subsequent research by Chew suggests that the thermal cycling of the silicon steel could be damaging. The open circuit tests, usually a good measure of core losses, that Chew performed showed an increase in core losses between the copper winding tests and the HTS winding tests. While this may be attributed to the fact that the core was disassembled and reassembled between tests, it is also possible that damage has occurred to the crystalline structure of the steel. Inspection of the core material revealed that corrosion has appeared on the surface of the core steel, Figure 3.15. The rust was likely to have formed due to condensation buildup during the heating of the core from cryogenic temperatures. Mitigation methods could include encasing the core in epoxy resin, using a closed warm up system to prevent moisture ingress, or isolating the core from the LN_2 by using a Dewar such as the one from Section 3.4.1. The third option will be used in this thesis work.
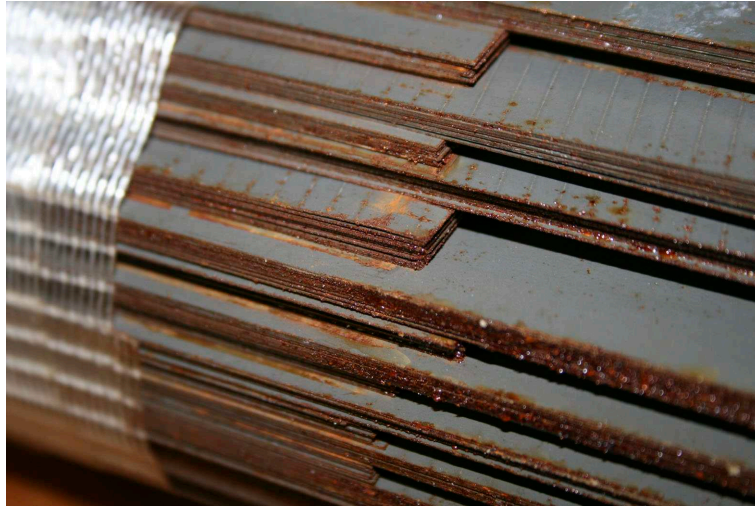
Figure 3.15   Corrosion forming on the core steel of the Chew transformer.

The 15 kVA HTSPCT prototype, whilst failing catastrophically, had some success. The performance of the vacuum Dewar and core vessel were as expected with the outside of the Dewar remaining at room temperature for the duration of testing. Degradation of the Dewar material did not occur over several thermal cycles filling and draining of the Dewar with LN_2. The copper busbar system for joining the HTS winding to the transformer bushings was also a success with no damage to the windings from thermal expansion of the copper busbars.

Some aspects of the design could have been improved upon and concern the winding layout. Firstly, is the uneven voltage distribution between the three winding sections. This is apparent from the open circuit test results from Table 3.5, the nominal voltage for the middle and outside windings is 115 V, whereas the measured voltage was 113 V and 111 V. This is caused by leakage flux increasing as the windings are positioned further from the core. An alternative winding layout to that of Figure 3.3 would be needed.

Secondly, is the failure of the windings during high loading. The investigation into the cause of the winding failure proposed that a combination of operating too close to the critical limits of the transformer and a poor cooling layout for the windings contributed to the failure. Subsequent work by Chew has shown that with adequate cooling the Chew transformer can be operated at high loading and the windings will not fail. Furthermore, dc testing on samples of the tape used in the Chew transformer has revealed that the tape used had a critical current of around 90 A, Figure 3.16, whereas the tape used in the HTSPCT prototype had a critical current of approximately 125 A. This data tends to suggest that for part of the ac cycle, the Chew transformer was operating beyond the critical limits of the tape though the transformer did not fail. The implication of this result is that provided there is sufficient cooling to remove the excess heat from the winding, the HTS conductor can be operated beyond the critical limits, albeit with a reduction in the transformers' efficiency.
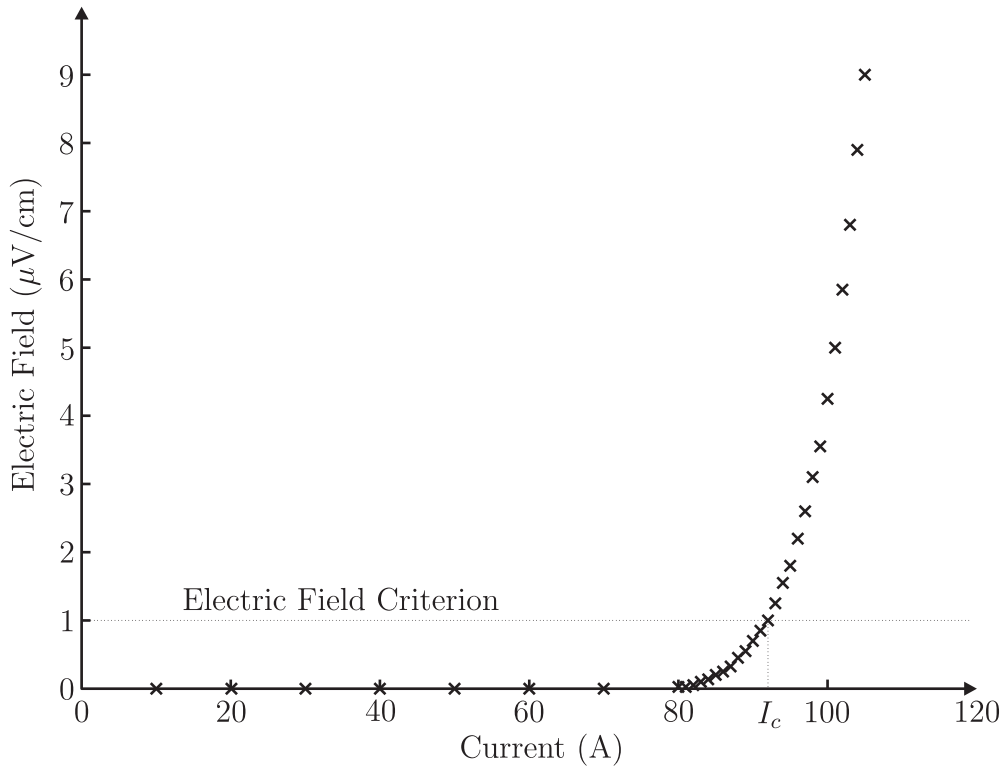
Figure 3.16 Critical current test results from samples of tape used in the Chew transformer.

While the ability of the Chew transformer to remove heat is beneficial, the large series impedance is problematic to the voltage regulation of the transformer, as illustrated in the load test results of Tables 3.8 and 3.10. A careful redesign will be necessary to improve the regulation without impeding the flow of LN_2 to the HTS conductor surface.

3.7 CONCLUSIONS

A method for designing partial core transformers using a computer program has been developed by Bodger et al. The program employs a unique transformer design concept called the reverse design method. This method determines the transformer performance based on the physical characteristics and dimensions of the materials used. The program was used to design several PCTs including a HTS transformer.

Research on cryogenic material testing was also completed. The research found useful properties for materials to use in HTS transformers. The research found that the dielectric breakdown strength of LN_2 was comparable to that of standard transformer mineral oil. It also found that Nomex® was a suitable insulation material for use with LN_2 and had superior mechanical strength to Kraft paper.

The design and construction of a high temperature superconducting partial core transformer

prototype has been completed. The windings were layer wound with Bi2223 HTS wire. The partial core was a slug of laminated silicon steel. A composite material Dewar was constructed to contain the liquid nitrogen. A series of electrical tests were performed on the transformer while submerged in liquid nitrogen. The open circuit test illustrates the relatively high magnetising current that is present with the partial core design. Nevertheless, the performance under full load shows good efficiency and regulation and demonstrates the viability of the partial core HTS transformer design. Failure of the transformer occurred as a result of operating the transformer too close to the HTS tape's critical current density in a magnetic field. It is also the case that the design does not allow for heat removal once produced and conductor movement during thermal cycling. Some observations were made about the damage to the windings, the possibility of oxygen in the LN_2 and the buckling of the HTS wire.

Finally, an alternative winding design has been developed and a full core HTS transformer constructed using this design. Testing of the full core transformer has demonstrated the winding design's capability at removing heat and preventing a winding failure despite operation of the windings beyond the critical limits of the conductor. Further refinement of the winding design will be needed to improve the series impedance of the transformer while still retaining the thermal properties.

Chapter 4

MODEL DEVELOPMENT

4.1 OVERVIEW

This chapter presents the modelling techniques used in the design of a HTSPCT. It is built upon a modification of the existing PCT modelling techniques previously developed by Bodger et al. As there already exists in the literature a thorough explanation of the reverse design method of PCT design [Bodger *et al.* 2000, Liew and Bodger 2001, Liew and Bodger 2002, Bodger and Liew 2002, Bell and Bodger 2007, Bell 2008, Chew 2010] only a brief description of this method will be given here. Instead emphasis will be given to new modifications to the models developed for this thesis. These modifications are largely based on the ac loss modelling for HTS wires.

The PCT modelling will be introduced, starting first with the core loss modelling. This includes the first implementation of a new eddy current loss model developed by Xi Ting Huo [Huo 2009]. The core loss modelling is followed by a brief examination of the winding losses in traditional transformer winding materials such as copper. Following the winding losses, the reactive components of the model, the leakage and magnetising reactances, are presented where two separate methods, a circuit theory and a finite element method for calculation are used. The two methods are compared through a series of simulations and electrical tests on PCTs.

Finally, an ac loss model for HTS wire, specifically Bi2223, is developed and presented. The ac loss is comprised of two parts, a transport current component and a magnetisation component. Each component is developed from a combination of applied theory and empirical models based on measured data from some samples. The ac loss model is influenced by the dc characteristics of the tape and also the magnetic field, hence these aspects are also discussed.

4.2 PARTIAL CORE TRANSFORMER MODEL

The PCT model is based upon the reverse design method of transformer design where the physical dimensions and characteristics of the core and the windings determine the performance of the
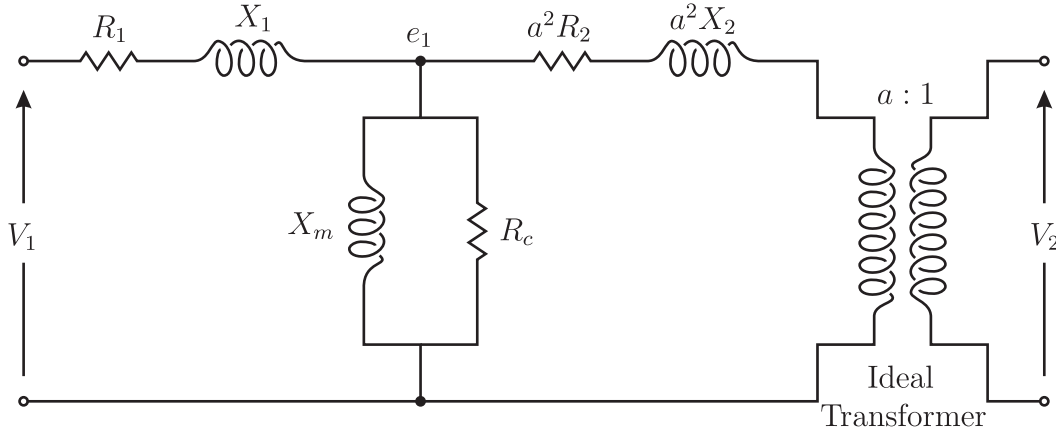
Figure 4.1   Equivalent circuit for a mains frequency transformer.

transformer. By manipulation of the materials actually used in the design of the transformer, the performance can be calculated and tailored to design needs. The model is based upon the Steinmetz 'exact' transformer equivalent circuit [Lynch *et al.* 2007] as depicted in Chapter 2 and repeated here in Figure 4.1. The model uses a combination of circuit theory and finite element analysis to determine the equivalent circuit components for the Steinmetz model. The performance of the transformer can then be determined by solving the Steinmetz model for various load and supply conditions.

4.2.1   Core Loss Modelling

The core losses of a PCT are due to two components, magnetic hysteresis of the core material and induced eddy currents due to changing magnetic fields. The core losses are represented by a resistance R_c in the Steinmetz model of Figure 4.1. The hysteresis and eddy current losses are proportional to the square of the induced emf in the core, e_1. The core resistance, R_c, is sized so that the power dissipated in it is equal to the combined hysteresis and eddy current losses such that,

$$R_c = \frac{R_h R_{ec}}{R_h + R_{ec}} \tag{4.1}$$

where R_h represents the core hysteresis losses and R_{ec} represents the core eddy current losses. The resistances, R_h and and R_{ec} are derived from the associated hysteresis and eddy current power losses, P_h and P_{ec}, and the induced emf, e_1.

$$R_h = \frac{e_1^2}{P_h} \tag{4.2}$$

and

$$R_{ec} = \frac{e_1^2}{P_{ec}} \tag{4.3}$$

Core Hysteresis Losses

The hysteresis losses are caused by movement of magnetic domains, called Weiss domains [Kittel 1949], of the core material as they align themselves with the external time varying magnetic field. This loss is proportional to the frequency and depends on the area of the hysteresis loop depicted in Figures 2.5 and 2.8 of Chapter 2. The hysteresis loop is a characteristic of the core material and is a function of the peak flux density in the core. A formula for calculating the hysteresis power loss can be found in many transformer text books [Heathcote 2007, Slemon 1966, Matsch and Morgan 1986] and is given by,

$$P_h = k_h f B_{max}^x W T_c \tag{4.4}$$

where k_h is a material constant (typically k_h can vary from about 0.11 for older steel to 0.011 for modern transformer steel), f is the frequency of the changing magnetic field, B_{max} is the peak magnetic flux density of the field in Tesla, x is the *Steinmetz exponent*, and WT_c is the weight of the core in kg. The Steinmetz exponent can vary between 1.6 and 2.2 depending on the core material used. Boglietti et al. give an average value of 1.86 which is the value used in this thesis [Boglietti *et al.* 2003].

Core Eddy Current Losses

The eddy current losses are Joule heating due to induced currents circulating in the core material. The time varying magnetic field in the core induces a current in the core in a direction that opposes the field according to Lenz's law. The classical equation for calculating the eddy current losses in traditional full core transformers is, [Heathcote 2007, Matsch and Morgan 1986],

$$P_{ec} = \frac{c_{lam}^2}{12\rho_c} \frac{l_c}{N_1^2 A_c} e_1^2 \tag{4.5}$$

where c_{lam} is the thickness of a lamination in meters, ρ_c is the core resistivity, l_c is the core flux path length in meters and A_c is the cross sectional area of the core in square meters. While this formula is widely used in full core transformer design, the tendency is for it to underestimate the eddy current power loss [Bertotti 1998, Boglietti *et al.* 2003, Zirka *et al.* 2008], especially in
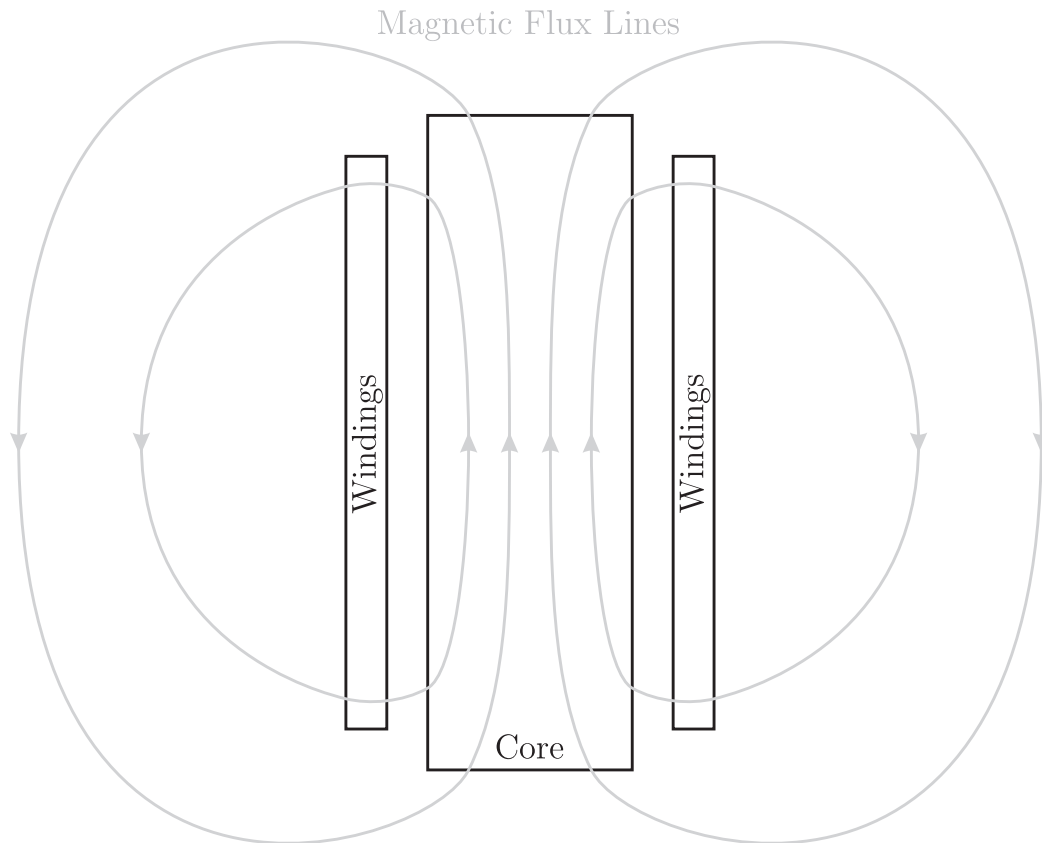
Figure 4.2   Diagram illustrating how the magnetising flux (grey arrows) spreads radially in a PCT.

PCTs. The original PCT model introduced an eddy current scaling factor to compensate for the loss calculation error. The scaling factor modified the calculated eddy current resistance and was typically equal to 0.1, i.e. this increased the calculated eddy current losses by ten times.

A reason for the inaccuracy in the eddy current power loss calculation is due to radial spreading of the magnetic flux in the end regions of the partial core. It was originally believed that the magnetic flux was contained within the core and then spread out from the ends of the core [Liew 2001]. Subsequent investigation using FEA software suggests that radial spreading of the flux occurs throughout the end regions of the core. Figure 4.2 illustrates the flux spreading effect on a typical PCT geometry.

Xi Ting Huo proposed a new method for calculating the eddy current power loss in PCTs which takes into account the radial spreading of the flux [Huo 2009]. Huo developed simple quantitative expressions, based on theory and empirical methods, for the eddy current loss by representing the flux in any rectangular lamination in three orthogonal directions. Figure 4.3 depicts the orthogonal flux directions labeled a, b and c for a single lamination and includes other key dimensions used in the model. Each lamination is divided into three sections, a top, middle, and bottom section. The flux is assumed uniform and in direction a only in the middle section. The top and bottom sections contain flux in all three directions.
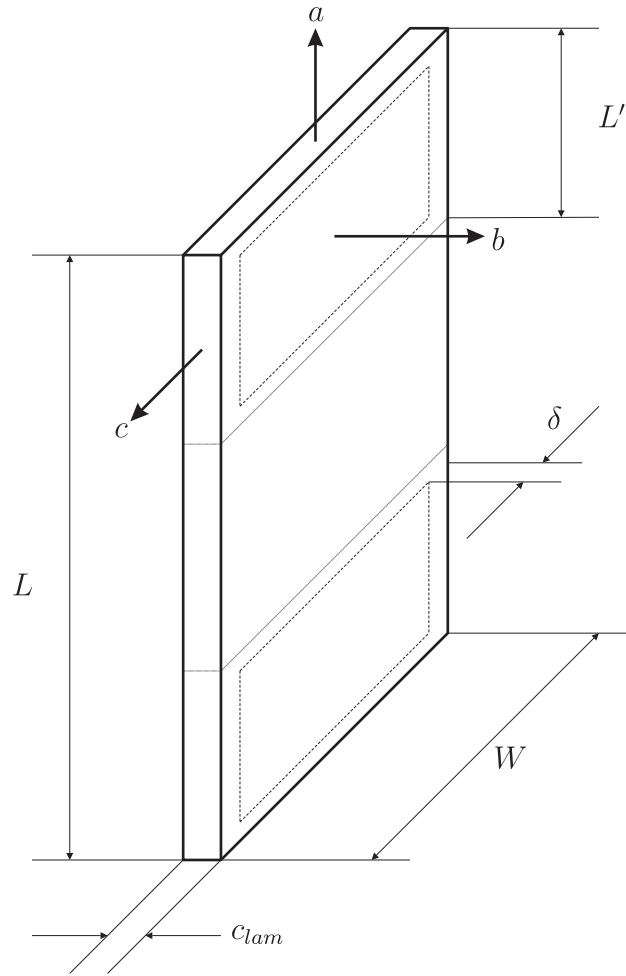
Figure 4.3 Diagram illustrating the orthogonal flux vectors used in eddy current loss model and the key dimensions of a single lamination.

Three factors (β_a, K_{ec} and L') are used to determine the nature of the spreading flux. β_a, the transformer aspect ratio, is the ratio of the winding axial length and winding thickness and is equal to,

$$\beta_a = \frac{l_w}{\tau_{12}} \tag{4.6}$$

where l_w is the average axial length of the windings in meters and τ_{12} is the winding thickness factor, the radial thickness of the windings and insulation. L' is a percentage of the core length, l_c, which indicates the region of the flux spreading at the ends of the core and is calculated by the fitted formula,

$$L' = \left[9.34 \left(\frac{l_c}{l_w} \right) + 16.83 \right] \% \tag{4.7}$$

Finally, K_{ec} is a spreading factor which indicates how much of the total flux spreads at the ends of the core. The spreading factor can be found by the fitted formula,

$$K_{ec} = 0.013\beta_a + 0.39 \tag{4.8}$$

Having determined the parameters defining the spreading flux for the PCT, the eddy current resistance for a single lamination can then be calculated. A separate eddy current resistance for each of the orthogonal flux vectors, a, b, and c, is calculated for the top section of the core, denoted with the subscript T, and the bottom section, denoted with the subscript B. As the flux in the middle section, subscript M, of the core is assumed to be uniform and in the a direction only, the eddy current resistance in the a direction is all that is calculated.

Assuming that the skin depth of the eddy current, δ, is greater than half the lamination thickness, c_{lam}, which is almost always the case, the resistances for the top section are,

$$R_{ec\_Ta} = \rho_c \frac{4W}{L' c_{lam}} \tag{4.9}$$

$$R_{ec\_Tb} = \rho_c \frac{2W + 2L' + 4\delta}{\delta c_{lam}} \tag{4.10}$$

$$R_{ec\_Tc} = \rho_c \frac{4L'}{W c_{lam}} \tag{4.11}$$

where ρ_c is the resistivity of the core material in ohm meters. The resistance of the middle section is,

$$R_{ec\_Ma} = \rho_c \frac{4W}{(l_c - 2L') c_{lam}} \tag{4.12}$$

Finally because the flux spreading is symmetrical between the top and bottom sections the eddy current resistances for the bottom section are the same as for the top section. The resistances for the bottom section are,

$$R_{ec\_Ba} = \rho_c \frac{4W}{L' c_{lam}} \tag{4.13}$$

$$R_{ec\_Bb} = \rho_c \frac{2W + 2L' + 4\delta}{\delta c_{lam}} \tag{4.14}$$

$$R_{ec\_Bc} = \rho_c \frac{4L'}{W c_{lam}} \tag{4.15}$$

The resistivity of the core material is temperature dependent such that,

$$\rho_c = \rho_{c20°C} \left(1 + \rho_{c\Delta T}\left(T_c - 20\right)\right) \tag{4.16}$$

where $\rho_{c20°C}$ is the core resistivity at 20°C, $\rho_{c\Delta T}$ is the thermal resistivity coefficient of the core material, and T_c is the core operating temperature.

With the resistances for a single lamination calculated, the eddy current power loss for a number, n_{lam}, of stacked laminations of equal dimensions can be calculated. The power loss for the top section is given by

$$P_{ec\_Ta} = \frac{\left(\frac{e_1(1-K_{ec})}{N_1 n_{lam}}\right)^2}{R_{ec\_Ta}} n_{lam} \tag{4.17}$$

$$P_{ec\_Tb} = \frac{\left(\frac{e_1 K_{ec}}{N_1}\right)^2}{R_{ec\_Tb}} n_{lam} \tag{4.18}$$

$$P_{ec\_Tc} = \frac{\left(\frac{e_1 K_{ec}}{N_1 n_{lam}}\right)^2}{R_{ec\_Tc}} n_{lam} \tag{4.19}$$

The power loss for the middle section is given by,

$$P_{ec\_Ma} = \frac{\left(\frac{e_1}{N_1 n_{lam}}\right)^2}{R_{ec\_Ma}} n_{lam} \tag{4.20}$$

The power loss of the bottom section is the same as the top section so that,

$$P_{ec\_Ba} = P_{ec\_Ta} \tag{4.21}$$

$$P_{ec\_Bb} = P_{ec\_Tb} \tag{4.22}$$

$$P_{ec\_Bc} = P_{ec\_Tc} \tag{4.23}$$
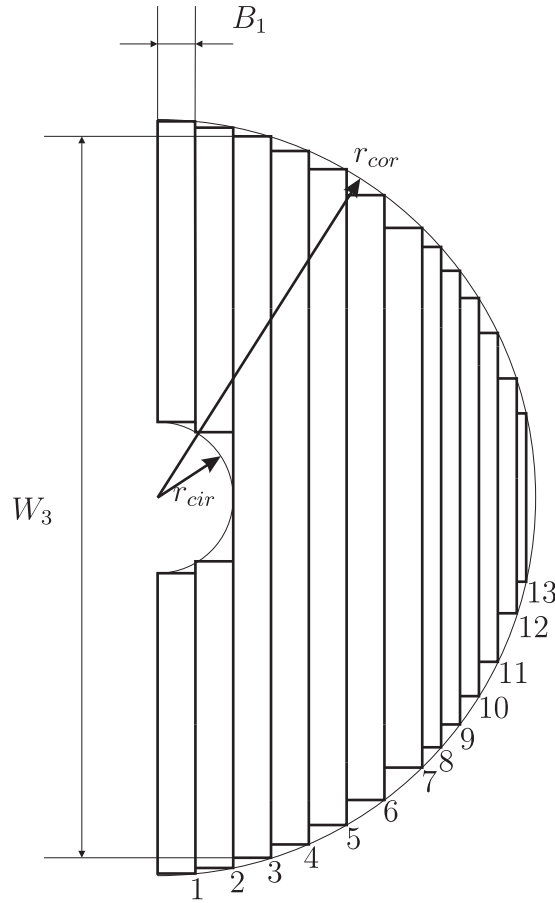
Figure 4.4   Diagram illustrating the generic arrangement of circular core comprised of thirteen sections.

Finally the eddy current power loss for the entire block, P_{ec1}, is the summation of all the calculated power losses for the top, middle and bottom sections.

$$P_{ec1} = 2\left(P_{ec\_Ta} + P_{ec\_Tb} + P_{ec\_Tc}\right) + P_{ec\_Ma} \tag{4.24}$$

If the PCT is designed with a rectangular shaped core, the power loss calculated for the stacked block, P_{ec1}, will be equal to P_{ec}. However if the PCT is designed with a circular shaped core of parallel stacked laminations, the eddy current power loss of several blocks, 1 through n, will need to be calculated and added together. A generic arrangement of thirteen stacked blocks with a stacking factor of 0.96 has been developed and is illustrated in Figure 4.4. In this arrangement, the blocks labeled 1 through 7 have a thickness, B_n, of $r_{cor}/10$, the blocks 8 through 12 a thickness of $r_{cor}/20$ and block 13 a thickness of $r_{cor}/40$. The widths of each block, W_n, can be determined from the inner, r_{cir}, and outer, r_{cor}, core radii.

The equations for calculating the eddy current power loss for each block are the same as Equations 4.6 to 4.24 with appropriate substitutions for the dimensions of the core blocks and number

of laminations of those blocks. The exception is that the induced emf in the block is no longer e_1 but instead must be scaled by the area of the block being calculated.

$$e_{cbn} = \frac{A_n}{A_c} e_1 \tag{4.25}$$

where e_{cbn} is the emf for the nth core block being calculated and A_n is the cross sectional area of the nth core block. Furthermore, due to the spreading flux penetration between adjacent blocks in the b direction, the emf for the b direction is modified further by the following equation,

$$e_{cbn\_b} = \frac{A_{n\_b}}{A_{(n-1)\_b}} e_{cb(n-1)\_b} + e_{cbn} K_{ec} \tag{4.26}$$

where e_{cbn_b} is the emf in the b direction for the nth core block, A_{n_b} is the spreading area, $L' \times W_n$, of the nth core block, $A_{(n-1)\_b}$ is the spreading area for the $(n-1)^{\text{th}}$ block, and $e_{cb(n-1)}$ is the emf calculated for the b direction of the $(n-1)^{\text{th}}$ block.

The eddy current power loss for each block, P_{ecn}, is the summation of the power losses calculated from Equation 4.24 with the appropriate substitutions, and the total eddy current power loss for the circular partial core is,

$$P_{ec} = 2 \sum_{n=1}^{13} P_{ecn} \tag{4.27}$$

4.2.2   Winding Loss Modelling

The winding losses are represented by the resistances R_1 and R_2 of Figure 4.1 which are sized such that power dissipated in them is equal to,

$$P_1 = I_1^2 R_1 \tag{4.28}$$

and

$$P_2 = I_2^2 R_2 \tag{4.29}$$

where P_1 and P_2 are the power loss of the primary and secondary windings respectively and I_1 and I_2 are the rms currents through each winding which is dependent on the applied voltage and the load conditions.

In a traditional transformer, the windings are usually made from copper or aluminium wire and the resistance of the winding depends on the conductor resistivity and its dimensions.

$$R_w = \rho_w \frac{l_w}{A_w} \tag{4.30}$$

where R_w is the resistance of the winding, ρ_w is the resistivity of the winding material in ohm meters, l_w is the length of the winding wire in meters and A_c is the cross sectional area of the winding wire in meters squared. Furthermore, the resistivity of the winding changes with temperature such that,

$$\rho_w = \rho_{w20^\circ C} \left(1 + \rho_{w\Delta T} \left(T_w - 20\right)\right) \tag{4.31}$$

where $\rho_{w20^\circ C}$ is the resistivity of the winding material at 20°C, $\rho_{w\Delta T}$ is the thermal resistivity coefficient of the winding material, and T_c is the winding operating temperature. A list of resistivity and thermal coefficients for common transformer winding materials is listed in Table 4.1 [Davies and Simpson 1979, Davies 1990, Stansel 1949, Smith and Fickett 1995, Zinn and Semiatin 1988].

Table 4.1   Resistivity of common transformer materials.

Metal	$\rho_{20^\circ C}$ $(\Omega m \times 10^{-8})$	$\rho_{\Delta T}$ $(/^\circ C \times 10^{-3})$
Aluminium	2.67	4.3 4.9
Copper	1.68	3.9 - 4.4
Silver	1.47	60×10^{-9}
Mild Steel	9.71 - 16.0	6.5

For the superconducting transformer, part of the winding losses are due to ac losses of the HTS material which is covered in Section 4.4. The rest is due to the connecting lead-outs and bushings whose resistance can be calculated in the above manner.

4.2.3   Reactive Component Modelling

The reactive components of the Steinmetz model, X_1, X_2 and X_m, represent the magnetic energy of the transformer. Two methods to calculate these reactive components have been developed. The first method, called the circuit theory method (CTM), uses a combination of text book theory and empirical calculations to determine the reactive components. The second method, called the finite element method (FEM), uses a commercial finite element modelling

program called MagNet$^{\circledR}$ from Infolytica Corporation to model the PCT and derive the reactive components. The CTM is computationally faster than the FEM and does not require commercial software but the FEM has proven to be more accurate [Bell 2008].

Circuit Theory Method

The CTM for determining the reactive components is split into two parts. The magnetising reactance and the leakage reactance.

MAGNETISING REACTANCE

The reluctance of the magnetic circuit for a PCT is comprised of the reluctance of the core, $\mathfrak{R}_c$, and the reluctance of the air path, $\mathfrak{R}_{air}$. The reluctance of the core is given by,

$$\mathfrak{R}_c = \frac{l_c}{\mu_0 \mu_r A_c} \tag{4.32}$$

where μ_0 is the permeability of free space equal to $4\pi \times 10^{-7}$ and μ_r is the relative permeability of the core material which for grain orientated silicon steel is around 2500.

The reluctance of the air path is given by [Liew 2001],

$$\mathfrak{R}_{air} = 338712 \left[\left(\frac{1}{A_c} \right)^{0.345} \left(\frac{1}{l_c} \right)^{0.31} \right] \tag{4.33}$$

so that the total reluctance is,

$$\mathfrak{R}_T = \mathfrak{R}_c + \mathfrak{R}_{air} \tag{4.34}$$

The total relative permeability of the magnetic circuit is derived from the total reluctance and a magnetising function. This magnetising function takes into account the winding aspect ratio of the PCT and scales the reactance accordingly [Liew and Bodger 2002]. The magnetising function is,

$$\gamma(\beta_a) = 1 - e^{\left(\frac{-\beta_a}{0.32\beta_a + 0.8} \right)} \tag{4.35}$$

where, β_a is the transformer winding aspect ratio from Equation 4.6.

The total relative permeability then becomes,

$$\mu_{rT} = \frac{l_c}{\mu_0 \mathfrak{R}_T A_c} \gamma \left(\beta_a \right) \tag{4.36}$$

and the magnetising reactance of the PCT is,

$$X_m = \frac{2\pi f N_1^2 \mu_0 \mu_{rT} A_c}{l_c} \tag{4.37}$$

LEAKAGE REACTANCE

In the CTM the leakage reactance for each winding is assumed equal. The leakage reactance is calculated from the physical dimensions of the windings and the core. Figure 4.5 illustrates the key dimensions used in the leakage calculation.

The total leakage reactance for a PCT is derived from,

$$X_1 = a^2 X_2 = \frac{1}{2} \left(\frac{2\pi f \mu_0 N_1^2}{l_w \Gamma \left(\beta_a \right)} \right) \left(\frac{l_1 d_1 + l_2 d_2}{3} + l_{12} \Delta d \right) \tag{4.38}$$

where, l_w is the winding height, $\Gamma(\beta_\alpha)$ is the leakage function, l_1 is the mean circumferential length of the primary winding, d_1 is the primary winding radial thickness, l_2 is the mean circumferential length of the secondary winding, d_2 is the secondary winding radial thickness, l_{12} is the mean circumferential length of the inter-winding space and Δd is the inter-winding space radial thickness.

The leakage function for a PCT is derived from the transformer aspect ratio and is given as [Liew and Bodger 2001],

$$\Gamma \left(\beta_a \right) = 1 - e^{\left(\frac{-\beta_a}{0.4\beta_a + 1.59} \right)} \tag{4.39}$$

Finite Element Model

The finite element method (FEM) is based on 2D magneto-static finite element analysis from a commercial computer simulation to model the reactive components of the Steinmetz 'exact' transformer equivalent circuit. This package removes the assumption of a uniform flux density and the empirical constants of the CTM [Bell and Bodger 2008].

Each layer of the PCT was modelled as a block of solid copper that covers all turns of that winding layer. The insulation between the layers was modelled as air. This model is considered
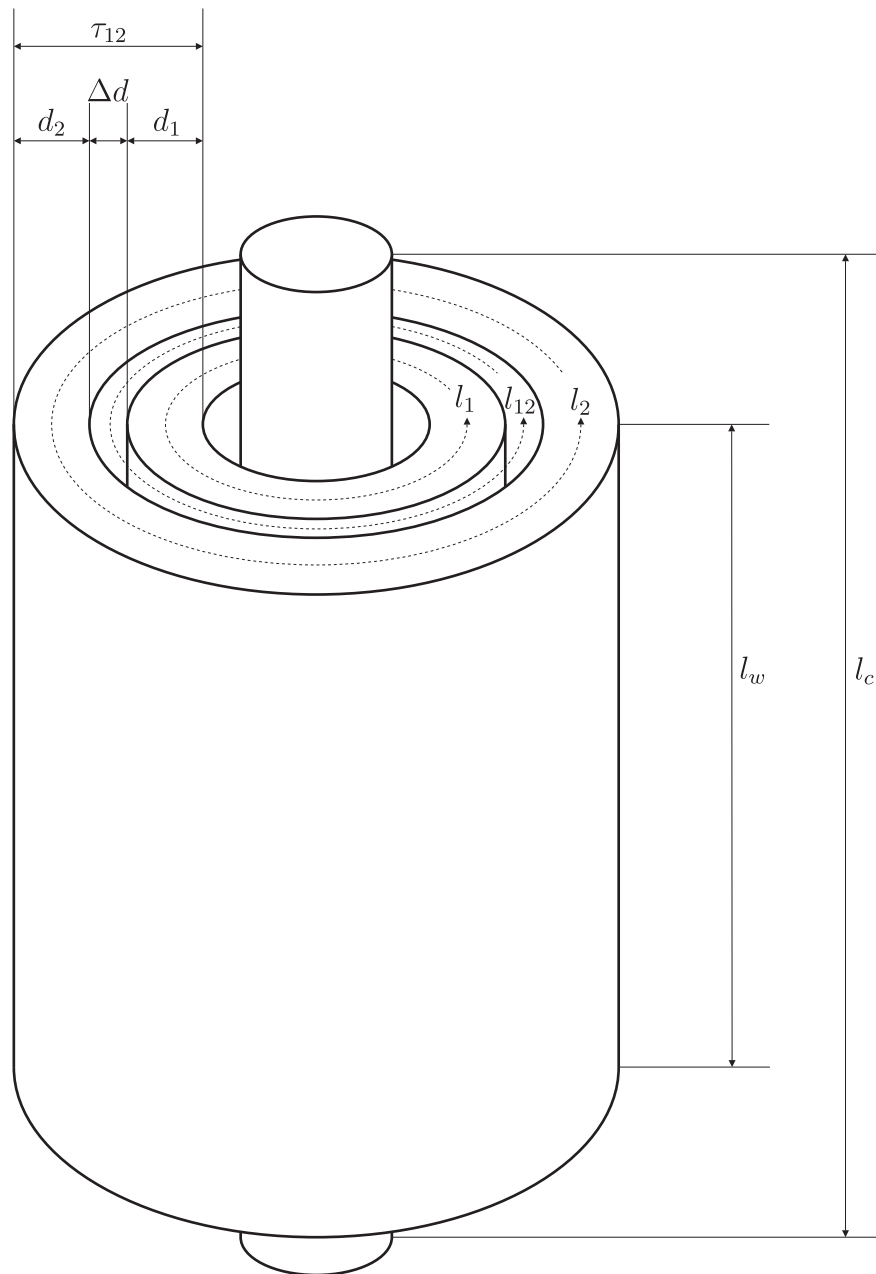
Figure 4.5 Key dimensions for calculating the leakage reactance for a PCT.

(a) Magnetic field plot for an open circuit test.   (b) Final solution mesh for static 2D simulation.
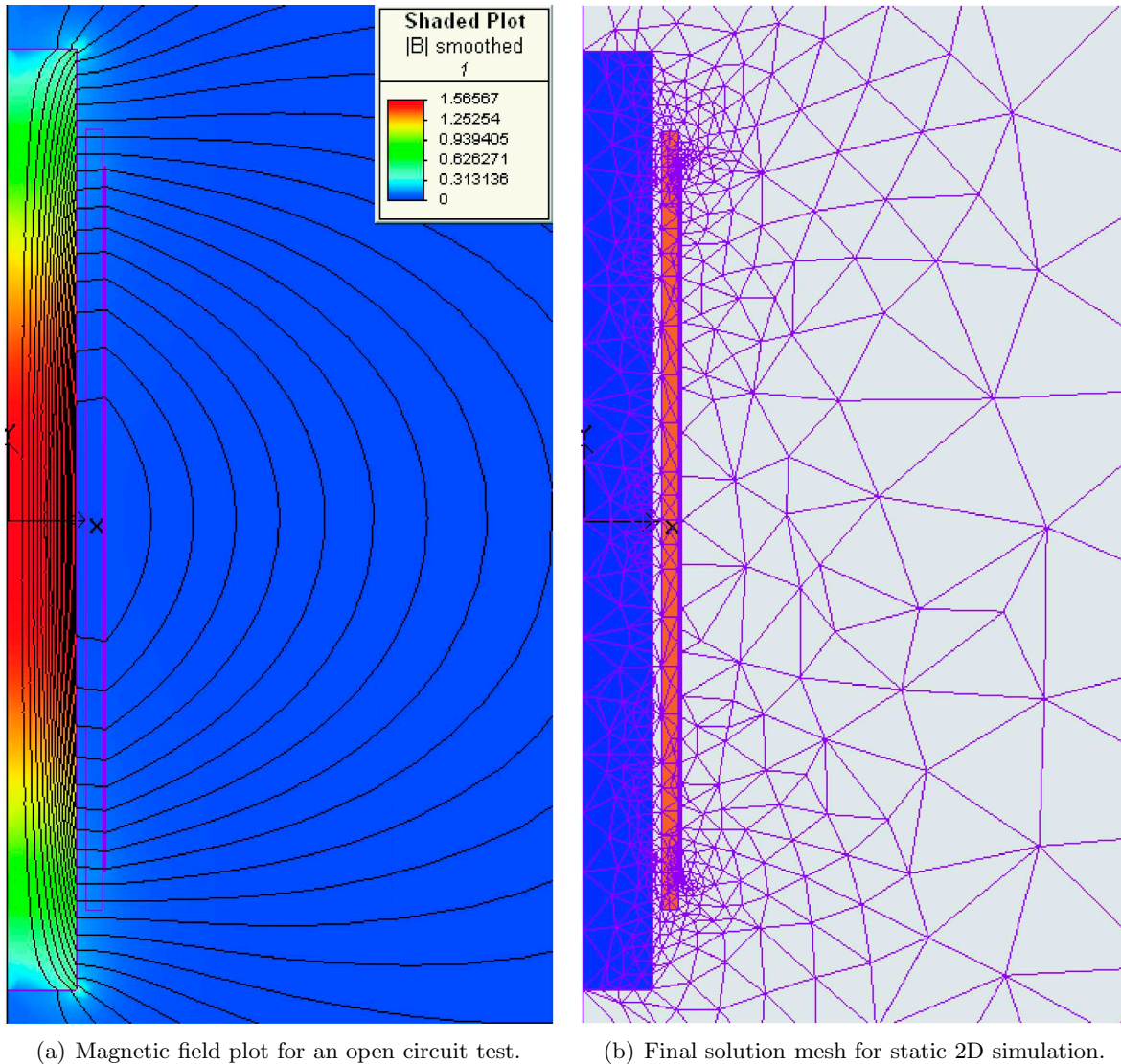
Figure 4.6   Finite Element Model of a partial-core transformer.

sufficient as the winding turns were packed close together. Inter-winding eddy currents were assumed to have negligible effect on the global field distribution.

The core was modelled as a single block of isotropic linear material with a relative permeability of 2500. This model does not take into account the non-linear effects such as core saturation and radial flux not being restricted to the lamination plane. These non-linearities were assumed to have minimal effect on the global field distribution.

The modelling of the PCT is considered an open-bounded problem because the flux return path is air. For this reason a simple truncation method was used where the outer air boundaries were located far from the transformer and a Dirichlet (flux tangential) constraint was applied. Figure 4.6 shows an example of the finite element flux plot and solution mesh for a sample PCT.

Reactance Parameters

A permeance matrix ($\mathbf{P}$) for an n layer PCT is defined as,

$$\mathbf{P} = \begin{bmatrix} P_{11} & \cdots & P_{1n} \\ \vdots & \ddots & \vdots \\ P_{n1} & \cdots & P_{nn} \end{bmatrix} \tag{4.40}$$

where $P_{ij} = P_{ji}$

$\mathbf{P}$ is obtained from the finite element model by performing n simulations. In each simulation a single winding layer, assigned with a unity number of turns, is excited with unit-current and a row of $\mathbf{P}$ is calculated.

The winding section inductance matrix, $\mathbf{L}$, can then be obtained from $\mathbf{P}$. The elements of $\mathbf{L}$ are calculated as [Ong 1997],

$$L_{ij} = N_i N_j P_{ij} \tag{4.41}$$

where N_i and N_j are the number of turns of the ith and j^{th} winding sections.

The primary and secondary windings are formed via series connections of one or more layer sections. Let $W = WS1, \ldots, WSn$ be the set of n winding layer sections (numbered from the inside) and P and S be subsets of W containing nP and nS elements respectively. Let $P(i)$ and $S(j)$ denote the ith and j^{th} elements of P and S. The inside and outside winding self-inductances are given by [Wirgau 1976]

$$L_P = \sum_{i=1}^{nI} L_{P(i)P(i)} + \sum_{i=1}^{nP} \sum_{\substack{j=1 \\ i \neq j}}^{nP} L_{P(i)P(j)} \tag{4.42}$$

$$L_S = \sum_{i=1}^{nS} L_{S(i)S(i)} + \sum_{i=1}^{nS} \sum_{\substack{j=1 \\ i \neq j}}^{nS} L_{S(i)S(j)} \tag{4.43}$$

The primary-secondary mutual-inductance is given by

$$M_{PS} = \sum_{i=1}^{nP} \sum_{j=1}^{nS} L_{P(i)S(j)} \tag{4.44}$$

The inductances are transformed into the reactance components of the Steinmetz exact transformer equivalent circuit using [Bell and Bodger 2008]

$$X_m = j\omega(aM_{PS}) \tag{4.45}$$

$$X_1 = j\omega(L_P - aM_{PS}) \tag{4.46}$$

$$a^2 X_2 = j\omega a^2 (L_S - \frac{1}{a}M_{PS}) \tag{4.47}$$

4.3   A COMPARISON BETWEEN CTM AND FEM REACTIVE COMPONENTS

To test the validity of the two different methods for calculating the reactive components of the Steinmetz model, a combination of simulation and experiments were conducted on a variety of PCTs' designs.

4.3.1   Simulation

The first step in the comparison was a series of simulations on hypothetical PTCs.

Simulation Setup

A program was written in Visual Basic which reads in data from an Excel spreadsheet on the dimensions and material properties of the transformer being designed. From this data, the equivalent circuit elements are calculated for both the CTM model, and the FEM model via data calculated by the commercial FEA software including the reactive components discussed in Section 4.2.3. Chapter 5 contains more details on the program.

Seven different transformers were investigated with winding aspect ratios ranging from 36.36 to 0.62. Figure 4.7 shows an example of three of the simulated transformers. The dimensions were determined by increasing the number of layers on the simulated PCT while decreasing the winding height so that the total number of turns was constant. Also, to ensure that the different aspect ratio transformers were as similar as possible, the core weight was kept constant. The simulations used a former thickness of 10 mm. Information on the material properties of the core is presented in Table 4.2 and the dimensions used for each of the winding aspect ratios are presented in Table 4.3.
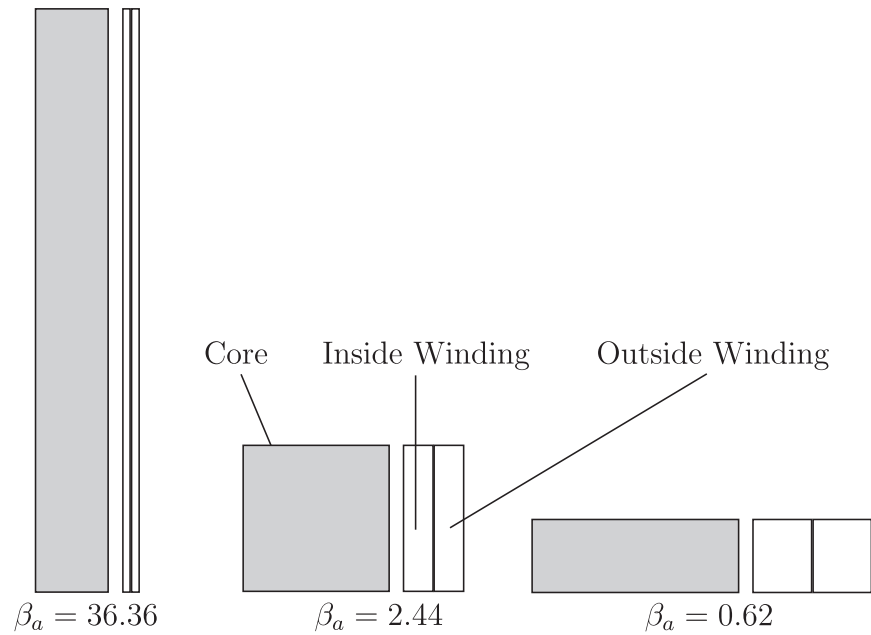
Figure 4.7 Cross sectional diagram of simulated PCTs for different winding aspect ratios. Note: only half of each transformer is shown for clarity.

Table 4.2   Material properties of the core.

Core Type	Partial-Core	
Core Shape	Circular	
Lamination Thickness	0.23	mm
Stacking Factor	0.95	
Relative permeability	3000	
Resistivity at 20 $^\circ$ C	47.2E-9	$\Omega-$m
Thermal resistivity coefficient	6.0E-3	$^\circ$C^{-1}
Operating Temperature	20	$^\circ$ C
Material Density	7650	kg/m^3

Table 4.3   Core Dimensions for the different aspect ratio simulations.

Radius (mm)	Length (mm)	Weight (kg)
50.00	400	24.03
63.25	250	24.03
70.71	200	24.03
89.44	125	24.03
100.00	100	24.03
111.80	80	24.03
141.42	50	24.03

The simulations modelled a 1 to 1 PCT with 2000 turns on both the primary (inside) and secondary (outside) windings. To change the winding aspect ratio whilst keeping the number of turns constant, the height of the winding window was decreased while the number of layers was increased as shown in Table 4.4. The wire size was chosen to be 1 mm in diameter with no inter-layer insulation, and a stacking factor of 1 for simplicity in calculating the number of turns per winding. There was a 1 mm gap between the two layers.

Table 4.4   Winding data.

Length (mm)	Primary Layers	Secondary Layers	Aspect Ratio
400	5	5	36.36
250	8	8	14.71
200	10	10	9.52
125	16	16	3.79
100	20	20	2.44
80	25	25	1.57
50	40	40	0.62

Simulation Results

The results of the simulation are given in Table 4.5 and are plotted in Figure 4.8. Figure 4.8(a) shows how the magnetising reactance changes with respect to the winding aspect ratio. It can be noted that there is a significant difference between the CTM and the FEM. The CTM suggests the magnetising reactance will tend towards zero as the winding aspect ratio approaches zero. This is because of the magnetising function Equation 4.35 which is an exponential function forcing the reactance to zero for small aspect ratios. The FEM in contrast is tending towards infinity for small aspect ratios. For aspect ratios above 15, both models have a reasonably constant magnetising reactance although there is a 13% difference.

The primary side leakage reactance of Figure 4.8(b) shows good correlation between both models for aspect ratios above 10. For lower aspect ratios the CTM calculation increases rapidly as governed by the leakage function of Equation 4.39, whereas the FEM value increases much slower. For the secondary winding leakage reactance shown in Figure 4.8(c), the CTM calculation is exactly the same as that of the primary winding as defined by Equation 4.37. The FEM calculation however, is about 50% less at high aspect ratios and starts to increase from an aspect ratio below 5. From Table 4.5, it is apparent that for large winding aspect ratios, the primary leakage reactance is larger than the secondary, but for small winding aspect ratios the opposite is true. The cross over point where $X_1 = X_2$ occurs between aspect ratios of 2.44 and 1.57, which is similar to traditional full core transformer aspect ratios and justifies the assumption made in Equation 4.37.
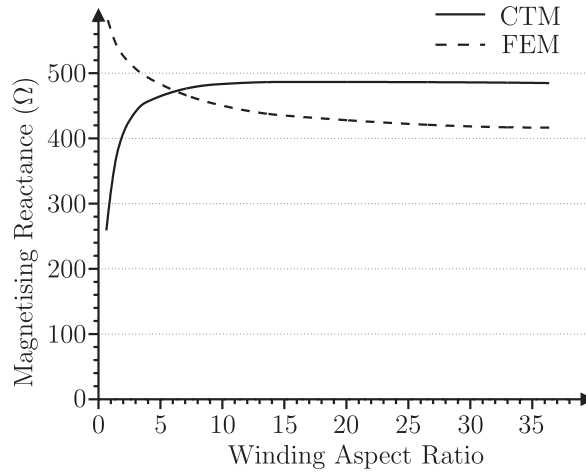
(a) Plot of simulation results for magnetising reactance against winding aspect ratio.
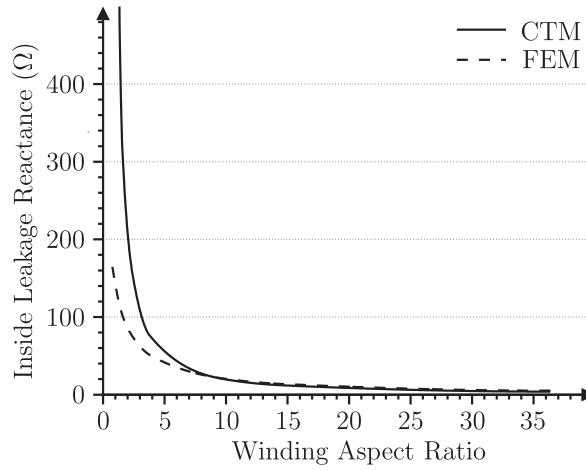
(b) Plot of simulation results for inside leakage reactance against winding aspect ratio.
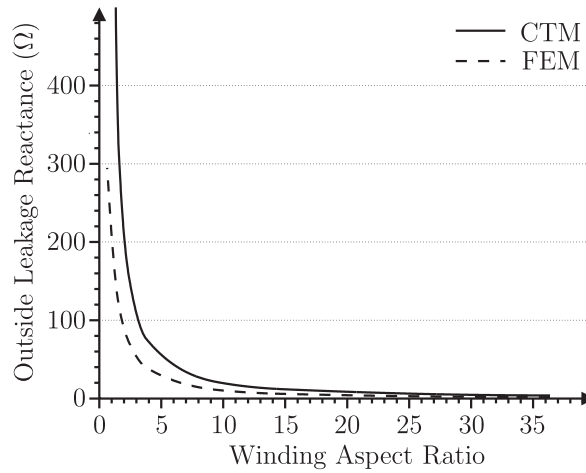
(c) Plot of simulation results for outside leakage reactance against winding aspect ratio.

Figure 4.8   Results from simulations investigating the CTM and FEM reactive components.
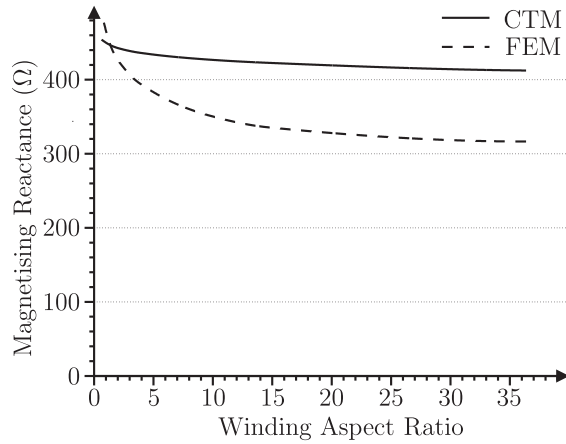
(a) Plot of simulation results for magnetising reactance against winding aspect ratio with magnetising function set to 1.
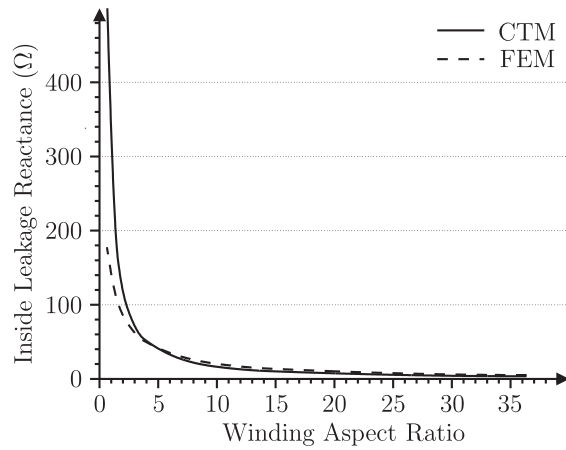
(b) Plot of simulation results for primary leakage reactance against winding aspect ratio with leakage function set to 1.
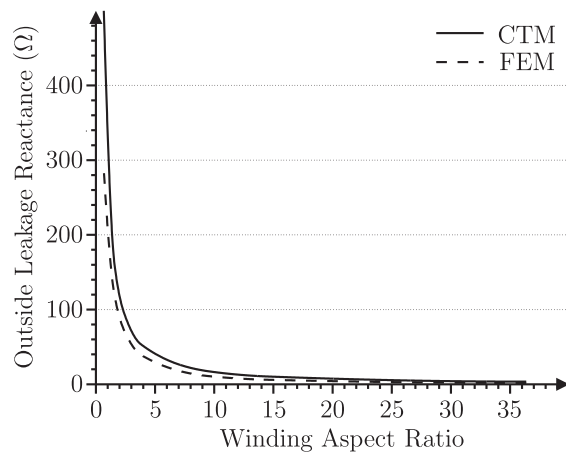
(c) Plot of simulation results for secondary leakage reactance against winding aspect ratio with leakage function set to 1.

Figure 4.9   Results from simulations investigating the CTM and FEM reactive components after removal of magnetising and leakage functions.

Table 4.5   Results from simulation.

Aspect Ratio	CTM			
	X_m	X_1	X_2	$X_1 + X_2$
36.36	484.88	3.93	3.93	7.87
14.71	486.56	11.94	11.94	23.88
9.52	482.90	20.93	20.93	41.87
3.79	454.83	76.18	76.18	152.35
2.44	425.24	151.25	151.25	302.50
1.57	381.73	318.25	318.25	636.51
0.62	255.74	1845.92	1845.92	3691.84
Aspect Ratio	FEM			
	X_m	X_1	X_2	$X_1 + X_2$
36.36	416.53	5.16	1.73	6.89
14.71	435.38	13.64	5.93	19.57
9.52	452.40	21.36	10.92	32.28
3.79	495.54	51.20	39.47	90.67
2.44	517.20	73.86	70.22	144.08
1.57	538.91	102.40	119.45	221.85
0.62	591.11	179.35	299.20	478.55

Table 4.6   Results from simulation with magnetising function and leakage function set to 1.

Aspect Ratio	CTM			
	X_m	X_1	X_2	$X_1 + X_2$
36.36	512.40	3.52	3.52	7.04
14.71	522.73	10.27	10.27	20.55
9.52	527.26	17.35	17.35	34.69
3.79	536.49	53.68	53.68	107.37
2.44	540.81	92.80	92.80	185.59
1.57	545.12	161.38	161.38	322.76
0.62	554.25	526.84	526.84	1053.68
Aspect Ratio	FEM			
	X_m	X_1	X_2	$X_1 + X_2$
36.36	416.53	5.16	1.73	6.89
14.71	435.58	13.64	5.93	19.57
9.52	452.40	21.36	10.92	32.29
3.79	495.54	51.20	39.47	90.67
2.44	517.20	73.86	70.22	144.09
1.57	538.91	102.40	119.45	221.85
0.62	591.11	179.35	299.20	478.55

Due to the added magnetising function of Equation 4.35 and leakage function of Equation 4.39 resulting in large deviations from the FEM results for small aspect ratios, the simulations were then repeated with the magnetising function and the leakage function set to 1, i.e. essentially removing them from the calculations. The results of those simulations are given in Figures 4.9 and Table 4.6.

With the magnetising function set to 1, the CTM magnetising reactance in Figure 4.9(a) is no longer forced to zero and increases with small aspect ratios. There is still a difference of about 18% between the two models at high aspect ratios. Correlation between the two models has been improved with the leakage function set to 1 as shown in Figures 4.9(b) and 4.9(c).

4.3.2   Test Results

The results from the second simulation show an overall improvement in the correlation between the CTM and FEM techniques suggesting the removal of the leakage function and magnetising function. Three PTCs were constructed and used for high potential testing of hydro generator stator insulation [Enright and Bodger 2002]. A series of tests were conducted on these three PCTs to ascertain which modelling method is more accurate, Figure 4.10 shows testing of the Manapouri PCT. The specifications of the PCTs are outlined in Table 4.7.

Measurement of the applied voltage and current were taken on each of the PCTs in both open circuit and short circuit configurations with a calibrated Fluke 41 meter. The measurements were used to determine the open circuit and short circuit impedance of the transformers and this was compared to simulation results from both the finite element model and both the circuit

Figure 4.10   Testing the Manapouri Partial-Core Transformer.

theory models. These results are presented in Table 4.8 where CTMm is the modified circuit theory model with the leakage and magnetising factors set to 1.

Table 4.7 Partial core transformer specifications.

		Lynch	Matahina	Manapouri
Core	Length	700	710	1200
	Radius	37.5	125	175
	Lamination Thickness	0.5	0.5	0.5
	Stacking Factor	0.96	0.95	0.95
Primary Winding (outside)	Length	600	680	900
	Layers	2	1	1
	Total Turns	160	65	62
	Voltage (V)	230	230	443
Secondary Winding (inside)	Length	700	735	995
	Layers	37	13	9
	Total Turns	1600	8840	502
	Voltage (V)	80000	30800	32000
Aspect Ratio		12.69	22.87	35.35

Table 4.8 Comparison between test results and simulation results.

		Lynch		Matahina		Manapouri	
		$\mathfrak{Re}$	$\mathfrak{Im}$	$\mathfrak{Re}$	$\mathfrak{Im}$	$\mathfrak{Re}$	$\mathfrak{Im}$
Parallel Impedance OCT(Ω)	Measured	62.05	3.25	9.37	0.65	21.40	1.10
	FEM	59.44	3.23	7.15	0.66	20.38	1.13
	CTM	55.82	3.26	8.98	0.77	17.84	1.03
	CTMm	55.58	3.25	8.96	0.77	17.83	1.03
% difference from measured	FEM	-1.9	1.6	-23.9	-0.7	-3.0	2.9
	CTM	-7.9	2.6	-4.4	16.4	-15.1	-6.7
	CTMm	-8.3	2.3	-4.6	16.2	-15.2	-6.8
Series Impedance SCT(Ω)	Measured	0.167	0.161	0.048	0.016	0.041	0.015
	FEM	0.145	0.155	0.056	0.017	0.033	0.016
	CTM	0.139	0.140	0.055	0.017	0.033	0.013
	CTMm	0.140	0.120	0.055	0.015	0.033	0.012
% difference from measured	FEM	-13.0	-3.8	15.7	5.7	-19.8	9.3
	CTM	-16.5	-12.8	14.4	5.9	-20.6	-12.5
	CTMm	-16.4	-25.6	14.5	-6.6	-20.6	-21.7

The open circuit test gives an indication of the magnetising current and the core losses, as the leakage reactance and winding resistance of the excited winding tend to be small by comparison. From Table 4.8, it can be seen that the partial-core transformer has quite a low magnetising

reactance, the $\mathfrak{Im}$ part of the impedance, when compared to the core loss component, the $\mathfrak{Re}$ part of the impedance. The calculated impedance has generally underestimated the real component when compared to the measured impedance, by as much as 25%. The reactive component of the modelling was much closer to the measured value with the FEM model being the most accurate (within %3). The FEM model showed an unusual result for the Matahina transformer. The real part of the impedance was overestimated for this transformer and underestimated for the other two transformers. This could be due to the relatively low impedance of the transformer compared with the other two.

The short circuit test results show the winding loss and leakage reactance. The results show a larger percentage difference between measured and calculated values when compared to the open circuit test results. This indicates that the models for the leakage reactance components are not as accurate as the models for the magnetising reactance. The short circuit connecting wire was not modelled, which could contribute to this error as the measured impedance is quite low. In practical terms, the model will tend to give incorrect results for a short circuit test, but will be more accurate for a loaded transformer because the load impedance is much larger compared to the series impedance of the transformer.

Simulation vs Field Testing Conclusions

During the simulations it was found that the magnetising function, Equation 4.35, and leakage function, Equation 4.39, were resulting in deviations in the CTM results when compared to the FEM results. By removing those functions, an improvement was made in the correlation between the two models at lower aspect ratios, $\beta_a < 7$. Comparisons with measured results show that overall, the FEM was more accurate and there was little difference between the two forms of the CTM for the magnetising reactance. However, the leakage function improved the results for the leakage reactance calculations. Thus it is proposed that the following equations replace those of Equation 4.35 and 4.39.

$$\gamma\left(\beta_a\right) = \begin{cases} 1 & \text{for}\,\beta_a < 7 \\ 1 - e^{\left(\frac{-\beta_a}{0.32\beta_a + 0.8}\right)} & \text{for}\,\beta_a \geq 7 \end{cases} \tag{4.48}$$

$$\Gamma\left(\beta_a\right) = \begin{cases} 1 & \text{for}\,\beta_a < 7 \\ 1 - e^{\left(\frac{-\beta_a}{0.4\beta_a + 1.59}\right)} & \text{for}\,\beta_a \geq 7 \end{cases} \tag{4.49}$$

4.4   AC LOSS MODEL FOR HTS WIRE

Under DC conditions, HTS tapes have essentially zero resistance, and therefore losses, provided that the current, temperature, and external magnetic field remain below critical values [Mawatari *et al.* 1995]. However, with alternating currents and magnetic fields this is not the case. The total ac loss for Bi2223 tape is dependent on both the ac current through the conductor and any external magnetic fields [Oomen *et al.* 2003, Rabbers *et al.* 2001a], both of which are present in a superconducting transformer. Furthermore, the orientation of the magnetic field to the tape surface has a large impact on the losses with fields perpendicular to the wide surface of the transformer causing larger losses than parallel fields.

The ac loss for the HTS windings is comprised of two components which can be calculated separately and is of the form,

$$P_{HTS} = P_{tc}(I, B, \theta) + P_B(B, \theta) \tag{4.50}$$

where P_{HTS} is the total power loss for the HTS winding, $P_{tc}(I, B, \theta)$ is the transport current loss which is a function of the current through the winding, I, the magnetic flux density, B, and the flux orientation θ, and $P_B(B, \theta)$ is the power loss due to magnetic interaction of the HTS and is a function of the magnetic flux density only. The angle θ is defined as between the normal of the tape's wide surface and the magnetic field and is illustrated in Figure 4.11.
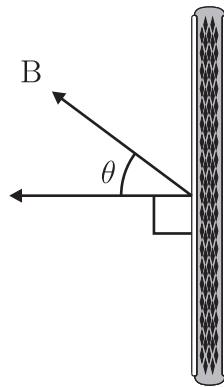
Figure 4.11   Definition of θ for the HTS loss modelling.

To calculate the winding losses, the model assumes a zero resistance for the HTS windings in the Steinmetz circuit and solves the circuit to obtain the currents and magnetic field in the windings. P_{HTS} for each turn in the winding is then calculated using Equation 4.50 and summed together for the total power dissipated in the winding. The calculated power loss for each winding is then converted into an equivalent resistance by the formulae,

$$R_1 = \frac{P_{HTS\_1}}{I_1^2} \qquad (4.51)$$

and

$$R_2 = \frac{P_{HTS\_2}}{I_2^2} \qquad (4.52)$$

where P_{HTS_1} and P_{HTS_2} are the losses calculated for windings 1 and 2 respectively. Following the calculation of R_1 and R_2 the Steinmetz model is resolved and the process repeated until sufficient accuracy is met. This is normally only one or two iterations as the winding resistances tend to be small compared to other components in the model and have little effect on the current.

In order to calculate the transport current loss and the magnetising loss, knowledge of the dc properties of the conductor and the magnetic field are needed.

4.4.1   DC Properties

As described in Chapter 2, the transition from a zero resistance superconducting state and a resistive normal state is not an immediate transition but rather follows a power law,

$$E(J) = E_C \left(\frac{J}{J_C} \right)^n \qquad (4.53)$$

where E_C is the electric field criterion, usually taken as $100\mu V/m$, and J_C is the critical current density. This increase of electric field is due to flux creep. The current through the HTS wire creates a magnetic field which penetrates the superconductor in the form of flux vortices. The de-pinning and movement of the flux vortices due to a Lorentz force ($\mathbf{J} \times \mathbf{B}$) interaction with the transport current results in the electric field. Larger currents result in more flux vortices and therefore more flux creep until a point where superconductivity is lost.

The flux vortices can also be de-pinned via thermal energy. This leads to a temperature dependance property of the critical current of a HTS wire, where the critical current decreases as the temperature increases, until an upper limit of T_c is reached. The modelling in this thesis assumes a constant temperature of $77\,\mathrm{K}$ (the boiling point of LN_2). This assumption can be made provided there is sufficient contact of LN_2 with the HTS wire and that the losses in the wire are sufficiently small.

As the critical current is related to the movement of flux vortices in the HTS wire, it follows that the critical current is also affected by externally applied magnetic fields. This is demonstrated in

Figure 4.12(a). Because of the orientation of the grains in the HTS wire so that the c direction lines up with the wide surface of the tape, there is a highly anisotropic effect on the critical current. Magnetic fields parallel to the tape's wide surface have less impact on the critical current than fields perpendicular to the tape's wide surface. In addition, the exponent n from Equation 4.53 has a similar relationship to I_c in a magnetic field as shown in Figure 4.12(b).

The above relationships can, and have been, verified through experimentation by performing a series of tests on a sample HTS wire in a dc magnetic field and measuring the voltage generated for various dc transport currents using a standard four wire measurement system. Kim et al. proposed a method for fitting calculated curves to measured data [Kim *et al.* 1962]. The Kim method fits curves to data collected from measurement of I_c and n in perpendicular fields, $\theta = 0°$ and parallel fields, $\theta = 90°$ by the formulae,

$$I_{c\perp} = \frac{I_{c0}}{1 + \left(\frac{B}{B_\perp}\right)^{P_\perp}} \tag{4.54}$$

and

$$I_{c\|} = \frac{I_{c0}}{1 + \left(\frac{B}{B_\|}\right)^{P_\|}} \tag{4.55}$$

where $I_{c\perp}$ is the critical current in the perpendicular field, $\theta = 0°$, I_{c0} is the critical current in the self-field, and $B_\perp$ and $P_\perp$ are the fitted parameters. The subscript $\|$ denotes parallel field, $\theta = 90°$. Similar equations are used to fit the n value data. The fitting parameters were found using a least squares approximation on the measured data from a sample piece of HTS wire used in the HTSPCT and are listed in Table 4.9.

Table 4.9 Fitting parameters used in Equations 4.53 and Eqn:4.52 found using least squares approximation of measured data.

Parameter	I_c	n
$B_\perp$	0.0712	0.0686
$B_\|$	0.5335	0.4025
$P_\perp$	1.3210	0.8560
$P_\|$	1.8520	1.4470

The angular dependence of I_c and n is approximately found by taking the minimum value returned from Equations 4.54 and 4.55 where B is equal to $B\sin(\theta)$ for parallel fields and $B\cos(\theta)$ for perpendicular fields such that,
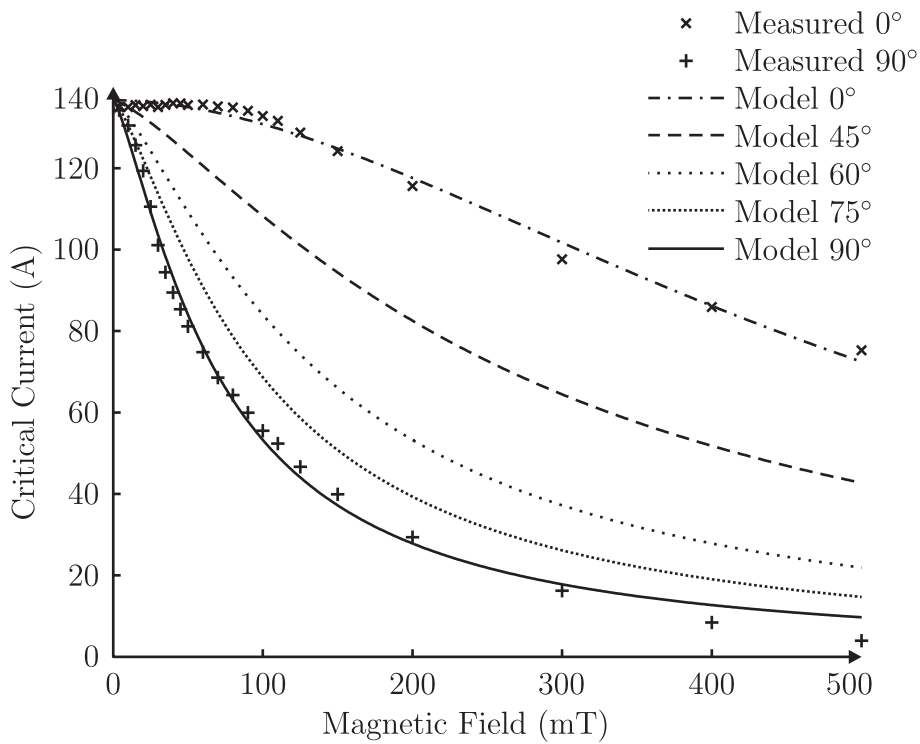
(a) Critical current for various external magnetic fields.
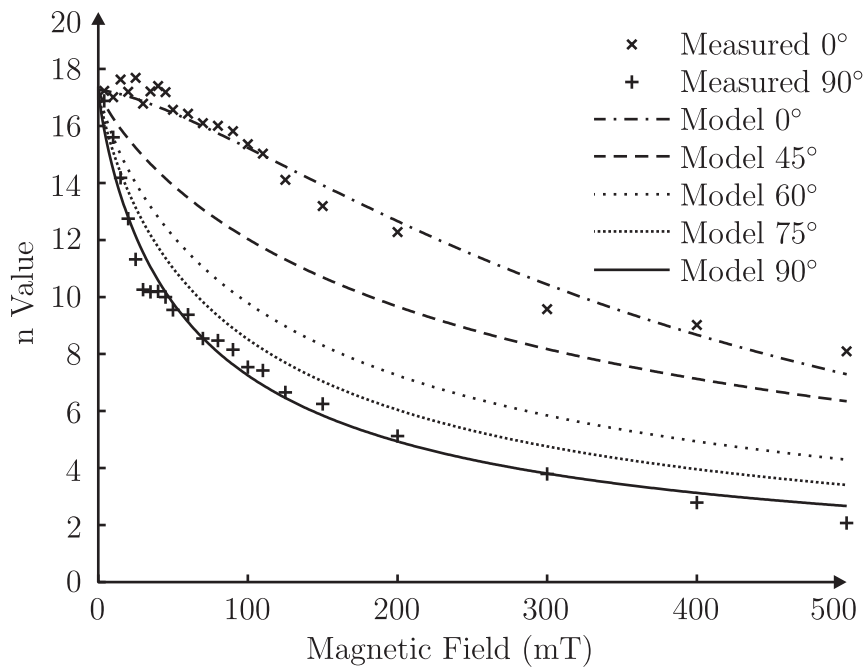
(b) n value for various external magnetic fields.

Figure 4.12   Plots of critical current and n value for various magnetic fields. The plots show measured data, from a sample of HTS wire used in the HTSPCT, for two field orientations and curves plotted from the Kim model.

$$I_c(B, \theta) = \text{minmum} \left[I_{c\parallel} \left(B sin \left(\theta \right) \right), I_{c\perp} \left(B cos \left(\theta \right) \right) \right] \qquad (4.56)$$

and

$$n(B, \theta) = \text{minmum} \left[n_{\parallel} \left(B sin \left(\theta \right) \right), n_{\perp} \left(B cos \left(\theta \right) \right) \right] \qquad (4.57)$$

The model results are plotted in Figure 4.12 for various values of θ. Figure 4.13 shows the angular dependance of I_c and n for a magnetic flux density of $70\,\text{mT}$. Measured data on a HTS sample is compared to the model results from Equations 4.56 and 4.57 and shows good agreement, validating this method for determining the angular dependance.

4.4.2   Modelling the Magnetic Field

In order to use the model in Equation 4.50, it is necessary to know what the magnetic field throughout the transformer is. This was achieved by using the finite element analysis software from Section 4.2.3. Because of the radial symmetry present in the partial core transformer design, a 2D time-harmonic simulation was used to model the magnetic field of the transformer.

Each layer of the PCT windings was modelled as a block of perfect conductor that covers all turns of that winding layer. The insulation between windings was modelled as air. The core was modelled as a single block of isotropic linear material with a relative permeability of 2500. The model did not take into account non-linear effects such as magnetic field screening from the Meissner effect, core saturation, and radial flux not being restricted to the lamination plane. These non-linearities were assumed to have minimal effect on the global field distribution.

The time harmonic data from FEA software presents the magnetic field as a complex phasor field. For a two dimensional simulation the phasor field is split into orthogonal components $B_\perp$ and $B_\parallel$ so that,

$$\begin{aligned} B_\perp &= \mathfrak{Re} \left[A_\perp e^{j(\omega t + \phi_\perp)} \right] \\ &= A_\perp cos \left(\omega t + \phi_\perp \right) \end{aligned} \qquad (4.58)$$

where $\mathfrak{Re}$ represents the real part of the complex equation, $A_\perp$ is the amplitude of the radial component of the field and $\phi_\perp$ is the phase shift. The axial component of the field, $B_\parallel$, is of the same form as Equation 4.58 with the subscript $\parallel$ instead of $\perp$.
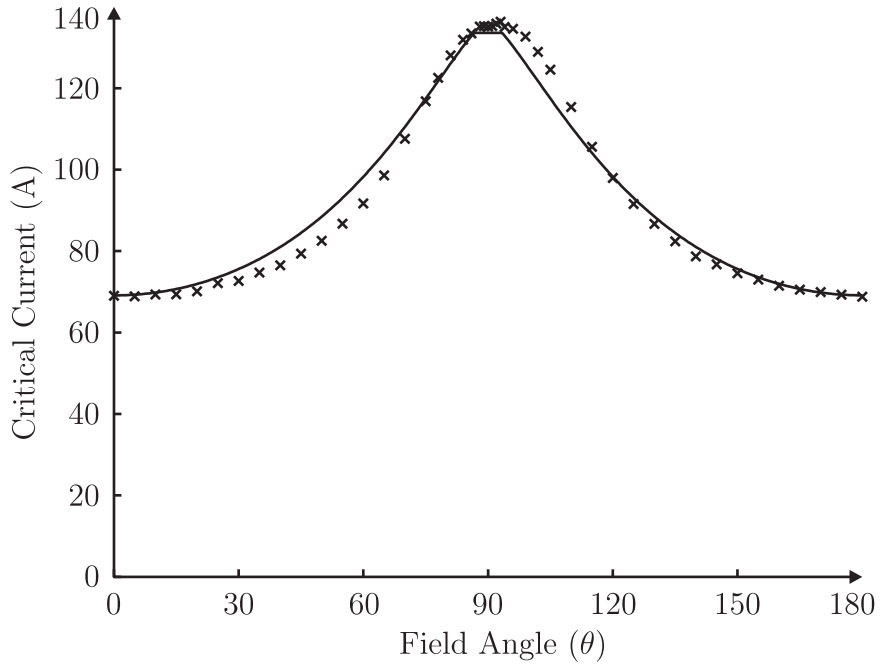
(a) Critical current for various applied field angles.
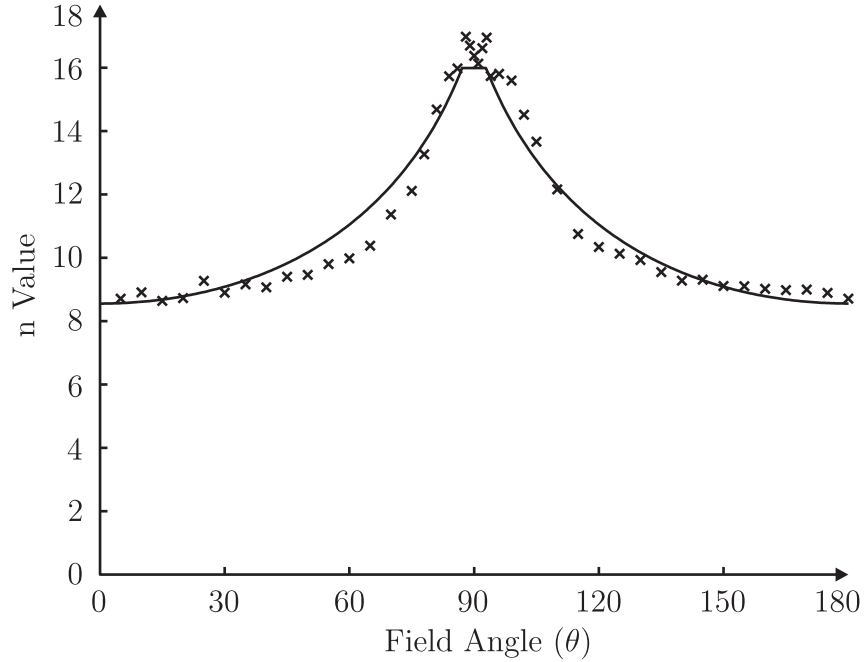
(b) n value for various applied field angles.

Figure 4.13   Plots of critical current and n value for various field orientations at a magnetic flux density of 70 mT. The plots show measured data for two field orientations and curves plotted from the Kim model.
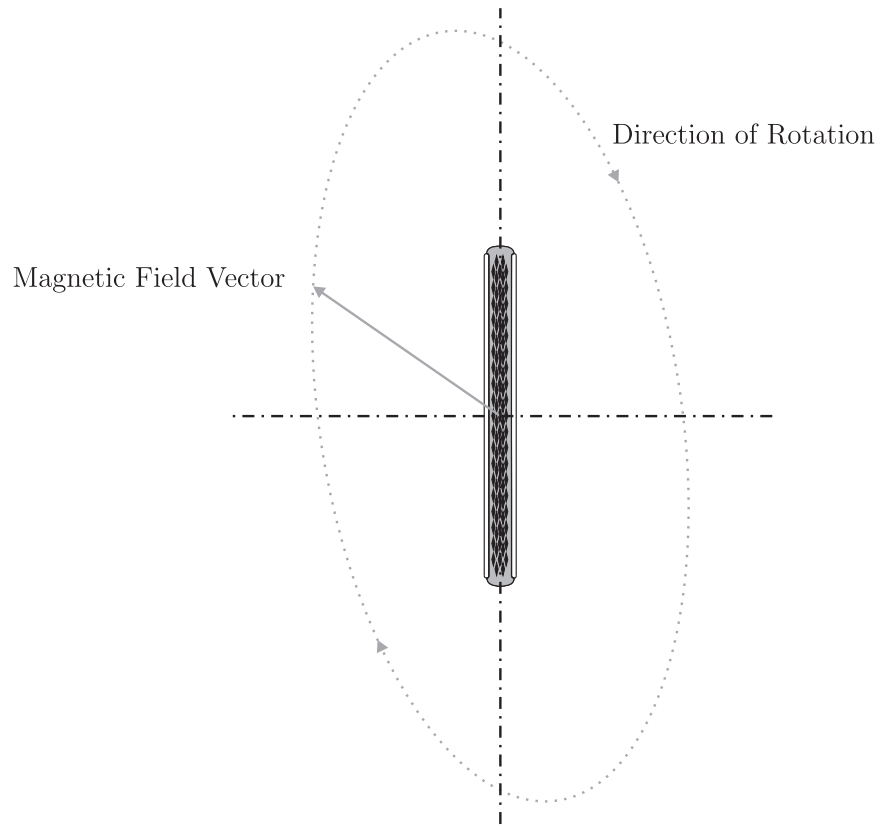
Figure 4.14   Diagram of the elliptical nature of the magnetic field for a partial core transformer.

Results from the simulation showed that the magnetic field at a point in the winding space did not have a static orientation throughout the simulation cycle. Instead, the field tended to rotate in an elliptical pattern with the magnitude and orientation changing over time, Figure 4.14.

4.4.3   Transport Current Losses

The power loss component due to the ac transport current through the HTS conductor, P_{tc}, is comprised of a combination of different losses. These are resistive losses, P_{rl}, a dynamic resistance loss, P_{dr}, and the self field loss, P_{sf}. These losses are assumed to be independent of each other and so can be summed together such that,

$$P_{tc} = P_{rl} + P_{dr} + P_{sf} \tag{4.59}$$

Resistive Losses

The superconducting filaments in the BSCCO HTS tape are encased in a silver or silver alloy matrix. For currents well below I_c, the electric field in the HTS tape is essentially zero. Therefore,

no current flows in the Ag matrix. As the current increases, an electric field develops and some of the current starts to flow in the Ag matrix. The resistance of the Ag matrix, R_{Ag}, per unit length is given by [Oomen *et al.* 2003],

$$R_{Ag} = \frac{\rho_{Ag\_77}}{A_w(1 - \lambda)} \tag{4.60}$$

where ρ_{Ag_77} is the resistivity of silver at $77\,\mathrm{K}$ which can be found using Equation 4.31 and Table 4.1, and λ is the fraction of superconducting filaments in the cross sectional area of the tape. Because the Ag matrix and the HTS are in parallel, the electric field per unit length due to flux creep must be equal to electric field per unit length along the matrix due to ohmic resistance. This leads to,

$$E_{HTS} = 10^{-4} \left(\frac{I_{sc}}{I_c(B,\theta)} \right)^{n(B,\theta)} = R_{Ag}(I - I_{sc}) \tag{4.61}$$

where E_{HTS} is the electric field developed per unit length along the HTS wire in volts per meter, I_{sc} is the portion of the current I flowing in the superconducting filaments. I_{sc} is found by numerically solving Equation 4.61.

The resistive losses per unit length are then,

$$P_{RL}(I,B,\theta) = f \int_{t=0}^{t_{per}} E_{HTS}(t)I(t)dt \tag{4.62}$$

where t_{per} is the period of the ac current in seconds.

Dynamic Resistance

When a HTS wire is exposed to an ac magnetic field while transport current is flowing, there has been observed an increase in the electric field [Rabbers *et al.* 1998, Friedman *et al.* 2006]. This loss has been called dynamic resistance because it is proportional to the square of the transport current and also it depends on the amplitude of the magnetic field. Friedman et al. suggest that the reduction in I_c, i.e. increase in electric field, is caused by the penetration of the ac magnetic field and associated screening currents forcing the transport current into a smaller area in the center of the conductor thereby increasing the transport current density. Rabbers et al. proposed a formula for the calculation of dynamic resistance losses in [Rabbers *et al.* 2001a],

$$P_{dr} = C_4(\theta) B_a I_a^2$$
$$= (C_5 cos\theta + C_6 sin\theta) B_a I_a^2 \qquad (4.63)$$
$$= C_5 B_{a\parallel} I_a^2 + C_6 B_{a\perp} I_a^2$$

where $C_4(\theta)$ is a constant which depends on the field angle and is found from measurements, B_a is the amplitude of the magnetic flux density, and I_a is the amplitude of the transport current. Ooman et al. noticed that the measured dependence of $C_4(\theta)$ given in Figure 6 of [Rabbers *et al.* 2001a] was of the form shown in the second part of Equation 4.63 [Oomen *et al.* 2003]. This relationship suggests that the parallel and perpendicular field components independently cause dynamic resistance losses and can be calculated separately.

Ooman goes on to estimate the dynamic resistance losses based on the critical state model for a slab with ac transport current in a parallel field [Oomen 2000]. The equations Ooman derived for the dynamic losses per unit length of conductor are

$$P_{dr\parallel} = \lambda_\parallel \frac{f d_{HTS}}{I_{c,avg}} B_{a\parallel} I_{a,sc}^2 \qquad (4.64)$$

and

$$P_{dr\perp} = \lambda_\perp \frac{f w_{HTS}}{I_{c,avg}} B_{a\perp} I_{a,sc}^2 \qquad (4.65)$$

where $\lambda_\parallel$ and $\lambda_\perp$ are the percentage of superconductor in the parallel and perpendicular directions respectively, d_{HTS} and w_{HTS} are the thickness and width of the HTS conductor in meters, $I_{c,avg}$ is the critical current averaged over the magnetic field cycle, and $I_{a,sc}$ is the amplitude of the current in the superconducting filaments.

Finally, the total dynamic resistance losses are,

$$P_{dr} = P_{dr\parallel} + P_{dr\perp} \qquad (4.66)$$

Self field losses

When an alternating transport current is flowing in a HTS wire, it experiences a loss known as self field loss. It is due to the penetration of the self field into the surface of the conductor. It is independent of any external magnetic fields. Rabbers et al. wrote that the self field loss
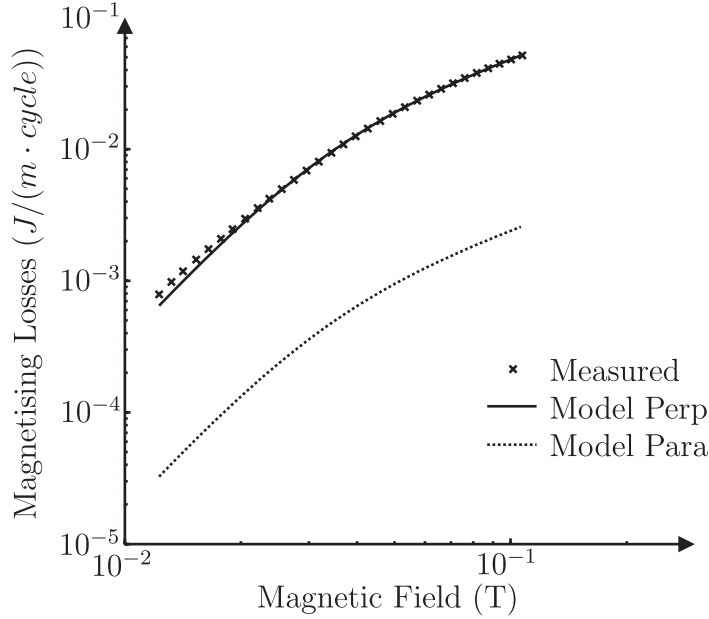
Figure 4.15   Measured and modelled magnetisation loss for a sample HTS tape. Measurements were taken at 48 Hz.

is described well with the critical state model description for an elliptical or thin rectangular conductor cross-section and that it was equal to $Q_{sf} = C_3 I^q$ where C_3 and q are determined from measurement [Rabbers *et al.* 2001a]. Ooman suggested that the constants could be estimated from theory [Oomen *et al.* 2003]. A modified version of the Ooman formula is used to calculate the self field losses per unit length,

$$P_{sf} = \frac{\mu_0 f}{4\pi} \frac{I_{sc}^q}{I_{c,avg}^{1.5}} C_{sf} \tag{4.67}$$

where q and C_{sf} are constants to be determined from measured data.

4.4.4   Magnetising losses

The magnetising losses are due to an interaction of an external ac magnetic field with the superconductor. It is present even in the absence of a transport current. While there is some evidence that the magnetising losses are affected by transport currents [Oomen 2000], this occurs only close to I_c where the transport current losses dominate and so this effect is ignored. The magnetising losses result from a combination of hysteresis in the superconducting filaments, coupling currents between the filaments and eddy currents in the normal-metal matrix.

The magnetisation losses can be split into parallel and perpendicular components and summed together such that,

$$P_B = P_{B,\parallel} + P_{B,\perp} \tag{4.68}$$

The magnetisation loss for a sample tape was measured using the pick-up coil method for a perpendicular field. A model was presented in [Oomen *et al.* 2003] for fitting to the measured data using a least squared approximation, Figure 4.15. The model was then used to estimate the magnetising losses for parallel fields which have been shown to be up to 20 times less than those of perpendicular fields. The formula for the parallel magnetising losses is,

$$P_{B,\parallel} = \frac{p_{c0,\parallel} B_{a,\parallel}^{m_\parallel}}{B_{c0,\parallel}^{m_\parallel} + B_{c0,\perp} B_{a,\parallel}^{m_\parallel - 1}} f \tag{4.69}$$

where p_{c0} and B_{c0} are the fitting parameters, and B_a is the amplitude of the magnetic flux density. The formula for the perpendicular field is the same with the subscript $\perp$

4.5 DISCUSSION

The two component method for core loss modelling, hysteresis and eddy currents, has been used for full core transformers for a number of years although proven to underestimate the losses. While the hysteresis power loss equation, (Equation 4.4), is applicable to PCTs, the eddy current loss equation, (Equation 4.5), significantly underestimated the losses. The reason for the underestimation was due to the magnetic flux spreading radially from the end sections of the core. Traditionally this was compensated through an eddy current scaling factor equal to 0.1.

The introduction of a new method for the eddy current power loss calculation which takes into account the spreading flux greatly improved the accuracy of the eddy current power loss calculation as demonstrated in [Huo 2009]. The new eddy current calculation splits the flux into three orthogonal directions, calculates resistances in each of the directions for a single lamination, then finds the power loss for a stack of equal sized laminations. The model was expanded for circular shaped cores by using a generic arrangement of 13 blocks of stacked laminations.

The winding loss model is based on the resistance of the windings and the current through them. The resistance calculation is based on the resistivity and the dimensions of the winding material, with the resistivity being temperature dependent. These calculations are well established and found in many textbooks. However, these calculations do not apply to HTS windings as the loss mechanisms are significantly more complicated.

The reactive components of the model are found via two differing methods, the circuit theory

method and the finite element method. Each method has its advantages and disadvantages. The CTM is computationally much faster than the FEM, also the FEM requires a commercial finite element software package which has a licensing cost associated with it. However experimental results have shown the FEM method is more accurate than the CTM. A series of simulations were carried out investigating the characteristics of the two modeling methods. These simulations showed discrepancies between the two modeling methods for low aspect ratios and resulted in modifications to Equation 4.35 and 4.39. Comparisons to measured results show FEM was more accurate.

The AC loss model for 1G HTS wire was developed using a combination of finite element analysis, theory, and empirical modelling. The model is comprised of two main components, a magnetising component, and a transport current component.

The magnetising component of the losses is related to the magnetic field in the winding space of the transformer. The magnetic field was modelled using the finite element software in a two dimensional time harmonic simulation of the winding space. The modelled field was used to calculate the magnetisation loss of the winding based on a fitted formula. The loss equation was fitted to measurement data for the magnetisation loss of a sample of HTS tape used in the HTSPCT. This method should produce a good approximation of the magnetisation losses for the HTSPCT.

The transport current component of the losses is related to the magnetic field and the ac current flowing in the HTS wire. The resistive losses are a semi-empirical calculation derived from the dc characteristics of the HTS wire. The dc characteristics were calculated using fitted models to measured data of an HTS sample tape and are considered to be reasonably accurate. However, the resistive losses component only makes up a small fraction of the transport current losses except at high current densities. The majority of the transport current losses consist of the dynamic resistance and self field losses. These loss components were derived from theory only as ac loss measurements were unable to be made on sample tapes. These two loss components are the least accurately known in the HTS ac loss model, but make up a significant percentage of the losses.

4.6   CONCLUSIONS

In this chapter, a model for calculating the performance of a HTSPCT was presented. The model uses a combination of empirical and theoretical calculations to determine the circuit components of the Steinmetz 'exact' transformer equivalent circuit. The modelling was based on the reverse design method with new additions to the core loss modelling and a new ac loss model for 1G HTS wire. Static, and time harmonic, two dimensional finite element analysis of the transformer were used to predict the global magnetic field distribution in the winding space.

The model was developed to aid in the design of a new HTSPCT which is presented in the next Chapter. By using the RDM, the performance of the new HTSPCT, subject to the physical dimensions and properties of the materials used, can be determined prior to construction. The design of the HTSPCT will be able to be optimised to meet desired performance criteria.

Chapter 5

DESIGN AND CONSTRUCTION OF A HIGH TEMPERATURE SUPERCONDUCTING PARTIAL CORE TRANSFORMER

5.1 OVERVIEW

This chapter presents the design and construction of a new prototype HTSPCT. The chapter begins by introducing the Transformer Design Program, an application written in VBA for the purpose of designing HTSPCT. The design process used in the program is explained as well as the basic function of the various subroutines used. The functions and content of each worksheet in the program is briefly outlined in this section with a more detailed description given in the Appendix.

This is followed by some detail on various aspects specific to the design of the new prototype HTSPCT which was to replace the failed one from Section 3.4. Design considerations such as winding dimensions and layout are discussed. The section concludes with details of the physical specifications used in the design program and the equivalent circuit parameters given as an output from the program.

Details of the construction of the new HTSPCT are then given. This includes discussion of the core design, development of the inter-layer insulation used, the winding construction, and the transformer assembly. This section concludes with details of some of the auxiliary systems developed for use with the transformer including detail of the cooling system used and the quench detection system.

5.2 TRANSFORMER DESIGN PROGRAM

A program has been written over the period of several years during this thesis in Visual Basic for Applications (VBA) for the purpose of designing HTSPCT based on the RDM. The program consists of a number of worksheets, which input or output various parameters of the design, and user control buttons. A transformer is designed by the user filling out the Input Data Sheet

Master Copy with the materials and dimensions to be used in the design. The Master Copy is then saved as a new file which is loaded into the Transformer Design Program (TDP). The TDP processes the design and displays the performance calculations for the user to review. The user can then modify the design or accept and save the data file.

Figure 5.1 depicts a flow chart of the user controlled design process using the TDP. The round elements in the flow chart represent clicking of the user control buttons, the rectangular elements represent the inputting of data by the user or outputting of data by the program for review by the user. The process involves developing a basic design using the CTM first and then refining the design with the FEM later. This is because the solve time for the FEM is much larger than the CTM and can take about 30 sec on a modern desktop PC. Also the FEM requires the use of a commercial finite element program which needs to be installed on the same machine as the TDP.

5.2.1   Input Data Master Sheet

The design process begins with the Input Data Master Sheet, a stand alone worksheet separate from the TDP. The user is able to specify many aspects of the design including materials and dimensions and save it as an Input Data Sheet. This saved file can then be loaded into the TDP to be processed. When the transformer design has been finalised, the user can then save the Input Data Sheet. The Input Data Sheet is divided into many sections where the user can specify the supply and load conditions, core properties and dimensions, and the winding specifications.

The winding specification of the design is based upon layer type windings and has been split into ten sections. Each section contains one or more winding layers of equal axial length and the same inter-layer insulation thickness. At least two winding sections need to specified in the Input Data Master Sheet in order to design a transformer. Each winding section can be designated as being primary connected (connected to the supply voltage) or secondary connected (connected to the load impedance).

5.2.2   Master Worksheet

The Master Worksheet contains all the user control buttons for the program, and a copy of Figure 5.1. The operation of each button is as follows;

Read Data Sheet This button opens a dialog box where the user can select which Input Data Sheet they would like to load into the TDP. Once chosen, the routine copies the data into the TDP on the Input Data Worksheet
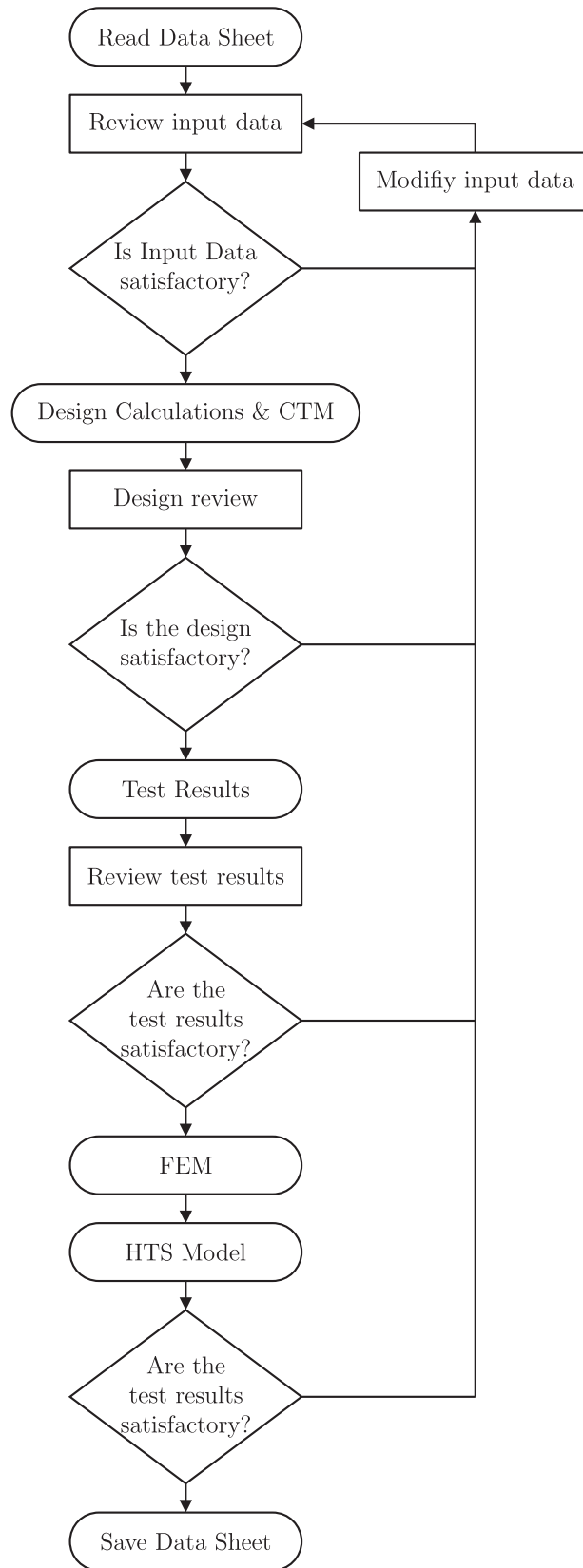
Figure 5.1   Flow chart of the Transformer Design Program process.

Save Data Sheet Saves the current design loaded into the TDP as a separate Input Data
     Sheet.

Design Calculations & CTM This routine calculates the physical parameters of the trans-
     former based on input materials and dimensions. Aspects such as the weights, number
     of laminations, wire length, and number of turns are calculated here. The routine then
     calculates the components of the Steinmetz equivalent circuit based on the CTM elements
     outlined in Section 4.2. The user can then check the results in the Design Review Sheet,
     and make changes to the Input Data Sheet if necessary.

FEM This button starts the finite element method from Section 4.2.3 for calculating the re-
     active components of the Steinmetz model. The FEM routine requires that the Design
     Calculations routine be run first to establish the geometry of the transformer. The geo-
     metric data is fed into the commercial finite element program where scripts build the model
     and return flux linkage data which is then processed by the TDP to calculate the reactive
     components of the Steinmetz model. Depending on the number of winding sections used
     in the design this routine can take some time to complete, (up to 1 minute).

Test Results This routine solves both the CTM and FEM versions of the Steinmetz model for
     various load and supply conditions. It takes, as inputs, the equivalent circuit components
     calculated from both the CTM and FEM models and solves the equivalent circuit for
     open circuit, short circuit, and loaded cases. The results from the calculations, including
     voltages, currents, and power losses are written to the Test Results Worksheet. The Test
     Results routine can also be run without having run the FEM, although results from the
     FEM section will not be calculated. This enables the design to be quickly adjusted to a
     desirable performance level using only the CTM, and when the design is satisfactory, the
     FEM can be run for greater accuracy in the reactive component section.

View Flux Plots This routine runs the commercial finite element program in visible mode to
     allow the user to view the distribution of the magnetic field of the designed transformer.
     The user can choose to use either the CTM results or the FEM results and view the field
     associated with either the open circuit, short circuit or loaded test results. The routine
     then builds the transformer model in the finite element software and loads the appropriate
     current phase and magnitude data based on the user selection. The user is then free to
     run static or time harmonic simulations and view the results as needed. When finished,
     the user can return to the TDP which will close the finite element software.

HTS Model This routine calculates the ac losses for the HTS wire based on the modelling
     presented in Section 4.4. The model requires the use of the finite element software, which
     is executed by the routine, to obtain the magnetic field information. The calculated losses
     are written to the Design Review Worksheet and the Test Results routine is then run again
     to update the Test Results Worksheet with the ac HTS losses.

5.2.3 Input Data Worksheet

The Input Data Worksheet is where the design data of the transformer is stored in the TDP. When the Read Data Sheet user control is run, the cells in the Input Data Sheet are filled with the design data. This worksheet contains all the data found in the Input Data Master Sheet such as the supply conditions, and core and winding dimensions. In addition to this data, when the *Read Data Sheet* user control is run, the material properties for each of the materials selected in the transformer design, i.e. the core, winding, and former materials, are copied into the worksheet. In this way the designer does not need to know the resistivity and density of copper for example, to use the program. The user can just select copper as a winding material from the drop down list in the Input Data Master Sheet and the program automatically uses the appropriate data. A list of the properties and their values used for each of the materials in the TDP is given in Table 5.1.

Once the data is in the Input Data Worksheet, the user can modify any of the cells to refine their design. When the design is satisfactory, the user can save the data from the Input Data Worksheet by using the *Save Data Sheet* routine.

5.2.4 Design Review Worksheet

The Design Review Worksheet contains all the calculated data for the design of the HTSPCT based on the information entered into the Input Data Worksheet. The worksheet is divided into several sections which are; Physical Parameters, Skin Effect Parameters, Circuit Theory Model Parameters, Finite Element Model Parameters, Equivalent Circuit Parameters, and High Temperature Superconductor Losses. Data is written to the cells when the *Design Calculations*, the *FEM*, and the *HTS Model* routines are run. The user does not directly write to any of these cells.

The Physical Parameters section calculates the physical properties of the transformer. For the core, this includes the number of laminations, the resistivity, cross sectional area, the volume, and the weight of the core. For the winding sections, this includes the number of turns, the radial position of the layers, the length of the wire, and many other physical aspects. A full description of each parameter is found in the Appendix.

The Skin Effects Section provides information on the frequency related properties of the core and windings. For the core section, the penetration depth at the fundamental frequency is given as well as the highest frequency for complete flux penetration. The winding section also calculates the penetration depth at the fundamental frequency but includes the maximum frequency for flux penetration in both the radial and axial directions. The RMS and maximum flux densities in the core are also given.

Table 5.1   The properties and values for each of the materials used in the Transformer Design Program.

Material	Property	Value	Unit
Grain Orientated Silicon Steel	Relative Permeability	5000	
	Resistivity @20°C	472×10^{-9}	Ωm
	Thermal Resistivity Coefficient	0.006	$\Omega m K^{-1}$
	Material Density	8954	$kg m^{-1}$
Copper	Volume Specific Heat	3.45	$J cm^{-3} K^{-1}$
	Resistivity @20°C	16.8×10^{-9}	Ωm
	Thermal Resistivity Coefficient	0.0039	$\Omega m K^{-1}$
	Material Density	8954	$kg m^{-3}$
Aluminium	Volume Specific Heat	2.422	$J cm^{-3} K^{-1}$
	Resistivity @20°C	26.7×10^{-9}	Ωm
	Thermal Resistivity Coefficient	0.00432	$\Omega m K^{-1}$
	Material Density	2700	$kg m^{-3}$
Bi-2223	Volume Specific Heat[§]	2.44	$J cm^{-3} K^{-1}$
	Resistivity @273K[§]	14.67×10^{-9}[ℵ]	Ωm
	Thermal Resistivity Coefficient[§]	60×10^{-12}[ℵ]	$\Omega m K^{-1}$
	Material Density[§]	10500	$kg m^{-3}$
	n-Value[†]	17.26	
	Critical Current[†]	136.7	A
	Fraction of HTS in Tape	0.85	
	$B_{\perp}$ for I_c[‡]	0.0712	
	$B_{\parallel}$ for I_c[‡]	0.5335	
	$P_{\perp}$ for I_c[‡]	1.321	
	$P_{\parallel}$ for I_c[‡]	1.852	
	$B_{\perp}$ for n[‡]	0.0686	
	$B_{\parallel}$ for n[‡]	0.4025	
	$P_{\perp}$ for n[‡]	0.856	
	$P_{\parallel}$ for n[‡]	1.447	

[§] For the silver matrix
[ℵ] [Smith and Fickett 1995]
[†] @ $77K$ in self field
[‡] Fitting parameters

The Circuit Theory Model Parameters section is where the parameters specific to the CTM from Section 4.2 are calculated. This includes the core flux reluctance, the reluctance of the air path, the magnetising and leakage correction factors from Equations 4.34 and 4.38, and the flux spreading parameters from the eddy current core loss model from Section 4.2.1.

The Finite Element Model Parameters section contains the permeance matrix from Equation 4.40 which is obtained from the FEA software. This is then converted to an inductance matrix using Equation 4.41. A coupling matrix is also present, which is an array of the coupling coefficient k between each winding section. This section also includes the winding reluctance and the self

and mutual inductances.

The Equivalent Circuit Parameters section is where the components of the Steinmetz model are calculated. It is divided into two parts, CTM and FEM. The CTM part includes winding resistances, core loss resistance, leakage reactance, and magnetising reactance calculated from Section 4.2. The FEM part includes the same winding and core loss resistances as the CTM, and the FEM reactive components from Section 4.2.3 as well as a comparison between the series mutual method and the energy method.

Finally, the ac losses for each winding section that uses HTS wire are given in the High Temperature Superconductor Losses section. The calculations are based on the modelling of Section 4.4. Each type of loss is presented for transport, magnetising and resistive losses as well as the total losses in the winding section.

5.2.5 Test Results Worksheet

The Test Results Worksheet contains the results from calculations solving the Steinmetz model for both the CTM and FEM equivalent circuit parameters for various load conditions. The worksheet is split into two main sections, Test Results - Circuit Theory Method and Test Results - Finite Element Method where the equivalent circuit components from the respective methods are used. Each main section is further split into the following sections; Open Circuit Performance, Short Circuit Performance, and Loaded Circuit Performance.

The Open Circuit Performance section gives an indication of the magnetising properties of the transformer. The primary (supply connected winding) and secondary (open circuit winding) voltages are calculated as well as the magnetising current, and the real and reactive power draw. An equivalent parallel impedance is calculated which would draw the same current from the supply. Finally, the power dissipated in each winding and the core is also calculated.

The Short Circuit Performance section gives an indication of the series impedance of the transformer. The primary voltage for this test is specified in the Input Data Worksheet and the primary and secondary currents are calculated, as well as the real and reactive power draw. An equivalent series impedance is calculated which would draw the same current from the supply. Finally, the power dissipated in each winding and the core is also calculated.

The Loaded Circuit Performance section is divided into several subsections and calculates results based on connecting the Steinmetz circuit to the load impedance specified in the Input Data Worksheet. The Voltages section includes the calculated input and output voltages, volts per turn, volts per insulation layer, and the voltage regulation. The Currents and Densities section includes the calculated primary and secondary current magnitude, phase, and density. The Power Generation section calculates the power dissipated in the windings, the core and the load,

and calculates the efficiency of power transfer. Finally, the power losses and apparent power are calculated per unit volume, weight, surface area, and cost.

5.3   A NEW HTSPCT – DESIGN DETAILS

With the development of the TDP, a new HTSPCT was designed as a replacement to the failed HTSPCT from Section 3.4. There were aspects to the original design that worked well enough and in an effort to keep the costs as low as possible, some of the materials from the original HTSPCT were reused. These included the fibreglass vacuum Dewar and the laminated steel core. Other aspects of the original design were not beneficial to the operation of the transformer and were changed in the new design. These included the winding insulation scheme and the three winding layout.

5.3.1   Design Considerations

Because of the decision to reuse the vacuum Dewar from Section 3.4, a number of design constraints on the transformer had to be made. The dimensions of the former on the main assembly meant that the design would be a solenoid based winding. It also placed a limit on the axial length and the radial width that would fit. The size of the partial core that could be used was also limited. Figure 5.2 illustrates the maximum dimensions for the winding window and the core.

In addition to the above size limits, allowances needed to be made for better cooling of the windings. The Chew transformer of Section 3.5 demonstrated that direct contact of the windings with the LN_2 enabled the HTS conductor to be operated at high current levels without failure of the windings. However, structurally, the Chew transformer insulation design was inadequate and a redesign was necessary. More information about the design of the winding insulation is given in Section 5.4.2.

The original HTSPCT was a three winding transformer, with a 230 V inside winding, a 115 V middle winding, and a 115 V outer winding as shown in Chapter 3 and repeated here in Figure 5.3. The problem with this design is that the leakage flux increases as the radial distance from the core increases.

This effect is shown in the open circuit voltages that were measured on the original HTSPCT. In an ideal transformer, voltages measured on the inside, middle, and outer windings would be 230 V, 115 V, and 115 V respectively. Instead, the voltages that are actually measured decrease as the radial distance from the core increases. From Table 3.5 the measured open circuit voltages from inside out were 230 V, 113 V, and 111 V.
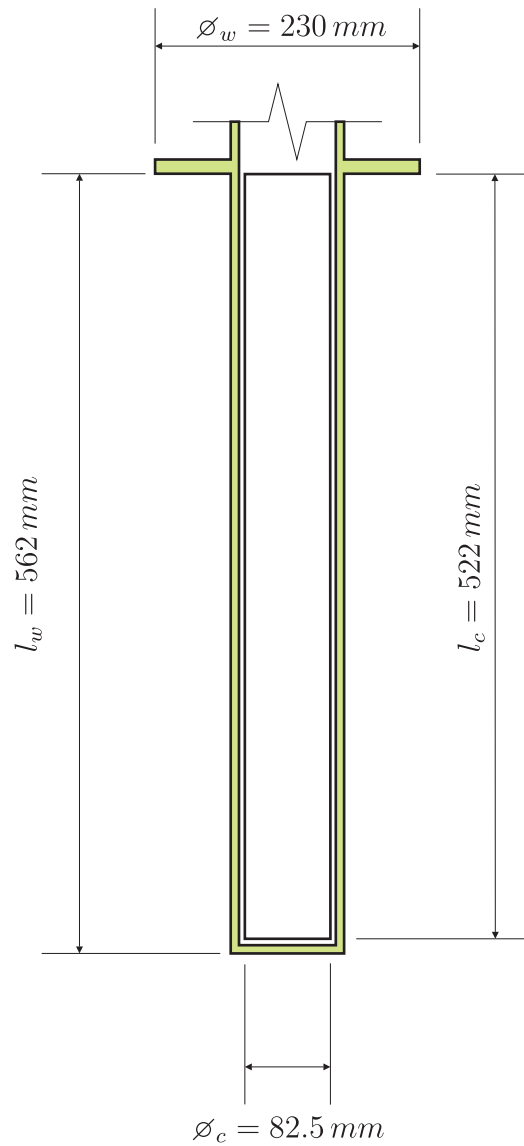
Figure 5.2 Diagram illustrating the maximum allowable dimensions for the new HTSPCT.
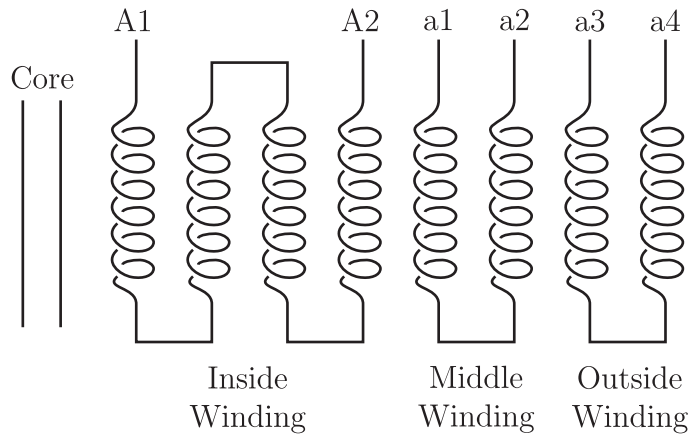
Figure 5.3 A schematic of the winding layout for the original HTSPCT.
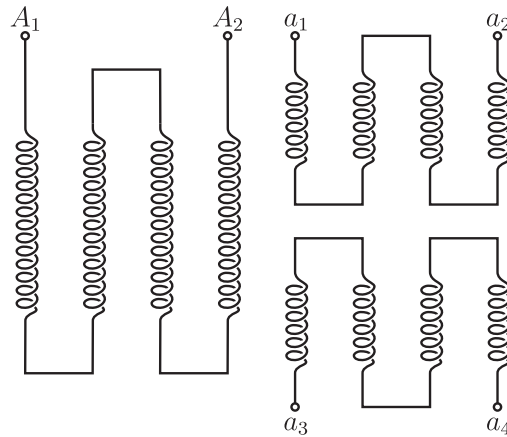
(a) First option.
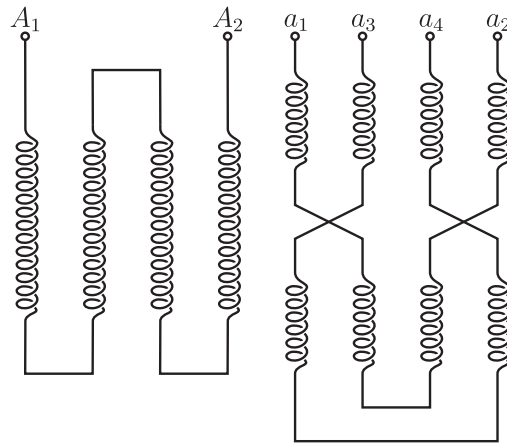
(b) Second option.

Figure 5.4   Possible winding layouts for the 3 winding transformer.

Two possible arrangements for a three winding transformer design are given in Figure 5.4. These layouts have an even amount of leakage flux on the two low voltage windings and therefore will have the same induced voltage. The first option is simpler to manufacture but has the disadvantage of having the a_3 – a_4 winding terminations out the bottom of the winding. This will require longer copper lead-outs to the bushings located at the top of the Dewar, which will result in larger winding losses for that winding. The second option has all the winding terminations at the same end so that the lead-outs will all be the same length. However, the second option has a complicated mid-layer transition that would be difficult to manufacture.

The original purpose for the three winding design was to investigate the coupling effects of the different winding configurations. At the time of construction, it was not apparent how well the transformer windings would be coupled, and a number of different winding configurations were to be investigated. Since that time, the modelling of PCTs has improved and more confidence is given to the modelling performance results. For this reason and to keep the design as simple as possible, it was decided to revert back to a two winding design for the new HTSPCT.

5.3.2   TDP Design

The TDP was used to design a new prototype HTSPCT. For reasons mentioned in 5.3.1, the design is based on the original 15 kVA HTSPCT from Chapter 3 with the most significant difference being that the transformer is now a two winding design. The design specifications for the physical dimensions of the transformer used in the TDP are given in Table 5.2.

Table 5.2   Physical Specifications of the HTSPCT.

Core	
Parameter	**Value**
Length	470 mm
Inside Radius	8.2 mm
Outside Radius	40 mm
Lamination Thickness	0.23 mm
Number of Laminations	348
Material	Grain Orientated Silicon Steel
Inside Winding	
Parameter	**Value**
Voltage Rating	230 V
Current Rating	65 A
Winding Length	338 mm
Wire Radial Width	0.305 mm
Wire Axial Width	4.1 mm
Number of Layers	4
Total Turns	320
Material	Bi-2223
Former Diameter	115 mm
Outside Winding	
Parameter	**Value**
Voltage Rating	230 V
Current Rating	65 A
Winding Length	338 mm
Wire Radial Width	0.305 mm
Wire Axial Width	4.1 mm
Number of Layers	4
Total Turns	320
Material	Bi-2223

Entering the parameters of Table 5.2 into the TDP and running through the process outlined in Figure 5.1, the program was able to determine the equivalent circuit parameters given in Table 5.3. The parameters listed in Table 5.3 are for full load conditions and some of the parameters, especially R_1 and R_2, change for different currents and magnetic field distribution. This design gave an efficiency of 98.1% and a voltage regulation of 3.27% at full load.

Table 5.3   The equivalent circuit parameters under full load conditions for the HTSPCT.

Parameter	Value (Ω)
R_1	0.01698
R_2	0.01701
R_{ec}	576
R_h	1233
R_c	392
X_1	0.2397
X_2	0.0745
X_m	12.81

5.4   CONSTRUCTION DETAILS

The construction of the new HTSPCT used a lot of aspects from the original HTSPCT of Chapter 3 such as the core, the vacuum Dewar, the main assembly, and the copper lead-out design. This was because these aspects performed well in the original design, and in the interests of saving time and money the decision was made to reuse them.

5.4.1   Core

The core used in the new design was the same core from the original HTSPCT, although the core had been cut into 8 sections as part of Huo's work on the heat distribution of the core during operation [Huo 2009]. The core was designed as a parallel stacked circular core; 348 laminations of 0.23 mm, high permeability, grain orientated silicon steel as shown in Figure 5.5. The core was bound with Vidatape S, a woven high shrink polyester tape, and hot dipped twice in an electrical baking varnish. A hole in the center of the core allows for a 1240mm G-10 fibreglass 5/8 UNC threaded rod to allow for correct positioning of the core inside the warm bore tank wall relative to the HTS windings.
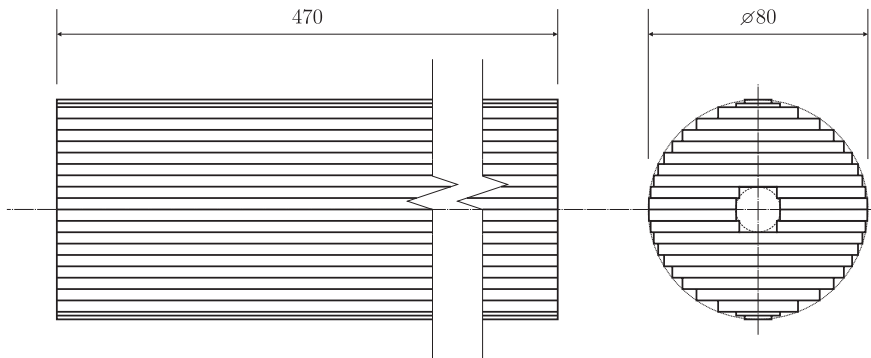
Figure 5.5   Drawing of the core design.
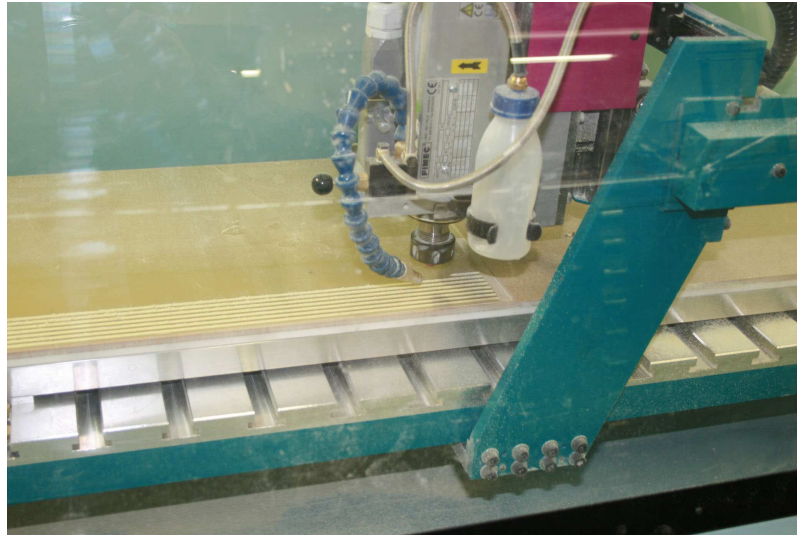
Figure 5.6 Photograph of the CAM machine cutting the inter-layer insulation.

5.4.2 Inter-layer Insulation

One of the most significant contributing factors to the original HTSPCT's failure was the inter-layer insulation design. The windings were bound in several layers of NOMEX® insulation paper. This prevented heat generated from the HTS conductor from being dissipated sufficiently by the liquid nitrogen (LN_2).

The new HTSPCT uses an alternative winding insulation design consisting of sheets of $2\,mm$ thick, g10 fibreglass. The fibre sheets had $3\,mm$ wide vertical channels machined into the material every $3\,mm$ using a computer-aided manufacturing (CAM) machine as seen in Figure 5.6.
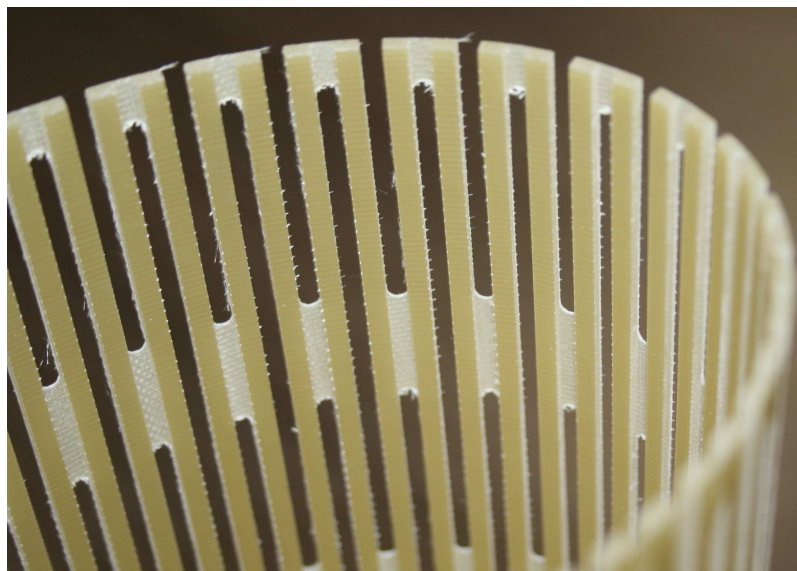
Figure 5.7 Photograph of the new inter-layer insulation design.

The depth of the cuts were $1.5\,\text{mm}$ leaving $0.5\,\text{mm}$ of fiber sheet. In addition to this, $85\,\text{mm}$ long slots were cut into the vertical channels with slots on adjacent channels offset, as shown in Figure 5.7. The result of this machining left the fibreglass very flexible in the horizontal direction while still retaining strength, freely allowing the flow of LN_2 around the HTS wire, and for any nitrogen gas bubbles that form to escape.
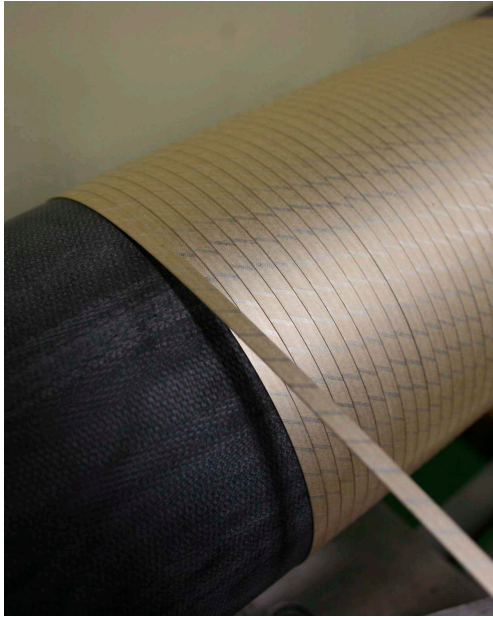
(a) The first layer being wound directly onto the former.

(b) The second layer being wound, showing the inter-layer insulation.

(c) The force gauge used to measure the wire tension.
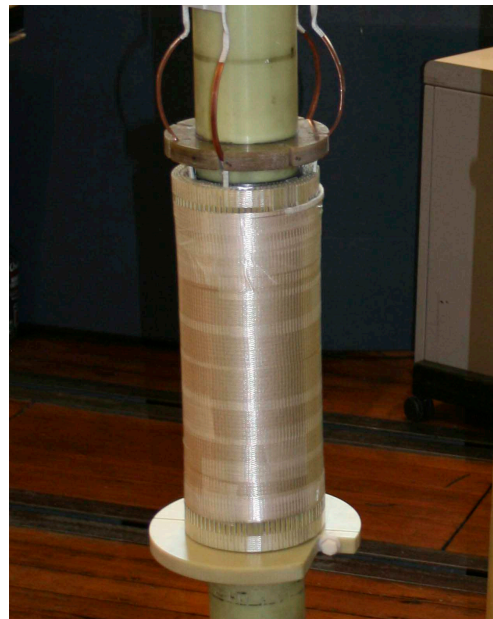
(d) Photograph of the finished winding.

Figure 5.8   Photographs of the winding process for the HTSPCT.

5.4.3 Winding Construction

The windings were wound with 1G BSCCO HTS wire from Trithor GmbH (now Zenergy Power GmbH). The manufacture's wire specification of the critical current at 77K is 136.7A in a self field. However, as discussed in Chapter 4, the alternating magnetic fields present in the transformer result in a reduction in the critical current [Zhu *et al.* 2004, Leghissa *et al.* 2007]. For this reason, the rated current for the windings was set to 65A rms. The HTS wire was insulated from turn to turn short circuits by the manufacture with a spiral wrap of an electrical-grade stretched polymer foil [Kellers *et al.* 2005].

The windings were layer wound onto a fibreglass former that was 115 mm in diameter and 402 mm long. The former was made to slide over the warm bore tank of the core vessel and was held in place with a clamping ring also made of fibreglass. The purpose of this arrangement was to allow for the removal of the windings so that other winding arrangements could be tested, including a proposed fault current limiter (FCL) and a 2G YBCO winding.

The first layer was wound directly onto the fiberglass former as shown in Figure 5.8(a), followed by a layer of the inter-layer insulation material which is held in place by the next layer of HTS wire as shown in Figure 5.8(b). The wire tension was controlled using a spring system and measured to ensure the wire tension remained below 15 N as shown in Figure 5.8(c), as too much strain can cause damage to the superconductor. The final layer was wrapped in fibre reinforced tape to hold the windings in place as shown in Figure 5.8(d).

Copper lead-outs were used to connect the HTS windings to the transformer bushings as shown in Figure 5.9. The lead-outs consisted of two 1.5 mm $\times$ 5 mm copper conductors and were positioned radially around the transformer. The lead-outs were connected to the bushing busbars using a compression joint as shown in Figure 5.9(a),which was located above the LN_2 level. The bends in the lower section of the lead-outs photographed in Figure 5.9(b) were present to allow for thermal expansion and contraction of the copper without pulling or pushing on the HTS windings.

The copper lead-outs were soldered to the HTS wire using Indium based solder, (97 % In 3 % Ag), and Ersin Red Jelly flux paste. The join was made by sandwiching approximately 10 cm of HTS wire between two specially formed copper lead-outs as shown in Figure 5.9(c) and soldered with a temperature limited soldering iron. Too high a temperature during this process would result in the HTS wire delaminating; the soldering temperature was limited to 160 °C using a variac to control the voltage to the soldering iron.
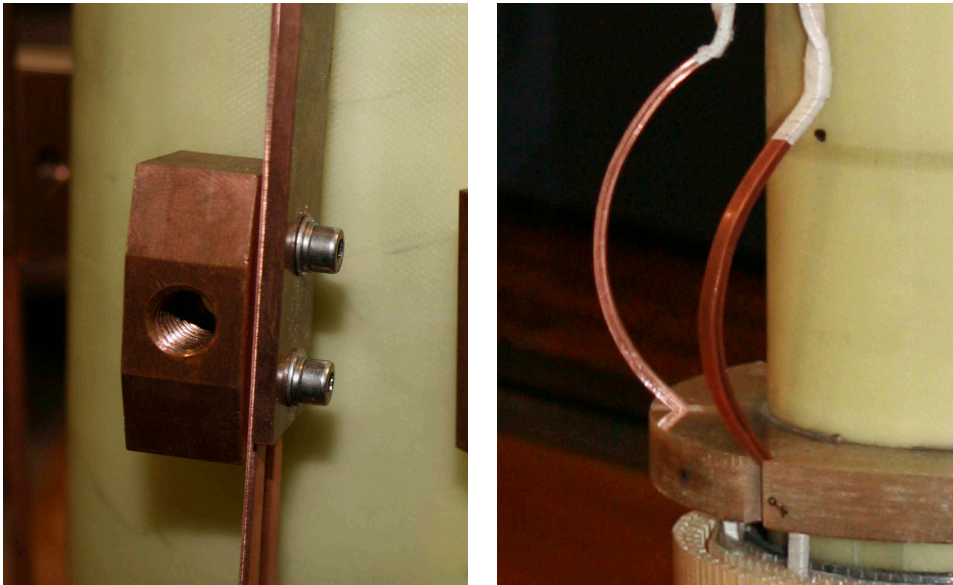
(a) The compression connection used to connect the copper lead-outs to the bushing busbars.

(b) bends in the copper lead-outs to allow for thermal expansion and contraction.
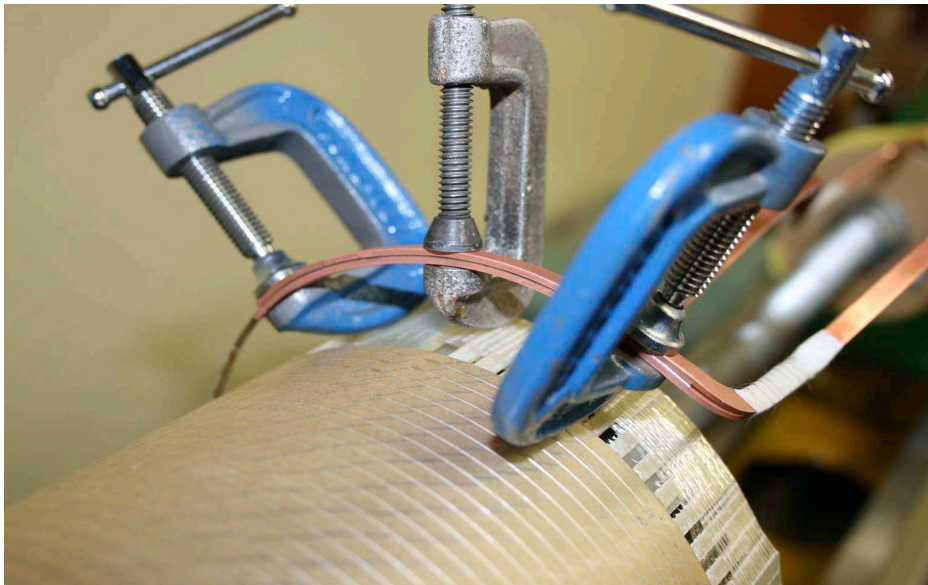
(c) One of the copper lead-outs about to be soldered to the HTS wire.

Figure 5.9   Details of the copper lead-outs connecting the transformer bushings to the HTS windings.

5.4.4   Transformer Assembly

The transformer main assembly is the same as that used in the original HTSPCT and is comprised of three parts; the liquid nitrogen vacuum Dewar, the core vessel, and the head unit as shown in Figure 5.10. The majority of the transformer main assembly was constructed using g10 fibreglass.
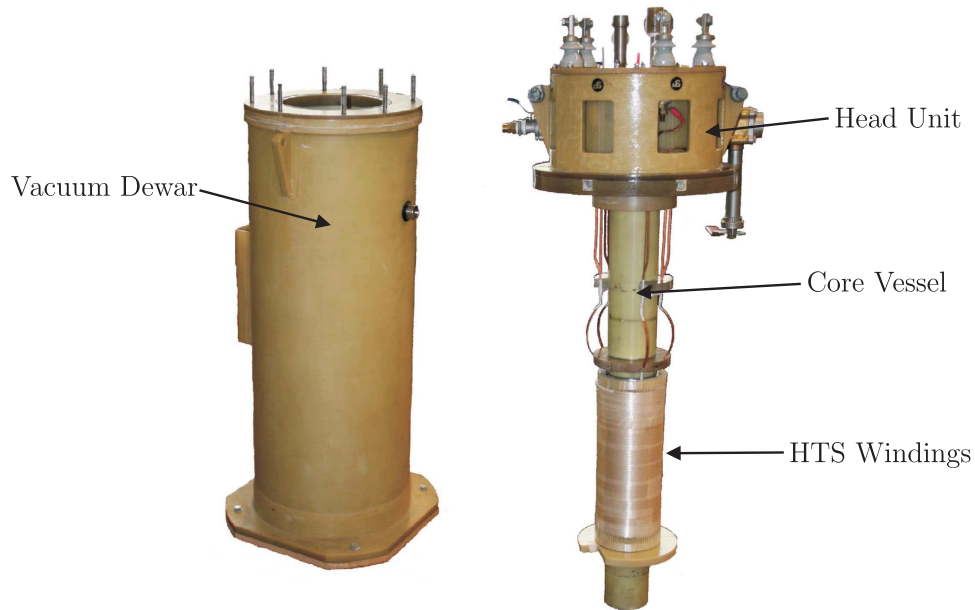
Figure 5.10 An exploded view of the main transformer assembly.

The vacuum Dewar consists of an inner vessel for the containment of LN_2 and an outer vessel exposed to room temperature with a vacuum between them. The vacuum is present to limit thermal convection losses to the LN_2 from the outside. To limit radiation losses, several layers of aluminized non-stretch polyester were wrapped around the inner vessel. Care was taken not to create shorted turns by insulating the aluminized non-stretch polyester with vacuum rated tissue paper. The bottom of the inner vessel was dome shaped so that the joint between the dome and the tube of the inner vessel, when exposed to LN_2, expanded and contracted evenly. A pressure relief port is present on the outside of the Dewar in case a failure of the inner vessel results in nitrogen gas venting into the vacuum chamber.

The core vessel is similar to the vacuum Dewar in that a vacuum is formed between the core and the LN_2. A similar arrangement of aluminized polyester and tissue was used in the core vessel. The HTS winding former is fitted over the core vessel and held in place with a clamping ring. A float is attached to the core vessel to indicate the minimum and maximum LN_2 levels. A filling tube for the LN_2 is also fitted to the outside of the core vessel. A pressure relief port is present on the top of the core vessel in case a failure vents nitrogen gas into the vacuum chamber.

The head unit provides mountings for the transformer bushings, nitrogen venting valves, a rupture disc for emergency venting, purging lines and a pressure gauge for the LN_2 chamber pressure. The transformer bushings, located on the top of the head unit, are connected to the bushing busbars via a short piece of braided copper wire. Two nitrogen venting valves are present, adjacent to the rupture disc. One valve is a full LN_2 rated manual vent to be used during initial filling and the other valve is a non return valve for normal operation venting. In

case the non return valve is unable to vent sufficient quantities of nitrogen gas, for example during fault conditions, an emergency venting rupture disc is fitted to prevent the pressure in the LN_2 chamber from reaching dangerous levels. The rupture disc consists of a thin aluminium sheet between two flanges of G-10 fibreglass. The diameter of the rupture disc is $80\,mm$. The purging lines consist of a vacuum line and a dry nitrogen gas line. Prior to filling the chamber with LN_2, a vacuum is held for 24 hours, then the vacuum is broken with dry nitrogen gas.

5.4.5   Cooling System

In order for the HTS wire to become superconducting, it needed to be cooled below the critical temperature (approximately $120\,K$). This was achieved using LN_2, which has a boiling point of $77\,K$. The use of the fibreglass vacuum Dewar for containing the LN_2 limited the effect of the outside temperature from evaporating the LN_2. However, boil off of the LN_2 still occurred even when the transformer was not operating and increased with increased transformer load. To prevent the transformer running dry, a system was developed to monitor the LN_2 level inside the Dewar and to top it up from a LN_2 reservoir when necessary.

The system consists of a float mechanism inside the Dewar to gauge the LN_2 level shown in Figure 5.11(a). The float mechanism extends through the top of the transformer main assembly
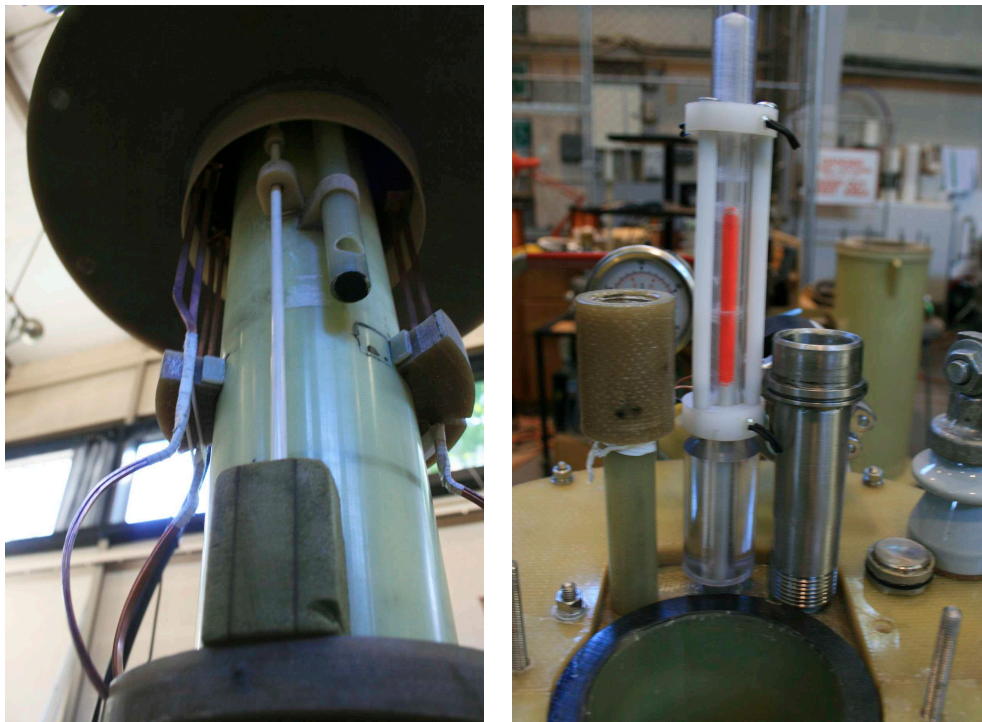
(a) The float inside the LN_2 Chamber.   (b) The cooling system optical sensor arrangement.

Figure 5.11   Photographs of the LN_2 level sensing components for the cooling system.
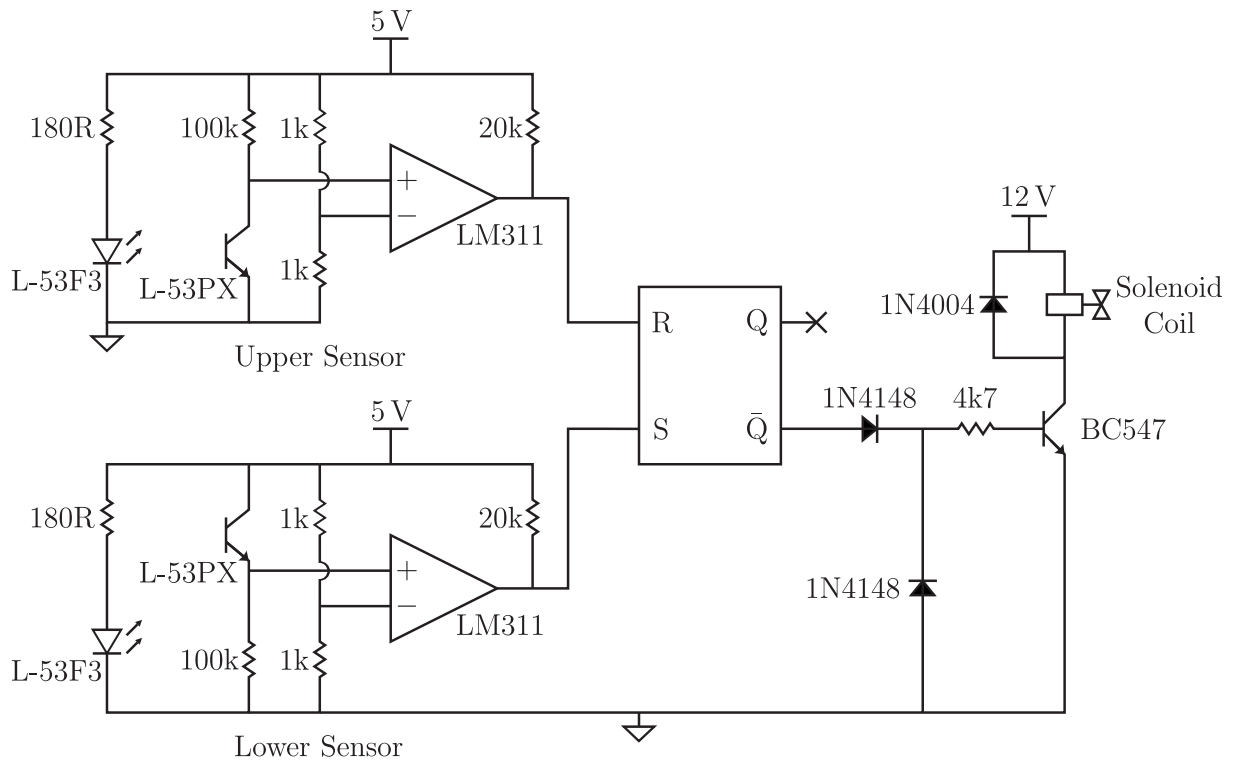
Figure 5.12   Schematic of the cooling system electronics.

inside a sight glass. Two optical sensors attached to the sight glass are used to measure the level of the float and can be seen in Figure 5.11(b). The optical sensors connect to a cryogenic rated solenoid valve via a controller circuit. The controller opens the solenoid valve, filling the LN_2 chamber until the uppermost optical sensor is triggered by the float, the controller then closes the solenoid valve. When the boil off of LN_2 lowers the float below the lower optical sensor, the controller opens the solenoid valve again to resume filling. The failure mode of the solenoid valve is the open state so in the case of a controller failure the HTS windings will not run dry.

Figure 5.12 shows a schematic of the electronic circuit used in the cooling system. The operation of the circuit is as follows; the LN_2 level is measured with two sensor circuits, an upper sensor and a lower sensor, consisting of an infra red (IR) light emitting diode (LED), an IR photo-transistor and a comparator circuit. Current flows through the IR LED, L-53F3, producing light which switches on the phototransistor, L-53PX. When the float blocks the light from the LED, the phototransistor switches off. The analogue signal from the phototransistor is fed into a comparator circuit where it is converted to a logic level. The logic of the upper sensor is 1 when the LED is blocked and the lower sensor is 1 when the LED is exposed.

The logic output from the comparators is connected to a set-reset flip-flop. The output of the flip-flop controls a LN_2 rated solenoid coil through a BC547 transistor. The three diodes are used to protect the transistor and flip-flop from switching transients associated with the relay coil.
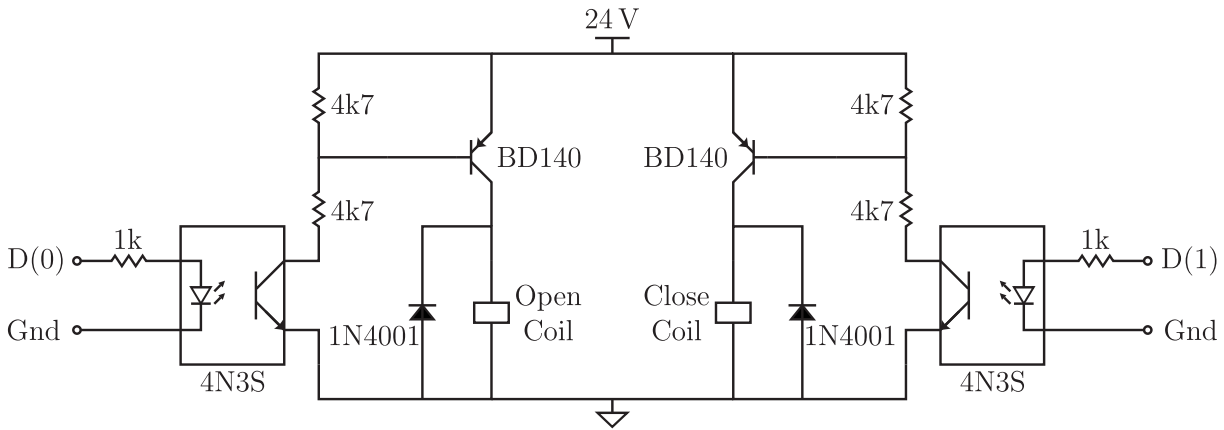
Figure 5.13   Schematic of the quench detection system electronics.

5.4.6   Quench Detection System

A quench detection system was used to protect the transformer from being damaged if the HTS wire was to quench during operation. Quenching can occur in HTS wire operating at high current density. Localised heating can increase the temperature in a section of the wire by a few degrees and may result in that section of wire changing to the normal resistive state. In the normal state, ohmic losses cause more localised heating and result in an unstable escalating process. This quenching process can be seen as an increase in resistance of the HTS wire [Meerovich *et al.* 1995, Weijers *et al.* 1995, Xiao *et al.* 1999, Coway *et al.* 2000].

The increase in the winding resistance during quenching will result in an increase in the series impedance of the transformer. As noted in [Lapthorn *et al.* 2011], the quenching process results in a rapid collapse of the secondary voltage of the transformer. This can be measured as an increase in the percentage voltage regulation.

The quench detection system monitors the primary and secondary voltage of the HTSPCT using two remote operated digital multi-meters(DMM). The DMMs are connected to a desktop computer where the voltages measured are read into a computer program. The computer program continuously reads the primary and secondary voltages of the HTSPCT and calculates the voltage regulation. When the voltage regulation reaches a threshold level, the quench detection system opens a circuit breaker via the computer's parallel port and de-energises the transformer. The typical response time from quench detection to breaker operation was measured at 200 ms.

Figure 5.13 is a schematic of the electronics required to operate the circuit breaker from the parallel port of the computer. The circuit breaker used has two 24 V dc relay coils with a common ground, one to open the breaker and one to close the breaker. The computer program energises one coil at a time for one second in order to change the state of the breaker. The computer parallel port was chosen to control the two coils because it was easy to program. However, the

computer parallel port has very limited electrical capability and needs to be protected from the 24 V supply, otherwise it may be damaged. This protection is achieved with an optical-isolator.

The circuit works as follows; the output of the parallel port is used to drive the LED in an optical-isolator, 4N3S. When the LED is on, this switches on the phototransistor, which pulls down the base of the PNP transistor, BD140, switching on the relay coil. The diode, 1N4001, is used to absorb the magnetic energy from the relay coil when the PNP transistor opens.

5.5   CONCLUSIONS

In this Chapter, the design and construction of a new HTSPCT has been presented. The transformer was designed using a computer program written in VBA. The TDP is based upon the reverse design method described in Chapter 4. By combining with a commercial finite element analysis software package and using the FEM data and theoretical modelling, the TDP was able to calculate a set of equivalent circuit parameters for the transformer design that gave satisfactory performance.

The design of the new HTSPCT used certain aspects of the first prototype HTSPCT from Chapter 3 that were considered to have performed well, such as the vacuum Dewar, the copper lead-out design and approximate dimensions for the winding space. Aspects of the design that were improved upon from the original were inter-layer insulation design, and the winding layout was simplified from three windings to two.

Details of all aspects of the construction of the HTSPCT were given. This included the laminated core, the inter-layer insulation, the HTS winding and the transformer assembly. Some auxiliary systems used in the transformer operation were also discussed; specifically these were the cooling system and the quench detection system. The cooling system used optical sensors on a LN_2 float system, combined with an electronic circuit to control a cryogenic rated solenoid valve. The valve was able to supply the HTSPCT with LN_2 from a storage Dewar. The quench detection system used voltage measurements combined with computer software and electronics to monitor the state of the HTS windings and control a circuit breaker supplying the transformer.

Chapter 6

EXPERIMENTAL RESULTS

6.1 OVERVIEW

A series of electrical tests were performed on the transformer to ascertain its operating characteristics. These tests include insulation resistance, DC resistance of the windings, open circuit, short circuit, and resistive load testing. Where applicable, the tests were undertaken according to the International Electrotechnical Commission, (IEC), standard on power transformers, IEC 60076. During the testing, the windings were submerged in LN_2 supplied from a storage Dewar.

The chapter begins with an overview of the experimental setup used throughout the testing with a discussion of the equipment used during the testing, including the meters used and other auxiliary equipment. In addition, the procedure used for preparing and filling the vacuum Dewar with LN_2 is presented. Also, the methods used in taking the electrical measurements are examined.

The results of the testing are then presented. This includes key performance indictors such as the open and short circuit characteristics, as well as results of other testing including short circuit faults and dielectric testing. The test results are then compared with the modelling from Chapter 4 and discussed.

6.2 EXPERIMENTAL SETUP

The testing of the HTSPCT was conducted in the UoC's high voltage laboratory. This facility has a controllable single phase supply capable of delivering up to $600\,A$ at $400\,V$ that was used to supply the HTSPCT. The room is also sufficiently large with plenty of ventilation to help minimise the risk of asphyxiation due to large amounts of LN_2 evaporation in the event of an accident. In addition, the laboratory is fitted with several emergency trip buttons located in
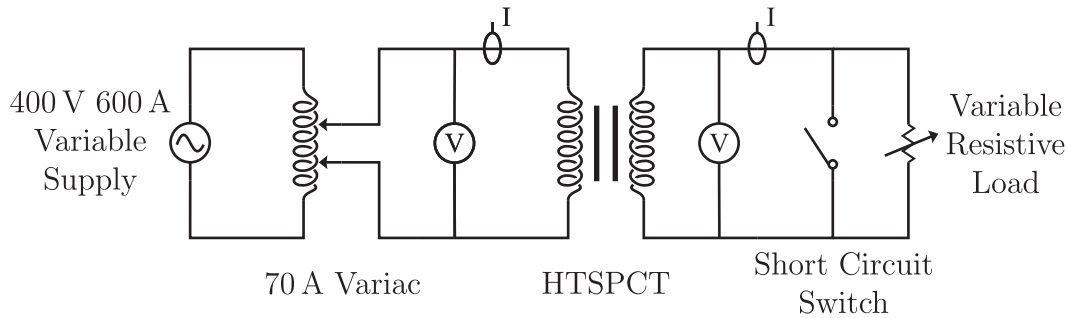
Figure 6.1   Circuit diagram of the test circuit for HTSPCT.

easily accessible positions. When activated, these buttons switch off the supply to the whole laboratory and sound an alarm.

The various tests discussed in this chapter were conducted over several test days. Prior to each test day, the transformer was filled with LN_2 using the procedure described in Section 6.2.3. After completion of the tests, the HTS windings were allowed to return to room temperature. Plastic tubing was used to vent the nitrogen gas to the outside.

6.2.1   Safety

A number of hazards do exist when performing electrical testing on a superconducting transformer. Nitrogen in a liquid state can cause serious burns, and sufficient boil off can reduce the oxygen content in a room resulting in asphyxiation. Other hazards relate to the electrical side with exposed terminals present during the test. Because of these hazards, a procedure used before testing was to fill out a hazard identification form (or Tailgate as it is commonly referred to). A typical tailgate filled out for the testing of the HTSPCT is given in Appendix B.

6.2.2   Equipment

The test circuit for the HTSPCT, shown in Figure 6.1, was used for the open circuit, short circuit, resistive load, overload and fault ride through tests. It consists of a variable voltage, 50 Hz, ac supply connected in series with a 70 A variac. The resistive load, adjustable from about 3.5 Ω to open circuit, is connected in parallel with a short circuiting switch. The voltmeters and ammeters shown in the circuit diagram indicate the positions of where the voltage and current measurements were taken.

A movable desk, seen in Figure 6.2(a), was setup to contain the main equipment for taking measurements and for control of the supply of the HTSPCT. This desk contained two calibrated Fluke 41B power quality meters for measuring the voltage, current and power of the primary and secondary windings. These meters were connected to two separate desktop computers via

(a) Main measurement and control desk.

(b) The variac used to control the supply to the HTSPCT.
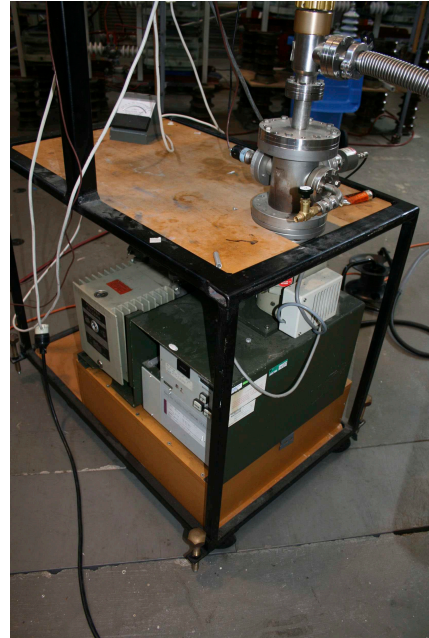
(c) 15 kW resistive load bank and switch for short circuiting the transformer output.

(d) The turbomolecular vacuum pump.

Figure 6.2   Photographs of the some of the equipment used for testing the HTSPCT.

a serial connection for storage of the logged measurement data. The desk also contained two HP digital multimeters used for measuring the voltage for the quench detection system. These meters were connected to the desktop computer running a MATLAB script via a IEEE-488 interface (GPIB).

Other measurement equipment used in the testing included two additional Fluke 43 power quality meters to compare with measurements taken from the calibrated Fluke 41B meters. A MPK254 Digital Micro-Ohmmeter from Megabras was used for dc resistance measurements. A S1-5005 insulation tester from Megger was used for insulation resistance measurements.

The supply voltage was controlled via two variacs in series. The first variac was the high voltage lab's 600 A supply. The second variac was a 70 A continuous rated portable unit pictured in Figure 6.2(b). The advantage of this system was to enable fine control of the supply voltage while monitoring the measurements being taken. This was especially useful during the short circuit test where fine control of the supply voltage is necessary.

Figure 6.2(c) shows the 15 kW resistive load bank used during some of the electrical tests. The amount of load is variable in discrete steps by switching in additional resistive elements in parallel. Also shown in the middle right of Figure 6.2(c) is the throw switch used to short circuit the secondary windings of the HTSPCT.

To pull a vacuum in the vacuum Dewar and the core vessel, a turbomolecular vacuum pump was used, Figure 6.2(d). This pump was able to pull a vacuum in the Dewar of 2×10^{-5} Torr. The pump was used to first make a vacuum in the core vessel, which was then sealed, then the pump was moved to the vacuum Dewar where it remained in operation during the entire test. Without the use of the vacuum pump, the outer surface of the vacuum Dewar would become frosted, indicating a loss in the insulating properties of the Dewar. With the vacuum in place, this frosting did not occur, thus demonstrating the importance of the vacuum in preventing heat from the room getting into the LN_2 chamber.

6.2.3   Filling Procedure

Before the commencement of the electrical testing, the vacuum Dewar was filled with LN_2. Because of the combustion noted in [Lapthorn *et al.* 2011], it was suspected that there could be oxygen present in the LN_2. To prevent the ingress of oxygen into the LN_2 chamber, the following filling procedure was performed.

- Close the two nitrogen venting valves.

- Apply a vacuum to the LN_2 chamber through the purging line.

- Hold the vacuum for 24 hours.

- Fill the LN_2 chamber through the dry nitrogen gas line.

- When positive pressure is obtained open the normal nitrogen venting valve.

- Fill with LN_2 through the LN_2 filling tube.

6.2.4 Taking Measurements

An important aspect in taking measurements is making sure the measuring devices are used correctly. This includes ensuring that the impedance of the probes used match the equipment they are used with. The voltage measurements were taken with 1:1 probes matched to the Fluke meters. The current clamps used were also matched to the Fluke meters. However, even with properly matched current clamps, it is important to locate the current clamps as far as possible from the HTSPCT to prevent stray flux from the transformer core affecting the measured current. At least 3 m clearance is recommended.

6.3 KEY PERFORMANCE INDICATORS

The key performance indicators of a power transformer are the efficiency of power transfer, the voltage ratio and regulation, and the distribution of losses. Also of importance in a partial core transformer are the magnetising characteristics. These factors can be found by conducting a series of electrical tests on the transformer. The tests for traditional power transformers are outlined in the IEC 60076 series of standards. While not strictly applicable to superconducting transformers, the IEC standard can act as a guide in conducting the relevant tests.

The tests include an open circuit test, a short circuit test and a load test. These tests were performed on the new HTSPCT built in Chapter 5 to ascertain the performance of this device as a power transformer. Measurements of the inside and outside winding's voltage and current were taken using calibrated Fluke 41B Power Meters. The measurements were taken every 10 seconds throughout the open circuit, short circuit, and resistive load tests.

6.3.1 Open Circuit Test Results

An open circuit test on a traditional transformer is often referred to as a no load loss test (IEC 60076-1 Section 10.5). This is because very little current is needed to energise the core as compared to the full load current, and the losses measured are almost entirely core losses. The core losses are proportional to the induced voltage in the core and the frequency of the applied

voltage which are both constant in steady state conditions. Hence, the core losses are constant and independent of the load of the transformer.

Because of the magnetic circuit in a PCT, a much higher excitation current is expected. Sometimes several 10s of a percent of the full load current can be measured. Therefore, losses measured during an open circuit test on a PCT will contain a significant amount of winding loss and this needs to be taken into account.

Another term often used when referring to an open circuit test is the ratio test(IEC 60076-1 Section 10.3). This is because with very little current flowing, the effects of leakage flux are minimised and the ratio of primary to secondary voltage is equal to the turns ratio of the transformer. Again, because of the high magnetising current in PCTs, the open circuit voltage ratio will not equal the turns ratio of the transformer and leakage flux effects will be evident.

For the open circuit test performed on the HTSPCT, the incoming supply was connected to the inside winding, with the outside winding left in open circuit. The voltage was slowly increased from 0 V to just over the rated voltage while measurements were taken. A summary of the measured results from the test are given in Table 6.1 and they are compared to calculated values using the modelling of Chapter 4.

Table 6.1   Open Circuit Test Result Summary.

Parameter	Measured	Calculated	% Difference
Inside winding voltage (V)	230.4	230	0.17
Outside winding voltage (V)	225.9	225.7	0.09
Voltage ratio	0.980	0.981	-0.10
Excitation current (A)	19.4	17.6	9.28
Excitation current's phase (deg)	-87.9	-87.6	0.34
Volt-amperes (VA)	4464	4054	9.18
Real power (W)	160	167	-4.37
Power factor	0.04	0.04	0

There is good agreement between the measured and calculated results with the largest difference being in the excitation current. The error in the current causes a similar error in the volt-amperes calculation as this is proportional to the current. The other calculated results are very close to the measured values.

The results show that there is a much larger excitation current, approximately 30 % of full load current, than would be expected if this was a full core transformer. This current causes a voltage drop across the series impedance of the primary winding, largely due to leakage reactance, resulting in a reduced secondary winding voltage. This is the reason why the open circuit voltage ratio is not equal to the turns ratio of the transformer.
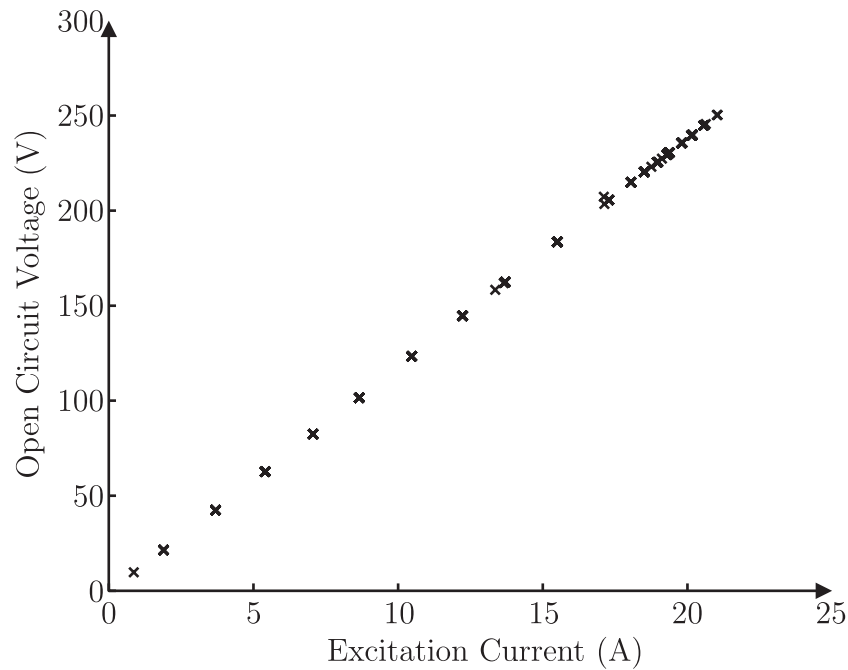
Figure 6.3   Open circuit voltage against excitation current.

Figure 6.3 is a plot of the open circuit voltage against the excitation current. This is a typical result for a PCT, and shows a linear increase in excitation current with applied voltage. The result also indicates that magnetic saturation of the core is not occurring in the HTSPCT. The onset of core saturation would be seen as a "flattening out" of the open circuit voltage/current relationship in Figure 6.3.

6.3.2   Short Circuit Test Results

A short circuit test is used to measure the impedance and the load losses of a transformer. When the secondary of a transformer is short circuited, its series impedance, $(a^2(R_2 + X_2))$, is in parallel with the shunt impedance, $(X_m \parallel R_c)$. Because the shunt impedance is much larger than the series impedance, the losses measured are almost entirely related to the load current.

IEC 60076-1 Section 10.4 describes the test procedure, stating that "*the losses shall be measured at rated frequency with approximately sinusoidal voltage applied to the terminals of one winding, with the terminals of the other winding short circuited. The supplied current should be equal to the relevant rated current but shall not be less than 50% thereof.*" For the short circuit test the outside winding was shorted using $95\,\mathrm{mm}^2$ cable to insure a low impedance connection. The supply was connected to the inside winding and the voltage increased while monitoring the supply current. Table 6.2 gives a summary of the test results for the short circuit test along with calculated values using the modelling from Chapter 4.

Table 6.2 Short Circuit Test Result Summary.

Parameter	Measured	Calculated	% Difference
Inside winding voltage (V)	21.1	21.1	0
Inside winding current (A)	66.9	67.2	-0.45
Inside winding current's phase (deg)	-88	-87.5	0.57
Outside winding current (A)	66.1	66.8	-1.06
Volt-amperes (VA)	1411	1417	-0.43
Real power (W)	65	61	6.15
Power factor	0.05	0.04	20
Impedance volts (%)	10.9	10.9	0

There is good agreement between the measured and calculated results. The biggest percentage error is in the power factor with 20 % error, although this result is misleading, as the power factor is very small in both cases and the actual error is small. There is also a difference between the ratio of currents and the reciprocal of the turns ratio. Once again this is because of the magnetising current component adding to the primary winding current.

Figure 6.4 is a plot of the short circuit voltage against short circuit current. This shows a linear increase in short circuit current with applied voltage.
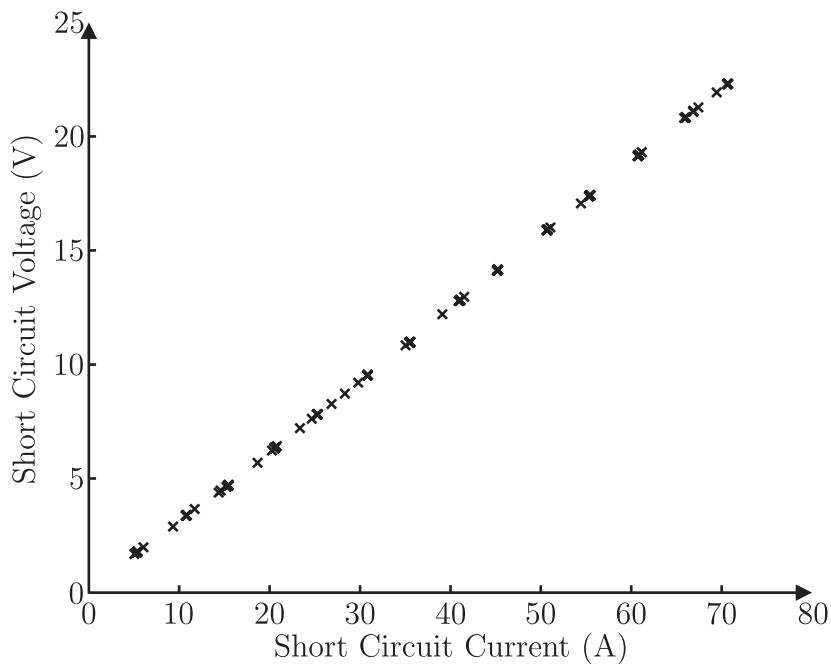
Figure 6.4 Short circuit voltage against short circuit current.

6.3.3   Resistive Load Test Results

The purpose of the resistive load test is to ascertain the performance of the HTSPCT as a power transformer over a range of operating load. This sort of testing is not usually performed on larger transformers as the power supply requirements are usually not achievable. However, as the HTSPCT has a 15 kVA rating, a suitable size load and power supply were available, and the test could proceed.

Several characteristics of the transformer are discernible with the resistive load testing. For example, by measuring the supply power and load power, the efficiency of power transfer over a wide load range is found. Load current through the HTSPCT results in a voltage drop across the series impedance. The ratio of the no load voltage to the load voltage, known as voltage regulation, can be found with this test. In addition, the power factor as seen from the supply side for varying load, is also a useful operating parameter found during this test.

The resistive load test was performed with the outside winding connected to the adjustable resistive load bank depicted in Figure 6.2(c), and the inside winding connected to the single phase voltage supply. The supply was brought up to rated voltage, and measurements of the primary voltage and current were taken as the load resistance was varied. The quench detection system of Section 5.4.6 was also used during this test to protect the HTSPCT from damage.

The test was performed over several hours with the load varied from a light load up to just above the full transformer rating. The cooling system of Section 5.4.5 was used to keep the HTS conductors submerged in LN_2 throughout the testing. A summary of the measured results for the resistive load test are given in Table 6.3 and compared with calculated values using the modelling from Chapter 4.

Table 6.3   Resistive Load Test Result Summary.

Parameter	Measured	Calculated	% Difference
Inside winding voltage (V)	230	230	0
Inside winding current (A)	68.5	67.7	1.17
Inside winding current's phase (deg)	-22	-20	9.09
Outside winding voltage (V)	223	222.7	0.13
Outside winding current (A)	64.5	64.4	0.16
Outside winding current's phase (deg)	0	0	0
Volt-amperes (kVA)	15.7	15.6	0.64
Real power (kW)	14.7	14.6	0.68
Power factor	0.93	0.94	-1.08
Load Power (kW)	14.4	14.3	0.69
Efficiency (%)	98.2	98.1	0.10
Voltage regulation (%)	2.86	3.27	-14.3
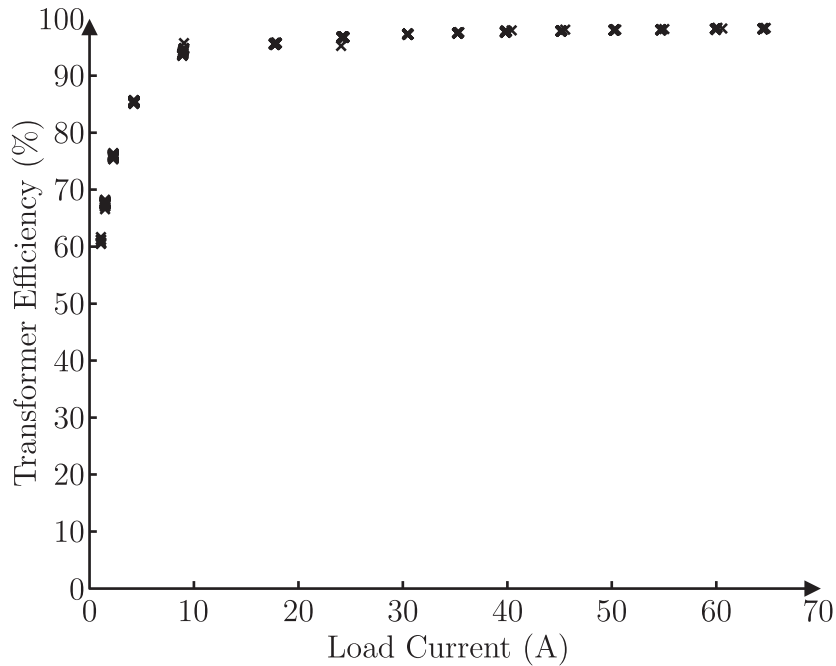
Figure 6.5   Measured efficiency of the HTSPCT for varying load current.

There is good agreement between the measured and calculated results with the largest errors occurring in the primary current's phase and the voltage regulation calculation. Both these errors can be attributed to the error in the magnetising current from Table 6.1. The difference in magnetising current is directly related to magnetising reactance, X_m, which has been calculated to be slightly higher than that measured. The higher magnetising current results in the primary current lagging the voltage more, as seen in the results. In addition, the difference in voltage regulation is related to the difference in no load voltage, which is again caused by the magnetising current.

Figure 6.5 gives the measured efficiency of the HTSPCT for varying load current. At very low loading, the no load losses measured in Section 6.3.1 dominate and the efficiency of power transfer is poor. When the load gets above $10\,A$, equivalent to $15\,\%$ of the rated load, the efficiency increases to the high $90\,\%$s where it remains across a wide load range.

Figure 6.6 shows the measured voltage regulation of the HTSPCT over the load range tested. The plot shows an increasing trend in the measured voltage regulation as the load is increased. The voltage regulation is also affected by the power factor of the load, with a lagging power factor increasing the voltage regulation, while a leading power factor can cause the secondary voltage to increase, resulting in negative voltage regulation. These aspects were not measured, as suitably rated inductive and capacitive loads were not available.

Figure 6.7 shows the relationship between the supply and the load currents for the HTSPCT under load and compares it to the measured power factor at the supply end. At very low loads,
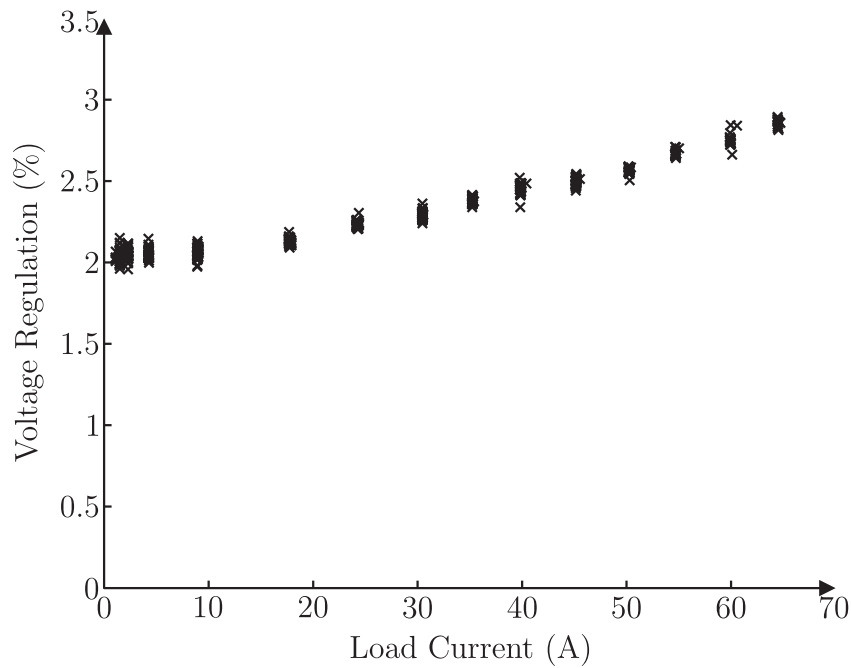
Figure 6.6   Measured voltage regulation of the HTSPCT for varying resistive load.
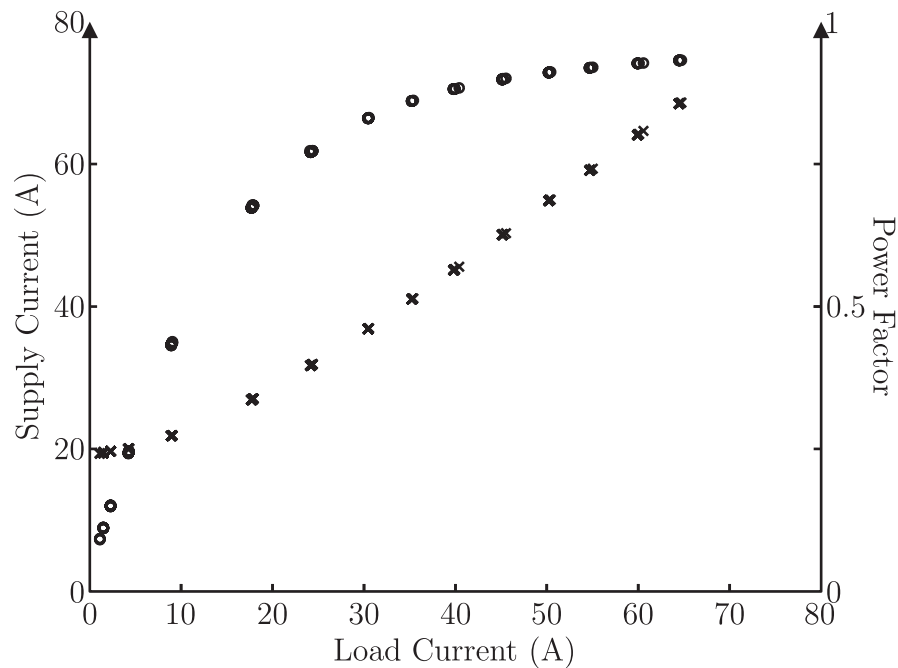
Figure 6.7   A plot of the measured supply current (circles) and power factor (crosses) for various resistive load.

the excitation current dominates, as compared with the load current. Because the excitation current is in quadrature with the load current, the power factor for this loading is poor. As the load is increased, the difference between the supply and the load current decreases to less than 5 A at high loading. As the load is resistive, the load current is in phase with the secondary voltage and the power factor improves to near unity.

Figure 6.8   Photograph of the test setup for the insulation resistance test.

6.4   OTHER EXPERIMENTAL DATA

Several other tests were conducted on the HTSPCT in addition to those mentioned in Section 6.3. Some of the tests, such as the insulation and dc resistance tests, were performed on the HTSPCT before those of Section 6.3 as they ensure the device is electrically safe to energise. Some of the other tests, like the fault ride through test, were performed later as they were considered potentially damaging to the transformer.

6.4.1   Insulation Resistance and DC Resistance Tests

The first test performed on the HTSPCT was an insulation resistance (IR) test. This was performed with a S1-5005 insulation tester from Megger shown in Figure 6.8. The insulation was tested between the inside and outside windings from the bushings both prior to and after filling the LN_2 chamber, as shown in the circuit diagram of Figure 6.9. Because the main transformer assembly was made from g10 fibre, IR tests were not performed between the windings and the tank. The test voltage was $500\,\mathrm{V}$ for 60 seconds. The results from the IR testing were $128\,\mathrm{G\Omega}$ for the dry test and $9.1\,\mathrm{G\Omega}$ for the wet test. This was a pass in both tests although the significant reduction in resistance was noted and is discussed in Section 6.6.4.
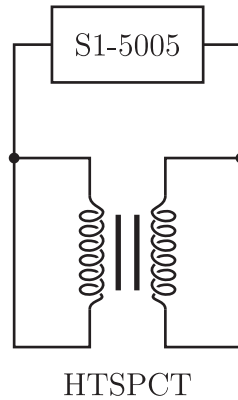
Figure 6.9   Circuit diagram for the insulation resistance test.

The second test performed was a dc resistance test for each winding using a MPK254 Digital Micro-Ohmmeter from Megabras. This test was performed both prior to and after filling the LN_2 chamber. Measurements were taken from between the winding's bushings. The results for the dry test were $4.133\,\Omega$ and $4.741\,\Omega$ for the inside and outside windings respectively. The dc resistance under LN_2 was measured as $2.3\,\text{m}\Omega$ for the inside winding and $2.5\,\text{m}\Omega$ for the outside winding. This result indicates that the HTS wire was superconducting and that the combined resistance of the copper lead-outs, busbars, and bushings was small.

6.4.2   Overload Test Results

The transformer was tested for an extended period of time with a 1.1 per unit resistive load. The original purpose of the test was to perform a high load endurance test of the transformer. However, the losses at this operating point causing LN_2 boil off were such that the test could only be run for 9 hours.

Cooling of the windings during the test was from a continuous-flow type cryostat system, where the LN_2 level was maintained using the cooling system of Section 5.4.5 fed from a $160\,\text{L}$ LN_2 Dewar. Approximately half of the LN_2 was used to fill the HTSPCT Dewar for the test, the rest was consumed during the testing of the transformer through mechanical and electrical losses.

The transformer performance was stable throughout the testing and it is believed that with an adequate cooling system, the transformer could run continuously at this load level. A summary of the results for the overload test are given in Table 6.4.

These results given in Table 6.4 are comparable to those from the resistive load test of Section 6.3.3. The current, volt-amperes and real powers have all consistently increased in the overload test from the resistive load test, while the voltages and phase angles have remained constant.

Table 6.4   Overload test measurements.

Parameter	Measured
Test duration (hours)	9
Inside winding voltage (V)	231
Inside winding current (A)	71.5
Inside winding current's phase (deg)	-22
Outside winding voltage (V)	224
Outside winding current (A)	67.5
Outside winding current's phase (deg)	0
Volt-amperes (kVA)	16.5
Real power (kW)	15.4
Power factor	0.93
Load Power (kW)	15.1
Efficiency (%)	98.1
Voltage regulation (%)	2.86

6.4.3   Separate Source AC Withstand Voltage Test

This test was performed in accordance with IEC 60076-3. Figure 6.10 shows a circuit diagram of the test setup. The secondary side of the HTSPCT was tied to earth and the primary winding connected to the test voltage. The test voltage was 3029 V and the test duration was 60 seconds. The test voltage was supplied from a 230 V to 11 kV distribution transformer fed from a variable ac source, and the test frequency was 50 Hz. Figure 6.11 shows the test setup with the 11 kV distribution transformer on the left.
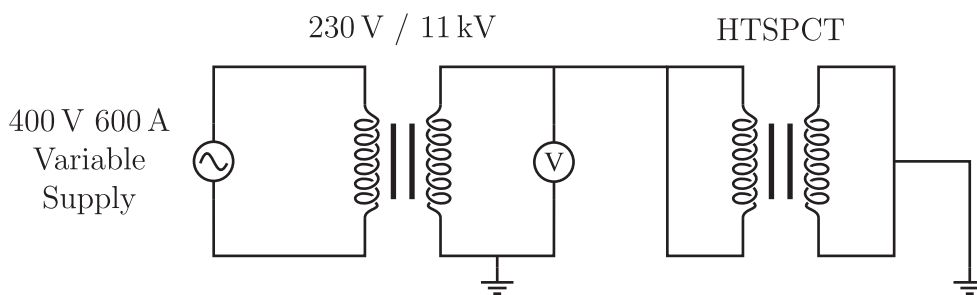
Figure 6.10   Circuit diagram of the test setup for the separate source ac withstand voltage test.

Although not necessary for this test, the high voltage current was not able to be measured due to the very low capacitance of the HTSPCT insulation. The low voltage side current was measured instead and converted to the high voltage current via the distribution transformer turns ratio. The low voltage current was measured at 109 mA which converted to 2.27 mA on the high voltage side. This gives an estimated insulation capacitance of 2.4 nF resulting in a resonant frequency of approximately 16 kHz.

Figure 6.11   Photograph of the test setup for the separate source ac withstand voltage test.

6.4.4   Fault Ride Through

The final test performed on the HTSPCT was a fault ride through test. This test was performed last as it was considered to have the highest potential for transformer failure. In this test, the HTSPCT secondary winding was connected to the 15 kW resistive load shown in Figure 6.2(c). The rated voltage was applied to the primary winding through the 600 A supply without the 70 A variac in the circuit. The secondary winding was then short circuited via the manually operated switch also shown in Figure 6.2(c).

The voltage and current for the primary and secondary windings was monitored with a four channel oscilloscope. The quench detection system was used to protect the transformer. When the manual switch was operated, the secondary voltage was reduced to zero. This resulted in the voltage regulation increasing above the threshold of the quench detection system, and a contactor was opened cutting power to the circuit. The measured fault level was approximately 350 A rms. This lasted for about 7 cycles before the contactor was operated.
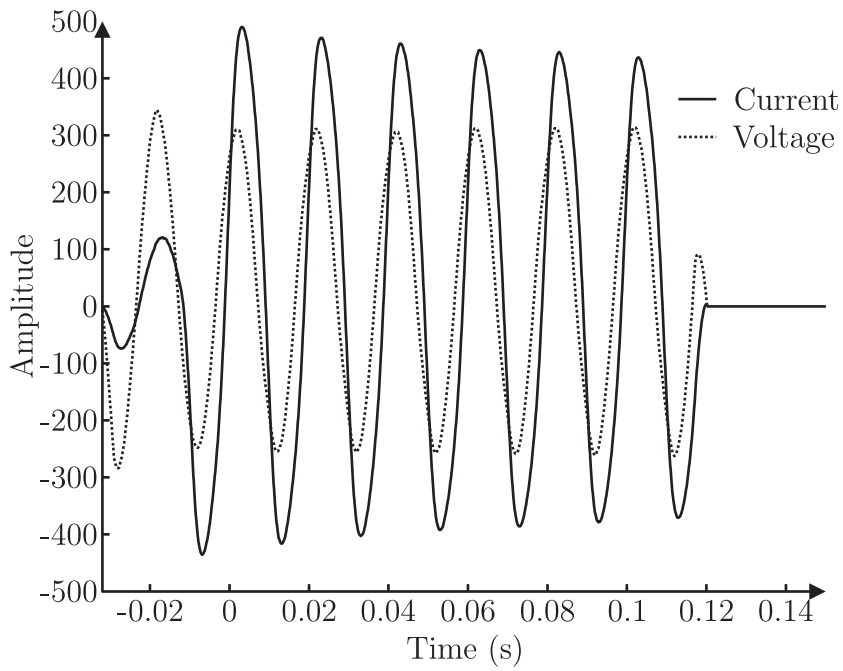
Figure 6.12   Oscilloscope traces of the primary voltage, (V), and current, (A), during the fault ride through test.
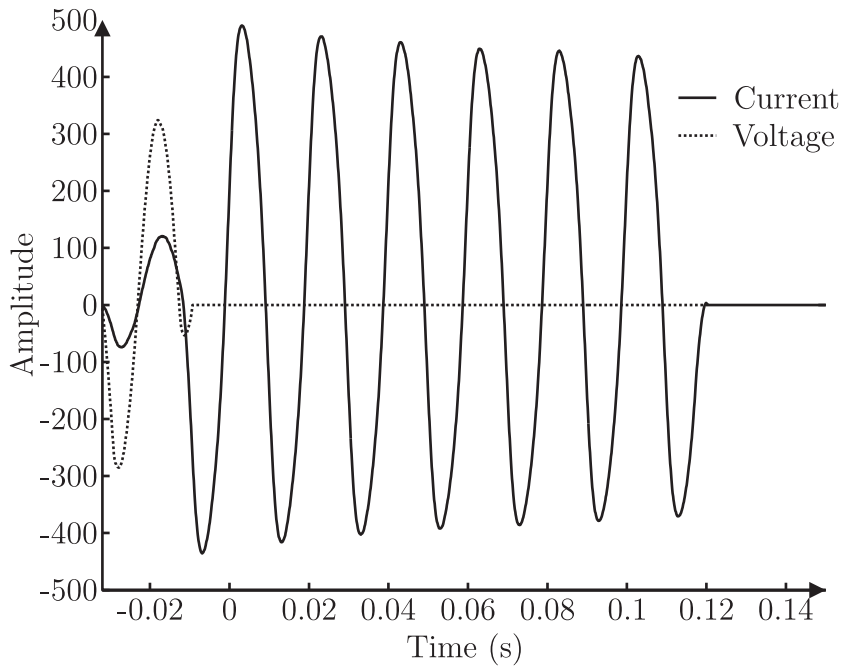
Figure 6.13   Oscilloscope traces of the secondary voltage, (V), and current, (A), during the fault ride through test.
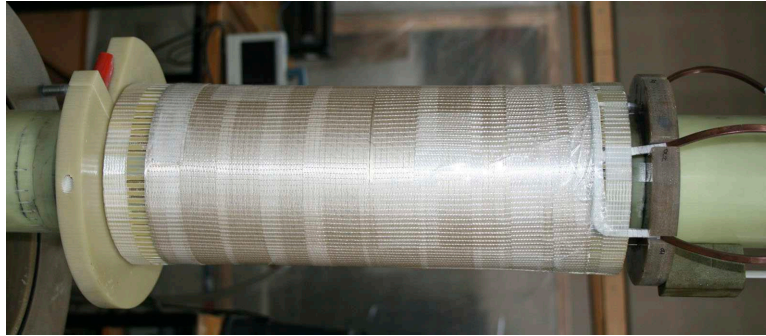
Figure 6.14 Photograph of the HTSPCT windings after the fault ride through testing showing no visible damage.

Oscilloscope traces of the primary voltage and current for one particular measurement are shown in Figure 6.12. From the trace, it is apparent that the inception of the fault occurred approximately 0.01 seconds before the oscilloscope triggered at time equal to 0 seconds. A slight reduction in the voltage magnitude as the fault current appears is apparent, which is due to the voltage drop across the impedance of the supply. The transient nature of the waveform is entirely dependent on the point of the wave where the fault occurs.

Figure 6.13 shows the measured voltage and current of the secondary winding for the same instance. At the time the fault is applied, the secondary voltage reduces to zero. The measured secondary current is very similar to that of the primary winding, with approximately the same magnitude and transient component.

A visual inspection was carried out on the transformer upon completion of the testing. The transformer was allowed to return to room temperature prior to opening the tank to prevent moisture from damaging the windings. Figure 6.14 shows a photograph of the of the HTS windings. The transformer suffered no visible damage as a result of this test.

IR and dc resistance tests were performed on the transformer at room temperature. The winding resistances for the inside and outside windings were measured as $4.144\,\Omega$ and $4.753\,\Omega$ respectively. These results are similar to those taken earlier. However, the insulation resistance was measured at $450\,\mathrm{M\Omega}$, a much smaller value than measured earlier. A second IR test was performed a few hours later and measured $380\,\mathrm{M\Omega}$, which is still a pass at this voltage rating. The reason for this change is unclear at this stage.

6.5 COMPARISON WITH MODEL

Results from the key performance tests were compared to the modelling given in Chapter 4. For each of the key tests; open circuit test, short circuit test, and resistive load test, the calculated losses were compared to the measured losses. These comparisons are presented in Figures 6.15,
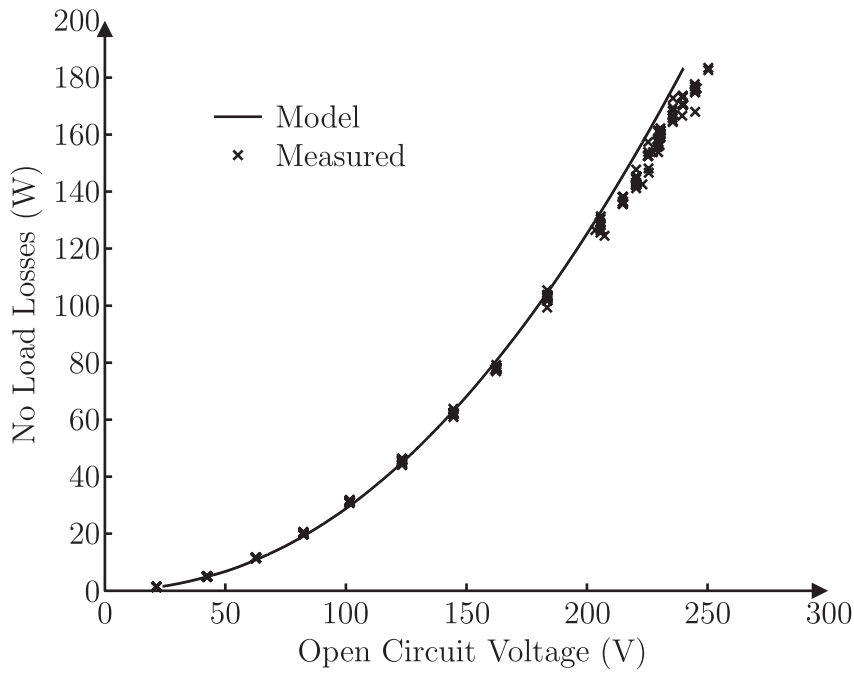
Figure 6.15   Comparison between the measured and modelled open circuit power loss.
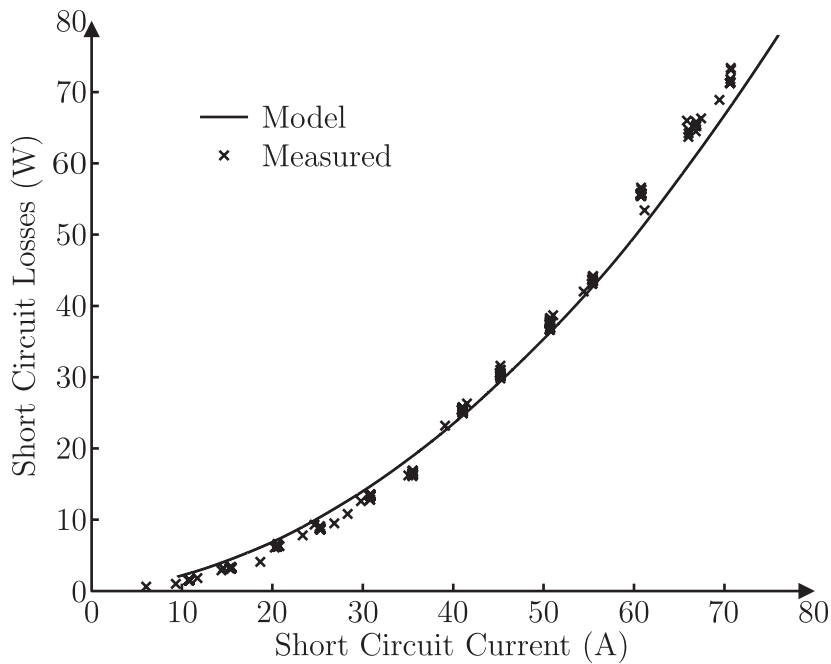
Figure 6.16   Comparison between the measured and modelled short circuit power loss.

6.16 and 6.17.

Figure 6.15 compares the measured and calculated losses for the open circuit test against the open circuit voltage. The model shows good agreement with the measured data with the model slightly overestimating the losses near the rated voltage where the model predicts about 130 W of core losses and about 38 W of winding losses attributed to the primary winding. The bulk of
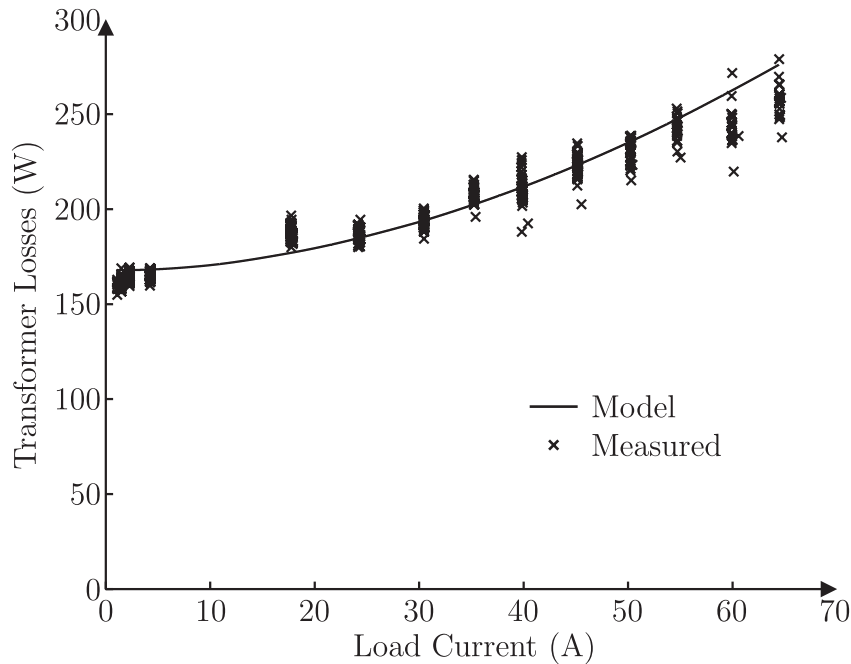
Figure 6.17   Comparison between the measured and modelled resistive load test power loss.

the winding losses, approximately 33 W, are due to magnetising loss in the perpendicular field. These results are expected as the core losses would be high due to rated voltage being applied, and the winding losses would be due to a strong radial field component.

Figure 6.16 compares the measured and calculated losses for the short circuit test against the short circuit current. The model again shows good agreement with the measured data with the model slightly underestimating the losses near the rated current. According to the model, at rated current, the losses are dominated by the winding losses with 60 W of losses spread evenly across the primary and secondary windings (there is less than a Watt of core losses). The model suggests the losses are mainly due to self field losses, 35 W, and dynamic resistance in a parallel field, 10 W.

Figure 6.17 compares the measured losses from the resistive load testing with those calculated with the model. The model shows good agreement with the measured data, with the model slightly overestimating the losses for high loadings. According to the model, at rated load, there are 128 W of core losses; about 70 W of primary winding losses and about 62 W of secondary winding losses. The losses are split between magnetising loss in the perpendicular field, 33 W, dynamic resistance losses in the perpendicular field, 49 W, and self field losses, 34 W.

6.6   DISCUSSION

6.6.1   Open Circuit Test

In Chapter 2, the differences in magnetising current between full core and partial core transformers were discussed. The main differences were that the magnitude is larger for a PCT and the amount of harmonic distortion is less. Figures 6.18 and 6.19 show the harmonic magnitudes of the open circuit voltage and current respectively up to the 30th harmonic. For clarity, the magnitude of the fundamental has been cropped, they were 230.3 V and 19.4 A, so that the higher harmonics can be seen.

The plots show that despite the applied voltage having distortion, (this is an unfortunate effect of the supply at UoC caused by a large number of computers) the excitation current distortion is very low, less than 2.5 % THD. The open circuit current is also in quadrature to the applied voltage as apparent from the measured phase in Table 6.1.

Even though the magnetising current is large when compared to a full core transformer, no onset of core saturation is evident in the results. This result was expected as the designed peak flux density was 0.7 T. However, the larger magnetising current for the HTSPCT has resulted in a reduction in the open circuit output voltage due to winding losses and leakage flux. This is modelled as a voltage drop across the series components of the primary winding which primarily consists of leakage reactance.
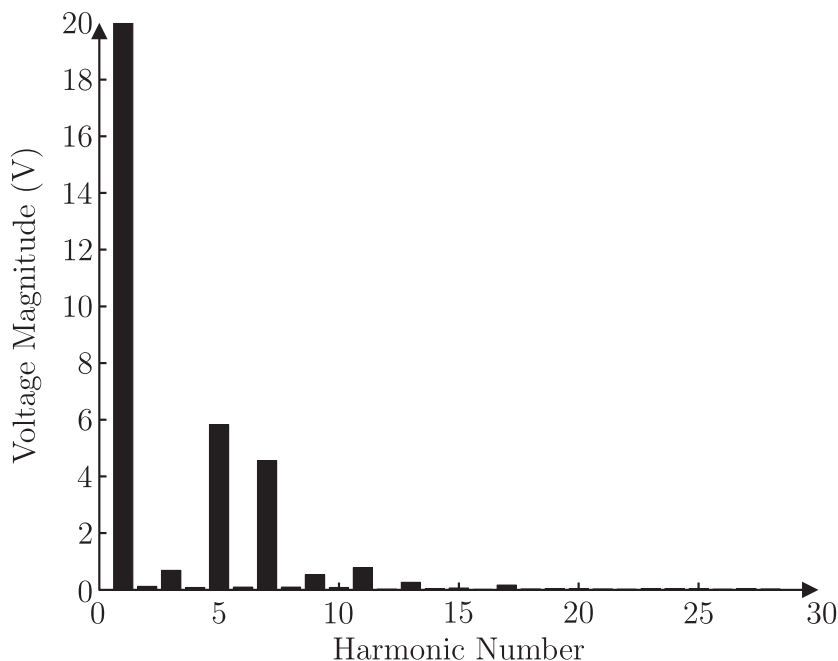
Figure 6.18   Plot of the harmonic content of the open circuit voltage up to the 30th harmonic. The fundamental voltage of 230.3 V has been cropped.
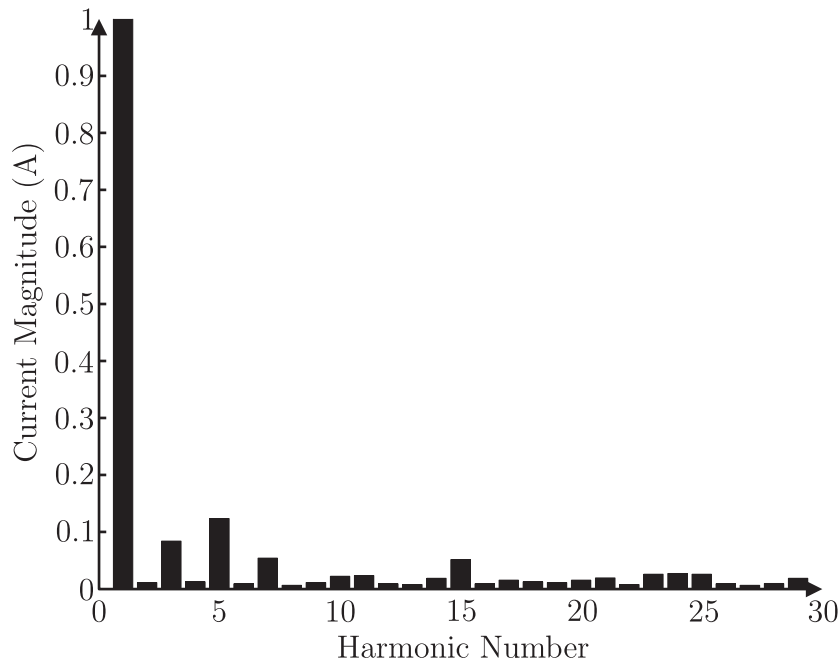
Figure 6.19 Plot of the harmonic content of the open circuit current up to the 30th harmonic. The fundamental current of 19.4 A has been cropped.

6.6.2 Short Circuit Test

The percentage impedance volts of the HTSPCT measured during the short circuit test was about 11 %. This is about twice the value compared to the 15 kVA distribution transformer used in the separate source ac withstand voltage test. This is not necessarily a detrimental aspect to the transformer, as a high impedance voltage can act to limit fault currents. However, it also increases the voltage regulation of the transformer.

The primary reason for this is due to the 2 mm inter-layer insulation used. This insulation was required to keep the windings sufficiently cool during operation, but this adds to the leakage flux by placing the windings further apart. This is confirmed by looking at the measured equivalent series impedance. The measured equivalent series resistance was $0.015\,\Omega$ and the measured equivalent series reactance was $0.315\,\Omega$. This means that the majority of the series impedance consists of leakage reactance.

6.6.3 Resistive Load Test

The resistive load test proved successful, in that the HTSPCT did not fail under full load conditions. This was a significant improvement on the original prototype design which failed after a few minutes at full load. This illustrates the benefits of the improved insulation design.

There is an expectation that because superconductors have zero resistance, a transformer made

with superconductor windings will be 100 % efficient. This is not the case because there are
core losses, and ac losses in the HTS windings. The HTSPCT efficiency was measured at 98.2 %
at just over full load. This is a high value for a transformer of this size and could be further
improved using better transformer steel to reduce core losses and improving the series losses of
the HTSPCT. The transformer was also efficient over a large loading range. Unfortunately, the
measured electrical efficiency is not the true efficiency of the transformer because the winding
power loss, about 50 % of the total losses at full load, is occurring at a cryogenic temperature.
According to the second law of thermodynamics, the best possible performance of a cryogenic
system operating between T_h and T_c is the Carnot efficiency,

$$\eta_c = \frac{T_c}{(T_h - T_c)} \tag{6.1}$$

where T_c is the cold temperature in Kelvin and T_h is the hot temperature in Kelvin. The Carnot
efficiency for the HTSPCT is 34.8 %, which means every 1 W dissipated at 77 K requires 2.87 W
of cooling. The reality is that most cryocooler efficiencies are only a few percent of the Carnot
value and the actual cooling power requirement is several times greater [Shu *et al.* 2000]. More
discussion on the HTS losses is given in Section 6.6.5.

The voltage regulation of the HTSPCT is reasonably constant, only varying by less than 1 % over
the whole load range. When compared to the 15 kVA distribution transformer, the HTSPCT
would have a larger variation in output voltage due to its higher series impedance, although the
output voltage is still within 5 % of nominal. If the HTSPCT was to be used in a power system,
additional winding taps could be beneficial.

The plot of Figure 6.7 demonstrates the ability of the partial core design to still perform as
a power transformer despite having a very large magnetising current component compared to
traditional full core transformers. While the magnetising current is a significant component at
the lower load levels, when the load is increased above 30 A, 45 % of rated current, the power
factor of the HTSPCT is comparable to similar rated full core designs.

6.6.4   Other Results

While the HTSPCT passed the insulation resistance test for both dry and wet conditions, the
test provided a significant finding. This was the drop in insulation resistance by an order of
magnitude from the dry test to the wet test. This was an unexpected result as the dielectric
strength of LN_2 measured by O'Neill in [O'Neill *et al.* 2000b] and shown in Section 3.3 of this
thesis was $> 10 \, \text{kVm}^{-1}$, whereas the breakdown of air is around $1 \, \text{kVm}^{-1}$. The reason behind
the drop in resistance is not clear at this this stage and will require more research.

The overload test demonstrated the ability of the HTSPCT to operate at very high levels for an extended period of time. This showed the effectiveness of the insulation design to keep the HTS windings cool even though the rate of LN_2 boil-off was high.

The separate source AC withstand voltage test proved the insulation design's ability to withstand voltages in excess of the rated voltage. This result was expected as the inter-layer insulation was designed for the cooling of the conductors and far exceeds the voltage insulation requirements. The maximum inter-layer electric field during normal operation is $81.3\,\mathrm{Vmm^{-1}}$ and the maximum turn to turn voltage is only $1\,\mathrm{V}$, whereas the breakdown of the LN_2 is $> 10\,\mathrm{kVm^{-1}}$ and the turn to turn insulation is $400\,\mathrm{V}$.

The fault ride through testing demonstrated the HTSPCT's ability to withstand short circuit forces. Even though the transformer showed no damage from this test, it must be noted that the layer winding design used in the HTSPCT is considered a mechanically weak design. For a transformer with concentric windings, forces acting on the windings during a short circuit fault try to pull the inside winding turns into the center of the transformer while pushing the outside winding turns outwards [de Azevedo *et al.* 2007]. If the forces are great enough, this can result in a collapse and/or buckling of the windings. For this reason, most large transformers use a pancake winding design and pre-load the windings. However, the forces generated in smaller transformers are usually not large enough to cause this damage and a layer winding design, which is significantly easier to manufacture, is often used.

Figures 6.12 and 6.13 show that the switching of the fault did not occur at the worst possible point in the supply waveform, namely the voltage zero crossing. This switching was considered close enough being that the switching was conducted manually and a synchronous switch was not able to be used.

In addition, the current amplitude was far in excess of the critical current of the HTS wire. The HTS wire would no longer be superconductive and would be in the resistive state. Therefore, it is likely that the majority of the fault current was traveling through the silver matrix of the tape resulting in very high current densities in the silver. For this reason, the fault ride through was limited to the response time of the protection circuit rather than longer tests as sometimes specified in factory acceptance testing.

6.6.5 HTS Losses

Table 6.5 lists the losses calculated from the model for the open circuit, short circuit and resistive load test. The calculated losses for the core and each winding are given, as well as the losses calculated for each part of the HTS ac loss model across the whole winding.

The open circuit test fully magnetises the core to its designed value without having a strong field

Table 6.5   Calculated Losses.

Power Loss	Open Circuit	Short Circuit	Load Test
Core	130	0.063	128
Inside Winding	38.0	30.3	77.7
Outside Winding	0	30.1	70.6
$P_{B,\parallel}$	0.32	8.82	8.94
$P_{B,\perp}$	33.0	1.25	33.1
$P_{dr,\parallel}$	0.047	9.54	9.57
$P_{dr,\perp}$	2.11	5.60	58.0
P_{rl}	4.33×10^{-12}	783×10^{-6}	0.045
P_{sf}	2.50	35.2	38.6

in the winding air gap as there is no current in the secondary winding. This results in the flux having a strong radial component, as seen in the $P_{B,\perp}$ calculation, while the current carrying component of the losses is small, reflected in the P_{rl} and P_{sf} calculations.

The short circuit test in traditional transformers provides a good indication of the winding losses for the transformer under load. Unfortunately, this is not strictly the case with HTS conductors. This is because of the influence of the magnetic field on the ac losses of the HTS wire and the high anisotropy of those losses. Under short circuit conditions, the flux in the transformer in mainly in the air gap between the primary and secondary windings. This flux is predominantly in the axial direction, with only a comparably small radial component. This is reflected in the calculations which show a strong axial component, $P_{B,\parallel}$, as well as larger current carrying components, seen in the increases of P_{dr}, P_{rl}, and P_{sf} compared to the open circuit calculations.

The resistive load test calculations are a combination of the open and short circuit cases with the individual loss components almost a sum of the open and short circuit calculations. The one notable exception to this is the $P_{dr,\perp}$ which makes up nearly half of the total calculated losses. This is due to the combination of both high currents and high radial magnetic field.

Figure 6.20 illustrates the total calculated HTS ac losses for each turn in the HTSPCT, where turn 1 is the topmost turn and turn 80 is the lowest turn and layers 1 to 8 are numbered from the closest to the core outwards. As shown in the figure, the losses are greatest at the ends of the windings closest to the core. This is where the strongest radial flux is found. The FEA software modelled the peak radial flux density at this point as being $0.04\,\mathrm{T}$. This flux density would reduce the dc critical current to around $89\,\mathrm{A}$. The peak current of $91\,\mathrm{A}$ at full load exceeds this value suggesting that the rated value of the transformer should be lower.

It is apparent from this analysis that the radial component of the magnetic field is a significant contributing factor to the ac losses of the HTSPCT. Also, the quantity of losses developed at
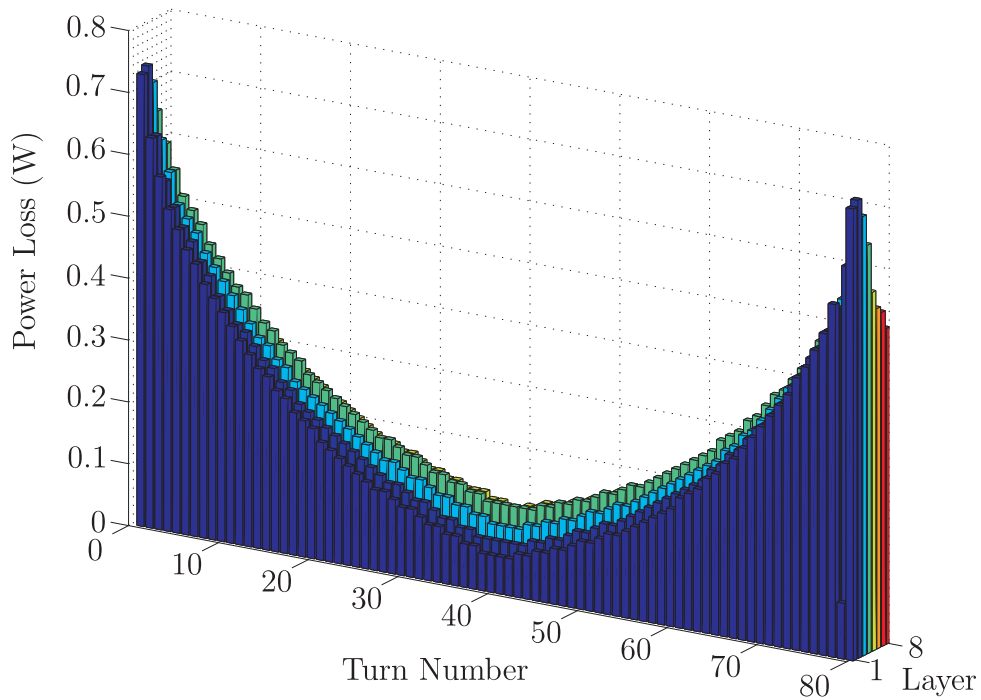
Figure 6.20   The total HTS ac losses calculated for each turn in the HTSPCT.

LN_2 temperatures are too high to make this design viable in a commercial environment when the "cooling penalty" (mentioned above) is taken into account. For these reasons, it would be advantageous to research ways to reduce the radial component of the field, for example incorporating the use of flux diverters into the design [Al Mosawi *et al.* 2001].

6.6.6   Model Limitations

There are some limitations to the modelling used in this thesis. While aspects of the model were based on measured data such as the magnetising losses P_B and the resistive losses P_{sf}, other parts of the model were unable to be verified through experiments. These include the parameters $\lambda_\parallel$ and $\lambda_\perp$ in the dynamic resistance model and q and C_{sf} in the self field losses model. $\lambda_\parallel$ and $\lambda_\perp$ were estimated to be 0.95 and 0.94 respectively and q and C_{sf} were adjusted to give a reasonable fit with the measured data with $q = 1.5$ and $C_{sf} = 45600$. As the dynamic resistance and self field losses made up a significant portion of the calculated losses, this is not the preferable solution.

Another limitation with the model lies with the finite element analysis of the magnetic field. The non linear effects of the core and of screening currents in the HTS itself were not modelled. The effect of these aspects on the global flux distribution was assumed to be negligible but this may not actually be the case. This could be a reason for the difference between calculated and measured excitation current as X_m is the main contributing factor to this current magnitude.

Despite these limitations, the model has been able to give a reasonable approximation to the measured data across a wide range of operating conditions. This suggests that although the calculated losses may not be exactly right for their individual components, the overall sum of the losses is probably correct.

6.7   CONCLUSIONS

This chapter presented the experimental setup and testing of the new prototype HTSPCT. Details of the experimental safety procedures and of the equipment used during the testing were given. Special mention of the LN_2 filling procedure and of important measurement techniques were also detailed.

The HTSPCT was extensively tested to ascertain its electrical performance. The key operating characteristics were found using open circuit, short circuit and resistive load tests. A linear relationship between the open circuit voltage and current was found indicating that saturation of the core did not occur. The series impedance of the HTSPCT was found to be larger than a similar rated $11\,\mathrm{kV}$ distribution transformer and was due to the inter-layer insulation increasing the leakage flux. The HTSPCT was found to be $98.2\,\%$ efficient at full load, with $2.86\,\%$ voltage regulation.

Additional tests included an insulation resistance test which found a drop in resistance between the dry and wet conditions. An overload test demonstrated the validity of the new insulation design to cool the windings over an extended period under very high loading. The separate source ac withstand voltage test proved the dielectric strength of the insulation system is sufficient for the rated voltage. The fault ride through test showed how the HTSPCT was able to withstand short circuit forces without damaging the windings.

The tests results were compared to the modelling from Chapter 4. There was good agreement between the measured and the calculated results. The various components of the modelling results were discussed with reference to the current and magnetic field distribution in the winding space, and the limitations to the modelling were examined. The major contributing factor to the HTS losses is believed to be the radial component of the magnetic field around the end winding space of the transformer.

The testing has shown that despite being a partial core design with the resulting large magnetising current associated with these designs, the HTSPCT was able to perform well as a power transformer. The power factor, voltage regulation, and efficiency of power transfer during resistive load testing were all acceptable for a transformer of that power rating.

The new winding design was successful at maintaining mechanical strength under large forces and thermal cycling. This was proven by the ability of the transformer to withstand short

circuits applied to the secondary terminals during full load as noted in Section 6.4.4. It should be noted however, that transformers with much larger power ratings would likely be unsuitable for the layer type winding design presented here. The forces under fault conditions would be enough to cause deformation of the windings. An alternative design using pancake coils would be more structurally robust.

The winding design also demonstrated the benefits of improved contact between the HTS wire and the LN_2 as was shown by the performance during the overload testing in Section 6.4.2. During this test, the peak currents were expected to be approaching the magnetic field reduced critical current of the tape although no failure of the windings occurred. This is a significant improvement of the previous generation of HTSPCT which was discussed in Chapter 3.

The ac losses of the HTS wire were found to be present at even at current levels well below the critical current of the tape. As discussed in Section 6.6.5, radial flux present in the HTSPCT design was found to be the most significant contributing factor to the ac losses. Some proposed methods for loss reduction of the HTSPCT are given in Chapter 7 as possible future research areas.

Because of the HTS ac losses, setting the rated current of the transformer is not about critical current, but rather a loss management issue as it is in most other electric power devices. This is further complicated with the ac HTS losses occurring at cryogenic temperatures and the cooling power requirements associated with this as discussed in Section 6.6.3. The designer of the transformer has to find a balance between the energy throughput of the transformer and the refrigeration power retirements.

Chapter 7

FUTURE WORK

7.1 MODEL REFINEMENT

As discussed in Chapter 6, there were some aspects of the modelling presented in this thesis that could be improved upon. This includes parts of the ac loss model and parts of the magnetic field modelling.

7.1.1 HTS AC Losses

The most significant aspects of the ac loss model for the HTS wire that need refinement include the parameters $\lambda_\parallel$ and $\lambda_\perp$ in the dynamic resistance model and q and C_{sf} in the self field losses model. These aspects of the model were unable to be specifically measured while researching this thesis. There has been quite a lot of research conducted in this area, such as the work from Rabbers et al. and Oomen et al. However, there does not seem to be a lot of agreement in the literature as to the correct modelling methods. The wide variety in quality and performance of the HTS wire available from manufacturers further complicates these issues.

A more robust model would be of benefit to future work in HTSPCT design. The research would involve experiments to be set up that can measure the ac losses on a variety of sample tapes for various ac transport currents, to determine self field losses. In addition, the effect of dc and ac magnetic fields at various angles on the transport current losses should be investigated to evaluate the effect of dynamic resistance. Possible methods for making the ac loss measurements are found in many papers including [Schmidt 2000, Rabbers *et al.* 2001b, Jiang and Amemiya 2004, Nguyen *et al.* 2005].

Finally the validity of the superposition assumption made should be investigated. Are the different aspects of the ac losses such as magnetising loss, self field loss and dynamic resistance truly independent of each other? If so, then the current modelling method is suitable to use, if not, then an alternative method should be investigated.

7.1.2   Finite Element Model

Another limitation with the model lies with the finite element analysis of the magnetic field. The difference between the calculated and measured shunt impedance of the HTSPCT is largely due to the reactance, X_m. Previous use of the FEM had shown it to be more accurate in predicting the magnetising reactance of a PCT [Bell and Bodger 2007, Lapthorn and Bodger 2009]. However, the non linear effects of the core, and the screening currents and Meissner effect in the HTS windings, were not modelled. The effect of these aspects on the global flux distribution have resulted in a larger difference between the measured and calculated magnetising current.

A new finite element model that takes into account some of these aspects could be investigated. Comparisons could be made with existing models to determine which aspects have the greatest impact on the HTSPCT performance.

7.2   HTSPCT LOSS REDUCTION

The results from the experiments have shown that efficiency of the HTSPCT needs to improve if the design is to be viable to use in the industry. Examples of ways to improve the design are given below and include using flux diverters, a radially stacked laminated core, an amorphous steel core or a coreless transformer.

7.2.1   Flux Diverters

The radial magnetic field components in the HTSPCT have been shown to be a major contributor to the ac losses in the HTS windings of the HTSPCT. The largest radial magnetic flux density was found to be located near the ends of the windings near the core, the same location as the largest HTS losses.

A possible way to limit the radial field and therefore the ac losses in the HTS wire is to use flux diverters. In [Al Mosawi *et al.* 2001], two powdered iron flux diverters were used inside a cryostat of a 10 kVA HTS full core transformer. The diverters were placed at both ends of the superconducting winding in order to reduce the radial component of leakage flux density in the HTS tapes. The use of the flux diverters was shown to reduce the AC losses by 40 % at the nominal current. Figure 7.1 shows the effect of the Al-Mosawi et al. flux diverters on the magnetic field distribution.

In [Li *et al.* 2008], finite element analysis of the effect of flux diverters on the radial magnetic flux density showed a 16 % reduction in the maximum radial flux density. These papers demonstrate
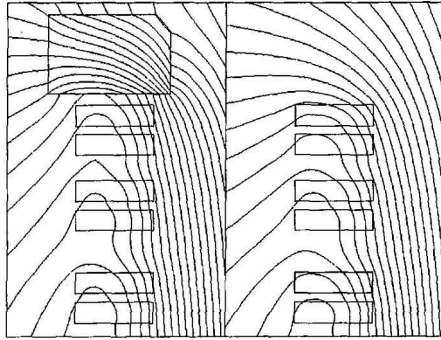
Figure 7.1 Filed plot with and without flux diverters [Al Mosawi *et al.* 2001].

that the use of flux diverters would result in a significant reduction in the ac losses of HTS windings in the HTSPCT, albeit at the cost of installing the diverters.

7.2.2 Radial Core

One of the contributing factors to the core losses measured in the HTSPCT was because of eddy current losses associated with inter-laminar magnetic flux. This effect was modelled in Chapter 4 and referred to as flux in the b direction. One way to reduce these losses is to construct the core with radially-oriented laminations.

In [Bell 2008], a radially-stacked laminated core was constructed and compared to a similar sized core with parallel-oriented laminations, as seen in Figure 7.2. Tests were conducted on a resonant PCT tuned to $1.1\,\mu$F using the different core configurations and the losses monitored. Testing showed that there was a reduction in losses of the transformer with the radial core used compared to the traditional parallel core. In addition, the heating effects of the two core designs were examined and the greatest heating was found to be on the ends of the parallel-stacked core
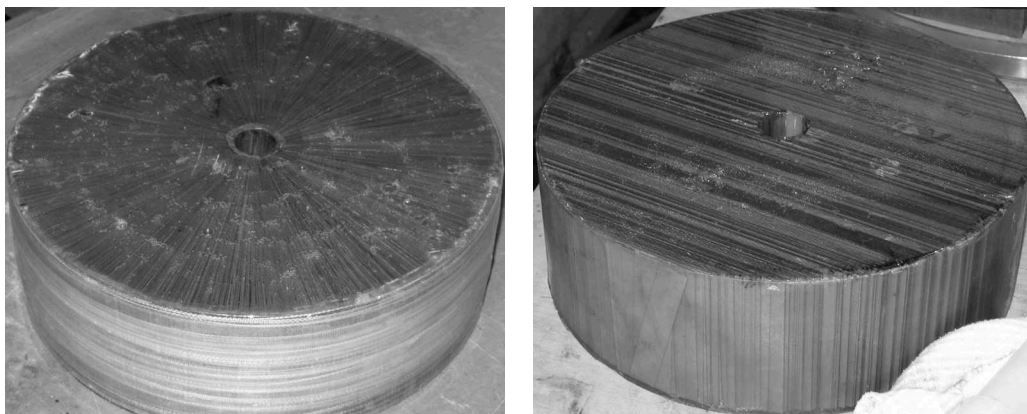
(a) Radially-oriented laminations.   (b) Parallel-oriented laminations.

Figure 7.2 Photographs comparing the two core construction methods used in [Bell 2008].

where there was the greatest inter-laminar magnetic flux.

A radially-stacked laminated core could be built for the HTSPCT as a replacement to the existing parallel-stacked core. Tests could be conducted and comparisons made between the two core designs.

7.2.3   Amorphous Steel Core

Amorphous metals are metallic materials with a noncrystalline liquid-like molecular structure. They are formed in long and thin strips by rapidly cooling molten metal to prevent crystallization of the material during solidification. Transformer cores made from amorphous materials have been shown to have significantly reduced losses compared with silicon steel cores [Luciano and Kiminami 1997, Bodger *et al.* 2002b].

An amorphous steel core could be built for the HTSPCT as a replacement to the existing parallel-stacked core. Tests could be conducted and comparisons made between the two core designs.

7.2.4   Coreless Transformers

Another way to reduce the losses of the HTSPCT is to remove the core altogether. With no core present, there can be no core losses. However, removing the core greatly increases the reluctance of the magnetic circuit, and therefore the inductance will be greatly reduced. This requires more ampere-turns to produce the needed magnetic flux. The output power and efficiency of an air-core transformer increases with the primary current, the frequency, and the mutual inductance between the transformer windings.

Traditionally, air-core transformers have been used in high frequency applications where eddy current losses in a core would be too large and to keep the power transfer and efficiency to acceptable levels. With the development of HTS wire, very high current densities are possible. Combined with near zero resistance, this makes the possibility of an efficient mains frequency air core transformer a reality.

A number of researchers have been investigating mains frequency, HTS, air-core transformers. In [Chen and Jin 2009], a brief summary is given on various air-core superconducting transformer designs from around the world, some of which are shown in Figure 7.3. Problems still exist with high leakage flux and high excitation currents in these devices and more research is needed.
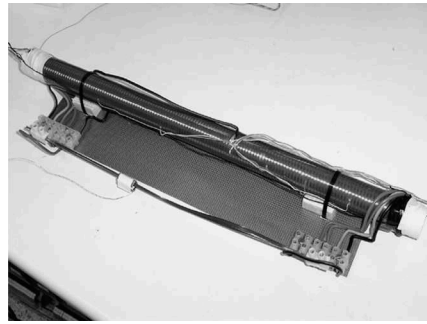
(a) A solenoidal air-core HTS transformer [Suárez *et al.* 2005].
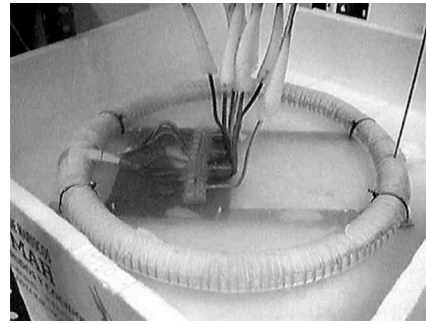
(b) A toroidal air-core HTS transformer [Pérez *et al.* 2003].
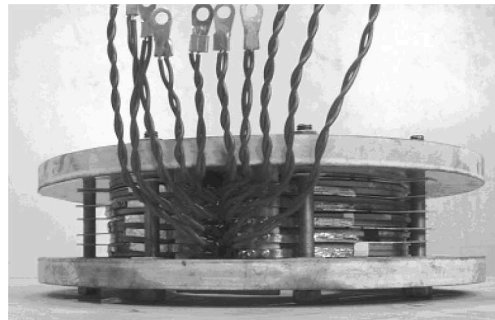
(c) A double pancake air-core HTS transformer [Song *et al.* 2008].

Figure 7.3   Photographs of various air-core HTS transformer designs.

7.3   2G HTS WIRE

The design of the HTSPCT windings is such that they can easily be removed from the transformer main assembly. This was done in part so that other winding designs can be trialled using the same vacuum Dewar. One such winding design that could be investigated would be using second generation (2G) HTS wire made from yttrium barium copper oxide (YBCO).

YBCO HTS has several advantages over 1G HTS in power transformer devices including higher critical current densities, improved mechanical properties and lower critical current anisotropy [Sytnikov *et al.* 2007]. Despite these advantages, devices made from 2G HTS wire are only just starting to be researched around the world. This is in part related to HTS manufacturers' ability to deliver 2G HTS tapes in commercial lengths at suitably high critical current densities, which has only been achieved in the last couple of years [Selvamanickam *et al.* 2009].

A new winding made from 2G HTS could be constructed and compared to the 1G HTS winding presented in this thesis. If the new winding was constructed to have the same dimensions and number of turns as the 1G winding, a direct comparison could be made and the benefits of the 2G HTS wire could be investigated.

7.4   THREE PHASE HTSPCT

A single phase HTSPCT is a useful and cost effective basis for research into novel supercon-
ducting power transformers. However, as the modern power system is based on three phases, a
logical progression of the research would be to study three phase HTSPCTs.
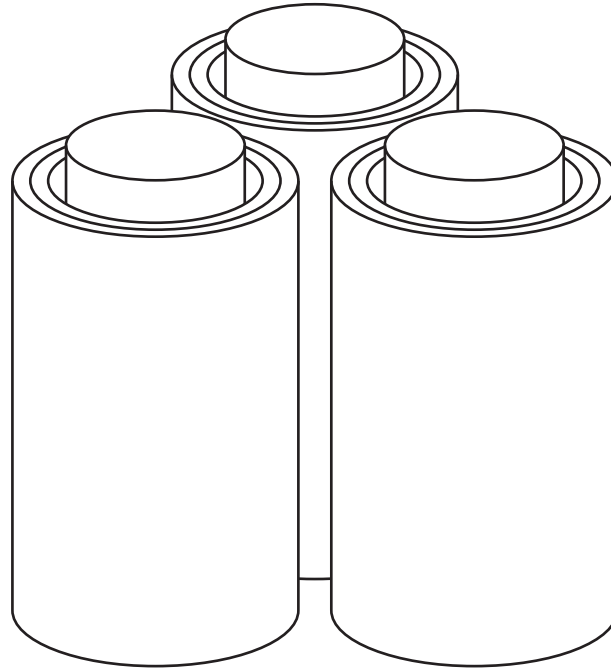
Figure 7.4   Diagram of the arrangement for a three phase HTSPCT.

If three identical HTSPCT windings are constructed and arranged in an equilateral triangular
configuration as shown in Figure 7.4, they can be connected as a three phase HTSPCT. The
magnetic flux from each partial-core would return through the remaining two cores reducing the
magnetic reluctance.

An analysis of a three phase air-core superconducting power transformer is given in [Yamaguchi
et al. 1999] and research into three phase partial core transformers at room temperature is given
in [Bell 2004]. These can be used as a basis for research into three phase HTSPCTs.

Chapter 8

CONCLUSIONS

This thesis began by introducing some basic transformer theory. An ideal transformer was discussed first and then the losses in the transformer were developed based on the Steinmetz equivalent circuit. The differences between full core and partial core transformers were then discussed, the most significant difference being the magnetising reactance value which is much smaller in the partial core transformer. Superconductors were then introduced where the origins and the basic theory of superconductivity were discussed. Then high temperature superconductivity was compared to conventional superconductors and some of the differences highlighted such as operating temperature and the high anisotropy of high temperature superconducting wires.

The previous research at UoC leading to a prototype high temperature superconducting partial core transformer was then presented. This included early partial core design and material testing at cryogenic temperatures. This early research lead to the design and construction of the first high temperature superconducting partial core transformer although it was unable to be fully tested at that time due to a Dewar failure. Repairs to the Dewar by the author enabled several electrical tests to be conducted on the transformer to determine its performance. The transformer failed while testing under full load with the primary winding becoming open circuit. An investigation into the failure mechanisms lead to the conclusions that operating near critical limits combined with insufficient cooling were main contributing factors. An alternative winding design with greater emphasis on conductor cooling was then trialled in a full core high temperature superconductor design. This design, while not optimised, was tested successfully at rated load and demonstrated the benefits of the new winding design.

A model for high temperature superconducting partial core transformers was then developed. The model was based on previous research on the reverse design method which determines the transformer's performance from the dimensions and properties of the materials used. The RDM modelling used a combination of circuit theory and finite element analysis to determine the equivalent circuit components of the Steinmetz transformer circuit. An ac loss model for the high temperature superconducting wire was also developed by the author. The model combined

empirical and theoretical models of different aspects of the ac losses along with time harmonic finite element modelling of the transformer's magnetic field to determine an equivalent resistance for each winding. This method for modelling the ac losses of HTS devices have never before been attempted and represents the core theoretical advance for this thesis.

A computer program was then written that uses the developed model to determine the performance of a high temperature superconducting partial core transformer. The program was used to design a replacement transformer to the prototype that failed. The new design had several aspects in common with the failed prototype including the core and liquid nitrogen containment vessel. The winding design used an improved version of the successfully tested cooling system employed in the full core high temperature superconductor transformer.

The new prototype high temperature superconducting partial core transformer was then built and a series of electrical tests were performed two determine the transformer's performance characteristics. The tests were based, where applicable, on international transformer testing standards. The key operating characteristics were found using open circuit, short circuit and resistive load tests. A linear relationship between the open circuit voltage and current was found indicating that saturation of the core did not occur. The transformer was found to be 98.2 % efficient at full load, with 2.86 % voltage regulation. Additional tests included an insulation resistance test which found a drop in resistance between the dry and wet conditions. An overload test demonstrated the validity of the new insulation design to cool the windings over an extended period under very high loading. The separate source ac withstand voltage test proved the dielectric strength of the insulation system is sufficient for the rated voltage. The fault ride through test showed how the transformer was able to withstand the short circuit forces without damaging the windings.

The tests' results were compared to the modelling. There was good agreement between the measured and the calculated results. The various components of the modelling results were discussed with reference to the current and magnetic field distribution in the winding space, and the limitations to the modelling were examined. The major contributing factor to the HTS losses is believed to be the radial component of the magnetic field around the end winding space of the transformer.

The research contained in this thesis demonstrates that the partial core transformer concept can be used with HTS wires to produce a working power transformer. The concepts introduced such as the RDM for transformer design, the modelling of the transformer performance and the inter-layer insulation design could be used by future users to develop their own HTSPCT designs. The RDM in particular shows great promise in being a useful design tool that can be used by transformer designers in industry today. It enables them to design transformers based on available materials and using specifications such as size and weight as design parameters rather than simply voltages and power ratings of traditional design methods.

The author believes that HTSPCTs used as power transformers will eventually become widespread throughout the world as benefits of reduced size and weight, simplified construction and less materials used see them become a more cost effective solution over traditional designs. Two barriers currently exist that are preventing the commercial viability of the HTSPCT design. Firstly is the availability and cost of the HTS wire which is currently prohibitively expensive and difficult to get in suitable sized lengths for transformer use. HTS wire is a relatively immature technology and the costs and manufacturing difficulties are likely to reduce greatly as the technology matures. Secondly are the losses associated with the radial magnetic field of the PCT affecting the efficiency of the device. This will require more research into how to limit these losses. Some of the possible methods for loss reduction are discussed in Chapter 7 and include 2G HTS wire, radial cores and flux diverters.

REFERENCES

AL-MOSAWI, M., BEDUZ, C., YANG, Y., WEBB, M. AND POWER, A. (2001), 'The Effect of Flux Diverters on AC Losses of a 10 kVA High Temperature Superconducting Demonstrator Transformer', *Applied Superconductivity, IEEE Transactions on*, Vol. 11, No. 1, mar, pp. 2800–2803.

BARDEEN, J., COOPER, L.N. AND SCHRIEFFER, J.R. (1957), 'Theory of Superconductivity', *Phys. Rev.*, Vol. 108, No. 5, Dec, pp. 1175–1204.

BEDNORZ, J.G. AND MÜLLER, K.A. (1986), 'Possible High T_c Superconductivity in the $Ba - La - Cu - O$ System', *Zeitschrift für Physik B Condensed Matter*, Vol. 64, No. 2, pp. 189–193.

BELL, S.C. (2004), 'An Investigation into the Magnetic Performance of a Three-Phase Partial-Core Transformer', *Third Professional Year Project*. University of Canterbury, Christchurch.

BELL, S.C. (2008), *High-voltage Partial-Core Resonant Transformers*, PhD thesis, Univ. of Canterbury, Christchurch, New Zealand.

BELL, S.C. AND BODGER, P.S. (2007), 'Power Transformer Design Using Magnetic Circuit Theory and Finite Element Analysis; A Comparison of Techniques', In *Australasian Universities Power Engineering Conference (AUPEC'07)*, Curtin University of Technology, Perth, Australia, June, pp. 1–6.

BELL, S.C. AND BODGER, P.S. (2008), 'Inductive Reactance Component Model for High-Voltage Partial-Core Resonant Transformers', *Electric Power Applications, IET*, Vol. 2, No. 5, pp. 288–297.

BELL, S.C., ENRIGHT, W.G., TUNSTALL, K. AND BODGER, P.S. (2007), 'Lightning Arc Drawings - Dielectric Barrier Discharges for Artwork', In *15th International Symposium on High Voltage Engineering (ISH'07)*, Ljubljana, Slovenia, Aug.

BERTAGNOLLI, G. (2007), *The ABB approach to short-circuit duty of power transformers*, ABB Management Services Ltd, Transformers, Affolternstrasse 44, 8050 Zurich, Switzerland, 3 ed.

BERTOTTI, G. (1998), 'General Properties of Power Lossses in Soft Ferromagnetic Materials', *Magnetics, IEEE Transactions on*, Vol. 24, No. 1, pp. 621–630.

BODGER, P.S. AND LIEW, M.C. (2002), 'Reverse as-built transformer design method', *International Journal of Electrical Engineering Education*, Vol. 39, No. 1, pp. 42–53.

BODGER, P.S., LIEW, M.C. AND JOHNSTONE, P.T. (2000), 'A Comparison of Conventional and Reverse Transformer Design', In *Australasian Universities Power Engineering Conference (AUPEC'00)*, Brisbane, Australia, Sep, pp. 80–85.

BODGER, P.S., HARPER, D., GAZZARD, M., O'NEILL, M.B. AND ENRIGHT, W.G. (2002a), 'Testing Full-Core and Partial-Core Transformers at Ambient and Cryogenic Temperatures', In *Electricity Engineers' Association of New Zealand Annual Conference (EEA'02)*, Christchurch, New Zealand, June, p. 8.

BODGER, P., HARPER, D., GAZZARD, M., O'NEILL, M. AND ENRIGHT, W. (2002b), 'The performance of Silicon and Amorphous Steel Core, Distrbution Transformers at Ambient and Cryogenic Temperatures', In *Australasian Universities Power Engineering Conference (AUPEC'02)*, Monash University, Melbourne, Australia, Sep - Oct, p. CD.

BODGER, P., HARPER, D., GAZZARD, M., O'NEILL, M. AND ENRIGHT, W. (2002c), 'Towards a Usable Mains Frequency Partial Core Transformer', In *Australasian Universities Power Engineering Conference (AUPEC'02)*, Monash University, Melbourne, Australia, Sep - Oct, p. CD.

BODGER, P.S., ENRIGHT, W.G. AND HO, V. (2005), 'A Low Voltage, Mains Frequency, Partial Core, High Temperature, Superconducting Transformer', In *Australasian Universities Power Engineering Conference (AUPEC'05)*, The University of Tasmania, Hobart, Australia, Sep, p. CD.

BOGLIETTI, A., CAVAGNINO, A., LAZZARI, M. AND PASTORELLI, M. (2003), 'Predicting Iron Losses in Soft Magnetic Materials With Arbitrary Voltage Supply: An Engineering Approach', *Magnetics, IEEE Transactions on*, Vol. 39, No. 2, march, pp. 981–989.

CHEN, X. AND JIN, J. (2009), 'Superconducting Air-Core Transformers and their Electromagnetic Analysis', In *Applied Superconductivity and Electromagnetic Devices, 2009. ASEMD 2009. International Conference on*, sept., pp. 30–33.

CHEW, I. (2010), *Superconducting Transformer Design and Construction*, Master's thesis, Univ. of Canterbury, Christchurch, New Zealand.

COOPER, L.N. (1956), 'Bound Electron Pairs in a Degenerate Fermi Gas', *Phys. Rev.*, Vol. 104, No. 4, Nov, pp. 1189–1190.

Coway, L., Hobl, A., Krischel, D. and Bock, J. (2000), 'Quench testing of HTS Subelements for 13 kA and 600 A Leads Designed to the Specifications for the CERN Large Hadron Collider Project', *Applied Superconductivity, IEEE Transactions on*, Vol. 10, No. 1, march, pp. 1466–1469.

Davies, E.J. (1990), *Conduction and induction heating*, Peter Peregrinus Ltd. for the IET, London, United Kingdom.

Davies, J. and Simpson, P. (1979), *Induction Heating Handbook*, McGraw Hill, 20 Canada Square, London, United Kingdom.

de Azevedo, A.C., Delaiba, A.C., de Oliveira, J.C., Carvalho, B.C. and de S. Bronzeado, H. (2007), 'Transformer Mechanical Stress Caused by External Short-Circuit: A Time Domain Approach', In *International Conference on Power Systems Transients (IPST07)*, Lyon, France, June.

Dolbear, E.A. (1896), 'Report of the Council, Edward Samuel Ritchie', *Proceedings of the American Academy of Arts and Sciences*, Vol. 23, pp. 359–360.

Emery, V.J. (1987), 'Theory of High-T_c Superconductivity in Oxides', *Phys. Rev. Lett.*, Vol. 58, No. 26, Jun, pp. 2794–2797.

Enright, W.G. and Bodger, P.S. (2002), 'Short Time Rated and Protected High Voltage Ac Testing of Generator Stators Using Parallel Resonant Circuits', In *Electricity Engineers' Association of New Zealand Annual Conference (EEA'04)*, Christchurch, New Zealand, June, p. CD.

Faraday, M. (1834), 'Experimental Researches in Electricity. Seventh Series', *Philosophical Transactions of the Royal Society of London*, Vol. 124, pp. 77–122.

Friedman, A., Lukovsky, G., Roitberg, V., Wolfus, Y., Kopansky, F., Kalisky, B. and Yeshurun, Y. (2006), 'Time dependent electric field and E-I curves in Bi-2223 tapes carrying DC currents and exposed to perpendicular AC magnetic fields', *Journal of Physics: Conference Series*, Vol. 43, No. 1, p. 572.

Ginzburg, V.L. and Landau, L.D. (1950), 'On the Theory of Superconductivity', *Zhurnal Éksperimentalnoi i Teoreticheskoi Fiziki*, Vol. 20, pp. 1064–1082.

Gorter, C.J. and Casimir, H.B.G. (1934), '', *Physik. Z*, Vol. 35, p. 963.

Heathcote, M.J. (2007), *J & P Transformer Book*, Newnes, Linacre House, Jordan Hill, Oxford 0X2 8DP, England, 13 ed.

Huo, X.T. (2009), *New Model of Eddy Current Loss Calculation and Application for Partial Core Transformers*, Master's thesis, Univ. of Canterbury, Christchurch, New Zealand.

Jiang, Z. and Amemiya, N. (2004), 'An experimental method for total AC loss measurement of high Tc superconductors', *Superconductor Science and Technology*, Vol. 17, No. 3, pp. 371–379.

Kellers, J., Bäcker, M., Bührer, C., Müller, J., Rath, A., Remke, S. and Wiezoreck, J. (2005), 'Flexible HTS Wires: From Start-Up of a Full-Sized Plant to Industrial Applications', *Applied Superconductivity, IEEE Transactions on*, Vol. 15, No. 2, June, pp. 2522–2525.

Kim, Y.B., Hempstead, C.F. and Strnad, A.R. (1962), 'Critical Persistent Currents in Hard Superconductors', *Physical Review Letters*, Vol. 9, No. 7, pp. 306–309.

Kim, S.H., Kim, W.S., Choi, K.D., Joo, H.G., Hong, G.W., Han, J.H., Lee, H.G., Park, J.H., Song, H.S. and Hahn, S.Y. (2005), 'Characteristic Tests of a 1 MVA Single Phase HTS Transformer With Concentrically Arranged Windings', *Applied Superconductivity, IEEE Transactions -*, Vol. 15, No. 2, pp. 2214–2217.

Kim, J.H., Park, M., Ali, M.H., Cho, J., Sim, K., Kim, S., Kim, H.J., Lee, S.J. and Yu, I.K. (2008), 'Investigation of the Over Current Characteristics of HTS Tapes Considering the Application for HTS Power Devices', *Applied Superconductivity, IEEE Transactions -*, Vol. 18, No. 2, pp. 1139–1142.

Kirtley, J.R. (1990), 'Gap anisotropy in high-T_c superconductors: A unified picture', *Phys. Rev. B*, Vol. 41, No. 10, Apr, pp. 7201–7204.

Kittel, C. (1949), 'Physical Theory of Ferromagnetic Domains', *Reviews of Modern Physics*, Vol. 21, No. 4, Oct, pp. 541–583.

Lapthorn, A.C. and Bodger, P.S. (2009), 'A Comparison Between the Circuit Theory Model and Finite Element Model Reactive Components', In *Australasian Universities Power Engineering Conference (AUPEC'09)*, Adalide, Austrialia, Sep, pp. 1–5.

Lapthorn, A.C., Chew, I., Enright, W.G. and Bodger, P.S. (2011), 'HTS Transformer: Construction Details, Test Results, and Noted Failure Mechanisms', *Power Delivery, IEEE Transactions on*, Vol. 26, No. 1, pp. 394–399.

Leghissa, M., Fischer, B., Roas, B., Jenovelis, A., Wiezoreck, J., Kautz, S. and Neumuller, H.W. (2007), 'Bi-2223 Multifilament Tapes and Multistrand Coniductors for HTS Power Transmission Cables', *Applied Superconductivity, IEEE Transactions -*, Vol. 7, No. 2, pp. 355–358.

Li, X., Hu, G., Long, G., Wu, S. and Zhou, Y. (2008), 'Analysis on Magnetic Field Aimed at Optimal Design of HTS Transformer', In *World Automation Congress (WAC 2008)*, Waikoloa, Hawaii.

LIEW, M.C. (2001), *Reverse Design Transformer Modelling Technique with Particular Application to Partial Core Transformers*, PhD thesis, Univ. of Canterbury, Christchurch, New Zealand.

LIEW, M.C. AND BODGER, P.S. (2001), 'Partial-Core Transformer Design Using Reverse Modelling Techniques', *Electric Power Applications, IEE Proceedings -*, Vol. 148, No. 6, pp. 513–519.

LIEW, M.C. AND BODGER, P.S. (2002), 'Applying a Reverse Design Modelling Technique to Partial Core Transformers', *International Journal of Electrical Engineering Education*, Vol. 22, No. 1, pp. 85–92.

LONDON, F. AND LONDON, H. (1935), 'The Electromagnetic Equations of the Supraconductor', *Proceedings of the Royal Society of London. Series A, Mathematical and Physical Sciences*, Vol. 149, No. 866, pp. 71–88.

LUCIANO, B.A. AND KIMINAMI, C.S. (1997), 'An Amorphous Core Transformer: Design and Experimental Performance', *Materials Science and Engineering: A*, Vol. 226–228, pp. 1079–1082.

LYNCH, K., BODGER, P.S., ENRIGHT, W.G. AND BELL, S.C. (2007), 'Partial Core Transformer for Energisation of High Voltage Arc-Signs', In *XVth International Symposium on High Voltage Engineering*, Ljubljana, Slovenia, Aug, pp. T3–304.

MATSCH, L.W. AND MORGAN, J.D. (1986), *Electromagnetic and Electromechanical Machines*, Harper & Row, Publishers, Inc., 10 East 53rd Street, New York, NY 10022, United States.

MAWATARI, Y., YAMASAKI, H., KOSAKA, S. AND UMEDA, M. (1995), 'Critical current properties and vortex-glass-liquid transition in Ag-sheathed Bi-2223 tapes', *Cryogenics*, Vol. 35, No. 3, pp. 339–354.

MEEROVICH, V., SOKOLOVSKY, V. AND BOCK, J. (1995), 'Quenching in a High-Tc Superconducting Ring', *Applied Superconductivity, IEEE Transactions on*, Vol. 5, No. 1, march, pp. 22–25.

MEISSNER, W. AND OCHSENFELD, R. (1933), 'Ein neuer Effekt bei Eintritt der Supraleitfähigkeit', *Naturwissenschaften*, Vol. 21, No. 44, pp. 787–788.

MOTT, N.F. AND PEIERLS, R. (1937), 'Discussion of the paper by de Boer and Verwey', *Proceedings of the Physical Society*, Vol. 49, No. 4S, p. 72.

NGUYEN, D.N., SASTRY, P.V.P.S.S., ZHANG, G.M., KNOLL, D.C. AND SCHWARTZ, J. (2005), 'AC Loss Measurement With a Phase Difference Between Current and Applied Magnetic Field', *Applied Superconductivity, IEEE Transactions -*, Vol. 15, No. 2, pp. 2831–2834.

O'Neill, M.B., Enright, W.G. and Bodger, P.S. (2000a), 'The Green Transformer; A Liquid Nitrogen Filled Power Transformer', In *Electricity Engineers' Association of New Zealand Annual Conference (EEA'00)*, Auckland, New Zealand, June, pp. 71–75.

O'Neill, M., Enright, W.G. and Bodger, P.S. (2000b), 'Electro-mechanical Testing of a Liquid Nitrogen Filled Power Transformer', In *13th Conference of the Electric Power Supply Industry (CEPSI'00)*, Manila, Philippines, October.

Ong, C.M. (1997), *Dynamic Simulations of Electric Machinery: Using MATLAB/SIMULINK*, Prentice Hall, Upper Saddle River, New Jersey, United States.

Onnes, H.K. (1911), 'On the sudden change in the rate at which the resistance of mercury disappears', *Commun. Phys. Lab. Univ. Leiden*, Vol. 124c, p. 1.

Oomen, M.P. (2000), *AC Loss in Superconducting Tapes and Cables*, PhD thesis, Univ. of Twente, Enschede, The Netherlands.

Oomen, M.P., Nanke, R. and Leghissa, M. (2003), 'Modelling and measurement of ac loss in BSCCO/Ag-tape windings', *Superconductor Science and Technology*, Vol. 15, pp. 339–354.

Pérez, B., Álvarez, A., Suárez, P., Cáceres, D., Ceballos, J., Obradors, X., Granados, X. and Bosch, R. (2003), 'AC Losses in a Toroidal Superconducting Transformer', *Applied Superconductivity, IEEE Transactions on*, Vol. 13, No. 2, june, pp. 2341–2343.

Pleva, E. and Schwenterly, S. (2004), 'Assembly and test of 5/10 MVA HTS transformer', In *Power Engineering Society General Meeting, 2004. IEEE*, june, pp. 1431–1435.

Poole, C., Farach, H. and Creswick, R. (1995), *Superconductivity*, Academic Press, 525 B Street, Suite 1900. San Diego CA 92101-4495. USA.

Rabbers, J.J., ten Haken, B. and ten Kate, H.H.J. (1998), 'Measuring Transport Current Loss of BSCCO/Ag Tapes Exposed to External AC Magnetic Field', *Physica C: Superconductivity*, Vol. 310, No. 1-4, pp. 101–105.

Rabbers, J.J., ten Haken, B., Shevchenko, O.A. and ten Kate, H.H.J. (2001a), 'An Engineering Formula to Describe the AC Loss of BSCCO/Ag Tape', *Applied Superconductivity, IEEE Transactions -*, Vol. 11, No. 1, pp. 2623–2626.

Rabbers, J.J., ten Haken, B. and ten Kate, H.H.J. (2001b), 'Advanced ac loss measurement methods for high-temperature superconducting tapes', *Review of Scientific Instruments*, Vol. 72, No. 5, pp. 2365–2373.

Rose-Innes, A.C. and Rhoderick, E.H. (1978), *Introduction to Superconductivity*, Pergamon Press, Headington Hill Hall, Oxford 0X3 OBW, England.

SCHMIDT, C. (2000), 'Calorimetric ac-loss measurement of high Tc-tapes at 77 K, a new measuring technique', *Cryogenics*, Vol. 40, No. 2, pp. 137–143.

SCHWENTERLY, S.W., MCCONNELL, B.W., DEMKO, J.A., FADNEK, A., HSU, J., LIST, F.A., WALKER, M.S., HAZELTON, D.W., MURRAY, F.S., RICE, J.A., TRAUTWEIN, C.M., SHI, X., FARRELL, R.A., BASCUIIAN, J., HINTZ, R.E., MEHTA, S.P., AVERSA, N., EBERT, J.A., BEDNAR, B.A., NEDER, D.J., MCILHERAN, A.A., MICHEL, P.C., NEMEC, J.J., PLEVA, E.F., SWENTON, A.C., SWETS, W., LONGSWORTH, R.C., JOHNSON, R.C., JONES, R.H., NELSON, J.K., DEGENEFF, R.C. AND SALON, S.J. (1999), 'Performance of a 1-MVA HTS Demonstration Transformer', *Applied Superconductivity, IEEE Transactions* -, Vol. 9, No. 2, pp. 680–684.

SELVAMANICKAM, V., CHEN, Y., XIONG, X., XIE, Y.Y., MARTCHEVSKI, M., RAR, A., QIAO, Y., SCHMIDT, R.M., KNOLL, A., LENSETH, K.P. AND WEBER, C.S. (2009), 'High Performance 2G Wires: From R&D to Pilot-Scale Manufacturing', *Applied Superconductivity, IEEE Transactions* -, Vol. 19, No. 3, pp. 3225–3230.

SHU, Q.S., KITTEL, P., GLAISTER, D. AND HULL, J. (2000), *Advances in Cryogenic Engineering*, Springer, 11 West 42nd Street, New York, NY 10036, United States.

SLEMON, G.R. (1966), *Magnetoelectric Devices: Transducers, Transformers, and Machines*, John Wiley and Sons, Inc., 111 River Street Hoboken, NJ 07030. United States.

SMITH, D.R. AND FICKETT, F.R. (1995), 'Low-Temperature Properties of Silver', *Journal of Research of the National Institute of Standards and Technology*, Vol. 100, No. 2, pp. 119–171.

SONG, M., TANG, Y., CHEN, N., LI, Z. AND ZHOU, Y. (2008), 'Theoretical Analysis and Experiment Research of High Temperature Superconducting Air-Core Transformer', In *Electrical Machines and Systems, 2008. ICEMS 2008. International Conference on*, Wuhan, China, pp. 4394–4397.

STANLEY, W. AND WESTINGHOUSE, JR, G. (1886), 'Induction-Coil', *United States Patent No. 349,611*, Sep.

STANSEL, N.R. (1949), *Induction heating*, McGraw-Hill Book Co., 1221 Avenue of the Americas, New York, NY 10020. United States.

SUÁREZ, P., ÁLVAREZ, A., PÉREZ, B., CÁCERES, D., CORDERO, E. AND CEBALLOS, J.M. (2005), 'Influence of the Shape in the Losses of Solenoidal Air-Core Transformers', *Applied Superconductivity, IEEE Transactions on*, Vol. 15, No. 2, june, pp. 1855–1858.

SURHONE, L.M., TIMPLEDON, M.T. AND MARSEKEN, S.F. (2010), *War of Currents*, VDM Verlag Dr. Müller GmbH & Co. KG, Dudweiler Landstr. 99, 66123 Saarbrcken, Germany.

Sytnikov, V., Vysotsky, V., Radchenko, I. and Polyakova, N. (2007), '1G versus 2G comparison from the practical standpoint for HTS power cables use', In *8th European Conference on Applied Superconductivity (EUCAS 2007)*, Brussels Expo, Belgium, pp. 1–4.

Therond, P.G., Levillain, C., Picard, J.F., Bugnon, B., Zueger, H., Hornfeldt, S., Fogelberg, T., Papst, G. and Bonmann, D. (1998), 'High Temperature 630 kVA Superconducting Transformer', In *Cigré Paris Sessions*, Paris, France.

van Beijnen, C. and Elen, J. (1979), 'Multifilament Nb3Sn superconductors produced by the E.C.N. technique', *Magnetics, IEEE Transactions on*, Vol. 15, No. 1, jan, pp. 87–90.

Weijers, H.W., Hascicek, Y.S. and Sciver, S.W.V. (1995), 'Critical Current, Quench and Stability of a BSCCO/Ag High Field Shim Coil', *Applied Superconductivity, IEEE Transactions on*, Vol. 5, No. 2, june, pp. 499–502.

Weiss, K.P., Schwarz, M., Heller, A.L.R., Fietz, W.H., Nyilas, A., Schlachter, S.I. and Goldacker, W. (2007), 'Electromechanical and Thermal Properties of Bi2223 Tapes', *Applied Superconductivity, IEEE Transactions* -, Vol. 17, No. 2, pp. 3079–3082.

Westinghouse, Jr, G. (1887), 'Electrical Converter', *United States Patent No. 366,362*, July.

Wirgau, K. (1976), 'Inductance calculation of an air-core disk winding', *Power Apparatus and Systems, IEEE Transactions on*, Vol. 95, No. 1, jan., pp. 394–400.

Wu, M.K., Ashburn, J.R., Torng, C.J., Hor, P.H., Meng, R.L., Gao, L., Huang, Z.J., Wang, Y.Q. and Chu, C.W. (1987), 'Superconductivity at 93 K in a New Mixed-Phase $Y-Ba-Cu-O$ Compound System at Ambient Pressure', *Phys. Rev. Lett.*, Vol. 58, No. 9, Mar, pp. 908–910.

Xiao, L., Kiyoshi, T., Ozaki, O. and Wada, H. (1999), 'Case study on quench evolution and passive protection of high Tc superconducting pancake coil', *Cryogenics*, Vol. 39, No. 4, pp. 293–298.

Xiaoping, L., Rupich, M.W., Thieme, C.L.H., Teplitsky, M., Sathyamurthy, S., Thompson, E., Buczek, D., Schreiber, J., DeMoranville, K., Lynch, J., Inch, J., Tucker, D., Savoy, R. and Fleshler, S. (2009), 'The Development of Second Generation HTS Wire at American Superconductor', *Applied Superconductivity, IEEE Transactions on*, Vol. 19, No. 3, june, pp. 3231–3235.

Yamaguchi, H., Kataoka, T. and Sato, Y. (1999), 'Analysis of a 3-Phase Air-Core Superconducting Power Transformer', *Applied Superconductivity, IEEE Transactions on*, Vol. 9, No. 2, june, pp. 1300–1303.

Zhu, Q., Chen, D.X. and Han, Z.H.. (2004), 'Field dependent critical current of Bi-2223/Ag tapes at different thermo-mechanical stages', *Superconductor Science and Technology*, Vol. 17, pp. 756–763.

Zinn, S. and Semiatin, S.L. (1988), *Elements of Induction Heating*, ASM International, Metals Park, Ohio, United States.

Zipernowsky, K., Déri, M. and Bláthy, O.T. (1886), 'Induction-Coil', *United States Patent No. 352,105*, November.

Zirka, S.E., Moroz, Y.I., Marketos, P. and Moses, A.J. (2008), 'Comparison of engineering methods of loss prediction in thin ferromagnetic laminations', *Journal of Magnetism and Magnetic Materials*, Vol. 320, No. 20, May, pp. 2504–2508.

Appendix A

TRANSFORMER DESIGN PROGRAM OUTPUT

This appendix provides details on the output of the transformer design program for the 15 kVA high temperature superconducting partial core transformer. The Figures A.1 through to A.4 show the output from the the various worksheets of the transformer design program. A brief description of each of the variables is given along with the Figures.

A.1 INPUT DATA WORKSHEET

The input data worksheet is where the inputs for the reverse design method is made. It contains the dimensions and properties of the materials used in the design as well as load and supply specifications. Figure A.1 contains the data used for the 15 kVA HTSPCT.

A.1.1 Material Specifications

Core Properties

Core type The core type of the transformer. Options are Core type (a full core transformer), and Partial Core. The shell type full core transformer has not been implemented yet.

Core shape The shape of the limb of the core. Options are Square and Circular.

Core stacking type The lamination stacking orientation. At the time of writing only parallel stacked laminations have been implemented. Radial stacked laminations, (see Chapter 7), are planned to be included in the future.

Lamination thickness The thickness of an individual core lamination in millimeters.

Stacking factor The ratio of core material to lamination insulation.

Relative permeability The relative permeability of the core material used in the modelling.

Resistivity at 20°C The resistivity of the core material at room temperature in ohm meters.

Thermal resistivity coefficient The amount the resistivity of the core material changes in ohm meters per degree Celsius.

Material Specifications

Core Properties

CTP	Core type	Partial-Core	
CS	Core shape	Circular	
CST	Core stacking type	Parallel	
LT	Lamination thickness	0.23	mm
CSF	Stacking factor	0.96	
CUR	Relative permeability	2500	
CR20C	Resistivity at 20°C	47.2E-9	Ω-m
CTRC	Thermal resistivity coefficient	6.0E-3	Ω-m / °C
COT	Operating temperature	-20	°C
CMD	Material density	7650	kg/m³
CMC	Material cost	4	$/kg

Core Dimensions

CSL	Length	470	mm
CSR1	Inner radius	8.2	mm
CSR2	Outer radius	40	mm
CSW1	Width 1 (breadth)	0	mm
CSW2	Width 2 (depth)	0	mm

Former

FM	Material	Composite	
FT	Thickness	17.5	mm

Overall

		Section 1	Section 2	Section 3	Section 4	Section 5	Section 6	Section 7	Section 8	Section 9	Section 10	
WSLE	Length	338	338	338	338	338	338	338	338			mm
WSLS	Layers	1	1	1	1	1	1	1	1			

Wire

		Section 1	Section 2	Section 3	Section 4	Section 5	Section 6	Section 7	Section 8	Section 9	Section 10	
WSMT	Material type	Bi-2223	Bi-2223	Bi-2223	Bi-2223	Bi-2223	Bi-2223	Bi-2223	Bi-2223			
WSS	Shape	Rectangular	Rectangular	Rectangular	Rectangular	Rectangular	Rectangular	Rectangular	Rectangular			
WSWD	Diameter											mm
WSWW1	Radial width	0.305	0.305	0.305	0.305	0.305	0.305	0.305	0.305			mm
WSWW2	Axial width	4.1	4.1	4.1	4.1	4.1	4.1	4.1	4.1			mm
WSWIT	Insulation thickness	0.05	0.05	0.05	0.05	0.05	0.05	0.05	0.05			mm
WSWIRP	Insulation relative permeability	1	1	1	1	1	1	1	1			
WSSF	Stacking factor (axial direction)	1	1	1	1	1	1	1	1			
WSOT	Operating temperature	-196	-196	-196	-196	-196	-196	-196	-196			°C
WSR20C	Resistivity at 20°C (0°C for HTS)	14.7E-9	14.7E-9	14.7E-9	14.7E-9	14.7E-9	14.7E-9	14.7E-9	14.7E-9			Ω-m
WSTRC	Thermal resistivity coefficient	60.0E-12	60.0E-12	60.0E-12	60.0E-12	60.0E-12	60.0E-12	60.0E-12	60.0E-12			Ω-m / °C
WSN77	n-value in self field at 77K	17.26	17.26	17.26	17.26	17.26	17.26	17.26	17.26			
WSSCVF	Superconducting volume fraction	0.85	0.85	0.85	0.85	0.85	0.85	0.85	0.85			
WSCC77	Critical current in self field at 77K	136.7	136.7	136.7	136.7	136.7	136.7	136.7	136.7			A
WSMD	Material density	10500	10500	10500	10500	10500	10500	10500	10500			kg/m³
WSMC	Material cost	1439	1439	1439	1439	1439	1439	1439	1439			$/kg

Inter-layer Insulation

		Section 1	Section 2	Section 3	Section 4	Section 5	Section 6	Section 7	Section 8	Section 9	Section 10	
WSILIT	Thickness	0	0	0	0	0	0	0	0			mm
WSILIO	Circumferential overlap	0	0	0	0	0	0	0	0			mm
WSILIWEO	Winding ends overlap	0	0	0	0	0	0	0	0			mm
WSILIRP	Relative permittivity	1	1	1	1	1	1	1	1			
WSILIMW	Material weight per CSA	0.027	0.027	0.027	0.027	0.027	0.027	0.027	0.027			kg/m²
WSILIMC	Material cost per CSA	250	250	250	250	250	250	250	250			$/m²

Inter-Section Insulation

		Section 1	Section 2	Section 3	Section 4	Section 5	Section 6	Section 7	Section 8	Section 9	Section 10	
WSISIT	Thickness	2	2	2	2	2	2	2	2			mm
WSISIO	Circumferential overlap	0	0	0	0	0	0	0	0			mm
WSISIWEO	Winding ends overlap	25	25	25	25	25	25	25	25			mm
WSISIRP	Relative permittivity	1	1	1	1	1	1	1	1			
WSISIMW	Material weight per CSA	0.027	0.027	0.027	0.027	0.027	0.027	0.027	0.027			kg/m²
WSISIMC	Material cost per CSA	250	250	250	250	250	250	250	250			$/m²

Superconductor Fitting Parameters

		Section 1	Section 2	Section 3	Section 4	Section 5	Section 6	Section 7	Section 8	Section 9	Section 10
WSIcBII	Ic parallel field turning point	0.5335	0.5335	0.5335	0.5335	0.5335	0.5335	0.5335	0.5335		
WSIcBT	Ic perpendicular field turning point	0.0712	0.0712	0.0712	0.0712	0.0712	0.0712	0.0712	0.0712		
WSIcPII	Ic parallel field slope	1.852	1.852	1.852	1.852	1.852	1.852	1.852	1.852		
WSIcPT	Ic perpendicular field slope	1.321	1.321	1.321	1.321	1.321	1.321	1.321	1.321		
WSnBII	n-value parallel field turning point	0.4025	0.4025	0.4025	0.4025	0.4025	0.4025	0.4025	0.4025		
WSnBT	n-value perpendicular field turning point	0.0686	0.0686	0.0686	0.0686	0.0686	0.0686	0.0686	0.0686		
WSnPII	n-value parallel field slope	1.447	1.447	1.447	1.447	1.447	1.447	1.447	1.447		
WSnPT	n-value perpendicular field slope	0.856	0.856	0.856	0.856	0.856	0.856	0.856	0.856		

Winding Connections

	Winding Section	Section 1	Section 2	Section 3	Section 4	Section 5	Section 6	Section 7	Section 8	Section 9	Section 10
PWC	Primary winding connected (Yes/No)	Yes	Yes	Yes	Yes						
SWC	Secondary winding connected (Yes/No)					Yes	Yes	Yes	Yes		

Supply Conditions

Supply Specifications

PV	Voltage	230	V
PVF	Frequency	50	Hz
VSCT	Voltage for short circuit test	24	V

Load Conditions

Load Characteristics

LRE	Load resistance	3.457	Ω
LIM	Load reactance	0.00E+00	Ω

File Locations

MFN	Main file name	15kVA HTS 2nd Gen

Figure A.1   The Input Data Worksheet.

Operating temperature The steady state temperature of the core in degrees Celsius.

Material density The density of the core material in kilograms per cubic meter.

Material cost The cost of the core material in dollars per kilogram.

Core Dimensions

Length The axial length of the core in millimeters.

Inner radius The radius of a hole in the center of a circular core in millimeters. Zero if no hole is present.

Outer radius The radius of a circular core in millimeters.

Width 1 (breadth) The breadth of a rectangular core in millimeters.

Width 2 (depth) The depth of a rectangular core in millimeters.

Former

Material The material of the former.

Thickness The distance from the core the the first winding layer.

Overall

Length The axial length of the winding section in millimeters.

Layers The number of winding layers in that winding section.

Wire

Material type The material used in the winding section. Options are copper, aluminium or Bi2223.

Shape The wire shape of the winding section. Options are rectangular or round.

Diameter The wire diameter for round wire in millimeters.

Radial width The width in the radial direction for rectangular wire in millimeters.

Axial width The width in the axial direction for rectangular wire in millimeters.

Insulation thickness The wire insulation thickness in millimeters.

Insulation relative permeability The relative permeability of the wire insulation in millimeters.

Stacking factor (axial direction) The ratio of wire, wire insulation and air in the axial direction.

Operating temperature Operating temperature of the winding section.

Resistivity at 20°C The resistivity of the wire at room temperature, (0°C for HTS), in degrees Celsius.

Thermal resistivity coefficient The amount the resistivity of the wire changes in ohm meters per degree Celsius.

n-value in self field at 77K The n-value for HTS conductors at 77 Kelvin in self field.

Critical current in self field at 77K The n-value for HTS conductors at 77 Kelvin in self field.

Material density The density of the wire section material in kilograms per cubic meter.

Material cost The cost of the wire section material in dollars per kilogram.

Inter-Layer Insulation

Thickness The radial thickness of the inter-layer insulation for the winding section in millimeters.

Circumferential overlap The amount of circumferential overlap of the inter-layer insulation for the winding section in millimeters.

Winding ends overlap The overlap in the axial direction of the inter-layer insulation for the winding section in millimeters.

Material weight per CSA The weight in kilograms of one square meter of the inter-layer insulation for the winding section.

Material cost per CSA The cost in dollars of one square meter of the inter-layer insulation for the winding section.

Inter-Section Insulation

Thickness The radial thickness of the inter-section insulation for the winding section in millimeters.

Circumferential overlap The amount of circumferential overlap of the inter-section insulation for the winding section in millimeters.

Winding ends overlap The overlap in the axial direction of the inter-section insulation for the winding section in millimeters.

Material weight per CSA The weight in kilograms of one square meter of the inter-section insulation for the winding section.

Material cost per CSA The cost in dollars of one square meter of the inter-section insulation for the winding section.

Superconductor Fitting Parameters

Ic parallel field turning point The fitting parameter $B_\parallel$ from Equation 4.55.

Ic perpendicular field turning point The fitting parameter $B_\perp$ from Equation 4.54.

Ic parallel field slope The fitting parameter $P_\parallel$ from Equation 4.55.

Ic perpendicular field slope The fitting parameter $P_\perp$ from Equation 4.54.

n-value parallel field turning point The fitting parameter for the n-value similar to $B_\parallel$.

n-value perpendicular field turning point The fitting parameter for the n-value similar to $B_\perp$.

n-value parallel field slope The fitting parameter for the n-value similar to $P_\parallel$.

n-value perpendicular field slope The fitting parameter for the n-value similar to $P_\perp$.

A.1.2 Winding Connections

Winding Section

Primary winding connected (Yes/No) Denotes whether the winding section is connected to the primary.

Secondary winding connected (Yes/No) Denotes whether the winding section is connected to the secondary.

A.1.3 Supply Conditions

Supply Specifications

Voltage The rms vale of voltage applied to the primary winding in volts.

Frequency The fundamental frequency of the supply voltage in hertz.

Voltage for short circuit test The rms value of voltage applied to the primary winding during the short circuit test in volts.

A.1.4 Load Conditions

Load Characteristics

Load resistance The value of the resistive component for the loaded test in ohms.

Load reactance The value of the reactive component for the loaded test in ohms. Negative value denotes capacitive loading.

A.1.5   File Locations

Main File Name The filename used for saving the input data sheet when the *Save Data Sheet* routine is run.

A.2   DESIGN REVIEW WORKSHEET

The Design Review Worksheet contains the results from the *Design Calculations & CTM* and *FEM* routines. The inputs for these routines are from the Input Data Worksheet. Figures A.2 and A.3 contain the output for the 15 kVA HTSPCT.

A.2.1   Supply Specifications

Voltage The rms vale of voltage applied to the primary winding in volts.
Frequency The fundamental frequency of the supply voltage in hertz.

A.2.2   Physical Parameters

Core

Core Type The core type of the transformer. Used in size calculations.
Number of laminations The number of laminations based on core size, lamination thickness and stacking factor.
Resistivity The resistivity of the core at the operating temperature in ohm meters.
Cross sectional area The cross sectional area of the core in square meters.
Volume The volume of the core in cubic meters.
Weight The weight of the core in kilograms.
Cost The cost of the core material.
Winding window width The width of the winding area for core type transformers in millimeters. Includes windings, insulation and former thickness.

Winding Sections - Overall

Designation Indicates if the winding section is primary connected (P) or secondary connected (S).
Length The axial length of the winding section in millimeters.
Layers The number of layers in the winding section.

Design Review

Supply Specifications

PVP	Voltage	230	V
F	Frequency	50	Hz

Physical Parameters
Core

CTP2	Core Type	Partial-Core	
CSLN	Number of laminations	333	
CRE	Resistivity	47.2E-9	Ω-m
SCCAA	Cross sectional area	4.6E-3	m^2
CSCV	Volume	2.2E-3	m^3
CSCW	Weight	16.62	kg
CSCC	Cost	66.48	$
WWW	Winding window width	36.74	mm

Winding Sections

	Overall	Section 1	Section 2	Section 3	Section 4	Section 5	Section 6	Section 7	Section 8	Section 9	Section 10	
WSD	Designation	P	P	P	P	S	S	S	S			
WSLS2	Length	338	338	338	338	338	338	338	338			mm
WSL	Layers	1	1	1	1	1	1	1	1			
WST	Thickness	0.405	0.405	0.405	0.405	0.405	0.405	0.405	0.405			mm
WSSPF	Space factor	0.73	0.73	0.73	0.73	0.73	0.73	0.73	0.73			
WSW1	Outside width 1	115.81	120.62	125.43	130.24	135.05	139.86	144.67	149.48			mm
WSW2	Outside width 2	115.81	120.62	125.43	130.24	135.05	139.86	144.67	149.48			
	Wire											
WSTL	Turns per layer	80	80	80	80	80	80	80	80			
WSTT	Turns total	80	80	80	80	80	80	80	80			
WSCSA	Conductor cross sectional area	1.251	1.251	1.251	1.251	1.251	1.251	1.251	1.251			mm2
WSR	Resistivity	78.2E-9	78.2E-9	78.2E-9	78.2E-9	78.2E-9	78.2E-9	78.2E-9	78.2E-9			Ω-m
WSWL	Length	29.01	30.22	31.42	32.63	33.84	35.05	36.26	37.47			m
WSW	Weight	0.38	0.40	0.41	0.43	0.44	0.46	0.48	0.49			kg
WSC2	Cost	548.06	570.90	593.74	616.58	639.42	662.26	685.10	707.94			$
	Inter-layer Insulation											
WSILIL	Length	0.00	0.00	0.00	0.00	0.00	0.00	0.00	0.00			m
WSILIB	Breadth	0.00	0.00	0.00	0.00	0.00	0.00	0.00	0.00			m
WSILIW	Weight	0.00	0.00	0.00	0.00	0.00	0.00	0.00	0.00			kg
WSILIC	Cost	0.00	0.00	0.00	0.00	0.00	0.00	0.00	0.00			$
	Inter-Section Insulation											
WSISIL	Length	0.36	0.38	0.39	0.41	0.42	0.44	0.45				m
WSISIB	Breadth	0.39	0.39	0.39	0.39	0.39	0.39	0.39				m
WSISIW	Weight	3.8E-3	4.0E-3	4.1E-3	4.3E-3	4.4E-3	4.6E-3	4.8E-3				kg
WSISIC	Cost	35.29	36.76	38.22	39.69	41.15	42.62	44.09				$

Primary / Secondary Winding

PWTT	Primary winding total turns	320	
SWTT	Secondary winding total turns	320	
PWL	Primary winding length	123.28	m
SWL	Secondary winding length	142.62	m
WTF	Winding thickness factor	17.24	
AR	Aspect ratio	19.61	
PPW	Mean perimeter of primary winding	385.22	mm
PSW	Mean perimeter of secondary winding	445.67	mm
PSP	Mean perimeter of interwinding space	415.44	mm
PWT	Primary winding thickness	7.62	mm
SWT	Secondary winding thickness	7.62	mm
PST	Interwinding space thickness	2.00	mm

Turns Ratio

PS	Primary / secondary	1	
SP	Secondary / primary	1	

Weight

WTWS	Winding	3.49	kg
WC	Core	16.62	kg
WTI	Insulation	0.03	kg
WO	Other	0.00	kg
WT	Total	20.14	kg

Cost

CTWS	Winding	5023.99	$
CTC2	Core	66.48	$
CTI	Insulation	277.82	$
CTO	Other	0.00	$
CT	Total	5368.30	$

Skin Effect Parameters
Core

LPD	Penetration depth at fundamental frequency	0.31	mm
CMFCP	Maximum frequency for complete flux penetration	361.62	Hz
CSCASD	Cross sectional area (inc. sf and skin depth)	4.6E-3	m^2
CSVEFF	Core effective volume	2.2E-3	m^3

Winding Sections

	Overall	Section 1	Section 2	Section 3	Section 4	Section 5	Section 6	Section 7	Section 8	Section 9	Section 10	
WSPD	Penetration depth at fundamental freq	19.91	19.91	19.91	19.91	19.91	19.91	19.91	19.91			mm
WSEA	Effective cross sectional area	1.25	1.25	1.25	1.25	1.25	1.25	1.25	1.25			mm2
WSMFCRP	Maximum frequency for radial flux penetration	851835.50	851835.50	851835.50	851835.50	851835.50	851835.50	851835.50	851835.50			Hz
WSMFCAP	Maximum frequency for axial flux penetration	4713.98	4713.98	4713.98	4713.98	4713.98	4713.98	4713.98	4713.98			Hz
WSRES	Winding resistance	0.00	0.00	0.00	0.00	0.00	0.00	0.00	0.00			Ω

Core Flux Density

CMB	Maximum flux density from V1 at fundamental frequency	699.92E-3	T
CRB	RMS flux density estimate	494.92E-3	T

Figure A.2   The Design Review Worksheet.

Circuit Theory Model Parameters

LF	Leakage reactance correction factor	0.8748913	
MF	Magnetising reactance correction factor	0.9374371	
LCA	Length of core magnetic flux path	0.470	m
CTMCRU	Core flux reluctance	32.36E+3	1/H
CTMARU	Air flux reluctance at each end	1.37E+6	1/H
CURE	Core effective relative permeability	27.40	
CHL	Core hysteresis loss	42.95	W
KEC	Flux Spreading Factor	0.66	
LPRIME	Flux Spreading Length	29.82	%
RED	Eddy current loss resistance	530.9E+0	Ω

Finite Element Model Parameters

FEMLTE	Leakage flux (energy method)	0.00099975	H

Permeance Matrix

		Section 1	Section 2	Section 3	Section 4	Section 5	Section 6	Section 7	Section 8	Section 9	Section 10
FEMPM	Section 1	4.0993E-07	4.0764E-07	4.0525E-07	4.0287E-07	4.0050E-07	3.9812E-07	3.9575E-07	3.9338E-07		
	Section 2	4.0764E-07	4.0843E-07	4.0612E-07	4.0373E-07	4.0133E-07	3.9894E-07	3.9656E-07	3.9417E-07		
	Section 3	4.0525E-07	4.0612E-07	4.0703E-07	4.0471E-07	4.0229E-07	3.9989E-07	3.9749E-07	3.9509E-07		
	Section 4	4.0287E-07	4.0373E-07	4.0471E-07	4.0572E-07	4.0339E-07	4.0096E-07	3.9854E-07	3.9613E-07		
	Section 5	4.0050E-07	4.0133E-07	4.0229E-07	4.0339E-07	4.0452E-07	4.0217E-07	3.9973E-07	3.9730E-07		
	Section 6	3.9812E-07	3.9894E-07	3.9989E-07	4.0096E-07	4.0217E-07	4.0341E-07	4.0105E-07	3.9859E-07		
	Section 7	3.9575E-07	3.9656E-07	3.9749E-07	3.9854E-07	3.9973E-07	4.0105E-07	4.0240E-07	4.0003E-07		
	Section 8	3.9338E-07	3.9417E-07	3.9509E-07	3.9613E-07	3.9730E-07	3.9859E-07	4.0003E-07	4.0150E-07		
	Section 9										
	Section 10										

Inductance Matrix

		Section 1	Section 2	Section 3	Section 4	Section 5	Section 6	Section 7	Section 8	Section 9	Section 10
FEMIM	Section 1	0.00262355	0.00260887	0.00259363	0.0025784	0.00256318	0.00254966	0.002532773	0.002517603		
	Section 2	0.00260887	0.00261396	0.00259919	0.00258384	0.00256852	0.00255228	0.002537957	0.002522715		
	Section 3	0.00259363	0.00259919	0.00260498	0.00259012	0.00257468	0.00259275	0.00254391	0.002528581		
	Section 4	0.0025784	0.00258384	0.00259012	0.00259663	0.00258168	0.00266143	0.002550662	0.00253523		
	Section 5	0.00256318	0.00256852	0.00257468	0.00258168	0.0025889	0.00273871	0.002558249	0.002542693		
	Section 6	0.00254797	0.00255323	0.00255928	0.00256614	0.00257387	0.00281819	0.002566712	0.002551005		
	Section 7	0.00253277	0.00253796	0.00254391	0.00255066	0.00255825	0.00266712	0.002575386	0.002560206		
	Section 8	0.0025176	0.00252271	0.00252858	0.00253523	0.00254269	0.002551005	0.002560206	0.002569608		
	Section 9										
	Section 10										

Coupling matrix

		Section 1	Section 2	Section 3	Section 4	Section 5	Section 6	Section 7	Section 8	Section 9	Section 10
FEMKM	Section 1	1	0.9962258	0.9921115	0.98787102	0.98350278	0.97900683	0.974384153	0.969636409		
	Section 2	0.99622581	1	0.99605912	0.99177154	0.98736134	0.982826799	0.978167993	0.973385874		
	Section 3	0.99211147	0.99605908	1	0.99589173	0.99143085	0.986851062	0.982150544	0.977329281		
	Section 4	0.98787104	0.99177155	0.99589176	1	0.99572424	0.99109013	0.986340945	0.981474825		
	Section 5	0.98350271	0.98736128	0.99143089	0.99572426	1	0.995556857	0.990749704	0.985831621		
	Section 6	0.97900687	0.98282684	0.98685115	0.99109016	0.99555682	1	0.99538961	0.9904098		
	Section 7	0.97438421	0.97816802	0.98215065	0.98634107	0.99074974	0.995389657	1	0.99522275		
	Section 8	0.96963642	0.9733858	0.97732929	0.98147487	0.98583156	0.990409824	0.995222784	1		
	Section 9										
	Section 10										

Primary / Secondary winding reluctances

PWTFR	Primary winding total flux reluctance	24.07	1/H
PWLFR	Primary winding leakage flux reluctance	1310.41	1/H
SWTFR	Secondary winding total flux reluctance	24.38	1/H
SWLFR	Secondary winding leakage flux reluctance	4217.58	1/H
PSMFR	Primary / secondary mutual flux reluctance	24.52	1/H

Primary / Secondary winding inductances and coupling

PWSI	Primary winding self inductance	0.04154721	H
SWSI	Secondary winding self inductance	0.04102119	H
MIPS	Primary - secondary mutual inductance	0.0407841	H
PSK	Primary - secondary coupling	0.98790633	

Equivalent Circuit Parameters

a	Turns ratio	1	
PR1	Primary resistance at fundamental frequency	17.0E-3	Ω
SR2	Secondary resistance at fundamental frequency	17.0E-3	Ω
aaR2	Secondary resistance referred to primary	17.0E-3	Ω

Circuit Theory Model

CTMRH	Hysteresis loss resistance	1.2E+3	Ω
CTMRC	Core loss resistance	367.1E+0	Ω
CTMX1	Primary leakage reactance	201.1E-3	Ω
CTMX2	Secondary leakage reactance	201.1E-3	Ω
CTMaaX2	Secondary leakage reactance referred to primary	201.1E-3	Ω
CTMXLT	Total leakage reactance referred to primary	402.1E-3	Ω
CTMXM	Magnetising reactance	11.621E+0	Ω

Finite Element Model

FEMRH	Hysteresis loss resistance	1.2E+3	Ω
FEMRC	Core loss resistance	367.1E+0	Ω
FEMX1	Primary leakage reactance	239.7E-3	Ω
FEMX2	Secondary leakage reactance	74.5E-3	Ω
FEMaaX2	Secondary leakage reactance referred to primary	74.5E-3	Ω
FEMXLT	Total leakage reactance referred to primary S&M Method	314.2E-3	Ω
FEMXLTE	Total leakage reactance referred to primary energy method	314.1E-3	Ω
FEMXLTD	Difference between leakage inductance methods	0.05	%
FEMXM	Magnetising reactance	12.81E+0	Ω
FEMRUN	Has finite element model been run?	1	

High Temperature Superconductor Losses

		Section 1	Section 2	Section 3	Section 4	Section 5	Section 6	Section 7	Section 8	Section 9	Section 10	
WSQML_II	Magnetisation Loss Parallel Field	17.3E-3	440.7E-3	1.3E+0	2.3E+0	2.5E+0	1.6E+0	671.2E-3	114.5E-3			W
WSQML_T	Magnetisation Loss Perpendicular Field	5.0E+0	5.0E+0	4.6E+0	4.3E+0	3.9E+0	3.7E+0	3.4E+0	3.2E+0			W
WSQDR_II	Dynamic Resistance Parallel Field	244.3E-3	801.0E-3	1.4E+0	2.1E+0	2.0E+0	1.5E+0	968.7E-3	486.7E-3			W
WSQDR_T	Dynamic Resistance Perpendicular Field	7.8E+0	7.9E+0	7.8E+0	7.7E+0	6.8E+0	6.7E+0	6.7E+0	6.6E+0			W
WSQRL	Resistive Loss	9.2E-3	8.8E-3	7.9E-3	7.0E-3	3.8E-3	3.3E-3	2.9E-3	2.5E-3			W
WSQSF	Self Field Loss	4.5E+0	4.6E+0	4.8E+0	5.0E+0	4.7E+0	4.9E+0	5.0E+0	5.1E+0			W
WSQ	Total AC Loss	17.6E+0	18.8E+0	20.0E+0	21.4E+0	20.0E+0	18.4E+0	16.7E+0	15.5E+0			W

Figure A.3   The Design Review Worksheet continued.

Thickness The radial thickness of the winding section in millimeters.

Space factor the ratio of conductor to insulation in the winding section.

Outside width 1 The outer breadth of the winding section for square core transformers in millimeters. Outer diameter for circular cores.

Outside width 2 The outer width of the winding section for square core transformers in millimeters. Outer diameter for circular cores.

Winding Sections - Wire

Turns per layer The number of turns per layer of the winding section.

Turns total The total number of turns in that winding section.

Conductor cross sectional area The cross sectional area of the wire in winding section in square millimeters.

Resistivity The resistivity of the wire in winding section at the operating temperature in ohm meters.

Length The length of the wire in the winding section in meters.

Weight The weight of the wire in the winding section in kilograms.

Cost The cost of the wire in the winding section in dollars.

Winding Sections - Inter-Layer Insulation

Length The circumferential length of the inter-layer insulation for the winding section in meters .

Breadth The breadth of the inter-layer insulation for the winding section in meters.

Weight The weight of the inter-layer insulation for the winding section in kilograms.

Cost The cost of the inter-layer insulation for the winding section in dollars.

Winding Sections - Inter-Section Insulation

Length The circumferential length of the inter-section insulation for the winding section in meters .

Breadth The breadth of the inter-section insulation for the winding section in meters.

Weight The weight of the inter-section insulation for the winding section in kilograms.

Cost The cost of the inter-section insulation for the winding section in dollars.

Primary / Secondary Winding

Primary winding total turns The total number of turns of the primary connected windings.

Secondary winding total turns The total number of turns of the secondary connected windings.

Primary winding length The total length of wire of the primary connected winding in meters.

Secondary winding length The total length of wire of the secondary connected winding in meters.

Winding thickness factor The radial thickness of the windings and insulation.

Aspect ratio Ratio of the maximum axial height of the windings and the winding thickness factor.

Mean perimeter of primary winding The average circumferential length of the primary winding in millimeters. Parameter l_1 in Figure 4.5.

Mean perimeter of secondary winding The average circumferential length of the secondary winding in millimeters. Parameter l_2 in Figure 4.5.

Mean perimeter of interwinding space The average circumferential length of the interwinding space in millimeters. Parameter $l_1 2$ in Figure 4.5.

Primary winding thickness The radial thickness of the primary winding and insulation in millimeters. Parameter d_1 in Figure 4.5.

Secondary winding thickness The radial thickness of the secondary winding and insulation in millimeters. Parameter d_2 in Figure 4.5.

Interwinding space thickness The radial thickness of the inter-winding space in millimeters. Parameter Δd in Figure 4.5.

Turns Ratio

Primary / secondary The ratio between the primary winding total turns and the secondary winding total turns. Referred to as a in the thesis.

Secondary / primary The ratio between the secondary winding total turns and the primary winding total turns.

Weight

Winding The total weight of the winding material in kilograms.

Core The total weight of the core material in kilograms.

Insulation The total weight of the winding insulation material in kilograms.

Other The total weight of any other materials used in the transformer in kilograms.

Total The total weight of the transformer materials in kilograms.

Cost

Winding The total cost of the winding material in dollars.

Core The total cost of the core material in dollars.

Insulation The total cost of the winding insulation material in dollars.

Other The total cost of any other materials used in the transformer in dollars.

Total The total cost of the transformer materials in dollars.

A.2.3 Skin Effect Parameters

Core

Penetration depth at fundamental frequency The distance of one skin depth in the core
laminations at the fundamental frequency in millimeters.

Maximum frequency for complete flux penetration The maximum frequency of "uniform
flux density" in the core lamination in Hertz.

Cross sectional area (inc. sf and skin depth) The effective cross sectional area of the core
taking into account the stacking factor and skin depth in square meters.

Core effective volume The effective volume of the core taking into account the stacking factor
and skin depth in meters cubed.

Winding Sections - Overall

Penetration depth at fundamental freq The distance of one skin depth in the winding sec-
tion material at the fundamental frequency in millimeters.

Effective cross sectional area The effective cross sectional area of the winding section ma-
terial taking into account the skin depth in square millimeters.

Maximum frequency for radial flux penetration The maximum frequency for "uniform
flux density" in the radial direction of winding section material in Hertz.

Maximum frequency for axial flux penetration The maximum frequency for "uniform flux
density" in the axial direction of winding section material in Hertz.

Winding resistance The effective winding section resistance taking into account skin effect in
ohms.

A.2.4 Core Flux Density

Maximum flux density from V_1 at fundamental frequency The maximum flux density
in the core at the fundamental frequency in tesla.

RMS flux density estimate The estimated rms flux density in the core at the fundamental frequency in tesla.

A.2.5   Circuit Theory Model Parameters

Leakage reactance correction factor The factor calculated from Equation 4.49.

Magnetising reactance correction factor The factor calculated from Equation 4.48.

Length of core magnetic flux path The length of the magnetic flux path through the core material in meters.

Core flux reluctance The magnetic reluctance of the core in turns per henry.

Air flux reluctance at each end The magnetic reluctance of the air path for partial-cores in turns per henry.

Core effective relative permeability The effective relative permeability of the magnetic flux path taking into account the air flux reluctance.

Core hysteresis loss The hysteresis losses in the core at the supply voltage in watts.

Flux Spreading Factor The factor L' calculated from Equation 4.7.

Flux Spreading Length The factor K_{ec} calculated from Equation 4.8.

Eddy current loss resistance The equivalent resistance R_{ec} for eddy current losses in ohms.

A.2.6   Finite Element Model Parameters

Leakage flux (energy method) The leakage flux using the energy method given in [Bell 2008].

Permeance Matrix The permeance matrix $\mathbf{P}$ defined in Equation 4.40.

Inductance Matrix The inductance matrix $\mathbf{L}$ defined in Equation 4.41.

Coupling matrix A matrix of the magnetic coupling between winding sections.

Primary / Secondary winding reluctances

Primary winding total flux reluctance The magnetic reluctance of the primary winding in turns per henry.

Primary winding leakage flux reluctance The leakage flux reluctance of the primary winding in turns per henry.

Secondary winding total flux reluctance The magnetic reluctance of the secondary winding in turns per henry.

Secondary winding leakage flux reluctance The leakage flux reluctance of the secondary winding in turns per henry.

Primary / secondary mutual flux reluctance The mutual flux reluctance between the primary winding and the secondary winding in turns per henry.

Primary / Secondary winding inductances and coupling

Primary winding self inductance The self inductance L_P of the primary winding in henrys.

Secondary winding self inductance The self inductance L_S of the secondary winding in henrys.

Primary - secondary mutual inductance The mutual inductance M_{PS} between the primary winding and the secondary winding in henrys.

Primary - secondary coupling The coupling between the primary winding and the secondary winding.

A.2.7 Equivalent Circuit Parameters

Turns Ratio The ratio between the primary winding total turns and the secondary winding total turns. Referred to as a in the thesis.

Primary resistance at fundamental frequency Equivalent resistance R_1 of the primary winding.

Secondary resistance at fundamental frequency Equivalent resistance R_2 of the secondary winding.

Secondary resistance referred to primary The equivalent resistance of the secondary winding referred to the primary $a^2 R_2$.

Circuit Theory Model

Hysteresis loss resistance The equivalent resistance R_h for the hysteresis losses in ohms.

Core loss resistance The equivalent resistance R_c for the total core losses in ohms.

Primary leakage reactance The equivalent leakage reactance X_1 for the primary winding in ohms.

Secondary leakage reactance The equivalent leakage reactance X_2 for the secondary winding in ohms.

Secondary leakage reactance referred to primary The equivalent leakage reactance $a^2 X_2$ for the secondary winding referred to the primary winding in ohms.

Total leakage reactance referred to primary The total leakage reactance X_{12} referred to the primary winding in ohms.

Magnetising reactance The equivalent magnetising reactance X_m in ohms.

Finite Element Model

Hysteresis loss resistance The equivalent resistance R_h for the hysteresis losses in ohms.

Core loss resistance The equivalent resistance R_c for the total core losses in ohms.

Primary leakage reactance The equivalent leakage reactance X_1 for the primary winding in ohms.

Secondary leakage reactance The equivalent leakage reactance X_2 for the secondary winding in ohms.

Secondary leakage reactance referred to primary The equivalent leakage reactance $a^2 X_2$ for the secondary winding referred to the primary winding in ohms.

Total leakage reactance referred to primary S&M Method The total leakage reactance X_{12} referred to the primary winding in ohms using the series mutual method described in Chapter 4.

Total leakage reactance referred to primary energy method The total leakage reactance X_{12} referred to the primary winding in ohms using the series mutual method described in [Bell 2008].

Difference between leakage inductance methods The percentage difference between the series mutual method and the energy method.

Magnetising reactance The equivalent magnetising reactance X_m in ohms.

Has finite element model been run? Variable to check if the FEM routine was run. 0 means not run 1 means has been run.

A.2.8   High Temperature Superconductor Losses

Magnetisation Loss Parallel Field The magnetisation losses for the winding section calculated using Equation 4.69 in a parallel field in watts.

Magnetisation Loss Perpendicular Field The magnetisation losses for the winding section calculated using Equation 4.69 in a perpendicular field in watts.

Dynamic Resistance Parallel Field The dynamic resistance losses for the winding section calculated using Equation 4.64 in a parallel field in watts.

Dynamic Resistance Perpendicular Field The dynamic resistance for the winding section calculated using Equation 4.65 in a perpendicular field in watts.

Resistive Loss The resistive losses for the winding section calculated using Equation 4.62 in watts.

Self Field Loss The self field losses for the winding section calculated using Equation 4.67 in watts.

Total AC Loss The total ac losses for the winding section calculated using Equation 4.50 in watts.

A.3   TEST RESULTS WORKSHEET

The Test Results Worksheet contains the results from the *Test Results* routine. This solves the steinmetz equivalent circuit for various load conditions. The *HTS Model* routine also writes to this worksheet updating it with the HTS ac losses. Figure A.4 contains the output for the 15 kVA HTSPCT.

A.3.1   Open Circuit Performance

Primary winding voltage The rms value of the primary winding terminal voltage under open circuit conditions in volts.

Secondary winding voltage The rms value of the secondary winding terminal voltage under open circuit conditions in volts.

Magnetising current The rms value of the primary winding current under open circuit conditions in amps.

Primary current's phase The phase angle of the primary winding current under open circuit conditions with respect to the voltage in degrees.

Volt-amperes The apparent power from the supply under open circuit conditions in volt-amperes.

Real power The real power from the supply under open circuit conditions in watts.

Power factor The power factor on the supply side under open circuit conditions.

Equivalent parallel resistance The equivalent parallel resistance to draw the calculated current from the supply in ohms.

Equivalent parallel reactance The equivalent parallel reactance to draw the calculated current from the supply in ohms.

Primary winding real power The real power dissipated in the primary winding in watts.

Secondary winding real power The real power dissipated in the secondary winding in watts.

Core real power The real power dissipated in the core in watts.

A.3.2   Short Circuit Performance

Primary winding voltage The rms value of the primary winding terminal voltage under short circuit conditions in volts.

Primary winding current The rms value of the primary winding current under short circuit conditions in amps.

Primary current's phase The phase angle of the primary winding current under short circuit conditions with respect to the voltage in degrees.

Test Results - Finite Element Method

Open Circuit Performance

FOCPV	Primary winding voltage	230.0E+0	V
FOCSV	Secondary winding voltage	225.8E+0	V
FOCMC	Magnetising current	17.6E+0	A
FOCPCP	Primary current's phase	-88.0E+0	deg
FOCVA	Volt-amperes	4.1E+3	VA
FOCP	Real power	144.1E+0	W
FOCPF	Power factor	0.04	

FOCEPRE	Equivalent parallel resistance	367.07	Ω
FOCEPIM	Equivalent parallel reactance	13.05	Ω

FOCPWRP	Primary winding real power	38.0E+0	W	21.50 %
FOCSWRP	Secondary winding real power	000.0E+0	W	0.00 %
FOCCRP	Core real power	138.7E+0	W	78.50 %

Short Circuit Performance

FSCPWV	Primary winding voltage	24.0E+0	V
FSCPWC	Primary winding current	76.0E+0	A
FSCPCP	Primary current's phase	-83.8E+0	deg
FSCSWC	Secondary winding current	75.6E+0	A
FSCSCP	Secondary current's phase	-83.8E+0	deg
FSCVA	Volt-amperes	1.8E+3	VA
FSCRP	Real power	195.5E+0	W
FSCPF	Power factor	0.11	

FSCESRE	Equivalent series resistance	33.8E-3	Ω
FSCESIM	Equivalent series reactance	313.8E-3	Ω

FSCPWRP	Primary winding real power	39.6E+0	W	50.50 %
FSCSWRP	Secondary winding real power	38.7E+0	W	49.39 %
FSCCRP	Core real power	87.9E-3	W	0.11 %

Loaded Circuit Performance

FLCPWV	Primary winding voltage	230.0E+0	V
FLCPWC	Primary winding current	67.7E+0	A
FLCVA	Volt-amperes	15.6E+3	VA
FLCRP	Real power	14.6E+3	W
FLCPF	Power factor	0.94	

FLCESRE	Equivalent series resistance	3.2E+0	Ω
FLCESIM	Equivalent series reactance	1.2E+0	Ω

Voltages

FPTV	Primary terminal voltage	230.0E+0	V
FPVPT	Primary voltage per turn	718.8E-3	V
FPVPIL	Primary voltage per insulation layer	115.0E+0	V
FPVIG	Insulation gradient	57.5E+0	V/mm
FPVR2S	Referred to secondary	230.0E+0	V

FIRTP	Internal referred to primary	223.87	Ω
FIRTS	Internal referred to secondary	223.87	Ω

FSTV	Secondary terminal voltage	222.7E+0	V
FSVPT	Secondary voltage per turn	696.0E-3	V
FSVPIL	Secondary voltage per insulation layer	111.4E+0	V
FSVIG	Insulation gradient	55.7E+0	V/mm
FSVR2P	Referred to primary	222.7E+0	V

FPSTR	Primary/secondary terminal ratio	1.03	
FSPTR	Secondary/primary terminal ratio	0.97	
FVR	Voltage regulation	3.27	%

Currents and Densities

FPWC	Primary winding current	67.7E+0	A
FPCP	Primary winding current's phase	-20.0E+0	deg
FPWCSA	Primary winding cross sectional area	1.25	mm^2
FPWCD	Primary winding current density	54.14	A/mm^2

FSWC	Secondary winding current	64.4E+0	A
FSCP	Secondary winding current's phase	-5.0E+0	deg
FSWCSA	Secondary winding cross sectional area	1.25	mm^2
FSWCD	Secondary winding current density	51.52	A/mm^2

Power Generation

FPGC	Core	136.5E+0	W	0.93 %
FPGPW	Primary winding	77.8E+0	W	0.53 %
FPGSW	Secondary winding	70.6E+0	W	0.48 %
FPGL	Load	14.3E+3	W	98.05 %

FPGT	Total	14.6E+3	W
FEOT	Efficiency of transfer	98.05	%

Real Power Densities

FRPDCSA	Core surface area	927.7E+0	W/m^2
FRPDPWSA	Primary winding surface area	71.7E+0	W/m^2
FRPDSWSA	Secondary winding surface area	56.2E+0	W/m^2

FRPDCV	Core volume	62.8E+3	W/m^3
FRPDPWV	Primary winding volume	504.8E+3	W/m^3
FRPDSWV	Secondary winding volume	395.9E+3	W/m^3

FRPDCW	Core weight	8.2E+0	W/kg
FRPDPWW	Primary winding weight	48.1E+0	W/kg
FRPDSWW	Secondary winding weight	37.7E+0	W/kg

FRPDTLV	Total loss/volume	113.7E+3	W/m^3
FRPDTLW	Total loss/weight	14.2E+0	W/kg
FRPDTLC	Total loss/cost	53.1E-3	W/$

FRPDTSV	Total supply/volume	5.8E+6	W/m^3
FRPDTSW	Total supply/weight	727.6E+0	W/kg
FRPDTSC	Total supply/cost	2.7E+0	W/$

Apparent Power Densities

FAPDCSA	Core surface area	103.0E+3	VA/m^2
FAPDPWSA	Primary winding surface area	14.3E+3	VA/m^2
FAPDSWSA	Secondary winding surface area	11.4E+3	VA/m^2

FAPDCV	Core volume	7.0E+6	VA/m^3
FAPDPWV	Primary winding volume	101.0E+6	VA/m^3
FAPDSWV	Secondary winding volume	80.5E+6	VA/m^3

FAPDCW	Core weight	911.9E+0	VA/kg
FAPDPWW	Primary winding weight	9.6E+3	VA/kg
FAPDSWW	Secondary winding weight	7.7E+3	VA/kg

FAPDTSV	Total supply/volume	6.2E+6	VA/m^3
FAPDTSW	Total supply/weight	774.2E+0	VA/kg
FAPDTSC	Total supply/cost	2.9E+0	VA/$

Figure A.4   The Test Results Worksheet.

Secondary winding current The rms value of the secondary winding current under short circuit conditions in amps.

Secondary current's phase The phase angle of the secondary winding current under short circuit conditions referred to the primary in degrees.

Volt-amperes The apparent power from the supply under short circuit conditions in volt-amperes.

Real power The real power from the supply under short circuit conditions in watts.

Power factor The power factor on the supply side under short circuit conditions.

Equivalent series resistance The equivalent series resistance to draw the calculated current from the supply in ohms.

Equivalent series reactance The equivalent series reactance to draw the calculated current from the supply in ohms.

Primary winding real power The real power dissipated in the primary winding in watts.

Secondary winding real power The real power dissipated in the secondary winding in watts.

Core real power The real power dissipated in the core in watts.

A.3.3 Loaded Circuit Performance

Primary winding voltage The rms value of the primary winding terminal voltage under loaded conditions in volts.

Primary winding current The rms value of the primary winding current under loaded conditions in amps.

Volt-amperes The apparent power from the supply under loaded conditions in volt-amperes.

Real power The real power from the supply under loaded conditions in watts.

Power factor The power factor on the supply side under loaded conditions.

Equivalent series resistance The equivalent series resistance to draw the calculated current from the supply in ohms.

Equivalent series reactance The equivalent series reactance to draw the calculated current from the supply in ohms.

A.3.4 Voltages

Primary terminal voltage The rms value of the primary winding terminal voltage under loaded conditions in volts.

Primary voltage per turn The rms value of the primary winding voltage per turn in volts.

Primary voltage per insulation layer The rms value of the maximum voltage per insulation layer in volts for the primary winding.

Insulation gradient The maximum electric field experienced by the primary winding insulation in volts per millimeter.

Referred to secondary The primary voltage referred to the secondary in volts.

Internal referred to primary The rms value of the internal induced voltage referred to the primary winding.

Internal referred to secondary The rms value of the internal induced voltage referred to the secondary winding.

Secondary terminal voltage The rms value of the secondary winding terminal voltage under loaded conditions in volts.

Secondary voltage per turn The rms value of the secondary winding voltage per turn in volts.

Secondary voltage per insulation layer The rms value of the maximum voltage per insulation layer in volts for the secondary winding.

Insulation gradient The maximum electric field experienced by the secondary winding insulation in volts per millimeter.

Referred to primary The secondary voltage referred to the primary in volts.

Primary/secondary terminal ratio The ratio of the primary to secondary terminal voltage.

Secondary/primary terminal ratio The ratio of the secondary to primary terminal voltage.

Voltage regulation The percentage voltage regulation of the transformer under loaded conditions.

A.3.5   Currents and Densities

Primary winding current The rms value of the primary winding current under loaded conditions in amps.

Primary winding current's phase The phase angle of the primary winding current under loaded conditions with respect to the voltage in degrees.

Primary winding cross sectional area The cross sectional area of the primary winding wire in square millimeters.

Primary winding current density The current density in the primary winding in amps per square millimeter.

Secondary winding current The rms value of the secondary winding current under loaded conditions in amps.

Secondary winding current's phase The phase angle of the secondary winding current under loaded conditions referred to the primary in degrees.

Secondary winding cross sectional area The cross sectional area of the secondary winding wire in square millimeters.

Secondary winding current density The current density in the secondary winding in amps per square millimeter.

A.3.6   Power Generation

Core The real power dissipated in the core in watts.

Primary winding The real power dissipated in the primary winding in watts.

Secondary winding The real power dissipated in the secondary winding in watts.

Load The real power dissipated in the load in watts.

Total The total real power drawn from the supply in watts.

Efficiency of transfer The percentage of power delivered to the load from the supply.

A.3.7   Real Power Densities

Core surface area The power dissipated in the core over the surface area of the core in watts per square meter.

Primary winding surface area The power dissipated in the primary winding over the surface area of the primary winding in watts per square meter.

Secondary winding surface area The power dissipated in the secondary winding over the surface area of the secondary winding in watts per square meter.

Core volume The power dissipated in the core over the volume of the core in watts per meter cubed.

Primary winding volume The power dissipated in the primary winding over the volume of the primary winding in watts per meter cubed.

Secondary winding volume The power dissipated in the secondary winding over the volume of the secondary winding in watts per meter cubed.

Core weight The power dissipated in the core over the weight of the core in watts per kilogram.

Primary winding weight The power dissipated in the primary winding over the weight of the primary winding in watts per kilogram.

Secondary winding weight The power dissipated in the secondary winding over the weight of the secondary winding in watts per kilogram.

Total loss/volume The total power dissipated in the transformer over the volume of the transformer in watts per meter cubed.

Total loss/weight The total power dissipated in the transformer over the weight of the transformer in watts per kilogram.

Total loss/cost The total power dissipated in the transformer over the cost of the transformer in watts per dollars.

Total supply/volume The total real power supplied in the transformer over the volume of the transformer in watts per meter cubed.

Total supply/weight The total real power supplied in the transformer over the weight of the transformer in watts per kilogram.

Total supply/cost The total real power supplied in the transformer over the cost of the transformer in watts per dollars.

A.3.8   Apparent Power Densities

Core surface area The apparent power in the core over the surface area of the core in volt-amps per square meter.

Primary winding surface area The apparent power in the primary winding over the surface area of the primary winding in volt-amps per square meter.

Secondary winding surface area The apparent power in the secondary winding over the surface area of the secondary winding in volt-amps per square meter.

Core volume The apparent power in the core over the volume of the core in volt-amps per meter cubed.

Primary winding volume The apparent power in the primary winding over the volume of the primary winding in volt-amps per meter cubed.

Secondary winding volume The apparent power in the secondary winding over the volume of the secondary winding in volt-amps per meter cubed.

Core weight The apparent power in the core over the weight of the core in volt-amps per kilogram.

Primary winding weight The apparent power in the primary winding over the weight of the primary winding in volt-amps per kilogram.

Secondary winding weight The apparent power in the secondary winding over the weight of the secondary winding in volt-amps per kilogram.

Total supply/volume The total apparent power supplied in the transformer over the volume of the transformer in volt-amps per meter cubed.

Total supply/weight The total apparent power supplied in the transformer over the weight of the transformer in volt-amps per kilogram.

Total supply/cost The total apparent power supplied in the transformer over the cost of the transformer in volt-amps per dollars.

Appendix B

EXAMPLE TAILGATE FOR HTSPCT TESTING

College of Engineering

Laboratory Class Safety Sheet

This sheet must be completed at the beginning of *every* laboratory exercise

The purpose of this sheet is to teach and ensure safe practise by asking you to
1. understand the experiment you are about to perform,
2. identify the hazards involved,
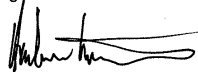3. determine how to manage these hazards safely.

Experiment name: _HTSPCT Testing_   Date: _13-10-11_

In the spaces provided below list the hazards you have identified and the appropriate control measures for managing them. Each hazard may need more than one control.

Hazard (EXAMPLES)	Controls (Precautions)
Nitric acid - could cause burns to skin and eyes	Eye protection, gloves, eyewash
Drill - Chuck key left in chuck - a missile	Check key removed before switching drill on
Noise - Hearing damage	Hearing protection
Electricity - shock	Current permit

Hazard	Controls (Precautions)
Handling liquid nitrogen	Use PPE (covered arms, gloves, faceshield)
Asphyxiation	Vent nitrogen Outside, if Dewar fails leave Lab
Single phase up to 400 Vac / exposed terminals	Isolate Earth prior to touch / Emergency Trip
Tripping hazard	Be alert, Watch Step
Fire risk	Operate alarm, Attempt to fight while feel safe to do so.

Signature of each student;

Permission to carry out experiment

Safety Supervisor name:

Andrew Lapthorn

Signature:

Figure B.1 A scan of a hazard identification form used in testing.